IMPACTS OF COARCTATION COEXISTING WITH OTHER CARDIOVASCULAR DISEASES ON HEMODYNAMICS USING PATIENT-SPECIFIC LUMPED PARAMETER AND LATTICE BOLTZMANN MODELING

IMPACTS OF COARCTATION COEXISTING WITH OTHER CARDIOVASCULAR DISEASES ON HEMODYNAMICS USING PATIENT-SPECIFIC LUMPED PARAMETER AND LATTICE BOLTZMANN MODELING

BY

REZA SADEGHI, M.Sc.

A Thesis Submitted to the Department of Mechanical Engineering and School of Graduate Studies in Partial Fulfilment of the Requirements for the Degree Doctor of Philosophy

Doctor of Philosophy (2021), Department of Mechanical Engineering, McMaster University, Hamilton, Ontario

TITLE: Impacts of coarctation coexisting with other cardiovascular diseases on hemodynamics using patient-specific lumped parameter and Lattice Boltzmann modeling

AUTHOR: Reza Sadeghi, M.Sc.

SUPERVISOR: Dr. Zahra Keshavarz-Motamed

PAGES: xxii, 279

Lay Abstract

Coarctation of the aorta is a congenital narrowing of the proximal descending aorta which coexists with other cardiovascular diseases. Although accurate and early diagnosis of coarctation hinges on blood flow quantification, proper diagnostic methods for coarctation still lack because fluid-dynamics methods that can be used for accurate flow quantification are not well developed yet. We developed an image-based patient-specific computational framework that can quantify hemodynamics in patients with coarctation. Moreover, we investigated the impact of coarctation coexisting with other diseases and its interventions on hemodynamics to answer clinical questions.

Abstract

Effective diagnosis of COA hinges on quantifications of the global hemodynamics (heart function metrics and workload), and the local hemodynamics (3-dimensional flow dynamics in COA). In this study, we developed an image-based framework that can quantify local and global hemodynamics for COA diagnosis. The proposed framework uses lattice Boltzmann method and lumped-parameter modeling that only needs routine non-invasive clinical patient data. The computational framework was validated against clinical cardiac catheterization data and Doppler echocardiographic measurements.

One of the complicating factors of COA is its common association with mixed valvular diseases (MVD), which include varying combinations of aortic and mitral valve pathologies. Treatment strategies for these patients are quite unclear and differ from patient to patient. In order to evaluate risk factors and create guidelines for intervention aimed at minimizing the progression of cardiovascular disease, the impact of COA and MVD on aortic fluid dynamics in patients with COA and MVD was investigated in this thesis. Our results show that interaction of MVD with COA fluid dynamics may amplify adverse hemodynamic effects especially downstream of COA and may contribute to speed up the progression of the disease. The results suggest that some more aggressive surgical approaches may be required as regularly chosen current surgical techniques may not be optimal for patients with both COA and MVD.

The appropriate surgical technique for COA repair often remains unclear for adult patients. Extra-anatomical bypass grafting has been recommended in some of the COA cases. To effectively evaluate risk status and create guidelines for intervention, precise quantification of aortic fluid dynamics and hemodynamics is required. We used a patient-specific numerical framework to investigate the impact of bypass grafts on aortic fluid dynamics in patients with COA. This study can partially explain the complications associated in patients with COA who underwent bypass grafting.

Acknowledgements

My sincerest gratitude and appreciation go out to my supervisor, Dr. Zahra K. Motamed for her unlimited supports and continuous guidance during the course of this research. This work could not have been accomplished without her professional supervision, persistent motivation, and encouragement as well as her scientific, moral and financial supports throughout my PhD study. Her valuable advice has not been only guided me throughout my entire research, but also prepared me for my next journey.

I am very honored to have very distinguished researchers in my PhD defense committee. I would like to thank Dr. Hoda Hatoum for accepting to be the external member of my PhD defense committee and for her valuable comments and Dr. Ali Emadi for accepting to chair my defense committee. I sincerely appreciate the members of my supervisory committee Dr. Javier Ganame and Dr. Chan Ching for their time and constructive comments throughout my study. I would like to give special thanks to Dr. Julio Garcia from University of Calgary to provide us clinical data and to assist us to analyze them.

In my entire research, I would like to recognize the invaluable assistance of my colleagues and friends in Motamed Lab, Seyedvahid Khodaei, Benjamin Tomka, Nikrouz Bahadormanesh, Krishna Gandhi whose inputs enormously helped me to fulfill the goals of my project. I also thank all the faculty, staff and graduate students at the department of mechanical engineering for all their help and support.

Most of all, I need to extend my appreciation and my deep gratitude to my parents and sister for their encouragement and consistent support. Thank you for instilling in me the self-belief to always search for my dreams, and for the never-ending sacrifices you have made throughout your lives which have allowed me to be standing here today.

Contents

List of Figures

List of Tables

Declaration of Academic Achievement

- Chapter 1, "Introduction and literature review", was drafted by Reza Sadeghi.

- Chapter 2, "Towards non-invasive computational-mechanics and imaging-based diagnostic framework for personalized cardiology for coarctation", Reza Sadeghi performed computational modeling, data collection and analysis, interpretation of data and manuscript writing; Seyedvahid Khodaei performed design and data analysis; Dr. Javier Ganame performed data analysis, interpretation of data and critical revision of the manuscript; Dr. Zahra K. Motamed performed conception and design, lumped parameter modeling, data collection and analysis, interpretation of data and manuscript writing.

- Chapter 3, "Impact of mixed valvular disease on coarctation hemodynamics using patient-specific lumped parameter and Lattice Boltzmann modeling", Reza Sadeghi performed computational development and modeling, image processing, data collection and analysis, interpretation of data and manuscript writing; Nadav Gasner and Seyedvahid Khodaei performed data analysis and manuscript writing; Dr. Julio Garcia performed clinical data collection, analysis and interpretation of data; Dr. Zahra K. Motamed performed conception and design, lumped parameter algorithm development, data analysis, interpretation of data and manuscript writing.

- Chapter 4, "Reducing morbidity and mortality in patients with coarctation requires systematic differentiation of impacts of mixed valvular disease on coarctation

hemodynamics", Reza Sadeghi performed computational modeling, image processing, data collection and analysis, interpretation of data and manuscript writing; Benjamin Tomka and Seyedvahid Khodaei performed data collection and analysis and manuscript writing; Dr. Javier Ganame and Dr. Julio Garcia performed clinical data analysis and interpretation of data; Dr. Zahra K. Motamed performed conception and design, lumped parameter algorithm development, data analysis, interpretation of data and manuscript writing.

- Chapter 5, "Impact of extra-anatomical bypass on coarctation fluid dynamics using patient-specific lumped parameter and Lattice Boltzmann modeling", Reza Sadeghi performed computational modelling, image processing, image analysis, interpretation of data and manuscript writing; Benjamin Tomka performed data analysis, interpretation of data, manuscript writing and critical revision; Krishna Gandhi performed interpretation of data and manuscript writing; Dr. Julio Garcia performed clinical data collection, analysis and interpretation of data; Dr. Zahra K. Motamed performed conception and design, lumped parameter algorithm development, data analysis, interpretation of data and manuscript writing.

- Chapter 6, "Conclusions and Future Direction" was drafted by Reza Sadeghi.

Chapter 1: Introduction and literature review

1.1   Isolated coarctation of the aorta

Coarctation of the aorta (COA) is a congenital narrowing of the isthmus zone, the section of the descending aorta distal to the left subclavian artery. The disease is characterized by stenosis in the proximal descending thoracic aorta. COA is one of the most common congenital heart defects, accounting for 5-8% of congenital heart diseases (CHD) cases with a reported prevalence of 3-4/10000 live births[1].

COA can be simple (i.e., isolated defect) or complex (i.e., associated with other cardiac defects). In most cases, COA is associated with other cardiovascular defects, including ventricular septal defect[2], persistent ductus arteriosus[3,4], and most commonly, valvular diseases[5].

Despite advancements in interventional and surgical techniques, patients with coarctation interventions and surgeries require close monitoring because of acute post-surgical complications, including hypertension, aortic dilation, re-coarctation, aneurysm and rupture[6].

1.2   Associated cardiovascular anomalies with coarctation of the aorta.

COA is not always isolated and is primarily associated with several congenital diseases and other cardiovascular anomalies. The most common anomalies coinciding with COA is the bicuspid aortic valve, but ventricular septal defect and persistent ductus arteriosus

also occur together with COA. Moreover, COA also occurs in almost 35% of female patients with Turner's syndrome which is a genetic disorder[7].

1.2.1 Valvular heart disease

Bicuspid aortic valve (BAV) is the most common associated defect with COA, occurring in approximately 60-85% of patients with COA[5]. Several subtypes of BAV and systems of classification of BAV have been described based on leaflet morphology and aortic valve shape[8,9]. Patients with concomitant COA and BAV are at increased risk of developing complications such as ascending aorta dilatation, aortic valve stenosis and aortic valve regurgitation[1]. Aortic regurgitation (AR) and aortic stenosis (AS) are seen in 4% and 5-17% of COA cases, respectively[5]. Furthermore, Association of COA and mitral valve abnormalities are also frequently found, most commonly mitral regurgitation (MR) in 4% of cases, but mitral stenosis (MS) is also prevalent[5].
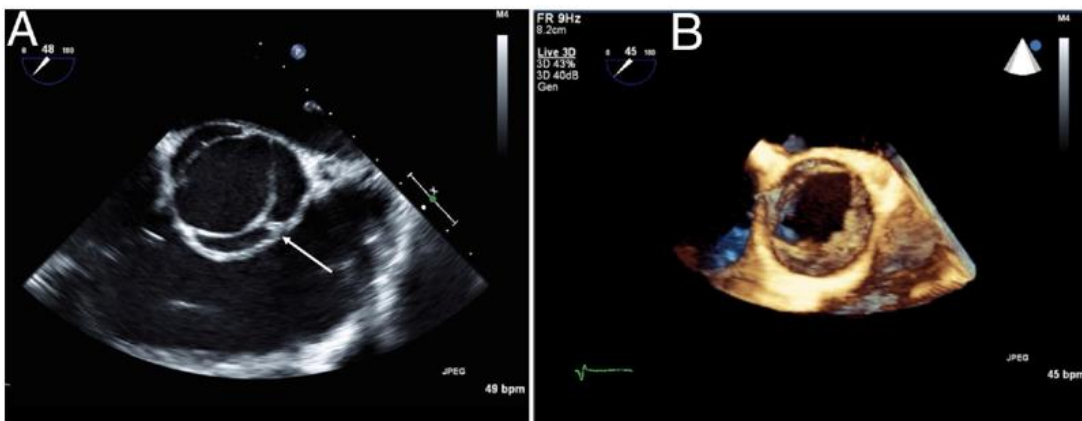
Figure 1-1. Bicuspid Aortic Valve (BAV). (A) Transesophageal short-axis view of BAV. (B) 3D Transesophageal view of BAV[10].

1.2.2 Ventricular septal defect

Ventricular septal defect (VSD) is a defect in the ventricular septum between the right and left ventricle. Large VSDs must be detected early and treated; otherwise, it may result in cyanosis, limitation of physical capacity, and a high risk of mortality[2,11]. The association of CoA with VSD in neonates is common and it may range from 6.2-14.8% depending on the studied population[6].
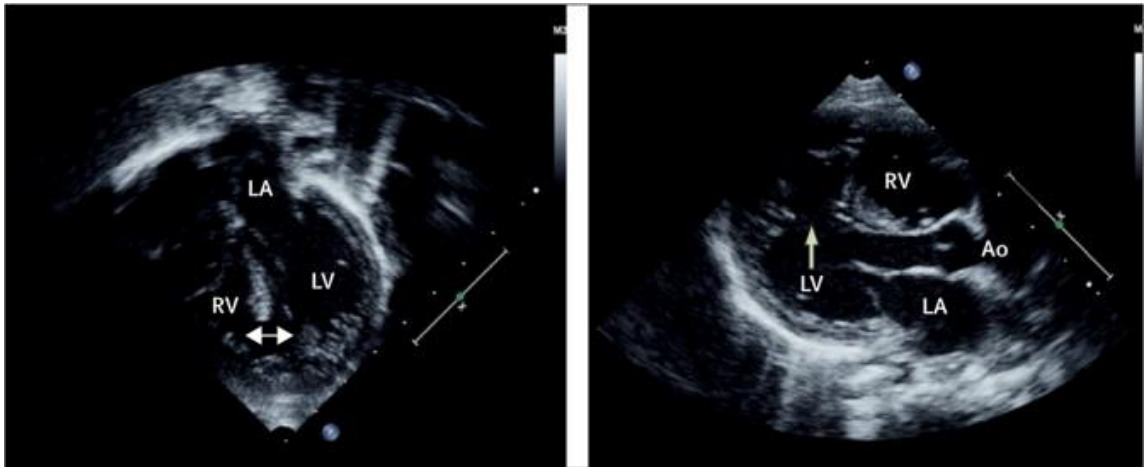
Figure 1-2. Echocardiogram of ventricular septal defect pointed by the arrows. LA is the left atrium, LV is the left ventricle, RV is the right ventricle, and Ao is the aortic valve[11].

1.2.3 Persistent ductus arteriosus

Persistent ductus arteriosus (PDA) is a vascular structure opening that connects the proximal descending aorta to the roof of the main pulmonary artery. The ductus arteriosus typically closes spontaneously early after birth. However, after the first few weeks of life, the persistence of ductal patency is abnormal[12]. PDA may lead to pulmonary hypertension followed by right-sided heart failure[3,4]. PDA is most frequently associated with aortic

coarctation. The association of PDA and COA may range from 11.5-20.6% depending on the studied population[6].
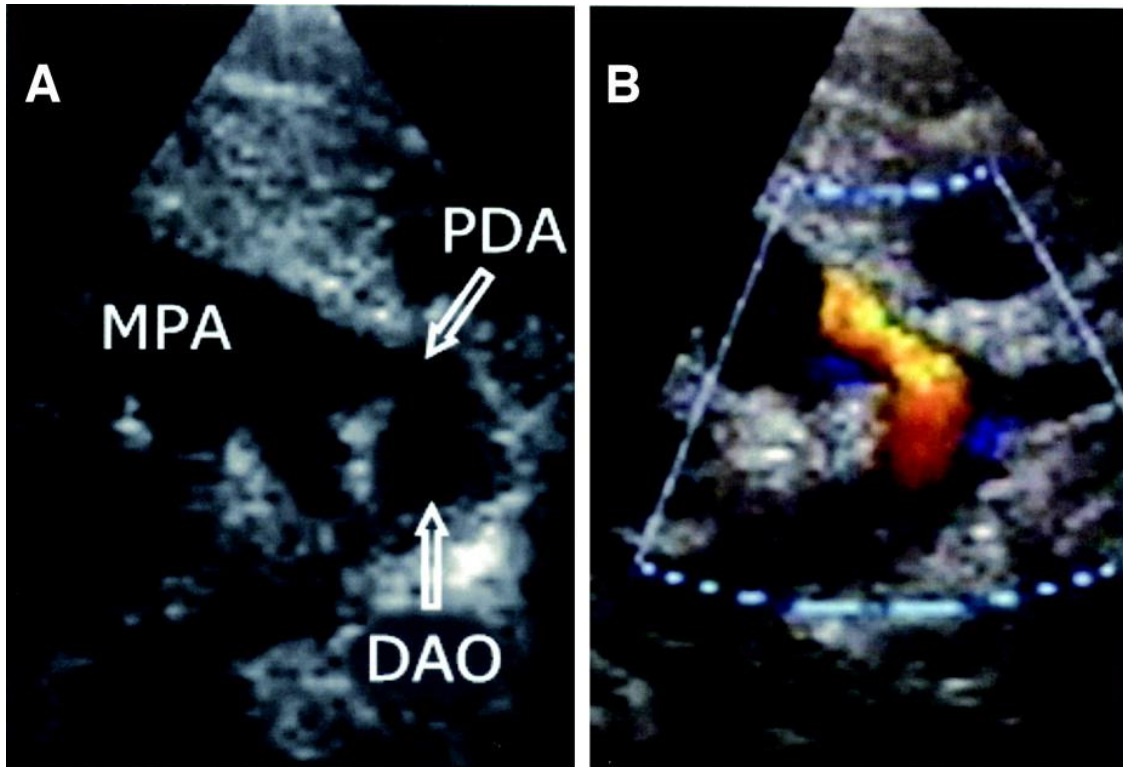
Figure 1-3. Echocardiograms of persistent ductus arteriosus (PDA). (A) 2D high parasternal short-axis view of PDA. DAO is the descending aorta and MPA is the main pulmonary artery. (B) Color Doppler image in the same view as A[12].

1.3   Long-term complications from coarctation of the aorta

Although operative repair for aortic coarctation has been performed since 1944[13], survivors have decreased life expectancy and many late life-threatening cardiovascular complications. Late cardiovascular complications after operative repair of COA, including aneurysm, aortic dilatation[14], hypertension[15,16], left ventricular hypertrophy[17], and recoarctation[18], still pose significant risks to the patients' health.

1.3.1 Aneurysm

The most common cause of death in COA is aneurysm and rupture of the aorta[19]. An aneurysm, classified by its location in the cardiovascular system, refers to a weakening of an artery wall that creates a bulge or distention. Almost 9% of patients develop aortic aneurysms late after the COA surgical repair (flap aortoplasty (17%), patch angioplasty (14%), bypass graft repair (6%) or end-to-end anastomosis (3%)).

Figure 1-4. Computed tomographic angiogram of a postoperative aneurysm of the left subclavian artery[20].

1.3.2 Aortic dilation

Aortic dilation is a severe vascular pathology that may occur in patients with COA, especially in the presence of BAV[21,22]. The aorta is considered pathologically dilated if the diameters of the ascending aorta and the aortic root exceed the norms for a given age,

gender, and body size[23]. Aortic dilation may end up with life-threatening complications such as aortic rupture and dissection[14].

1.3.3 Hypertension

Hypertension affects more than one billion adults worldwide, and it is a significant risk factor for many cardiovascular diseases[24]. Hypertension is a common long-term complication associated with COA, ranging from 25-68% depending on diagnostic method and studied population[15,16]. Early postoperative control of hypertension protects the aortic anastomosis, reduces the risk of an aneurysm formation, and alleviates post-coarctation syndrome. Hence, mean arterial pressure should be maintained in the normal range depending on the patient's age[25].

1.3.4 Left ventricular hypertrophy.

Left ventricular hypertrophy, is a condition in which the muscle wall of heart's left pumping chamber becomes thickened and may not pump efficiently. Left ventricular hypertrophy may also be a physiological response to exercise training[26].

COA imposes significant afterload on the left ventricular muscle, which results in increased wall stress and compensatory ventricular hypertrophy[17,27]. The patients with repaired COA are at risk of increased Left ventricular hypertrophy due to impairment of vascular mechanics and abnormal blood pressure regulation[28].
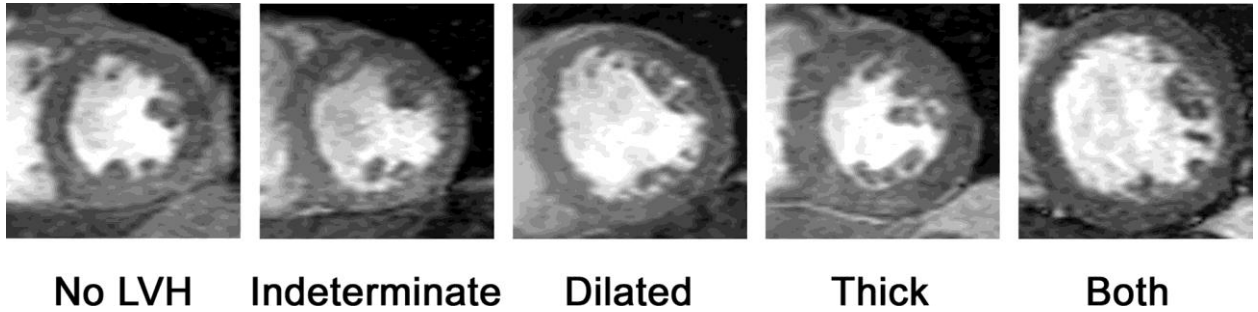
Figure 1-5. Magnetic Resonance Imaging (MRI) images of different patterns of left ventricular hypertrophy (LVH) compared to a patient without LVH[29].

1.3.5 Recoarctation

Recoarctation, one of the most common complications of COA surgery, is a term used to describe the narrowing of the same coarctation site after the surgical correction[18]. Recoarctation can be due to several mechanisms, such as thrombus formation at the suture line and incomplete initial repair. The prevalence of recoarctation is approximately 31% of the patients[18]. However, not all recoarctations are considered clinically significant. Common symptoms of recoarctation are increased arm-to-leg blood pressure drop, increased upper body high blood pressure, and weak femoral pulses. Reintervention may be needed when the catheter-measured pressure gradient over the recoarctation site is greater than or equal to 20 mmHg[30].

1.4   Coarctation of the aorta diagnosis

1.4.1 Arm-to-leg blood pressure difference measured by sphygmomanometer

Arm-to-leg blood pressure difference measured by sphygmomanometer may provide helpful information regarding the existence of aortic obstruction. Although there is no specific guideline on measuring arm-to-leg systolic pressure gradient in whom COA is suspected, several studies suggested that the reduction of ≥20 mmHg in arm-to-leg systolic pressure gradient may be considered a probable risk factor[31]. Several reports have also shown that arm-to-leg blood pressure difference may not accurately represent the hemodynamic severity of the stenosis[32].

1.4.2 Cardiac catheterization

Cardiac catheterization is the gold standard in assessing the pressure gradient across the coarctation site. Coarctation is classically defined as a catheterization-measured peak drop greater than 20 mmHg. Due to recent advances in non-invasive diagnosis techniques, cardiac catheterization is used more frequently in the setting of intervention than diagnosis[33].

1.4.3 Doppler echocardiography

Echocardiography has been used successfully to assess the morphology and hemodynamic severity of COA. Instantaneous peak trans-coarctation pressure gradients can be estimated by calculating the maximal velocity across the coarctation in the suprasternal view (V_1) and the velocity in the abdominal aorta in the subcostal view (V_2) and the correlation with the Bernoulli equation as follows[33]:

$$\Delta P_{CoA} = 4(V_1^2 - V_2^2) \tag{1}$$

Although due to its non-invasive, radiation-free, and low-cost nature, doppler echocardiography is currently preferred to assess coarctation severity, several theoretical and technical limitations may contribute to unavoidable sources of inaccuracy. The source of inaccuracy is first because of the improper use of the Bernoulli equation as the Bernoulli equation is applicable only to flow along a streamline, and it is not valid for non-steady or turbulent flow[33]. The other source of inaccuracy comes from the Doppler beam's misalignment with flow direction, resulting in velocity underestimation. Furthermore, low-quality images of echocardiography cause difficulties in determining the throat diameter of the coarctation and velocity measurement[33].

1.4.4 Computed tomographic angiography

Computed tomographic angiography (CTA) uses ionizing radiation and intravenous contrast to obtain intracardiac and extracardiac data with very high spatial resolution[34]. CTA provides invaluable information in diagnosing COA severity and managing patients

with COA. CT imaging does not produce significant artifacts due to metallic objects, making CT imaging an excellent utility for arch imaging in patients with prior stent implantation. However, the exposure to ionizing radiation, the reaction potential to contrast material and the inability to provide hemodynamic information, such as peak pressure gradient, are the primary drawbacks for CT imaging.

1.4.5 Magnetic resonance imaging

Magnetic resonance imaging (MRI) is one of the preferred non-invasive advanced imaging techniques for patients with COA. Like CTA, MRI provides high image resolution. However, unlike CTA, MRI does not include any exposure to ionizing radiation making it the method of choice for initial evaluation of aortic coarctation before repair and stent implant. MRI images are susceptible to metallic artifacts than CT, and hence it is not a promising modality of choice in patients with pre-existing stents in the region of interest[33].

1.4.6 Phase-contrast MRI

Phase-contrast magnetic resonance imaging (PC-MRI) is a specific magnetic resonance imaging type used primarily to determine flow velocities. Standard 2D PC-MRI was introduced in the late 1980s to enable through-plane assessment of moving fluids in magnetic resonance imaging (MRI). Since then, the development of 2D PC MRI has allowed the acquisition of a time-resolved three-dimensional velocity encoding, a

technique known as 4D (3D coordinates plus time) flow MRI. 4D flow MRI has made it possible to assess in-vivo hemodynamic velocity profiles non-invasively. After some improvements, including more powerful graphic processing units, lighter datasets, and cloud-based post-processing, this technique has gradually entered the field of clinical practice[35].
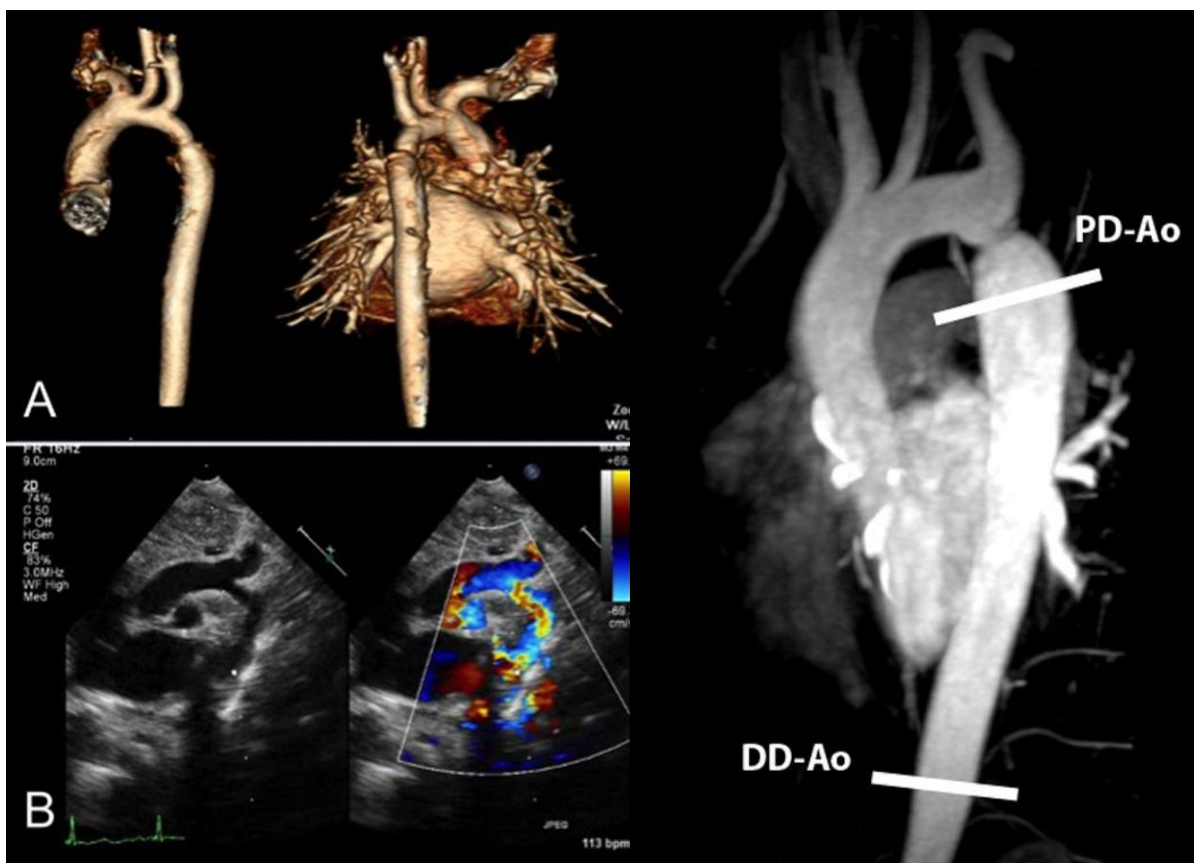
Figure 1-6. Coarctation imaging. (A) 3D CTA of a discrete distal coarctation. (B) 2D and coloured Doppler echocardiogram of a distal COA[36]. (C) PC-MRI of the proximal descending aorta (PDAo) and the distal descending aorta (DDAo)[37].

1.5   Current treatments for coarctation

Treatments for coarctation have developed considerably over the years and include surgical repair and catheter-based repair treatments. Treatment of choice mainly depends on the patient's age at the time of diagnosis and the severity of COA[38].

1.5.1 Surgical repair

Surgical intervention for coarctation of the aorta was first described in 1944[13]. Since the initial description of the surgical repair of COA, several successful surgical treatments, including end-to-end anastomosis, subclavian flap aortoplasty, patch aortoplasty, and bypass graft, have been proposed[39].

1.5.1.1 Resection with end-to-end anastomosis

In this procedure, the stenotic segment of the aorta is resected via open lateral thoracotomy surgery, and the two ends of the aorta are then anastomosed together. The incidence of re-coarctation in a direct end-to-end anastomosis is relatively high with reported incidence rates of 41% to 51%, and it is not commonly used nowadays[40]. A modification of the classic end-to-end anastomosis (EEA) is called extended EEA. Extended EEA involves end-to-side anastomosis of the aortic arch more proximally along its lesser curvature. It provides superior relief from the various levels of obstruction in COA. The extended EEA relatively has low re-coarctation incidence[33].

(a)   **(b)**

(c)   **(d)**
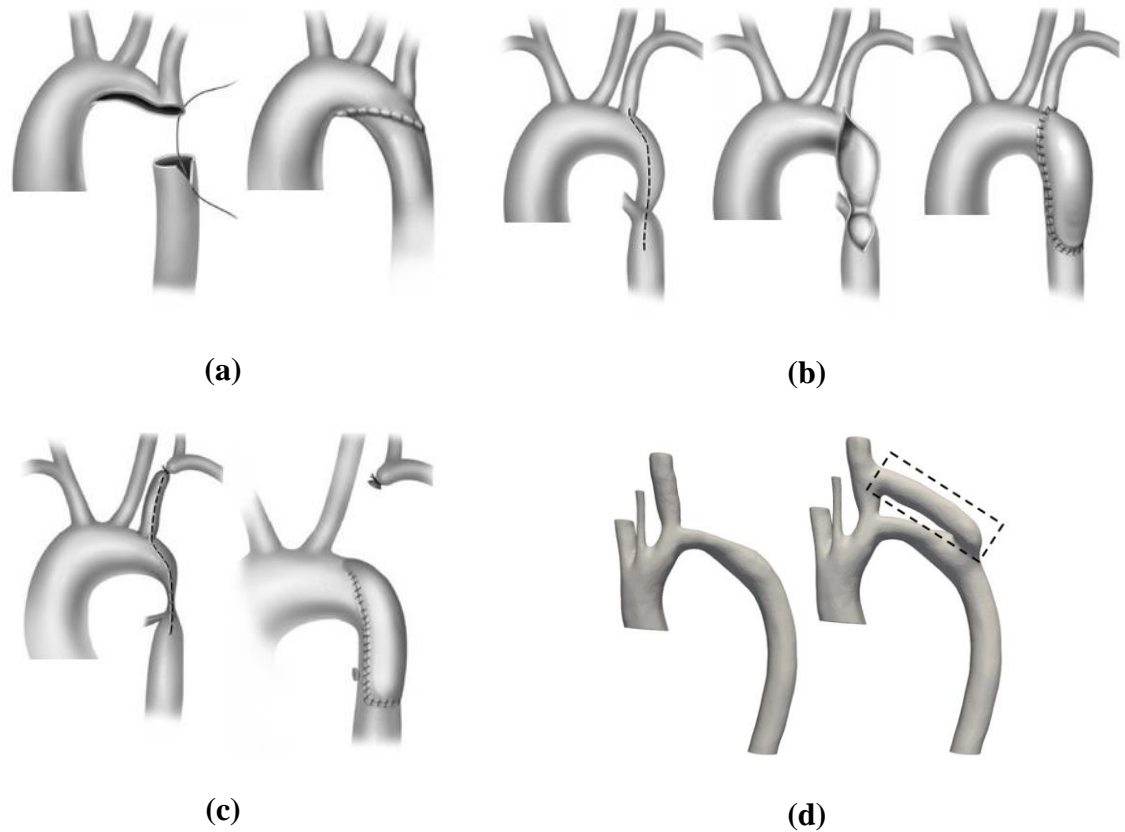
Figure 1-7. Surgical approaches to repair COA: (a) extended end-to-end anastomosis for repair coarctation of the aorta, (b) patch aortoplasty for the repair of coarctation, and (c) left subclavian flap aortoplasty for the repair of coarctation (d) Bypass graft surgery[33].

1.5.1.2 Patch aortoplasty

The patch aortoplasty surgery was introduced in 1957[41]. In this technique, the aorta is opened longitudinally through the coarctation region and extending to the left subclavian artery. Then, an elliptic woven Dacron patch is inserted to expand the diameter of the lumen. This operation had a significantly lower recoarctation rate than classic end-to-end anastomosis, ranging from 5-12%. Although patch aortoplasty led to a reduction in re-coarctation, it was met with a high incidence of aneurysmal formation[41].

1.5.1.3 Left subclavian flap aortoplasty

Another surgical procedure which was developed for the management of COA is left subclavian flap aortoplasty. Subclavian flap aortoplasty consists of dividing the left subclavian artery and folding down the subclavian artery flap over the aortic narrowing region. Although the COA repair by subclavian flap aortoplasty carries the disadvantage of impaired blood supply to the left arm[42], the recurrence rate is lower than with patch aortoplasty[43].

1.5.1.4 Bypass grafting

Although vascular surgeons currently use previous surgical treatments, they still rely on bypass graft procedures when other surgeries are unfeasible. When performing bypass grafting, proximally, the prosthetic conduit is anastomosed to the ascending aorta or the subclavian artery, distally the conduit is attached to the descending aorta[40,44,45]. Bypass graft surgery leaves the stenosed aorta in situ, but is able to divert blood around the area of coarctation and provide adequate blood flow to the distal aorta[40]. While extra-anatomic bypass can be performed with low risk[46], some adverse cases do exist and include prosthetic graft pseudoaneurysm, intimal hyperplasia and potential recoarctation, all of which may require reoperation[47-53].

1.5.2 catheter-based repair

During the ensuing four decades, surgical repair techniques remained the only treatment for COA. In the late 1970s, interventional catheter-based techniques were introduced as

an alternative to surgical repair procedures[54]. Since then, transcatheter interventions have become increasingly popular and emerge as the treatment of choice amongst clinicians. Transcatheter options include simple balloon angioplasty and angioplasty followed by stenting. While these catheter-based techniques offer minimally invasive treatments, reduced hospitalization time and promising outcomes, the needs for re-intervention and likelihood for recoarctation are their potential limitations[33].

(a)   (b)
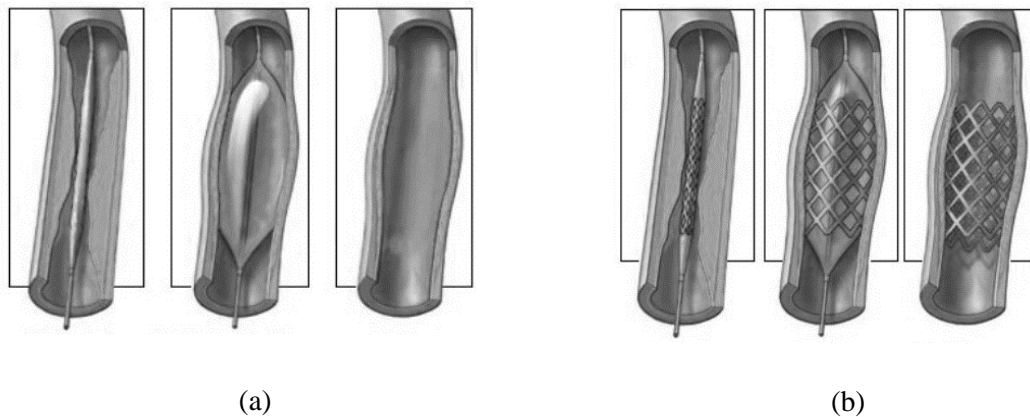
Figure 1-8. Catheter-based interventional approaches to repair COA: (a) Balloon angioplasty, (b) Stent placement[33].

1.5.2.1 Balloon angioplasty

Balloon angioplasty, first performed as early as 1982[55], is the first treatment of COA to stabilize newborns and infants who cannot receive immediate surgery[56]. A catheter wire is introduced into the femoral artery percutaneously and is positioned across the aortic coarctation region. Then, the balloon is inflated to widen a narrow part of the aorta. Balloon angioplasty stretches the target lesion; however, it may be followed by a tear of the intima, early and late retraction of the lesion, resulting in recurrence of the narrowing, dissection, pseudoaneurysm, and rupture[57].

1.5.2.2 Stent placement

The use of stent implantation, the other catheter-based technique for repairing COA, began in the 1990s[58]. Stents were introduced to overcome the shortcomings of balloon dilation in the balloon angioplasty technique by expanding and scaffolding the target region to avoid recurrent stenosis and recoil intima cells. Therefore, stenting may result in fewer aneurysms and ruptures. However, it has some shortcomings, including vascular trauma at the sheath insertion point, wall hyperplasia, and damaging the vessel[57].

1.6   Computational modelling of coarctation of the aorta

1.6.1 Numerical Modelling of the Cardiovascular System

In recent years, high fidelity multiscale cardiovascular modelling frameworks are becoming a powerful tool in cardiovascular research, medical device design, surgical planning and interventional procedures[59,60]. Despite ongoing advances in imaging techniques and non-invasive flow measurements, it remains challenging to acquire accurate in-vivo data and fully understand a patient's condition.

High spatial resolution imaging modalities such as three-dimensional magnetic resonance imaging (3D-MRI) and computed tomography (CT) provide a wealth of information on the morphology of aorta and echocardiography and Four-dimensional MRI (4D-MRI) enables measurement of the velocity field. However, neither of the aforementioned imaging techniques can provide data on the pressure along the aorta region nor have

sufficient spatial resolution to accurately calculate velocity gradient and the wall shear stress (WSS)[61]. The lack of capacity to accurately compute these influential hemodynamic parameters may result in unreliable interpretation of the data[62].

Computational fluid dynamics (CFD) with individualized inputs (e.g., patient's geometry from imaging modalities and flow measurement from ultrasound or 4D flow MRI) can yield high temporal and spatial resolution data on critical physiological parameters, such as velocity, velocity gradient, pressure, vorticity, and wall shear stress, which can aid to the clinicians' decision making[61]. In addition, the computational models could be predictive tools in such a way as to parametrically investigate the hemodynamics impact of various treatments or visually test specific parameters on the progression of diseases[61,63]. The following sections summarize the literature review on assumptions made to model blood flow in healthy aorta and aorta with coarctation.

1.6.2 Geometrical representation of the COA anatomy

One of the most critical aspects of COA is the morphology of the aorta and coarctation region[64]. Luminal diameter of the aorta, the whole length of the aorta, aortic arch curvature, and diameter of the aortic lumen at the coarctation site play essential roles in the flow behaviour at the coarctation site[65]. Furthermore, the inclusion or exclusion of the other arteries that branch off the aorta (subclavian, carotids, renal, etc.) and the effects of downstream vasculature are essential on flow patterns. Two fundamental approaches have been adopted in the modelling of aortic flow: (1) the use of patient-specific geometries[66]

(2) the use of idealized geometries, which is most appropriate for parametric studies[67,68].

Due to the skepticism of the clinicians, idealized models are rare in the literature, and

most COA models in the literature are 'patient-specific' in which the geometry domain is

derived from clinical imaging data of a given patient.

To reconstruct 3D patient-specific geometries, thresholds are applied to a stack of 2D

images to separate the vessel section of interest. The geometry is typically smoothened,

and the domain boundaries are trimmed. In several studies, the trimming step includes

removing the supraoptic branches[69,70] and visceral arteries[71,72] for simplicity. However,

such simplifications limit the utility of the patient-specific modelling approach. For

instance, approximately 15% of ascending aorta flow enters the supra-aortic branches and

removing these branches alters the local hemodynamics[73].

Some studies have shown that small virtual changes in geometry might be expected to

influence the predicted flow characteristics considerably[74]. However, the influence of

image reconstruction accuracy on numerical results has not, to the author's knowledge,

been reported in detail[75].

To wrap it up, from a purely morphological point of view, fewer simplifications and

omissions of smaller arteries will lead to a better representation of the hemodynamics in

the geometry of interest. However, proper boundary conditions must be applied for each

additional branch included in the model, making the model more sophisticated.

1.6.3 Boundary conditions

Given the complexity of the fluid dynamics of blood flow, a realistic full patient-specific numerical model of the entire cardiovascular system is prohibitively computationally expensive even though some studies consider a large proportion of entire vasculature[76-78]. The appropriate selection of boundary conditions in computational models is an essential component of producing realistic results. The appropriate application of boundary conditions in computational models of the aorta plays a crucial role in translating numerical blood flow models into the clinical context. Accurate data from specific patients at all the domain boundaries is often unavailable, and thus several reasonable assumptions must be made.

The most common wall boundary condition for modelling the aorta is an impenetrable boundary with a no-slip condition. Hence, the motion of the vessels is not included, and blood movement does not impact the movement of the wall[79]. This assumption is justified by the slight in-plane movement of wall motion at several locations across the descending aorta. In addition, arterial stiffening is a common long-term symptom among COA patients, and aortic rigidness is observed during aging[80]. Although several studies investigated fluid-structure interaction of aorta[81,82], it seems that an accurate patient-specific compliant wall model plays an essential role in the flow pattern prediction. On the other hand, many researchers found it reasonable to avoid computational expensive FSI modelling due to its large degree of freedom[83,84].

In the majority of COA simulations, the inflow boundary condition is frequently applied via a uniform or time and/or spatially varying velocity curve (flat, plug, parabolic or Womersley profile shaped)[85-89] derived from PC-MRI or via a lumped parameter modelling description of the heart coupled to the inlet boundary[84,90]. Some studies have shown that more realistic inlet conditions, including secondary flow features and valve morphology, are essential to capture local flow features[85,91]. On the other hand, others believe this impact is small in the downstream aorta and memory of inlet condition eventually will be lost downstream due to the substantial geometrical-driven flow[92].

The most common approaches for applying the BCs at the system outlets (branched arteries and the ascending aorta) are constant pressure (usually zero) and 'flow splitting'[92]. A conventional zero pressure condition was assigned in most studies as incompressible flows only dictated by the local pressure gradient at the descending aorta outlet[73]. An alternative option is to prescribe generic pressure waves from other studies[73,93]. Another common boundary condition is based on hydraulic-electrical analogue circuits. In this method, called zero-dimensional modelling or lumped parameter modelling, the compliant and resistive aspects of the vasculature components are modelled with electrical circuits. 0D models are integrated with 3D domain outlet boundaries to provide a dynamic representation of the influence of the downstream vasculature[76,84,94,95].

1.6.4 Fluid Modelling

Blood exhibits shear thinning, viscoelastic, and thixotropic non-Newtonian properties[92]. Several studies have indicated the importance of including shear-thinning non-Newtonian characteristics in patient-specific modelling[96-98]. However, the majority of blood flow simulations assume that the fluid is Newtonian[73,99]. Several classic and numerical resources report that it is reasonable to assume that the fluid in large arteries (e.g., aorta, carotid) is Newtonian because the flow in larger arteries primarily is driven by high shear rates and non-Newtonian contribution is negligible compared to other modelling uncertainties[79,100].

Another critical issue in modelling blood flow in the aorta is whether to model the fluid as laminar, transitional, or turbulent flow. Whereas laminar flow is deterministic, when flow becomes turbulent, random fluctuations in velocity occur, and turbulent eddies form and dissipate energy in the flow. The state of turbulence is often described in terms of Reynold's number (Re), which is the ratio of inertial forces to viscous forces. In steady pipe flow, the transition to turbulence occurs at a critical Reynold's number. Several CFD studies report critical Reynolds values in the range of 2700–15000[101,102]. Some studies use the laminar model by the justification that Reynolds numbers in laminar flow are up to 3700, and some refer to classic text that states arterial flow is always laminar[102]. However, some recent studies have shown that although blood flow is generally laminar in the whole cardiac cycle, the transitional and turbulent flow has been observed in either healthy aorta or COA cases[73]. A wide range of approaches, including direct numerical

simulations (DNS)[103,104], Large-eddy simulations (LES)[84,105-109] and Reynolds-Averaged Navier-Stokes (RANS)[67,110-112] were adopted to model and resolve the aortic flow.

Typically, computational models rely on solving the Navier Stokes equation. There are excellent references on quantifying blood flow in the aorta using 3-D conventional CFD methods based on the discretization of Navier–Stokes's equations (finite difference method[103], finite volume method[105,106,113], finite element method[72,83,88], etc.). An alternate to traditional numerical discretization schemes for NS solvers is the lattice Boltzmann method. The fluid is viewed as a population of particles, and these particles can move in discrete directions between lattice points. Due to the capability of LBM in handling complex geometries and performing efficiently on parallel architectures, it is becoming popular in modelling vascular flow[60,114]. Lattice Boltzmann method is recently used for modelling blood flow in patients with coarctation of the aorta[90,104,115].

1.7   Objectives of the thesis

The present research's aims and objectives are as follows:

Aim 1: To develop an innovative computationally fast and imaging-based framework for COA diagnosis that uses lattice Boltzmann method and lumped-parameter modeling that is solely based on routine non-invasive clinical patient data.

Aim 2: To validate the proposed framework against clinical cardiac catheterization data, calculations using the conventional finite-volume method, clinical Doppler echocardiographic measurements and 4D flow MRI measurements.

Aim 3: To investigate the impact of COA and associated mixed valvular diseases (MVD; various combinations of aortic and mitral valvular pathologies) on local and global hemodynamics and as a result effectively evaluate risk status and create guidelines for intervention aimed at minimizing the progression of cardiovascular disease in patients with MVD and COA.

Aim 4: To investigate the impact of COA and MVD on aortic fluid dynamics in patients with COA and MVD and assess the presence and the severity of the MVD on progression of the disease and irregular flow patterns at the COA region.

Aim 5: To investigate the impact of bypass grafts on aortic fluid dynamics in patients with COA and provide insights into possible reasons for graft failure.

1.8   Thesis organization

Chapter 1: *"Introduction and literature review".* This chapter provides a general introduction to the research by describing aortic coarctation in detail. In addition, clinical imaging modalities, invasive diagnostic methods, and treatments for COA are also assessed in terms of their advantages and shortcomings. This chapter also describes the background and reviews literature on patient-specific numerical modelling with a focus on COA. Finally, detailed research objectives and the outline of this thesis will be described.

Chapter 2: *"Personalized intervention cardiology with transcatheter aortic valve replacement made possible with a non-invasive monitoring and diagnostic framework".*

24

This chapter encompasses the development of new non-invasive methods that can quantify local and global hemodynamics for diagnosis of aortic coarctation. This computationally fast framework uses Lattice Boltzmann method and lumped-parameter modeling that only rely on routine non-invasive clinical patient data. Our findings position this framework as a promising new non-invasive diagnostic tool that can provide diagnostic analyses not possible with conventional diagnostic methods. The proposed framework was validated against clinical Doppler echocardiographic measurements, cardiac catheterization data, and calculations using the conventional finite-volume method. It is shown that the framework can provide diagnostic information that is needed to assess patient risk and clinical outcomes.

Chapter 3: *"Risk quantification in patients with coarctation, requires evaluation of severity of mixed valvular disease and coarctation".* In this chapter, we used our framework to investigate the impact of COA and mixed valvular diseases (MVD) on aortic fluid dynamics in patients with COA and MVD. The proposed patient-specific computational-mechanics framework integrates the local hemodynamics with the global circulatory cardiovascular system using the Lattice Boltzmann method along with lumped parameter modeling. The computational framework was also validated against clinical cardiac catheterization data and Four-dimensional flow magnetic resonance imaging data. The severity and presence of MVD on the evaluation of risks in patients with COA were investigated in this chapter as well.

Chapter 4: *"Reducing morbidity and mortality in patients with coarctation requires systematic differentiation of impacts of mixed valvular disease on coarctation hemodynamics".* In this chapter, it was shown that interaction of MVD and COA may amplify irregular flow patterns downstream of COA and contribute to speed up the progression of the disease. Since treatment strategies for patients with COA and MVD are quite unclear and differ on an individualized basis, we used our patient-specific numerical framework to investigate the effects of MVD on COA in terms of both local and global hemodynamic.

Chapter 5: *"Impact of extra-anatomical bypass on coarctation hemodynamics using patient-specific lumped parameter and Lattice Boltzmann modeling".* In this chapter, we investigated the impact of bypass grafts on aortic fluid dynamics in three patients with COA. Our non-invasive patient-specific framework was used to quantify blood flow through artery bypass grafts. Our results can provide insights into possible reasons for graft failure.

Chapter 6: *"Conclusion and future works".* This chapter draws together the important findings from each of the previous chapters. Moreover, some new exploratory lines of research for future work were offered.

Chapter 2: Towards non-invasive computational-mechanics and imaging-based diagnostic framework for personalized cardiology for coarctation

Reza Sadeghi[1], Seyedvahid Khodaei[1], Javier Ganame[2,3], Zahra Keshavarz-Motamed*[1,4,5]

1. Department of Mechanical Engineering, McMaster University, Hamilton, ON, Canada
2. Division of Cardiology, Department of Medicine, McMaster University, Hamilton, ON, Canada
3. St. Joseph's Healthcare and Hamilton Health Sciences, Hamilton, ON, Canada
4. School of Biomedical Engineering, McMaster University, Hamilton, ON, Canada
5. School of Computational Science and Engineering, McMaster University, Hamilton, ON, Canada

* Correspondence author

2.1   Abstract

Coarctation of the aorta (COA) is a congenital narrowing of the proximal descending aorta. Although accurate and early diagnosis of COA hinges on blood flow quantification, proper diagnostic methods for COA are still lacking because fluid-dynamics methods that can be used for accurate flow quantification are not well developed yet. Most importantly, COA and the heart interact with each other and because the heart resides in a complex vascular network that imposes boundary conditions on its function, accurate diagnosis relies on quantifications of the global hemodynamics (heart-function metrics) as well as the local hemodynamics (detailed information of the blood flow dynamics in COA). In this study, to enable the development of new non-invasive methods that can quantify local and global hemodynamics for COA diagnosis, we developed an innovative fast computational-mechanics and imaging-based framework that uses Lattice Boltzmann method and lumped-parameter modeling that only need routine non-invasive clinical patient data. We used clinical data of patients with COA to validate the proposed framework and to demonstrate its abilities to provide new diagnostic analyses not possible with conventional diagnostic methods. We validated this framework against clinical cardiac catheterization data, calculations using the conventional finite-volume method and clinical Doppler echocardiographic measurements. The diagnostic information, that the framework can provide, is vitally needed to improve clinical outcomes, to assess patient risk and to plan treatment.

2.2   Introduction

Coarctation of the aorta (COA) is a congenital narrowing of the proximal descending aorta. The hemodynamic severity and clinical manifestations of COA vary from asymptomatic mild narrowing of the aortic isthmus to severe obstruction associated with cardiac defects, congestive heart failure and shock in the neonatal period, persistent hypertension and aortic dissection[1]. Not all patients are symptomatic but with disease progression in severity, 60% of adults over 40 with uncorrected COA develop heart failure and 75% of them die by the age of 50, and 90% of them die by the age of 60[2]. Indeed, despite advancements in interventional/surgical techniques, the long-term morbidity and subsequent mortality of patients with COA remain high in comparison with the general population[3,4].

"Cardiology is flow"[5] and therefore the essential sources of COA morbidity can be explained on the basis of adverse hemodynamics: abnormal biomechanical forces, abnormal flow patterns - that often characterized by disturbed and turbulent flow- and in some cases by an increase in the heart workload that leads to the development and progression of cardiovascular diseases[5-8]. Flow quantification can be greatly useful for accurate and early diagnosis, but we still lack proper diagnostic methods for many cardiovascular diseases[6,9], including COA, because the fluid-dynamics methods that can be used as engines of new diagnostic tools are not well developed yet. In this research we contributed to advancing computational mechanics as a powerful means to augment

clinical measurements and medical imaging to create novel diagnostic methods for COA at no risk to the patient[6,7].

The heart resides in a sophisticated vascular network whose loads impose boundary conditions on the heart function[6,7,10-12] . Effective diagnosis of COA hinges on: (1) quantifications of the global hemodynamics (heart function metrics, e.g., left ventricle workload and instantaneous pressure), and (2) quantifications of the local hemodynamics (detailed information of the 3-D flow dynamics in COA). However, there is no method to invasively or noninvasively quantify the heart workload *(global hemodynamics)* while providing contribution breakdown of each component of the cardiovascular system. Moreover, current diagnostic methods cannot quantify details of the flow dynamics of the circulatory system *(local hemodynamics).* Although all of these can provide valuable information about the patient's state of cardiac deterioration and heart recovery, currently, clinical decisions are largely made based on the anatomy using medical imaging[9].

A clinically-useful computational diagnostic framework that can quantify both *local* and *global* hemodynamics for patients with coarctation should satisfy the following 3 requirements:

(1) The local fluid dynamics is influenced by the conditions downstream and upstream of coarctation. Therefore, in addition to performing the 3-D blood flow calculations in the patient-specific geometry, imposing accurate patient-specific flow and pressure boundary conditions is critically important for a computational diagnostic framework. This not only gives patient-specific flow and pressure

conditions to the local flow but also enables providing diagnostic information about the global circulatory physiology. The patient-specific boundary conditions should be obtained *non-invasively* in each patient because obtaining them invasively (e.g., with catheterization) contradicts the whole purpose of the computational framework.

(2) To reliably augment the current clinical diagnostics capabilities with calculations of blood flow through COA, the computational diagnostic framework should be fast enough to provide results in a matter of minutes rather than days.

(3) The computational framework should provide valid results to be considered as a reliable diagnostic tool. Upon development of a computational diagnostic framework, its results should be validated against clinical data that include data obtained using cardiac catheterization, Doppler echocardiography and magnetic resonance imaging. Cardiac catheterization is used as the clinical gold standard to evaluate pressure and flow through heart and circulatory system, but it can only provide access to the blood flow and pressure in very limited regions. Doppler echocardiography is the most versatile tool to evaluate local hemodynamics and has a high temporal resolution, but it has limited spatial access through chest. Phase-contrast magnetic resonance imaging can provide local flow, but it is not possible for many patients with implanted devices. As each of these modalities have their own limitations, a multi-modality validation of the computational framework would be required.

There have been attempts for quantifying blood flow through COA (local hemodynamics) using conventional macroscopic numerical methods based on the discretization of Navier–Stokes equations (finite difference method, finite volume method, finite element method, etc.) [11,13-20]. None of these models can satisfy Requirement #2 above because the conventional methods need days of calculations and therefore, they are not feasible for clinical diagnosis. Furthermore, many of these models were restricted to low Reynolds numbers. None of these models satisfy Requirement #3: most were not validated while some were only partially validated. Most of these studies do not satisfy Requirement #1 as they do not have patient-specific boundary conditions. Among all, three studies[15,20,21] coupled blood-flow calculations with lumped-parameter modelling to impose boundary conditions on the calculations. However, the lumped-parameter models either were not patient specific or needed information from blood-flow measurements using MRI that is not available in all clinics and is not feasible in patients with implanted devices.

Recently, Lattice Boltzmann method (LBM), rooted in mesoscopic kinetic equations[22], has been developed as a powerful and fast technique for accurate simulations of fluid flow. Since the birth of LBM, there has been an increasing popularity of this method as an alternative to computationally intensive conventional methods for fluid dynamics simulations[23] because of its simplicity, handling of complex flow phenomena, efficient executions[24] and the fact that LBM equations can be solved locally and explicitly, and they are intrinsically parallelizable[25]. These promising features have motivated researches to use LBM as the method of choice for computational cardiology[26-29]. Few studies used LBM for the investigation of local hemodynamics of COA without

considering any global effects. Although these studies showed effectiveness of LBM for flow analysis, their aim was not developing a diagnosis tool, so they did not satisfy requirements #1 and #3 above [26,30,31].

In this paper, using LBM and lumped parameter modeling (LPM), we developed an innovative fast computational-mechanics and imaging-based framework that can eventually, upon further development and validation, work as the main component of new diagnostic methods for COA. This computationally fast framework enables (1) quantifying details of 3-D fluid dynamics through the aorta and COA (*local hemodynamics*); (2) quantifying heart function metrics, e.g., left ventricle (LV) workload and instantaneous LV pressure (*global hemodynamics*). Currently, none of the above metrics can be obtained noninvasively in patients and when invasive procedures are undertaken, the collected metrics cannot be as complete as the results that the proposed framework can provide. Our LPM uses a limited number of input parameters all of which can be reliably measured using Doppler echocardiography and a sphygmomanometer with no risks to the patient and thus will make effective and personalized diagnosis possible. Note that the proposed method does not need any catheter data as input parameters of the model. We used clinical data of 3 patients with COA in both pre and post intervention states not only to validate the proposed framework but also to demonstrate its diagnostic abilities by providing novel analyses and interpretations of clinical data. The validation was done against clinical cardiac catheterization data, calculations using the conventional finite-volume method and clinical Doppler echocardiographic measurements. To the best of our knowledge, this is the first study that

couple LBM and LPM and satisfies all 3 requirements for developing a clinically-effective computational diagnostic framework to quantify both local and global hemodynamics in patients with COA in both pre and post intervention states.
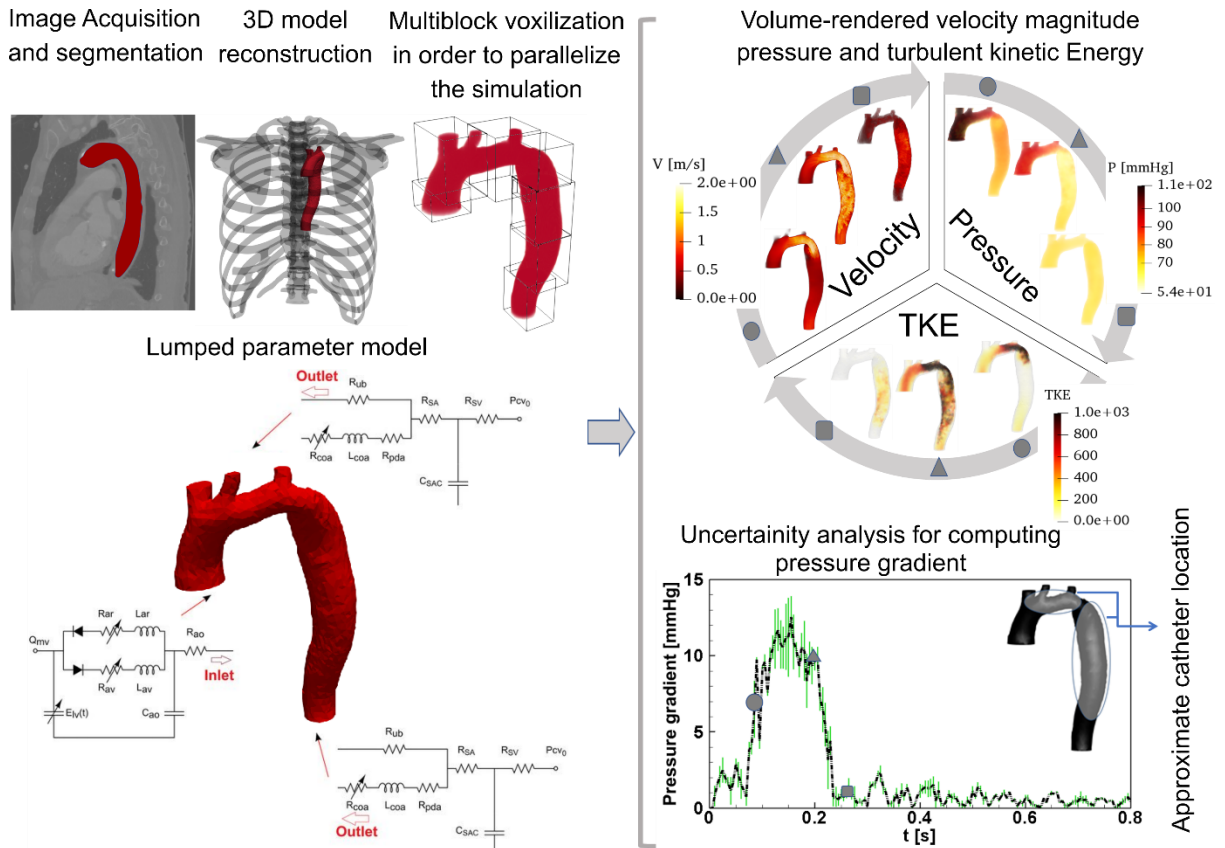
Figure 2-1. Reconstructed geometry and simulation domain. We used CT images from patients to segment and reconstruct the 3D geometries of the complete aorta. These 3-D geometries were used for investigating hemodynamic using computational fluid dynamics. Local flow dynamics is greatly influenced by upstream and downstream flow conditions that are absent in the flow simulation domain. A lumped-parameter model simulates the function of the left side of the heart. Time-dependent inlet flow and outlet pressure at descending aorta position were obtained from lumped parameter modeling and applied as the transient boundary conditions. Boundary conditions of the aortic branches were adjusted to match the flow distribution. This Figure was prepared completely by R. Sadeghi (First author of this manuscript).

Table 2-1. Computation time. Computation time on 24 Intel X5650@2.67GHz cores for both LBM and FVM simulations for all patients investigated in this study in both pre and post intervention states. FVM (OpenFOAM) solver was based on the PISOFOAM method and dynamicEqn LES model, with the minimum resolution of 6.0×10^{-5} (m) and the temporal resolution of 5.0×10^{-4} (s).

Cases		Wall time	
		LBM	FVM
Benchmark		$1^H 6^M$	$2^D 20^H$
Patient #1	Pre-Intervention	$1^H 41^M$	$3^D 2^H$
	Post-Intervention	$2^H 36^M$	$3^D 10^H$
Patient #2	Pre-Intervention	$1^H 49^M$	$4^D 14^H$
	Post-Intervention	$1^H 22^M$	$3^D 3^H$
Patient #3	Pre-Intervention	$1^H 58^M$	$4^D 3^H$
	Post-Intervention	$2^H 13^M$	$5^D 5^H$

Note: "D": day, "H": hour, "M": Minute.

2.3   Methods

We developed a fast computational fluid dynamics framework to simulate local and global hemodynamics in patients with COA in both pre- and post-intervention states (Figure 2-1, schematic diagram). This framework is based on lumped parameter modeling [11,32,33] and 3-D LBM (LES, Smagorinsky subgrid scale model) as implemented in the open-source OpenLB library [34] with some supplements as explained below. Table 2-1 compares the computation time for LBM and finite volume method (FVM) in similar patients and shows that days of calculations were shortened to few hours of calculation using our framework. Calculations of this computational fluid dynamics framework were
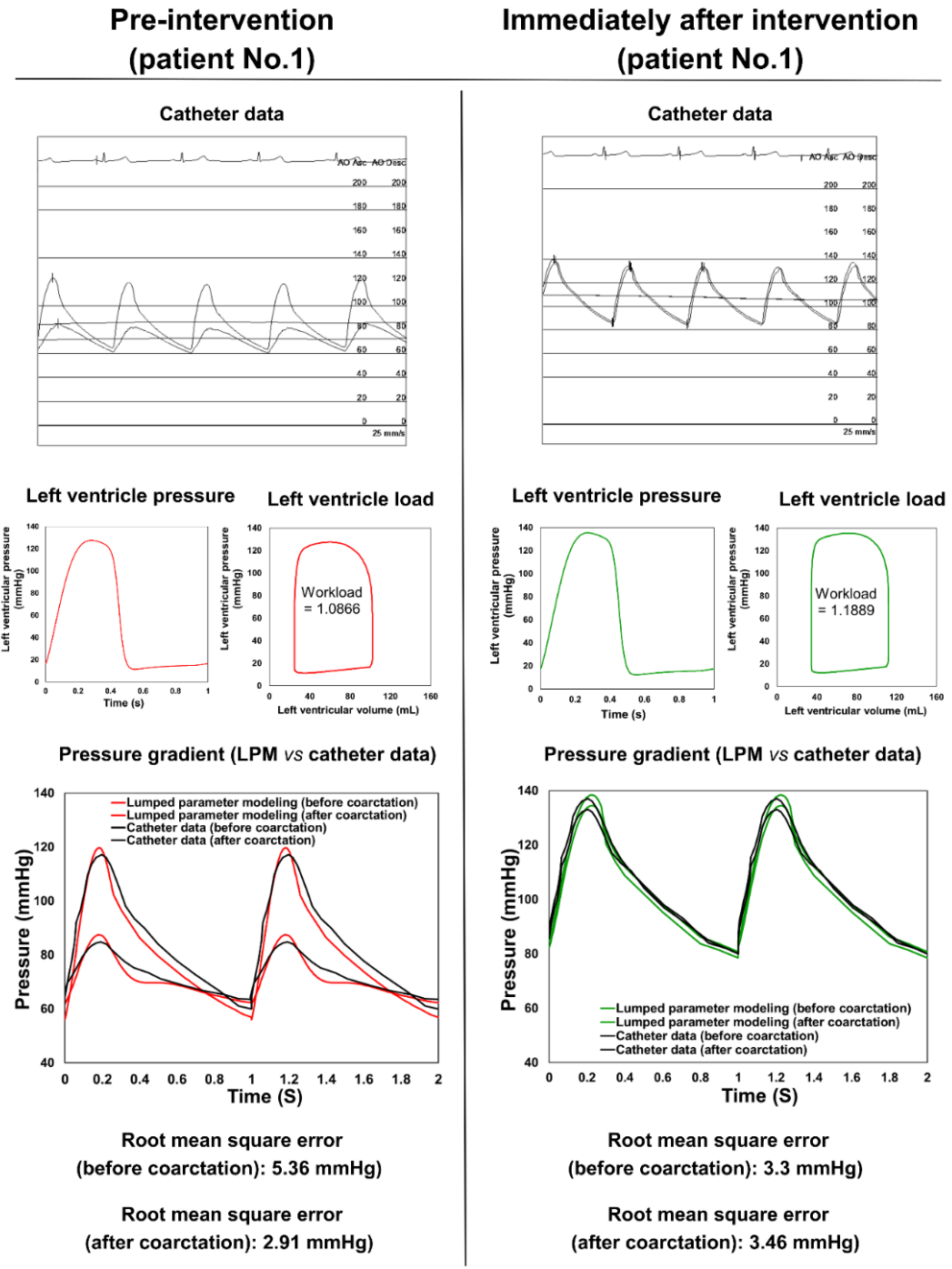
Figure 2-2. Validation against catheter data. Catheter data and results of lumped parameter modeling (aorta and LV pressures and workloads) in Patient No. 1.

validated against clinical cardiac catheterization data (Figure 2-2), LES calculations using conventional finite-volume method (Figures 2-3 and 2-4) and Doppler echocardiographic measurements (Figure 2-5).

2.3.1 Lattice Boltzmann Method (LBM)

The blood flow is mostly laminar in healthy vascular system, while under pathophysiological conditions the blood flow becomes turbulent distally. Approaches based on the Reynolds-averaged Navier Stokes (RANS) equations are the most prevalent to model but with noticeable limitations to model pulsatile flows [35]. Direct numerical simulations (DNS) tax computing resources and are restricted to low Reynolds numbers. Large eddy simulation (LES) approach, which sits between DNS and RANS, is a technique well suited for the computational modeling of turbulent vascular flows with a high potential in modeling the physiological low-Reynolds transitional flows [11]. Although the conventional LES has allowed turbulent modeling, it is still computationally expensive. To compensate this, here we used a rather fast 3-D LBM-based computational fluid dynamics approach using LES (Smagorinsky subgrid scale model) to simulate blood flow through the vascular system.
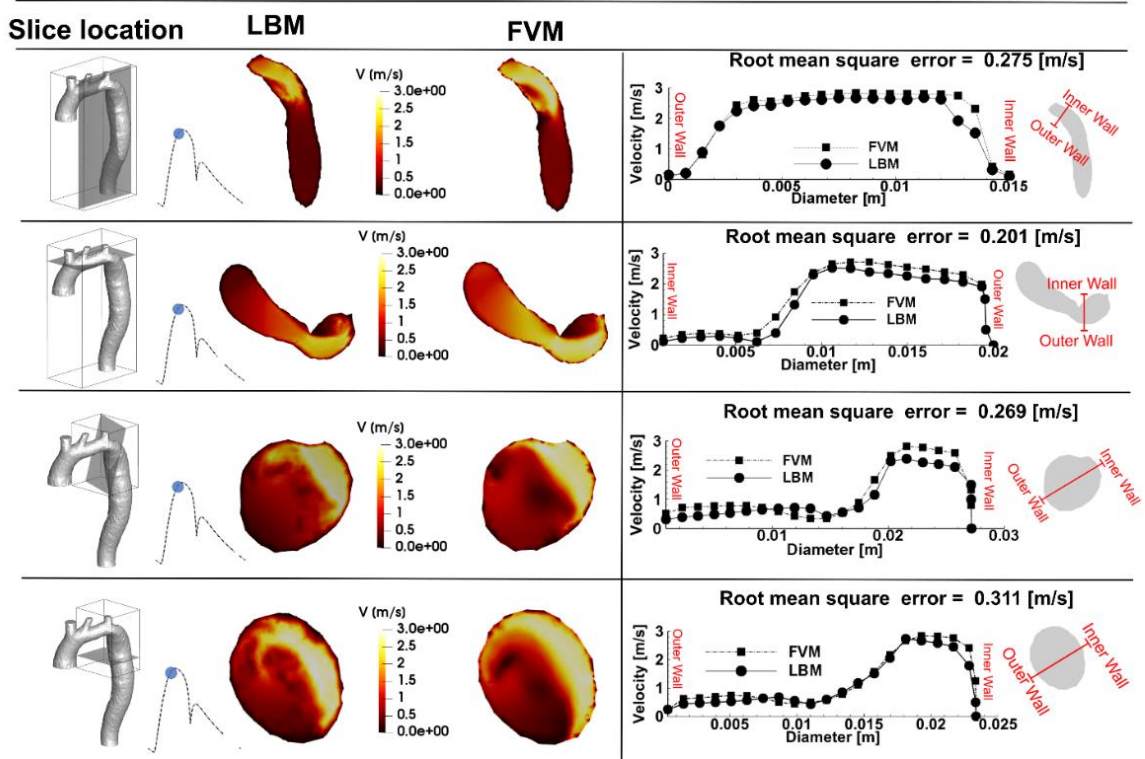
Figure 2-3. Velocity comparison. Velocity at different cross sections of the aorta, simulated using lattice Boltzmann method (LBM) and finite volume method (FVM).

❖ *Governing equations*

The simplest form of LBM equations is based on *Bhatnagar-Gross-Krook* (BGK) approximation with single relaxation time [36]. The discretized form of Boltzmann equation based on BGK approximation is as follows [37]:

$$f_\alpha(x + e_\alpha \delta t, t + \delta t) - f_\alpha(x, t) = -1/\tau \ (f_\alpha(x, t) - f_\alpha^{eq}(x, t) \tag{1}$$

For BGK-LBM model with Q velocities, a set of distribution functions $\{f_\alpha | \alpha = 0, 1, ..., Q-1\}$ is defined on each lattice node (x). τ, t and f^{eq} are relaxation time, discrete time and Maxwell-Boltzmann equilibrium distribution function, respectively. Note that subscript α depends on the number of lattice vectors.

The LBM follows D_xQ_y reference in which x and y are number of dimensions and number of particle velocities, respectively. In this study, we considered D_3Q_{19}, referred to the three-dimensional nineteen-velocity model, to simulate blood flow across the aorta (Figure 2-6, Panel A). The discrete velocity vectors in D_3Q_{19} is as follows [38]:

$$e_0, e_1, e_2, e_3, e_4, e_5, e_6, e_7, e_8, e_9, e_{10}, e_{11}, e_{12}, e_{13}, e_{14}, e_{15}, e_{16}, e_{17}, e_{18} =$$

$$\begin{bmatrix} 0 & 1 & 0 & -1 & 0 & 0 & 0 & 1 & -1 & -1 & 1 & 1 & 1 & -1 & -1 & 0 & 0 & 0 & 0 \\ 0 & 0 & 1 & 0 & -1 & 0 & 0 & 1 & 1 & -1 & -1 & 0 & 0 & 0 & 0 & 1 & 1 & -1 & -1 \\ 0 & 0 & 0 & 0 & 0 & 1 & -1 & 0 & 0 & 0 & 0 & 1 & -1 & -1 & 1 & 1 & -1 & -1 & 1 \end{bmatrix} \tag{2}$$

For the lattice speed of sound $c_s = 1/\sqrt{3}$, Maxwell–Boltzmann distribution function (f_α^{eq}) is defined as follows [39]:

$$f_\alpha^{eq} = w_\alpha \rho \left[1 + \frac{e_\alpha . u}{c_s^2} + \frac{(e_\alpha . u)^2}{2c_s^4} - \frac{(u.u)}{2c_s^2} \right] \tag{3}$$

In Equation (3), u is velocity, w_α is the weighting coefficients which is given by $w_0 = 1/3$, $w_{1\sim6} = 2/36$ and $w_{7\sim18} = 1/36$ for D_3Q_{19} model, e_α is the discrete velocity vector in α direction ($\alpha = 0, ..., 18$) and ρ is the lattice density.

In this study, a multi-relaxation time (MRT) LBM-based model was implemented to overcome some defects of BGK model such as fixed ratio of kinematic and bulk viscosities as well as fixed Prandtl number which cause instabilities at high Reynolds numbers [40]. In this regard, Equation (1) was modified to Equation (4) considering MRT scheme as follows:

$$f_\alpha(x + e_\alpha \delta t, t + \delta t) - f_\alpha(x, t) = -M_{\alpha\gamma}^{-1} \hat{S}_{\gamma k} (m_k(x, t) - m_k^{eq}(x, t) \tag{4}$$

where, $m_k(x,t)$ and $m_k^{eq}(x,t)$ indicate vectors of moments and their equilibrium functions. M and $\hat{S}$ are the transform matrix and collision matrix, respectively.

Mappings between moment and distribution functions were performed by linear transformation as follows:

$$m = M.[f_0, f_2, ..., f_{18}]^T \text{ and } [f_0, f_2, ..., f_{18}] = M^{-1}m \tag{5}$$

The Equilibrium distribution function must satisfy conservation of mass and momentum [41]. Therefore, mass and momentum were conserved by Equations (6) and (7), respectively:

$$\rho = \sum_{\alpha=0}^{\alpha=18} f_\alpha^{eq} = \sum_{\alpha=0}^{\alpha=18} f_\alpha \tag{6}$$

$$\rho u = \sum_{\alpha=0}^{\alpha=18} f_\alpha^{eq} e_\alpha = \sum_{\alpha=0}^{\alpha=18} f_\alpha e_\alpha \tag{7}$$

The transformation matrix M for D3Q19 is defined as the following:

$$\tag{8}$$

M

$$
=\begin{bmatrix}
1 & 1 & 1 & 1 & 1 & 1 & 1 & 1 & 1 & 1 & 1 & 1 & 1 & 1 & 1 & 1 & 1 & 1 & 1 \\
-3 & -11 & -11 & -11 & -11 & -11 & -11 & 8 & 8 & 8 & 8 & 8 & 8 & 8 & 8 & 8 & 8 & 8 & 8 \\
12 & -4 & -4 & -4 & -4 & -4 & -4 & 1 & 1 & 1 & 1 & 1 & 1 & 1 & 1 & 1 & 1 & 1 & 1 \\
0 & 1 & -1 & 0 & 0 & 0 & 0 & 1 & -1 & 1 & -1 & 1 & -1 & 1 & -1 & 0 & 0 & 0 & 0 \\
0 & -4 & 4 & 0 & 0 & 0 & 0 & 1 & -1 & 1 & -1 & 1 & -1 & 1 & -1 & 0 & 0 & 0 & 0 \\
0 & 0 & 0 & 1 & -1 & 0 & 0 & 1 & 1 & -1 & -1 & 0 & 0 & 0 & 0 & 1 & -1 & -1 & -1 \\
0 & 0 & 0 & -4 & 4 & 0 & 0 & 1 & 1 & -1 & -1 & 0 & 0 & 0 & 0 & 1 & -1 & -1 & -1 \\
0 & 0 & 0 & 0 & 0 & 1 & -1 & 0 & 0 & 0 & 0 & 1 & 1 & -1 & -1 & 1 & 1 & -1 & -1 \\
0 & 0 & 0 & 0 & 0 & -4 & 4 & 0 & 0 & 0 & 0 & 1 & 1 & -1 & -1 & 1 & 1 & -1 & -1 \\
0 & 2 & 2 & -1 & -1 & -1 & -1 & 1 & 1 & 1 & 1 & 1 & 1 & 1 & 1 & -2 & -2 & -2 & -2 \\
0 & -4 & -4 & 2 & 2 & 2 & 2 & 1 & 1 & 1 & 1 & 1 & 1 & 1 & 1 & -2 & -2 & -2 & -2 \\
0 & 0 & 0 & 1 & 1 & -1 & -1 & 1 & 1 & 1 & 1 & -1 & -1 & -1 & -1 & 0 & 0 & 0 & 0 \\
0 & 0 & 0 & -2 & -2 & 2 & 2 & 1 & 1 & 1 & 1 & -1 & -1 & -1 & -1 & 0 & 0 & 0 & 0 \\
0 & 0 & 0 & 0 & 0 & 0 & 0 & 1 & -1 & -1 & 1 & 0 & 0 & 0 & 0 & 0 & 0 & 0 & 0 \\
0 & 0 & 0 & 0 & 0 & 0 & 0 & 0 & 0 & 0 & 0 & 0 & 0 & 0 & 0 & 1 & -1 & 1 & 1 \\
0 & 0 & 0 & 0 & 0 & 0 & 0 & 0 & 0 & 0 & 0 & 1 & -1 & -1 & 1 & 0 & 0 & 0 & 0 \\
0 & 0 & 0 & 0 & 0 & 0 & 0 & 1 & -1 & 1 & -1 & -1 & 1 & -1 & 1 & 0 & 0 & 0 & 0 \\
0 & 0 & 0 & 0 & 0 & 0 & 0 & -1 & -1 & 0 & 1 & 0 & 0 & 0 & 0 & 1 & -1 & -1 & -1 \\
0 & 0 & 0 & 0 & 0 & 0 & 0 & 0 & 0 & 0 & 0 & 1 & 1 & -1 & -1 & -1 & -1 & 1 & 1
\end{bmatrix}
$$

The corresponding macroscopic moments vector are:

$$m_\alpha = (m_0, m_1, \ldots, m_{18})^T \tag{9}$$

Diagonal matrix $\hat{S}$ in Equation (4) is defined as follows:

$$\hat{S} = \text{diag}\,(0, 1.19, 1.4, 0, 1.2, 0, 1.2, v, 1.4, v, v, v, 1.98, 1.98, 1.98) \tag{10}$$

where v is physical viscosity and (m^{eq}) is equilibrium moments matrix, as shown below:

$$m_k^{eq} = \left(m_0{}^{eq}, m_1{}^{eq}, \ldots, m_{18}^{eq}\right)^T \tag{11}$$

The equilibrium moments in Equation (11) were obtained as follows:

$$m_0^{eq} = \rho, m_1^{eq} = -11\rho + \frac{19}{\rho}\left(j_x{}^2 + j_y{}^2 + j_z{}^2\right), m_2^{eq} = \frac{-475}{63}\frac{1}{\rho}\left(j_x{}^2 + j_y{}^2 + j_z{}^2\right) \tag{12}$$

$$m_3^{eq} = j_x, m_4^{eq} = -\frac{2}{3}j_x, m_5^{eq} = j_y, m_6^{eq} = -\frac{2}{3}j_y, m_7^{eq} = j_z, \tag{13}$$

$$m_8^{eq} = -\frac{2}{3}j_z, m_9^{eq} = \frac{1}{\rho}\left[2j_x^2 - \left(j_y^2 + j_z^2\right)\right], \tag{14}$$

$$m_{10}^{eq} = 0,, m_{11}^{eq} = \frac{1}{\rho}\left[j_y^2 - j_z^2\right], m_{12}^{eq} = 0, \tag{15}$$

$$m_{13}^{eq} = \frac{1}{\rho}j_x j_y, m_{14}^{eq} = \frac{1}{\rho}j_y j_z, m_{15}^{eq} = \frac{1}{\rho}j_x j_z, \tag{16}$$

$$m_{16}^{eq} = m_{17}^{eq} = m_{18}^{eq} = 0 \,, \tag{17}$$

The momentum $j = (j_x, j_y, j_z)$ was defined as follows:

$$j_x = \rho u_x, j_y = \rho u_y, j_z = \rho u_z \tag{18}$$

❖ *Lattice Boltzmann method & Large Eddy simulation*

In this study, turbulent modeling was performed via Large Eddy Simulation employing Smagorinsky subgrid scale model. The physical viscosity is a superposition of the molecular kinematic viscosity (v_{mol}) and turbulent viscosity (v_{turb}), related to the length scale or lattice size (Δ_x). Collision time (τ) was therefore changed as the following [42]:

$$\tau = \tau_{mol} + \tau_{turb} \tag{19}$$

The molecular and turbulent collision time in equation (19) were obtained as the following:

$$\tau_{mol} = 3v_{mol} + 0.5 \tag{20}$$

$$\tau_{turb} = 0.5 \left(\sqrt{\tau_{mol}^2 + \left((C_s\Delta_x)^2 \frac{\Delta_t}{C_s} 4\sqrt{2}\tau\overline{\Pi} \right)} \right) - \tau_{mol} \tag{21}$$

C_s and $\overline{\Pi}$ are Smagorinsky constant and second-order moment of the non-equilibrium term of the distribution functions, respectively. Total viscosity, v, is given as [42]:

$$v = v_{mol} + v_{turb} = \frac{1}{3}\left(\tau - \frac{1}{2}\right)c^2\delta_t = \frac{1}{3}\left(\tau_{mol} + \tau_{turb} - \frac{1}{2}\right)c^2\delta_t \tag{22}$$

❖ *Modeling surface curvature near the wall of complex geometries*

An interpolated bounce-back scheme proposed by Bouzidi et al. [43] was used to treat boundaries of inclined and complicated geometries. In this technique, for evaluating the post-propagation state of a fluid node A next to a curved solid wall, the distribution function (Figure 2-6, Panel B) was defined as:

$$f_{\bar{\alpha}}(x_A, t + \Delta t) = \begin{cases} 2q f_{\alpha}^c(x_A, t) - (1 - 2q) f_{\alpha}^c(x_B, t) & q < \frac{1}{2} \\ \frac{1}{2q} f_{\alpha}^c(x_A, t) + \frac{(2q-1)}{2q} f_{\alpha}^c(x_A, t) & q \geq \frac{1}{2} \end{cases} \tag{23}$$

where $f_{\bar{\alpha}}(x_A, t + \Delta t)$ is the post-collision and post-propagation state of the distribution function at point x_A and time $(t + \Delta t)$ and f_{α}^c is the value of distribution function after a collision and before propagation state of the fluid node. The factor q is the normalized distance from the wall which equals to $\frac{|AC|}{|AB|}$ (Figure 2-6, Panel B, schematic diagram for one dimensional problem).

❖ *Wall shear stress*

Wall shear stress (WSS) is a frictional force induced by fluid moving along a solid wall. The total stress tensor for the fluid is as the following:

$$T_{ij} = -p . \delta_{ij} + \sigma_{ij} \tag{24}$$

where p, δ_{ij} and σ_{ij} are pressure, Kronecker symbol and contribution from the viscous force. The stress on boundary surface element with normal vector $\vec{n}$ is $T_{ij} n_j$. The wall stress vector $\vec{\tau}$ is computed as:

$$\tau_i = T_{ij} n_j - (n_j T_{kj} n_k) n_i \tag{25}$$
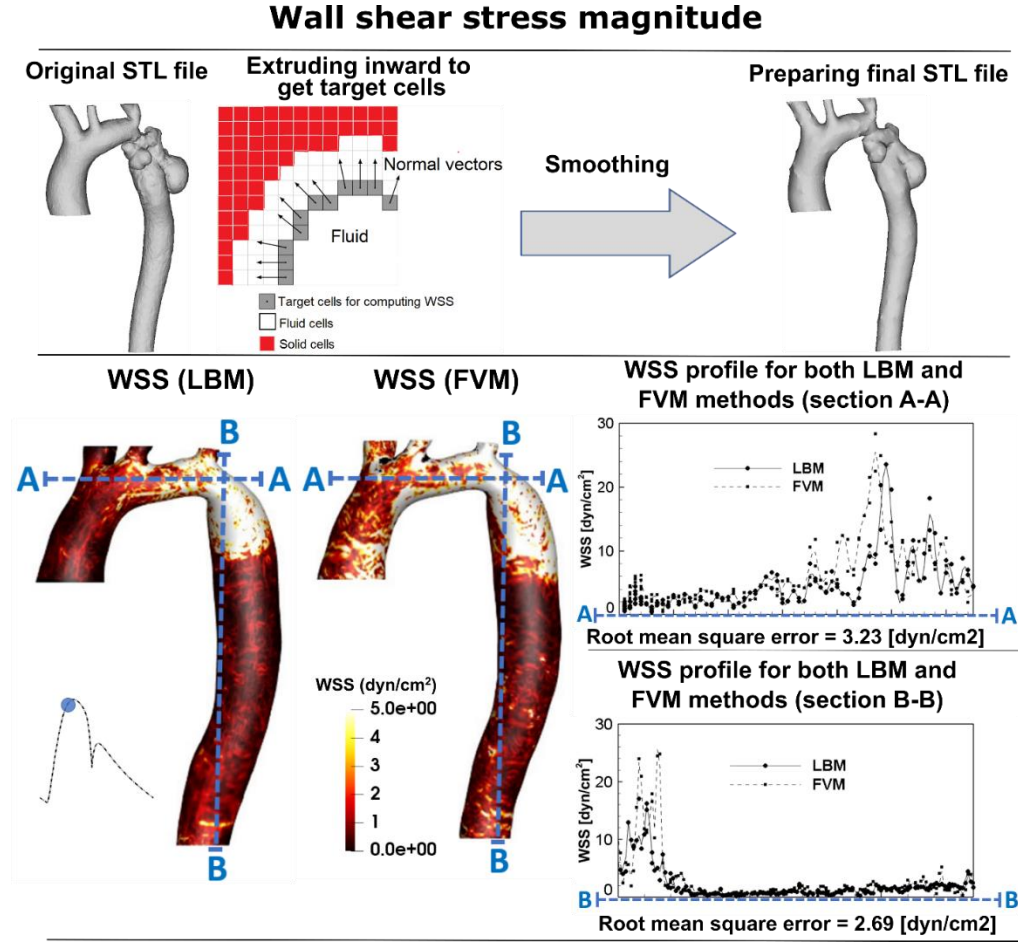
Figure 2-4. Wall shear stress comparison. Wall shear stress (WSS) through the aorta, simulated using LBM and FVM.

The total stress T_{ij} can be replaced by σ_{ij}, since the projection of normal stress $(p.\,\delta_{ij})$ on the tangential plane is zero. For a Newtonian fluid, the viscouse stress is proportional to the strain rate tensor (ε_{ij}) [44,45]:

$$\sigma_{ij} = 2\mu\varepsilon_{ij} = \begin{bmatrix} \tau_{xx} & \tau_{xy} & \tau_{xz} \\ \tau_{yx} & \tau_{yy} & \tau_{yz} \\ \tau_{zx} & \tau_{zy} & \tau_{zz} \end{bmatrix} = \begin{bmatrix} 2\mu\dfrac{\partial u}{\partial x} & \mu\left(\dfrac{\partial u}{\partial y}+\dfrac{\partial v}{\partial x}\right) & \mu\left(\dfrac{\partial u}{\partial z}+\dfrac{\partial w}{\partial x}\right) \\ \mu\left(\dfrac{\partial u}{\partial y}+\dfrac{\partial v}{\partial x}\right) & 2\mu\dfrac{\partial v}{\partial y} & \mu\left(\dfrac{\partial v}{\partial z}+\dfrac{\partial w}{\partial y}\right) \\ \mu\left(\dfrac{\partial u}{\partial z}+\dfrac{\partial w}{\partial x}\right) & \mu\left(\dfrac{\partial v}{\partial z}+\dfrac{\partial w}{\partial y}\right) & 2\mu\dfrac{\partial w}{\partial z} \end{bmatrix} \quad (26)$$

where (u,v,w) and μ are velocity components in three-dimensional coordinates and constant dynamic viscosity, respectively [46].

To supplement OpenLB calculations, we used finite difference method to compute WSS as follows. The derivatives of the velocity field and consequently the nine WSS tensor components (Equation 26) were computed using a first-order accuracy finite difference scheme. When estimating a smooth curved boundary by a series of staircases, the LBM captures the coarseness of this approximation and indeed generates a flow field different from the one produced by a smooth boundary. However, such a difference mainly impacts the thin layer close to the boundary because the roughness of the staircase wall can be considered smooth at a distance far enough from the boundary. Measurements of the WSS should be performed at the borders of this boundary layer, and not on cells which directly represent the aorta wall. To improve the accuracy of the WSS, we computed the velocity gradient and normal vectors (Equation 26) at a few lattice nodes away from the aorta wall, as proposed by the staircase approximation of boundaries method[46] (Figure 2-4). Additionally, we calculated WSS using the distribution function, as customarily done in LBM studies, and observed negligible differences with the WSS calculated with the above described method.

❖ *Model properties & Boundary conditions*

Blood was assumed to be a Newtonian and incompressible fluid with dynamic viscosity of 0.0035 Pa·s and density of 1050 kg/m^3. Aortic local flow dynamics is greatly influenced by upstream and downstream flow conditions and the correct choice of

boundary conditions is crucial as it chiefly affects the accuracy of the flow simulations. A lumped-parameter model (Figure 2-1; see below for details of the lumped parameter model), simulated the function of the left side of the heart was used to impose the time-dependent inlet flow at the ascending aorta position and the outlet pressure at the descending aorta position. We assumed that the flow at the inlet has a Poiseuille flow profile and the time-dependent flow rate obtained from the lumped-parameter model was used to scale this profile to realize this time-varying inlet boundary condition[26,27,47]. The inlet velocity boundary condition in lattice Boltzmann was implemented using the method suggested by Skordos[47], which uses a second-order finite difference scheme to compute the velocity gradient at the boundary nodes and extrapolates the pressure distribution at the inlet from bulk nodes[48]. Furthermore, in order to avoid pressure fluctuation artifacts at the inlet, a sinusoidal smooth start-up phase was used to the initiate the simulation and smoothly increase velocity from zero initial conition[26,27]. The total flow rate going to the branches was calculated using the lumped-parameter model and was distributed to the branches based on their relative cross-sectional areas at the inlet of each branch. Note our lumped parameter model used a limited number of input parameters that all can be reliably measured using Doppler echocardiography and a sphygmomanometer. The lumped parameter model does not need catheter data as input parameters to the model. No-slip boundary condition was applied at the solid walls as described above (Section: *Modeling surface curvature near the wall of complex geometries*). The aortic wall was treated as a rigid wall as Jin et al. [49] and Keshavarz-Motamed et al. [11,16,33] showed that rigid-wall assumption for the aorta is reasonable and as patients with COA are

usually hypertensive and characterized by reduced compliance and elevated stiffness in both proximal and distal aorta , e.g., [50-52].

❖ *Reconstructed geometries in patients with coarctation*

We used CT images for patients with coarctation of the aorta to segment and reconstruct the 3D geometries of the complete aorta including ascending aorta, aortic branches and descending aorta using ITK-SNAP (version 3.8.0-BETA), a 3-D image processing and model generation software package (Figure 2-1). These 3-D reconstructions were voxelized into multiblocks. Blocks were distributed between computer processor units in order to parallelize the simulation.

❖ *Numerical strategy*

Multiple relaxation time (MRT) LBM-based model was coupled with Smagorinsky turbulent model in order to stabilize complex turbulent fluid flow across the domain. For treating complex geometry, we utilized second order accuracy method proposed by Bouzidi et al. [43]. In order to suppress the undesired pressure fluctuation, a smooth startup phase was added to the inlet velocity condition. For turbulent modelling, Large Eddy Smagorinsky subgrid-scale model with constant $C_s = 0.1$ was applied [42]. Mesh independency was judged by two criteria: velocity and wall shear stress. Mesh definition was considered acceptable if no significant differences (lower than 5%) between successive mesh refinements were noticed in both wall shear stress and velocity fields.
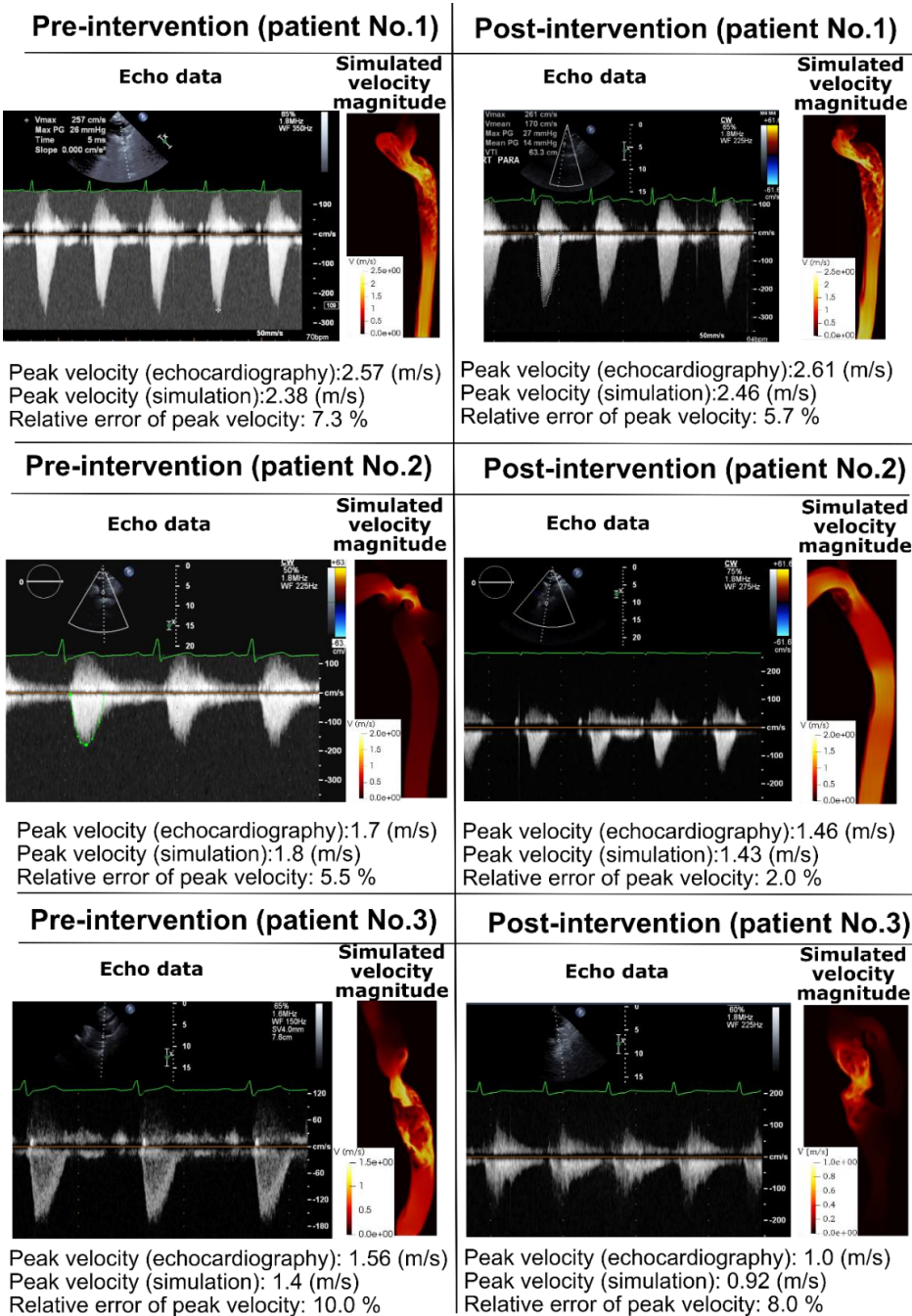
Figure 2-5. Validation against Doppler echocardiography. Doppler echocardiography data and results of the computational framework (based on LPM and LBM) in Patients No. 1 to 3 in pre and post intervention states.

(a) Geometry of the D3Q19 lattice Boltzmann model

(b) Detailes of bounce-back interpolation scheme

The wall node is closer to the fluid node than to the solid node (q < 1/2)	The wall node is closer to the solid node than to the fluid node (q ≥ 1/2)

Fluid node ○
Solid node ●
Location of interpolated ■
particle population

Figure 2-6. Modeling complex geometries in LBM. (a) Geometry of D3Q19 discrete velocity model with lattice vectors of e_i (Equation 2); (b) Details of bounce-back interpolation scheme (Here A and E are fluid nodes, B is solid nodes and D represents the location of an interpolated population): (I) The wall-node C is closer to the fluid-node A than to the solid-node B ($q < 1/2$). In this case, interpolations are required to construct post collision state at node D. We constructed the unknown quantities at node A from particles population at node D that will travel to node A after bouncing back off the wall. (II) The wall-node C is closer to the solid-node B than to the fluid-node A ($q \geq 1/2$). In this case, endpoint of propagation state (node D) lies between the boundary node (A) and the wall node (C) and the information of the particle leaving node A and arriving node D will be used to compute the unknown quantities at node A [43,74,75].

The non-dimensional wall distance y^+ was less than 1, which ensured that the near-wall

resolution was fine enough, and turbulence effects were resolved accurately.

2.3.2 Lumped parameter model

We developed a patient-specific lumped-parameter model, described in details elsewhere [11,16,32,33], that considers interactions of the aortic valve, LV, COA and arterial system to estimate the flow and pressure through circulatory system as well as the LV function non-invasively (Figure 2-1, schematic diagram; Table 2-2, parameters used in the model) in both pre and post intervention conditions. The model used a limited number of input parameters that can be reliably measured using Doppler echocardiography and a sphygmomanometer. Doppler echocardiography-based parameters (e.g., stroke volume, heart rate, ejection time, ascending aorta area, aortic valve effective orifice area and aortic regurgitation effective orifice area) were measured in the parasternal long axis, parasternal short axis, apical two-chamber, apical four-chamber, and apical five-chamber views of the heart. Other input parameters of the model were systolic and diastolic blood pressures measured using a sphygmomanometer. Note that the proposed method does not need any catheter data as input parameters to the model. The model and sub-models have already been used and validated against *in vivo* cardiac catheterization and *in vivo* MRI data [11,16,32,33].

❖ *Heart-arterial model*

The ventricle was filled by a normalized physiological mitral flow waveform adjusted for the required stroke volume. Coupling between LV pressure and volume was performed through a time varying elastance E(t), a measure of cardiac muscle stiffness.

$$E(t) = \frac{P_{LV}(t)}{V(t) - V_0} \tag{27}$$

where $P_{LV}(t)$, $V(t)$ and V_0 are left ventricular time-varying pressure, time-varying volume and unloaded volume, respectively. The amplitude of $E(t)$ was normalized with respect to maximal elastance E_{max}, *i.e.*, the slope of the end-systolic pressure-volume relation, giving $E_N(t_N)=E(t)/E_{max}$. Time was normalized with respect to the time to reach peak elastance, T_{Emax} ($t_N=t/T_{Emax}$). These normalized time-varying elastance curves $E_N(t_N)$ have similar shapes in the normal human heart under numerous inotropic conditions or in affected human hearts irrespective of disease etiology.

$$E_{max}E_N(t/T_{Emax}) = \frac{P_{LV}(t)}{V(t) - V_0} \tag{28}$$

This normalized curve can be described mathematically, and therefore, if $E_N(t_N)$ is given, the relation between $P_{LV}(t)$ and $V(t)$ can be concluded for any LV.

❖ *Modeling aortic valve*

Aortic valve was modeled using the following net pressure gradient formulation across the aortic valve during the LV ejection:

$$TPG_{net}|_{av} = P_{LV}(t) - P_A(t) = \frac{2\pi\rho}{\sqrt{E_L Co|_{av}}}\frac{\partial Q(t)}{\partial t} + \frac{\rho}{2E_L Co|_{av}^2}Q^2(t) \tag{29}$$

$$E_L Co|_{av} = \frac{(EOA|_{av})A}{A - EOA|_{av}} \tag{30}$$

where $E_L Co|_{av}$, $EOA|_{av}$, A, ρ and Q are the valvular energy loss coefficient, the aortic valve effective orifice area, ascending aorta cross sectional area, the fluid density and the transvalvular flow rate, respectively.

❖ *Modeling aortic valve regurgitation*

Aortic regurgitation (AR) was modeled using the following formulation. AR pressure gradient is the difference between aortic pressure and LV pressure during diastole.

$$TPG_{net}|_{ar} = \frac{2\pi\rho}{\sqrt{E_L Co|_{ar}}} \frac{\partial Q(t)}{\partial t} + \frac{\rho}{2E_L Co|_{ar}^2} Q^2(t) \tag{31}$$

$$E_L Co|_{ar} = \frac{(REOA)A_{LVOT}}{A_{LVOT} - REOA} \tag{32}$$

where $E_L Co|_{ar}$, $REOA$ and A_{LVOT} are regurgitation energy loss coefficient, regurgitant effective orifice area and LVOT area, respectively.

❖ *Modeling coarctation of the aorta*

The characteristics of the arterial system are important when modeling COA as only a portion of total flow rate will cross the COA. To consider this, two parallel branches were considered: (1) the first branch simulates the flow towards the upper body, or the flow bypassing the COA (including aortic arch arteries and potential collaterals); (2) a second branch simulates the flow crossing COA and directed towards descending aorta. This branch includes a resistance for the proximal descending aorta, and a time-varying resistance and an inductance which together represent the trans-coarctation net pressure gradient induced by the COA:

$$TPG_{net}|_{coa} = \frac{2\pi\rho}{\sqrt{E_L Co|_{coa}}} \frac{\partial Q(t)}{\partial t} + \frac{\rho}{2E_L Co|_{coa}^2} Q^2(t) \tag{33}$$

$$E_L Co|_{COA} = \frac{(EOA|_{coa})A}{A - EOA|_{coa}}$$ (34)

where $E_L Co|_{coa}$, $EOA|_{coa}$, A, ρ and Q are the energy loss coefficient of the COA, the effective orifice area of the COA, aortic cross-sectional area downstream of the COA, the fluid density and the trans-coarctation flow rate, respectively. The energy loss coefficient is then described in terms of the aortic cross section just downstream of the COA and the effective orifice area of the COA.

❖ *Determining arterial compliance and peripheral resistance*

The total systemic resistance was computed as the quotient of the average brachial pressure and the cardiac output. This total systemic resistance represents the electrical equivalent resistance for all resistances in the current model. Because what the left ventricle faces is the total systemic resistance and not the individual resistances, we considered the aortic resistance, R_{ao}, and systemic vein resistance, R_{SV}, as constants and adjusted the systemic artery resistance, R_{SA}, according to the obtained total systemic resistance.

For each degree of hypertension, we fit the predicted pulse pressure to the actual pulse pressure (known by arm cuff sphygmomanometer) obtained from clinical study by adjusting compliances (proximal COA (C_{ao}) and systemic (C_{SAC})). Therefore, compliance adjustment was done by a simple trial and error for each degree of hypertension.

Table 2-2. Summarized cardiovascular parameters used in the lumped parameter modeling to simulate all cases.

Description	Abbreviation	Value
COA and valve parameters		
Effective orifice area	EOA	From echocardiography data
Energy loss coefficient	E_LCo	$\dfrac{(EOA)A}{A-EOA}$ From echocardiography data
Variable resistance	R_{coa}, R_{av} and R_{ar}	$\dfrac{\rho}{2E_LCo^2}Q$
Inductance	L_{coa}, L_{av} and L_{ar}	$\dfrac{2\pi\rho}{\sqrt{E_LCo}}$
Systematic circulation parameters		
Aortic resistance	R_{ao}	0.05 mmHg.s.mL^{-1}
Aortic compliance	C_{ao}	Initial value: 0.5 mL/mmHg Adjust for each degree of hypertension (Proximal COA compliance)
Systemic vein resistance	R_{SV}	0.05 mmHg.s.mL^{-1}
Systemic arteries and veins compliance	C_{SAC}	Initial value: 2 mL/mmHg Adjust for each degree of hypertension (Systemic compliance)
systemic arteries resistance (including arteries, arterioles and capillaries)	R_{SA}	0.8 mmHg.s.mL^{-1} Adjust according to the calculated total systemic resistance
Proximal descending aorta resistance	R_{pda}	0.05 mmHg·s·mL^{-1}
Upper body resistance	R_{ub}	Adjusted to have 15% of total flow rate in healthy case
Output condition		
Central venous pressure	P_{CV0}	4 mmHg
Input condition		
Mitral valve mean flow rate	Q_{mv}	From echocardiography data
Other		
Constant blood density		1050 kg/m^3
Heart rate	HR	From echocardiography data
Duration of cardiac cycle	T	From echocardiography data

➢ *Computational algorithm*

A lumped parameter model developed and described in detail elsewhere (7,17,55) was analyzed numerically by creating and solving a system of ordinary differential equations in Matlab Simscape (MathWorks, Inc.), enhanced by adding additional codes to meet

demands of cardiac model in circuit. A Fourier series representation of an experimental normalized elastance curve for human adults was used to generate a signal to be fed into the main program. Simulations start at the onset of isovolumic contraction. Left ventricle volume, $V(t)$, is calculated using left ventricle pressure, P_{LV}, and time varying elastance values. P_{LV} used in the beginning of calculation is the initial value assumed across the variable capacitor and is automatically adjusted later by system of equations as solution advances. Left ventricle flow rate subsequently was calculated as time derivative of left ventricle volume. Matlab's ode23t trapezoidal rule variable-step solver was used to solve system of differential equations with initial time step of 0.1 milliseconds. The convergence residual criterion was set to 10^{-5} and initial voltages and currents of capacitors and inductors set to zero.

2.3.3 Study population

Three patients with COA who underwent intervention at St. Joseph's Healthcare and Hamilton Health Sciences (Hamilton, ON, Canada) and Massachusetts General Hospital (Boston, MA, USA) [11] were retrospectively considered. The protocols were reviewed and approved by the Institutional Review Boards of each institution as follows: the Hamilton Integrated Research Ethics Board (HiREB) of Hamilton Health Sciences and St. Joseph's Healthcare, both affiliated to McMaster University and the Ethics Committee of Massachusetts General Hospital. Informed consents were obtained from human participants. All methods and measurements were performed in accordance with the

relevant guidelines and regulations including guidelines of the American College of Cardiology and American Heart Association.

2.4   Results

❖ *Validation*

Pressure waveforms: The beat-to-beat pressure calculations of LPM were compared with cardiac catheter pressure measurements in patients investigated in this study. Results of our LPM show good qualitative agreements with cardiac catheter measurements in terms of both shape of the waveform, and specific wave features such as the amplitude and the timing of the systolic peak in the aorta (See Figure 2-2 for an example). Note cardiac catheterization is a gold standard in clinics to evaluate hemodynamics, e.g., pressures through the heart and circulatory system. The calculations done by LPM had an average root mean square (RMS) error of 8.6 mmHg in the aorta pressures of the 3 patients in both pre and post intervention states. Moreover, the LPM and its sub models already were validated against *in vivo* cardiac catheterization in patients with COA (N=34) [11].

Velocity field: Figure 2-3 compares examples of the simulated velocity contours calculated using LBM and FVM at different cross sections upstream and downstream of the COA. The results show very good qualitative agreements between LBM and FVM simulation results in all cases. Figure 2-3 also shows that the velocity profiles calculated using LBM and FVM methods along a diameter upstream and downstream of the COA are in good quantitative agreements with root mean square (RMS) errors between 0.201

and 0.311 m/s. Figure 2-4 shows good quantitative and qualitative agreements between the instantaneous WSS calculated using the two methods with RMS errors of 3.23 dyn/cm^2 and 2.69 dyn/cm^2 for sections A-A and B-B, respectively. Most importantly, the simulated peak velocities downstream of the COA correlated well with Doppler echocardiographic measurements in all 3 patients in both pre and post intervention states with a maximum relative error of 10% (Figure 2-5). The good agreements between results calculated using LBM with the ones calculated using FVM and measured using Doppler echocardiography permit us to accept LBM results with confidence to investigate other flow features.

❖ *Aorta fluid dynamics (local hemodynamics)*

The presence of the COA modified substantially the flow dynamics and vortical structure in the aorta. As the flow exited the COA, the fluid cannot immediately change direction and followed the steep curvature to reattach to the descending aorta wall (Figures 2-7 to 2-9). Indeed, the disturbed flow resulting from COA detached from the walls and developed into a high-speed and eccentric jet with maximal velocities of: 2.45 ,7.5 and 1.47 m/s, creating transitional to turbulent flow downstream of COA with maximum Reynolds numbers of 8400, 13846 and 6203 in Patients No. 1 to 3, respectively (Figures 2-7 to 2-9). Following intervention, the flow pattern was smooth with a relatively low magnitude and more attached to the wall with maximum velocities of: 2.84, 1.4 and 1.05 m/s and maximum Reynolds numbers of 9737, 5908 and 4431 in Patients No. 1 to 3, respectively (Figures 2-8 & 2-9). In patient No. 1, post intervention, the stent was

deployed with mild residual stenosis due to malapposition of the stent proximal to the COA (Figure 2-7). This could partly explain why the flow pattern was not improved substantially by intervention.

In order to investigate the onset of instability and the intensity of fluctuations in the fluid flow environment, we specifically elected the turbulent kinetic energy (TKE), which is derived using fluctuating components of the velocities and is a sum of the normal fluctuating stresses. Both TKE contours and volumetric integration of TKE during cardiac cycle were reduced in Patients No. 2 and 3 (Figures 2-8 and 2-9) while they were not improved in Patient No. 1 (Figure 2-7) by intervention. Note that volumetric integration of TKE during the cardiac cycle can quantify the level of fluctuations in the flow field through the aorta. In Patients No. 2 & 3 (pre intervention), the strong jet due to the presence of the COA generated high fluctuations in the flow field as evident from the high magnitudes of TKE. This adverse condition was alleviated by intervention (Patient No. 2: peak TKE in pre intervention = 1150 N/m^2, peak TKE in post intervention = 820 N/m^2, 29% decrease; Patient No. 3: peak TKE in pre intervention = 440 N/m^2, peak TKE in post intervention = 290 N/m^2, 34% decrease). In Patient No. 1, TKE didn't reduce and didn't improve by intervention (peak TKE in pre intervention = 890 N/m^2, peak TKE in post intervention = 920 N/m^2, 3% increase).
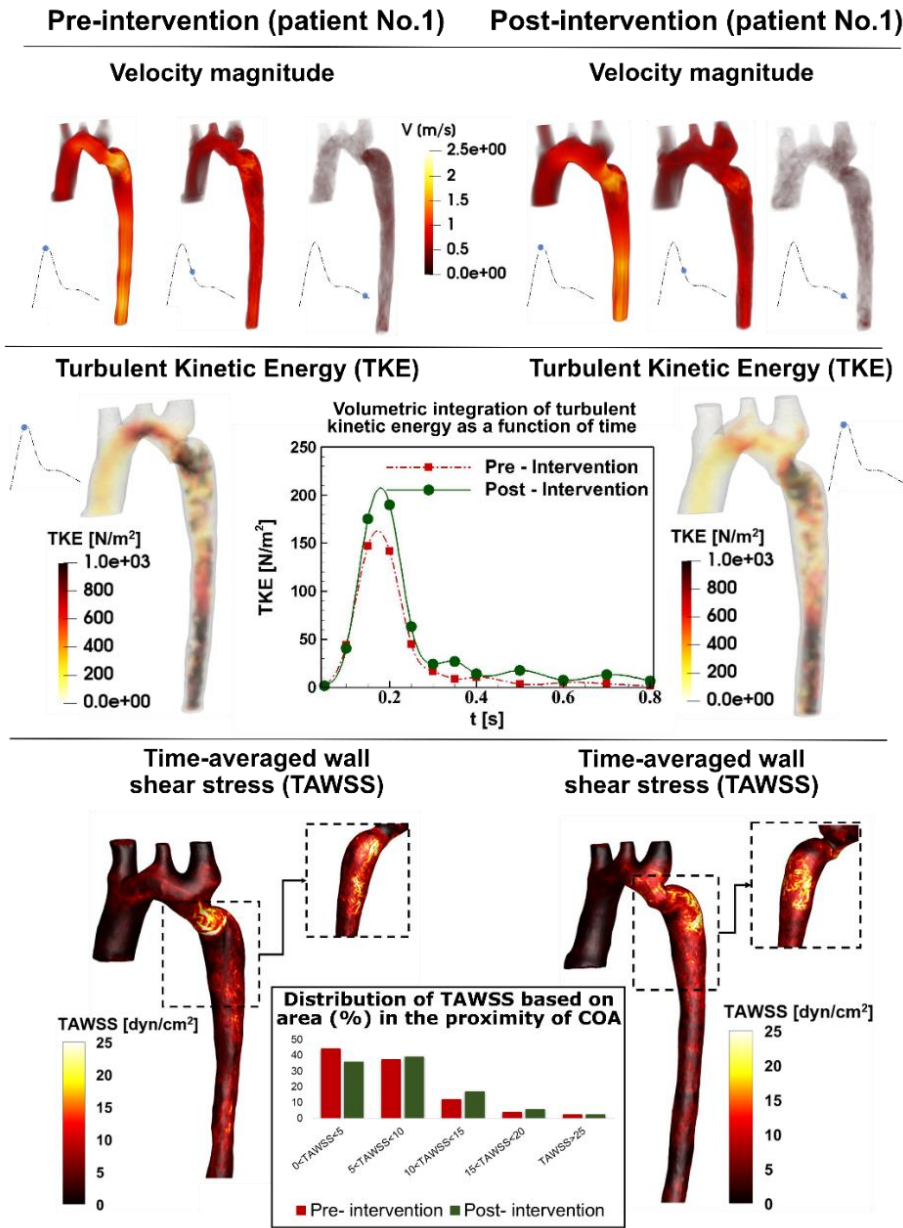
Figure 2-7. Flow modeling in Patient No. 1. Computed velocity magnitude, turbulent kinetic energy (TKE) and time-averaged wall shear stress (TAWSS) using the computational framework (based on LPM and LBM) in pre and post intervention states in Patient No. 1. Patient No. 1 underwent intravascular stent intervention to correct the coarctation. Post intervention, the stent was deployed with residual stenosis due to malapposition of the stent proximal to the coarctation. Angiography post dilatation did not reveal a dissection or extravasation of contrast. The patient tolerated the procedure well without complication. The total shear stress exerted on the wall throughout the

cardiac cycle was evaluated using the time-averaged wall shear stress (TAWSS) which is obtained as $\text{TAWSS} = \frac{1}{T}\int_0^T |\tau|\, dt$. Here, T and τ are the cardiac cycle period and instantaneous wall shear stress, respectively. Turbulent kinetic energy can be computed as $\text{TKE} = \frac{1}{2}\rho(\overline{u'^2} + \overline{v'^2} + \overline{w'^2})$ Here u, v, w and ρ correspond to the three components of the instantaneous velocity vector and density, respectively. The bar and prime denote the ensemble averaged and fluctuating components, respectively.

Such flow alterations contributed to elevated wall shear stress mainly at the neck of the COA as well as distal to the COA; the total shear stress exerted on the aorta wall was evaluated using time-averaged wall shear stress (TAWSS). Local perturbation in shear stress exposes endothelial cells to high shear stress which affects vessel distensibility and compliance and potentially lead to vascular diseases [53]. Heterogeneous changes in WSS indices occurred both proximal and distal to the coarctation region prone to atherosclerotic plaque development [54,55] which may lead to aortic wall complications such as rupture, aneurysm and aortic dissection [56-59]. Similar to TKE, TAWSS was reduced modestly by intervention in Patients No. 2 and 3 (Figures 2-8 and 2-9), moving the flow slightly farther from pure oscillatory to more stable domains (Patient No. 2: peak TAWSS in pre intervention = 197 dyn/cm^2, peak TAWSS in post intervention = 21 dyn/cm^2, 89% decrease; Patient No. 3: peak TAWSS in pre intervention = 46 dyn/cm^2, peak TAWSS in post intervention = 13 dyn/cm^2, 71% decrease). However, TAWSS was not improved and rose in Patient No. 1 following the intervention: elevated TAWSS is noticed at COA region and downstream of the COA (Figure 2-7; peak TAWSS in pre intervention = 31 dyn/cm^2, peak TAWSS in post intervention = 49 dyn/cm^2, 58% increase).
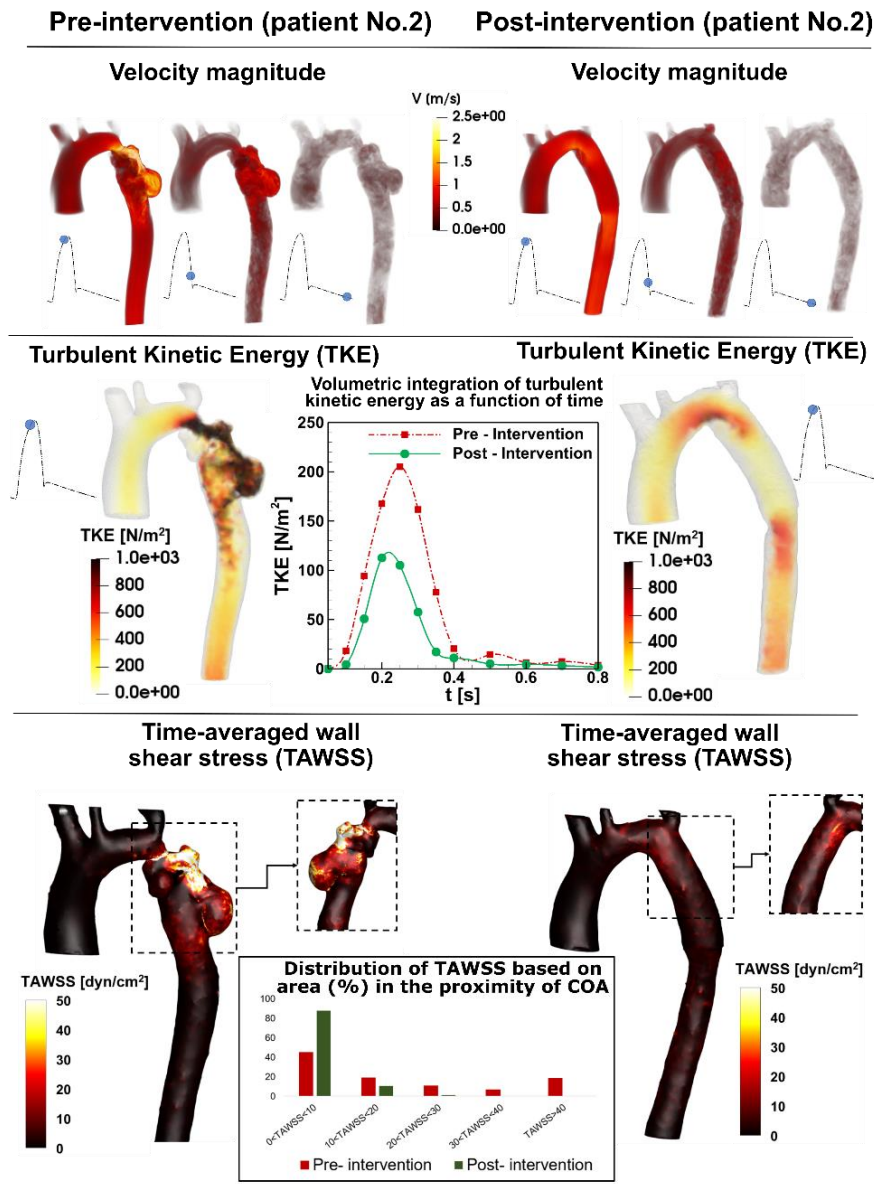
Figure 2-8**.** Flow modeling in Patient No. 2. Computed velocity magnitude, turbulent kinetic energy and time-averaged wall shear stress using the computational framework (based on LPM and LBM) in pre and post intervention states in Patient No. 2. Patient No. 2 underwent intravascular stent intervention to correct the coarctation which was coexisted with a major aneurysm downstream of the coarctation. Post intervention, the stent was successfully deployed without residual stenosis. Angiography and pressure measurement confirmed stent expansion with no extravasation, contrast staining or hemodynamic instability. There was no evidence of aneurysm. The patient tolerated the procedure well without complication.
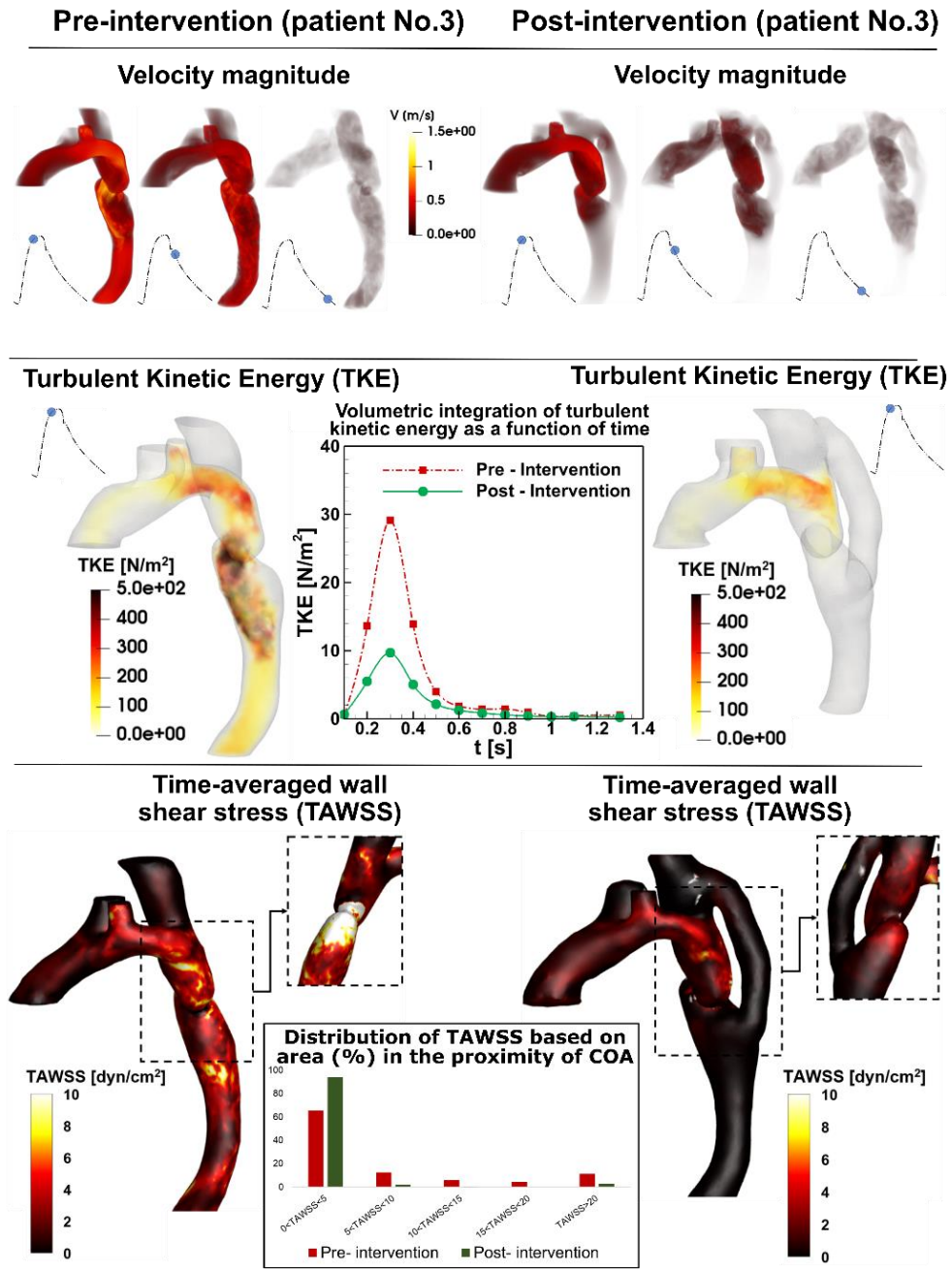
Figure 2-9. Flow modeling in Patient No. 3. Computed velocity magnitude, turbulent kinetic energy and time-averaged wall shear stress using the computational framework (based on LPM and LBM) in pre and post intervention states in Patient No. 3. Patient No. 3 underwent bypass grafting intervention to correct the coarctation. The patient tolerated the procedure well without complication and the intervention was performed successfully.

In addition to shear stress, the arterial vessel is subjected to another major hemodynamic force, pressure. Presence of COA induces an increase in the pressure drops at the neck of the COA in pre intervention states in all three patients (see Figure 2-2 for one example, Patient No. 1). This is very important since wall expansion, compression and collapse are caused by high pressure drops in the COA. Moreover, the pressure drops introduced by the presence of the COA must be compensated by the left ventricle, this in turn can lead to heart failure. Such high-pressure drops were reduced by intervention in all 3 patients, documented by catheter measurements as well LPM simulations (see Figure 2-2 for one example, Patient No. 1).

❖ *LV fluid dynamics (Global hemodynamics)*

LV stroke work represents the energy that the ventricle delivers to the blood during ejection and is an effective metric of LV load and clinical state. In Patients No. 2 & 3, LV workload and peak LV pressure were reduced following the intervention: Patient No. 2: LV workload: by 23% & LV peak pressure: by 8%; Patient No. 3: LV workload: by 16% & LV peak pressure: by 13%) (Table 2-3). However, in Patient No. 1, the modest reduction of the pressure drop was not accompanied by reduction in LV function parameters: LV workload and peak LV pressure were increased by 15% and 7.3%, respectively (Table 2-3). Our results reveal that though pre-intervention COA increases the burden on the left ventricle with augmented flow resistance, post-intervention the LV load does not improve as introducing a stent reduces the arterial systemic compliance, in fact increasing LV load. Percutaneous stenting of the aorta in Patient No. 1, therefore, had limited efficacy in reducing myocardial stress.

Table 2-3. Heart-function metrics in Patients No. 1 to 3. LV workloads and LV peak pressures resulted from lumped parameter modeling in Patients No. 1 to 3.

Cases		LV workload	LV peak pressure
		(J)	(mmHg)
Patient #1	Pre-Intervention	1.086	127.5
	Post-Intervention	1.249	136.8
Patient #2	Pre-Intervention	1.51	148.4
	Post-Intervention	1.16	136
Patient #3	Pre-Intervention	1.42	137
	Post-Intervention	1.19	119

2.5   Discussion

Quantification of the complex flow in COA plays an essential role in accurate and early diagnosis which may help the clinician optimize the planned interventions but we still lack proper diagnostic methods for COA in clinics because the fluid-dynamics methods that can be used as engines of new diagnostic tools are not well developed yet. Currently, clinical decisions are largely made based on the anatomy [9]. To augment anatomical information, clinics relies largely on data obtained by cardiac catheterization to evaluate

pressure and flow through heart and circulatory system but this is invasive, expensive, and high risk and therefore not practical for diagnosis in routine daily clinical practice or serial follow-up examinations [60,61]. Most importantly, cardiac catheterization only provides access to the blood pressure in very limited regions rather than details of the physiological pulsatile flow and pressures throughout the heart and the circulatory system. Phase-contrast magnetic resonance imaging can provide 3-D velocity field but it has poor temporal resolution [62-64], is costly, lengthy and not possible for many patients with implanted devices. Doppler echocardiography (DE) is potentially the most versatile tool for hemodynamics diagnosis [65-67]. Although there are some promising 2-D Doppler echocardiography methods [68-71], 2-D velocity field does not represent 3-D velocity field. On the other hand, existing 3-D Doppler echocardiography techniques suffer from low temporal resolution and there is no 3-D Doppler ultrasound to precisely quantify velocity field. Recent advances in DE velocity measurements are: (1) Echo-PIV is an adaptation of Particle Image Velocimetry (PIV) for computing flow velocity by tracking speckles often enhanced with contrast agents (microbubbles) [69-71]. Echo-PIV is promising but depending on the acquisition frame rate, high velocities can be underestimated [72], which has implications for diagnosis. In addition, the contrast agent must constantly and homogeneously fill the field to avoid both saturated and dark areas. These may hinder routine clinical application of the method [73].(2) Colour-Doppler vector flow mapping (VFM) permits calculation of the velocity field without contrast agents through colour DE [68]. Colour DE is fast and routinely used in clinics [73] but it cannot measure velocity in the direction perpendicular to the beam.

In this study, we developed an innovative fast computational-mechanics and imaging-based framework, using turbulent LBM and LPM, that can eventually, upon further development and validation, function as the main component of new diagnostic methods for complex lesions such as COA. Our proposed framework can investigate and quantify effects of COA on both local and global hemodynamics. The diagnostic information, that the framework can provide, is vitally needed to improve clinical outcomes, to assess patient risk and to plan treatment.

2.6   Limitations

This study was performed on 3 patients with COA in both pre and post intervention states (6 cases). Future studies must consider further validation of the computational framework in a larger population of COA patients. However, our results in this study demonstrate the ability of the framework to track changes in both cardiac, and vascular states before and after intervention. We also observed good agreements between the velocity fields calculated by our proposed framework and the MRI-measured velocity fields (in progress for our other study). These observations made us more confident that the limitation in the number of patients in this study does not affect our conclusions. Moreover, we implemented a novel approach to improve the accuracy of computing WSS in LBM models [46]. However, there is room for improving WSS calculations in LBM to be more comparable to those calculated using finite-volume based methods which we will consider in future studies.

Competing interest

The authors declare that they have no competing interests

Author contribution

R.S. Design, data collection and analysis, interpretation of data and manuscript writing; S.K. Design and data analysis; J.G. Data analysis, interpretation of data and critical revision of the manuscript; Z.K.M. Conception and design, data collection and analysis, interpretation of data, manuscript writing, critical revision and final approval of the manuscript. All authors read and approved the final manuscript.

Data availability

All data, code and algorithms used for this study are available from the author upon request.

2.7   References

1   Torok, R. D., Campbell, M. J., Fleming, G. A. & Hill, K. D. Coarctation of the aorta: management from infancy to adulthood. *World journal of cardiology* **7**, 765 (2015).

2   Brickner, M. E., Hillis, L. D. & Lange, R. A. Congenital heart disease in adults. *New England Journal of Medicine* **342**, 256-263 (2000).

3   Cohen, M., Fuster, V., Steele, P. M., Driscoll, D. & Mcgoon, D. C. Coarctation of the aorta. Long-term follow-up and prediction of outcome after surgical correction. *Circulation* **80**, 840-845 (1989).

4   Celermajer, D. & Greaves, K. Survivors of coarctation repair: fixed but not cured. *Heart* **88**, 113–114 (2002).

5   Richter, Y. & Edelman, E. R. Cardiology is flow. *Circulation* **113**, 2679-2682 (2006).

6   Marsden, A. L. Simulation based planning of surgical interventions in pediatric cardiology. *Physics of Fluids* **25**, 101303 (2013).

7   Taylor, C. A. & Steinman, D. A. Image-based modeling of blood flow and vessel wall dynamics: applications, methods and future directions. *Annals of biomedical engineering* **38**, 1188-1203 (2010).

8   Vlachopoulos, C., O'Rourke, M. & Nichols, W. W. *McDonald's blood flow in arteries: theoretical, experimental and clinical principles*. (CRC press, 2011).

9   Di Carli, M. F., Geva, T. & Davidoff, R. The future of cardiovascular imaging. *Circulation* **133**, 2640-2661 (2016).

10   Ben-Assa, E. *et al.* Ventricular stroke work and vascular impedance refine the characterization of patients with aortic stenosis. *Science translational medicine* **11**, eaaw0181 (2019).

11   Keshavarz-Motamed, Z. *et al.* Elimination of transcoarctation pressure gradients has no impact on left ventricular function or aortic shear stress after intervention in patients with mild coarctation. *JACC: Cardiovascular Interventions* **9**, 1953-1965 (2016).

12   Z. Keshavarz-Motamed, S. K., F. Rikhtegar Nezami, J. Mahesh Amrute, S. J. Lee, J. Brown, E. Ben-Assa, S. Sellers, P. Blanke, J. Leipsic, T. Garcia Camarero, J. Ruano Calvo, J. M. de la Torre Hernandez, E. R. Edelman. Mixed valvular disease following transcatheter aortic valve replacement: quantification and systematic differentiation using clinical measurements and image-based patient-specific in silico modeling. *Journal of American Heart Association* **9**, e015063 (2020).

13   Tossas-Betancourt, C. *et al.* Computational analysis of renal artery flow characteristics by modeling aortoplasty and aortic bypass interventions for abdominal aortic coarctation. *Journal of vascular surgery* **71**, 505-516 (2019).

14   LaDisa, J. F. *et al.* Computational simulations for aortic coarctation: representative results from a sampling of patients. *Journal of biomechanical engineering* **133**, 091008 (2011).

15   Coogan, J. S., Humphrey, J. D. & Figueroa, C. A. Computational simulations of hemodynamic changes within thoracic, coronary, and cerebral arteries following early wall remodeling in response to distal aortic coarctation. *Biomechanics and modeling in mechanobiology* **12**, 79-93 (2013).

16   Keshavarz-Motamed, Z., Garcia, J. & Kadem, L. Fluid dynamics of coarctation of the aorta and effect of bicuspid aortic valve. *PLoS one* **8**, e72394 (2013).

17   Youssefi, P. *et al.* Impact of Patient-Specific Inflow Velocity Profile on Hemodynamics of the Thoracic Aorta. *Journal of biomechanical engineering* **140**, 011002 (2018).

18   Arzani, A., Dyverfeldt, P., Ebbers, T. & Shadden, S. C. In vivo validation of numerical prediction for turbulence intensity in an aortic coarctation. *Annals of biomedical engineering* **40**, 860-870 (2012).

19   Andersson, M., Lantz, J., Ebbers, T. & Karlsson, M. Multidirectional WSS disturbances in stenotic turbulent flows: A pre-and post-intervention study in an aortic coarctation. *Journal of biomechanics* **51**, 8-16 (2017).

20   Kim, H. J. *et al.* On coupling a lumped parameter heart model and a three-dimensional finite element aorta model. *Annals of biomedical engineering* **37**, 2153-2169 (2009).

21   LaDisa, J. F. *et al.* Computational simulations for aortic coarctation: representative results from a sampling of patients. *Journal of biomechanical engineering* **133** (2011).

22   Chen, S. & Doolen, G. D. Lattice Boltzmann method for fluid flows. *Annual review of fluid mechanics* **30**, 329-364 (1998).

23   Succi, S. *The lattice Boltzmann equation: for fluid dynamics and beyond.* (Oxford university press, 2001).

24   Nitä, C., Itu, L. M. & Suciu, C. in *2013 IEEE High Performance Extreme Computing Conference (HPEC).* 1-6 (IEEE).

25   Sadeghi, R., Shadloo, M., Hopp-Hirschler, M., Hadjadj, A. & Nieken, U. Three-dimensional lattice Boltzmann simulations of high density ratio two-phase flows in porous media. *Computers & Mathematics with Applications* **75**, 2445-2465 (2018).

26   Mirzaee, H. *et al.* MRI-based computational hemodynamics in patients with aortic coarctation using the lattice Boltzmann methods: Clinical validation study. *Journal of Magnetic Resonance Imaging* **45**, 139-146 (2017).

27   Henn, T., Heuveline, V., Krause, M. J. & Ritterbusch, S. in *International Workshop on Statistical Atlases and Computational Models of the Heart.* 34-43 (Springer).

28   Randles, A. P., Kale, V., Hammond, J., Gropp, W. & Kaxiras, E. in *2013 IEEE 27th International Symposium on Parallel and Distributed Processing.* 1063-1074 (IEEE).

29   Rybicki, F. J. *et al.* Prediction of coronary artery plaque progression and potential rupture from 320-detector row prospectively ECG-gated single heart beat CT angiography: Lattice Boltzmann evaluation of endothelial shear stress. *The International Journal of Cardiovascular Imaging* **25**, 289-299 (2009).

30   Gounley, J. *et al.* in *2016 38th annual international conference of the IEEE Engineering in Medicine and Biology Society (EMBC).* 3429-3432 (IEEE).

31   Randles, A. P., Bächer, M., Pfister, H. & Kaxiras, E. in *International Workshop on Statistical Atlases and Computational Models of the Heart.* 17-25 (Springer).

32   Keshavarz-Motamed, Z., Garcia, J., Pibarot, P., Larose, E. & Kadem, L. Modeling the impact of concomitant aortic stenosis and coarctation of the aorta on left ventricular workload. *Journal of biomechanics* **44**, 2817-2825 (2011).

33   Keshavarz-Motamed, Z. *et al.* The role of aortic compliance in determination of coarctation severity: lumped parameter modeling, in vitro study and clinical evaluation. *Journal of biomechanics* **48**, 4229-4237 (2015).

34   Heuveline, V. & Latt, J. The OpenLB project: an open source and object oriented implementation of lattice Boltzmann methods. *International Journal of Modern Physics C* **18**, 627-634 (2007).

35   Mittal, R., Simmons, S. & Udaykumar, H. Application of large-eddy simulation to the study of pulsatile flow in a modeled arterial stenosis. *Journal of biomechanical engineering* **123**, 325-332 (2001).

36   Bhatnagar, P. L., Gross, E. P. & Krook, M. A model for collision processes in gases. I. Small amplitude processes in charged and neutral one-component systems. *Physical review* **94**, 511 (1954).

37   Mohamad, A. A. *Lattice Boltzmann method: fundamentals and engineering applications with computer codes.* (Springer Science & Business Media, 2011).

38   Sadeghi, R., Safdari Shadloo, M., Abdollahzadeh Jamalabadi, M. Y. & Karimipour, A. A three-dimensional lattice Boltzmann model for numerical investigation of bubble growth in pool boiling. *International Communications in Heat and Mass Transfer* **79**, 58–66, (2016).

39   Sadeghi, R. & Shadloo, M. Three-dimensional numerical investigation of film boiling by the lattice Boltzmann method. *Numerical Heat Transfer, Part A: Applications* **71**, 560-574 (2017).

40   d'Humieres, D. Generalized lattice-Boltzmann equations. *Progress in Astronautics and Aeronautics* **159**, 450-450 (1994).

41   Sukop, M. & DT Thorne, J. *Lattice Boltzmann Modeling* (Springer, Berlin, Heidelberg, 2006).

42   Nathen, P., Gaudlitz, D., Krause, M. & Kratzke, J. in *21st AIAA Computational Fluid Dynamics Conference. American Institute of Aeronautics and Astronautics.*

43   Bouzidi, M. h., Firdaouss, M. & Lallemand, P. Momentum transfer of a Boltzmann-lattice fluid with boundaries. *Physics of fluids* **13**, 3452-3459 (2001).

44   Porter, B., Zauel, R., Stockman, H., Guldberg, R. & Fyhrie, D. 3-D computational modeling of media flow through scaffolds in a perfusion bioreactor. *Journal of biomechanics* **38**, 543-549 (2005).

45   LaDisa Jr, J. F. *et al.* Circumferential vascular deformation after stent implantation alters wall shear stress evaluated with time-dependent 3D computational fluid dynamics models. *Journal of applied physiology* **98**, 947-957 (2005).

46   Stahl, B., Chopard, B. & Latt, J. Measurements of wall shear stress with the lattice Boltzmann method and staircase approximation of boundaries. *Computers & Fluids* **39**, 1625-1633 (2010).

47   Skordos, P. Initial and boundary conditions for the lattice Boltzmann method. *Physical Review E* **48**, 4823 (1993).

48   Heuveline, V., Krause, M. J. & Latt, J. Towards a hybrid parallelization of lattice Boltzmann methods. *Computers & Mathematics with Applications* **58**, 1071-1080 (2009).

49   Jin, S., Oshinski, J. & Giddens, D. P. Effects of wall motion and compliance on flow patterns in the ascending aorta. *Journal of biomechanical engineering* **125**, 347-354 (2003).

50   Vogt, M. *et al.* Impaired elastic properties of the ascending aorta in newborns before and early after successful coarctation repair: proof of a systemic vascular disease of the prestenotic arteries? *Circulation* **111**, 3269-3273 (2005).

51   Xu, J. *et al.* Intravascular ultrasound assessment of regional aortic wall stiffness, distensibility, and compliance in patients with coarctation of the aorta. *American heart journal* **134**, 93-98 (1997).

52   Brili, S. *et al.* Aortic elastic properties in patients with repaired coarctation of aorta. *Journal of the American College of Cardiology* **31**, 401 (1998).

53   Davies, P. F., Barbee, K. A., Lal, R., Robotewskyj, A. & Griem, M. L. Hemodynamics and Atherogenesis: Endothelial Surface Dynamics in Flow Signal Transduction a. *Annals of the New York Academy of Sciences* **748**, 86-102 (1994).

54   Jr. LaDisa, J. F. *et al.* Computational simulations demonstrate altered wall shear stress in aortic coarctation patients treated by resection with end-to-end anastomosis. *Congenital heart disease* **6**, 432-443 (2011).

55   Timmins, L. H. *et al.* Focal association between wall shear stress and clinical coronary artery disease progression. *Annals of biomedical engineering* **43**, 94-106 (2015).

56   Parks, W. J. *et al.* Incidence of aneurysm formation after Dacron patch aortoplasty repair for coarctation of the aorta: long-term results and assessment utilizing magnetic resonance angiography with three-dimensional surface rendering. *Journal of the American College of Cardiology* **26**, 266-271 (1995).

57   Kirsh, M., Perry, B. & Spooner, E. Management of pseudoaneurysm following patch grafting for coarctation of the aorta. *The Journal of thoracic and cardiovascular surgery* **74**, 636 (1977).

58   Fung, Y.-C. *Mechanical properties of living tissues*. Vol. 547 (Springer, 1993).

59   Oliver, J. M. *et al.* Risk factors for aortic complications in adults with coarctation of the aorta. *Journal of the American College of Cardiology* **44**, 1641-1647 (2004).

60   Mullins, C. E. *Cardiac catheterization in congenital heart disease: pediatric and adult*. (John Wiley & Sons, 2008).

61   Bergersen, L., Foerster, S., Marshall, A. C. & Meadows, J. *Congenital heart disease: the catheterization manual*. (Springer Science & Business Media, 2008).

62   Holloway, B. J., Rosewarne, D. & Jones, R. G. Imaging of thoracic aortic disease. *The British journal of radiology* **84**, S338-S354 (2011).

63   Kilner, P. J., Gatehouse, P. D. & Firmin, D. N. Flow measurement by magnetic resonance: a unique asset worth optimising. *Journal of Cardiovascular Magnetic Resonance* **9**, 723-728 (2007).

64   Elkins, C. J. & Alley, M. T. Magnetic resonance velocimetry: applications of magnetic resonance imaging in the measurement of fluid motion. *Experiments in Fluids* **43**, 823-858 (2007).

65   Nie, P. *et al.* The value of low-dose prospective ECG-gated dual-source CT angiography in the diagnosis of coarctation of the aorta in infants and children. *Clinical radiology* **67**, 738-745 (2012).

66   Karaosmanoglu, A. D., Khawaja, R. D. A., Onur, M. R. & Kalra, M. K. CT and MRI of aortic coarctation: pre-and postsurgical findings. *American Journal of Roentgenology* **204**, W224-W233 (2015).

67   Xu, J. *et al.* Accuracy, image quality, and radiation dose of prospectively ECG-triggered high-pitch dual-source CT angiography in infants and children with complex coarctation of the aorta. *Academic radiology* **21**, 1248-1254 (2014).

68   Garcia, D. *et al.* Two-dimensional intraventricular flow mapping by digital processing conventional color-Doppler echocardiography images. *IEEE transactions on medical imaging* **29**, 1701-1713 (2010).

69   Poelma, C. *et al.* 3D Flow reconstruction using ultrasound PIV. *Experiments in fluids* **50**, 777-785 (2011).

70   Kim, H.-B., Hertzberg, J. R. & Shandas, R. Development and validation of echo PIV. *Experiments in fluids* **36**, 455-462 (2004).

71   Trahey, G. E., Allison, J. W. & Von Ramm, O. T. Angle independent ultrasonic detection of blood flow. *IEEE Transactions on Biomedical Engineering* **BME-34**, 965-967 (1987).

72   Sengupta, P. P. *et al.* Left ventricular isovolumic flow sequence during sinus and paced rhythms: new insights from use of high-resolution Doppler and ultrasonic digital particle imaging velocimetry. *Journal of the American College of Cardiology* **49**, 899-908 (2007).

73   Jensen, J. A., Nikolov, S. I., Yu, A. C. & Garcia, D. Ultrasound vector flow imaging—Part I: Sequential systems. *IEEE Trans. Ultrason., Ferroelectr., Freq. Control* **63**, 1704-1721 (2016).

74   Guo, Z. & Shu, C. *Lattice Boltzmann method and its applications in engineering*. Vol. 3 (World Scientific, 2013).

75   Krüger, T. *et al. The lattice Boltzmann method*. Vol. 10 (Springer, 2017).

Chapter 3: Impact of mixed valvular disease on coarctation hemodynamics using patient-specific lumped parameter and Lattice Boltzmann modeling

Reza Sadeghi[1], Nadav Gasner[2], Seyedvahid Khodaei[1], Julio Garcia[3,4,5,6], PhD, Zahra Keshavarz-Motamed*[1,8,9], PhD

[1]Department of Mechanical Engineering, McMaster University, Hamilton, ON, Canada

[2]Department of Medicine, McMaster University, Hamilton, ON, Canada

[3]Stephenson Cardiac Imaging Centre, Libin Cardiovascular Institute of Alberta, Calgary, AB, Canada

[4]Department of Radiology, University of Calgary, Calgary, AB, Canada

[5]Department of Cardiac Sciences, University of Calgary, Calgary, AB, Canada

[6]Alberta Children's Hospital Research Institute, Calgary, AB, Canada

[7]Division of Cardiology, Department of Medicine, McMaster University, Hamilton, ON, Canada

[8]School of Biomedical Engineering, McMaster University, Hamilton, ON, Canada

[9]School of Computational Science and Engineering, McMaster University, Hamilton, ON, Canada

This paper was submitted and is under review.

* Correspondence author

3.1   Abstract

The optimal course of intervention for patients with coexisting coarctation of the aorta (COA) and mixed valvular disease (combinations of aortic and mitral valve pathologies, MVD) is an area of contention and uncertainty. To effectively evaluate risk status and create guidelines for intervention aimed at minimizing the progression of cardiovascular disease, precise diagnostic information, which hinges on the quantification of aortic fluid dynamics, is required. For this purpose, we developed an innovative patient-specific computational-mechanics framework that integrates the local hemodynamics with the global circulatory cardiovascular system using the 3-D Lattice Boltzmann method along with lumped parameter modeling to investigate the impact of COA and MVD on aortic fluid dynamics in patients with COA and MVD. The computational framework was validated against clinical cardiac catheterization data and Four-dimensional flow magnetic resonance imaging. Our results demonstrate that MVD interacts with COA fluid dynamics, amplifying irregular flow patterns especially downstream of COA and may contribute to speed up the progression of the disease. More specifically, aortic regurgitation and mitral regurgitation, when coexistent with COA, substantially lead to significant progression of the disease at the COA region. We concluded that not only the severity of the COA, but also the presence and the severity of the MVD should be considered in the evaluation of risks in patients with COA. The results suggest that some more aggressive surgical approaches may be required as regularly chosen current surgical techniques may not be optimal for patients with both COA and MVD.

Keywords: Coarctation, mixed valvular disease, aortic fluid dynamics, hemodynamics, Lattice Boltzmann method, patient-specific lumped parameter model, abnormal hemodynamics

3.2   Introduction

Coarctation of the aorta (COA) is among the most common congenital heart defects (CHD), accounting for 5-8% of CHD cases with an estimated incidence of 3-4/10000 live births [1-4]. COA was originally considered a simple lesion consisting of an isolated narrowing of the aortic isthmus, however, it is now recognized to be a general arteriopathy with increased mortality even after a clinically "successful" repair [5-8]. A complicating factor of COA is its common association with mixed valvular diseases (MVD), which include varying combinations of aortic and mitral valve pathologies. Bicuspid aortic valve (BAV) is the most prevalent MVD in patients with COA, occurring in 60-85% of cases [7-10]. Additionally, aortic regurgitation (AR) and aortic stenosis (AS) are seen in 4% and 5-17% of COA cases, respectively [9,10]. Mitral valve abnormalities are also frequently found alongside COA, most commonly mitral regurgitation (MR) in 4% of cases, but mitral stenosis (MS) is also prevalent [9-11]. The discovery of Shone's Complex, a tetralogy including COA and MVDs, suggests a strong link between the developmental origins of COA and MVDs [2,3,12].

Although COA is readily diagnosed and interventional and surgical treatments are employed, argument and uncertainty persist when COA coexists with MVD as the hemodynamic abnormalities of one lesion often amplify or mask the presence of the other [12-14]. The current clinical definition for a severe COA, warranting interventional therapy, is a 20 mmHg transcoarctation pressure gradient [15,16]. Even with an uncomplicated COA, the validity of using this transcoarctation pressure gradient threshold to classify the degree of COA has been questioned as it relies on few data, and may be an oversimplification of complex hemodynamic and vascular changes[3,17]. Furthermore, the impact of MVD on this gradient has yet to be quantified and may further complicate clinical diagnosis[17,18]. The optimal course of intervention for a patient with coexisting MVD and COA is an area of contention and uncertainty. Conventionally, surgery has been performed in a two-stage operation, repairing the COA prior to the MVD. This decreases the risk of poorly perfusing the lower-body, allows the myocardium to recover between operations, and has better intraoperative visibility [19,20]. However, there is increasing support for a one-stage operation as it can avoid overloading the heart and is associated with less trauma, reducing the post-operative ICU stay, while remaining as safe as conventional two-stage operations [19,21,22]. Ultimately, the choice of intervention is at the discretion of the health-care team, and is independently evaluated for each patient based on their anatomy and risk-factors [23,24]. An elucidation of the interplay between valvular pathologies and COA can provide clinically-relevant insight into how to best manage patients, both regarding the optimal timing of intervention, and the best strategy for minimizing post-operative complications and morbidity [22].

The essential sources of cardiovascular mortality and morbidity can be explained on the basis of adverse hemodynamics: abnormal biomechanical forces and flow patterns, leading to the development and progression of cardiovascular disease [7,25-28]. To effectively evaluate risk status and create guidelines for intervention aimed at minimizing the progression of cardiovascular disease, precise diagnostic information, which hinges on the quantification of a*ortic fluid dynamics* (e.g., details of the instantaneous 3-D flow), is required. A patient-specific computational or experimental diagnostic framework that can quantify hemodynamics in patients with coarctation should satisfy the following 2 requirements:

(1) The local fluid dynamics is influenced by the conditions downstream and upstream of coarctation. Therefore, in addition to performing the 3-D blood flow calculations in the patient-specific geometry, imposing accurate patient-specific flow and pressure boundary conditions is critically important for a patient-specific diagnostic framework. This not only gives patient-specific flow and pressure conditions to the local flow but also enables providing diagnostic information about the global circulatory physiology. The patient-specific boundary conditions should be obtained non-invasively in each patient because obtaining them invasively (e.g., with catheterization) contradicts the whole purpose of the computational framework.

(2) The patient-specific diagnostic framework should provide valid results to be considered as a reliable diagnostic tool. Upon development of a computational

diagnostic framework, its results should be validated against clinical data that include data obtained using cardiac catheterization, Doppler echocardiography and magnetic resonance imaging. Cardiac catheterization is used as the clinical gold standard to evaluate pressure and flow through heart and circulatory system, but it can only provide access to the blood flow and pressure in very limited regions. Doppler echocardiography is the most versatile tool to evaluate local hemodynamics and has a high temporal resolution, but it has limited spatial access through chest. Phase-contrast magnetic resonance imaging can provide local flow, but it is not possible for many patients with implanted devices. As each of these modalities have their own limitations, a multi-modality validation of the computational framework would be required.

There have been important attempts for quantifying blood flow through isolated COA (without mixed valvular diseases) computationally[17,28-36] and experimentally[32,37,38]. None of these models satisfy Requirement #2: most were not validated while some were only partially validated[28-31,33-36]. Most of these studies do not satisfy Requirement #1 as they do not have patient-specific boundary conditions. Among all, few studies[17,28,31,33,34] coupled blood-flow calculations with lumped-parameter modelling to impose boundary conditions on the calculations[28]. However, there is no (computational or experimental) study on investigating the effects of MVD on COA hemodynamics.

In this study, we developed an innovative patient-specific, image-based, computational-mechanics framework that integrates the local hemodynamics with the global circulatory cardiovascular system using the 3-D Lattice Boltzmann method (LBM) along with Doppler-based lumped parameter modeling (LPM) to investigate the impact of COA and MVD on aortic fluid dynamics in 3 patients with COA and MVD. The developed computational framework was validated against clinical cardiac catheterization data and Four-dimensional flow magnetic resonance imaging (4-D flow MRI). To the best of our knowledge, this is the first study that investigates the effects of MVD on COA hemodynamics.

3.3   Material and Method

We developed a patient-specific image-based computational fluid dynamics framework to simulate the hemodynamics in patients with COA and MVD (Figure 1, Panel A). This framework is based on a Doppler-based lumped parameter modeling[17,39] and 3-D lattice Boltzmann method[28] (LBM; large eddy simulation, Smagorinsky subgrid scale model), implemented in the open-source OpenLB library with some supplements as explained in *Lattice Boltzmann method section*. Calculations of this computational fluid dynamics framework were validated against 4-D flow MRI measurements (Figure 1, Panel B, schematic diagram; Figures 2 and 3, validation).
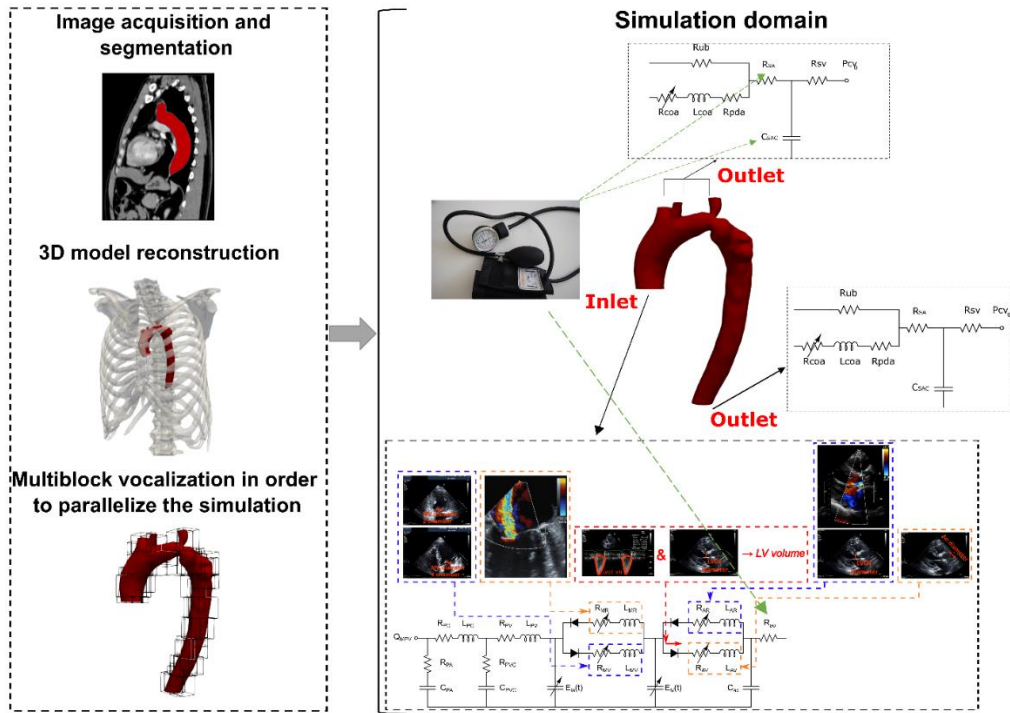
(a)
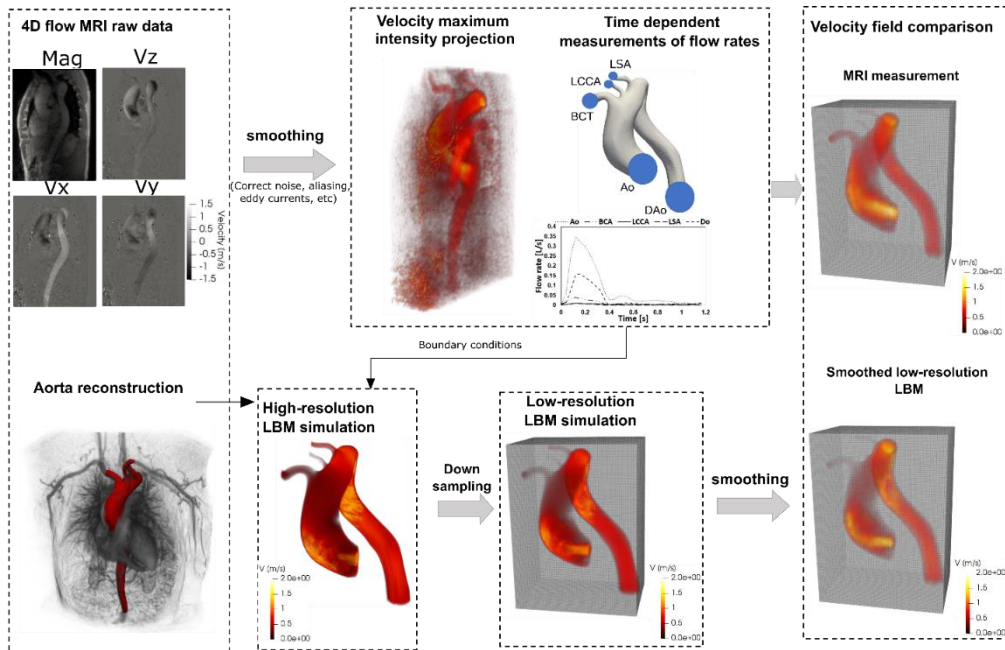
(b)

Figure 3-1 Reconstructed geometry and simulation domain. (a) In this study, we developed a patient-specific, imaged-based, computational-mechanics framework that dynamically couples the local hemodynamics with the global circulatory cardiovascular system to investigate the impact of COA and MVD on both local and global hemodynamics in these patients. We used CT images from patients to segment and reconstruct the 3D geometries of the complete aorta. These 3-D geometries were used for investigating hemodynamic using computational fluid dynamics. Local flow dynamics is greatly influenced by upstream and downstream flow conditions that are absent in the flow simulation domain. A lumped-parameter model simulates the function of the left side of the heart[28]. Time-dependent inlet flow at ascending aorta and outlet pressure at descending aorta position were obtained from lumped parameter modeling and applied as boundary conditions. Boundary conditions of the aortic branches were adjusted to match the flow distribution. (b) We compared 4-D flow MRI data and results of our computational framework. The 3-D geometry of the complete aorta was reconstructed using MRI images and the entire volume of Down-sampled LBM data was smoothed[34,35] (see *Four-dimensional flow magnetic resonance imaging (4-D flow MRI* section for more details).

3.3.1 Study population

Deidentified and anonymous patients with COA and MVD at Stephenson Cardiac Imaging Centre, Libin Cardiovascular Institute of Alberta (Calgary, AB, Canada) and St. Joseph's Healthcare (Hamilton, ON, Canada) were considered. Informed consent was obtained from all participants. The selections were done by operators blinded to the objectives and contents of this study at each institution and the protocols were reviewed and approved by the Institutional Review Boards of each institution (Hamilton Integrated Research Ethics Board and Libin Cardiovascular Institute of Alberta Ethics Board). All methods and measurements were performed in accordance with relevant guidelines and regulations including guidelines of the American College of Cardiology and American Heart Association. Moreover, the Doppler echocardiography (DE) metrics were measured

using OsiriX imaging software (version 8.0.2; Pixmeo, Switzerland) in patients as the inputs for our lumped parameter model. In addition. the lumped parameter model uses the brachial systolic and diastolic pressure measurements from the sphygmomanometer. Computed tomography (CT) data was collected including images and documented reports. CT images were segmented and the 3-D geometries of the complete aorta in patients were reconstructed to be used for our computational model.

3.3.2 Four-dimensional flow magnetic resonance imaging (4-D flow MRI)

Four-dimensional flow magnetic resonance imaging (4-D flow MRI) is a recent development of phase-contrast MRI (PC-MRI) with the capability of comprehensive blood flow assessment in three spatial dimensions over the cardiac cycle[17]. 4-D flow MRI provides visualization of the vascular territory of interest and allows for the estimation of hemodynamic biomarkers such as wall shear forces[17] and pressure gradients [40,41]. Additionally, 4-D flow MRI provides comprehensive information regarding complex flow patterns in vascular diseases[42]. *In this* study, acquisition of 4-D flow MRI data in patients with COA and valvular diseases was performed (Figure 1, Panel B, data acquisition and analysis workflow of 4-D flow MRI) by standard Cartesian 4-D flow sequence using 1.5T MRI scanners (Philips Achieva; Philips Medical Systems, Best, the Netherlands). Electrocardiogram gating synchronized and diaphragm navigator gated 4-D flow MRI were performed during free breathing. Acquisition parameters were as follows:

spatial resolution of (1.97–2.62, 1.97–2.62, 2.5–4 mm^3), temporal resolution of 36–40 ms. Velocity encoding was set to the range (1.5–4.5 m/s), the total scan time for each measurement varied from 8 to 15 min. All 4-D flow data was corrected for multiple sources of phase offset errors and noises such as velocity aliasing, Maxwell terms, and eddy currents using an in-house MATLAB-based code (MathWorks, Inc.). Data smoothing algorithm proposed by Garcia[43,44] was used to eliminate random errors of the velocity vectors. Garcia[43,44] proposed a fully automated smoothing procedure based on a penalized least squares approach that allows fast smoothing of the data and can replace spurious or missing vectors with the smoothed one.

The 3-D segmentation of thoracic aorta geometry and orifice shape of the bicuspid valve was performed by ITK-SNAP (Yushkevich et al., 2006; http://www.itksnap.org) and an in-house MATLAB-based code. Fusion 3-D (Autodesk, Inc) and Meshmixer (Autodesk, Inc) were used to smooth the geometry and fix the defects. Finally, the Stereolithography (STL) format of the geometry (domain) was extracted for our computational simulation. Time-varying flow velocity information extracted from patient-specific 4D flow MRI data was imposed at the inlet and outlets of each LBM computational model. To study the effect of resolution and comparing LBM to 4D flow MRI velocity fields on identical grids, we down sampled the high-resolution LBM velocities into PC-MRI resolution by linear interpolation of LBM velocity on MRI sub grid. Moreover, Down-sampled LBM data subjected to an imitation of the smoothing inherent in the 4D flow MRI measurement to have the closest LBM approximation to the 4D flow MRI data. The down-sampling and smoothing procedures are schematically shown in Figure 1 (Panel B).

Velocity field extracted from 4D flow MRI measurements was smoothed through a multidimensional spline smoothing technique proposed by Garcia[43,44]. The algorithm deals with occurrences of missing and outlying values and eliminates random errors automatically. The mathematics behind algorithm structure is based on penalized least squares approach that allows fast smoothing of the data and can replace spurious or missing vectors with the smoothed one. The algorithm allows fast unsupervised smoothing that combines the use of the discrete cosine transform (DCT) and the generalized cross-validation score. Garcia's algorithm was compared with conventional methods, including the normalized median test, and experimental raw PIV velocity fields and it was shown that it can easily deal with a large amount of missing data and reduce the experimental noise while keeping the most important characteristics of a dataset[43] (see Supplementary material, Appendix A1, for more information on the smoothing algorithm).

In the current study, to investigate the effect of resolution and to compare LBM and 4D flow MRI velocity fields on identical grids, we down sampled the high-resolution LBM velocity fields by linear interpolation on the 4D flow MRI grid. The down-sampling and smoothing procedures are schematically shown in Figure 1 (Panel B).

3.3.3 Lattice Boltzmann Method (LBM)

Blood flow in a healthy vascular system is mostly laminar, however, blood flood becomes distally turbulent under pathophysiological conditions. We used a 3-D LBM-based

computational fluid dynamics approach using Large eddy simulations (LES, Smagorinsky subgrid scale model) to simulate blood flow through the aorta. LES is well suited for computational modeling of turbulent vascular flows with a high potential in modeling the physiological low-Reynolds transitional flows[17,28].

❖ **Governing equations**

All details about governing equations were presented in Supplementary Material (Appendix A_2).

❖ **Lattice Boltzmann method & Large Eddy simulation**

Details about turbulent modeling were described in Supplementary material (Appendix A_2).

❖ **Modeling surface curvature near the wall of complex geometries**

In order to treat boundaries of inclined and complicated geometry, an interpolated bounce-back scheme proposed by Bouzidi et al. [45] was used. For evaluating the post-propagation state of fluid node A next to a curved solid wall, the distribution function used for this technique [28] was defined as:

$$f_{\bar{\alpha}}(x_A, t + \Delta t) = \begin{cases} 2q f_\alpha^c(x_A, t) - (1 - 2q) f_\alpha^c(x_E, t) & q < \frac{1}{2} \\ \frac{1}{2q} f_\alpha^c(x_A, t) + \frac{(2q-1)}{2q} f_\alpha^c(x_A, t) & q \geq \frac{1}{2} \end{cases} \quad (1)$$

where $f_{\bar{\alpha}}(x_A, t + \Delta t)$ is the post-collision and post-propagation state of the distribution function at the point x_A and time $(t + \Delta t)$. f_α^c is the value of the distribution function after a

collision and before propagation state of the fluid node; the factor q is the normalized distance from the wall [28].

❖ **Wall shear stress**

Wall shear stress (WSS) is the frictional force induced by fluid moving along a solid wall. The total stress tensor for the fluid is as follows:

$$T_{ij} = -p.\delta_{ij} + \sigma_{ij} \tag{2}$$

where p, δ_{ij} and σ_{ij} are pressure, Kronecker symbol and contribution from the viscous force, respectively. $T_{ij}n_j$ is the stress on the boundary surface element with normal vector $\vec{n}$. The wall stress vector, $\vec{\tau}$, is computed as:

$$\tau_i = T_{ij}n_j - (n_j T_{kj} n_k)n_i \tag{3}$$

Since the projection of normal stress $(p.\delta_{ij})$ on the tangential plane is zero, the total stress T_{ij} can be replaced by σ_{ij}. For a Newtonian fluid, the viscouse stress is proportional to the strain rate tensor $(\sigma_{ij} = 2\mu\varepsilon_{ij})$ [46,47] and strain rate tensor is as follows:

$$\varepsilon_{ij} = -\frac{1}{2\rho\tau c_s^2}\Pi_{ij} \tag{4}$$

where Π_{ij} is second order non equilibrium moment and can be computed locally from the particle distribution *functions*.

❖ **Model properties & Boundary conditions**

Aortic local flow dynamics are greatly influenced by upstream and downstream flow conditions which must be accounted for. Additionally, the proper choice of boundary conditions is crucial as they influence the accuracy of flow simulations. Blood was assumed to be a Newtonian and incompressible fluid with dynamic viscosity of 0.0035 Pa·s and density of 1050 kg/m^3. A lumped-parameter model (Figure 1) simulated the function of the left side of the heart in the presence of COA and MVD and was used to impose the time-dependent inlet flow at the ascending portion of the aorta along with the outlet pressure at the descending portion of the aorta. The time-dependent flow rate obtained from the lumped-parameter model was used to scale this profile in order to observe this time-varying inlet boundary condition (Figure 1). The inlet velocity boundary condition in lattice Boltzmann was implemented using the method suggested by Skordos[48] which uses a second-order finite difference scheme to compute the velocity gradient of the boundary nodes and extrapolates the pressure distribution at the inlet from bulk nodes[49]. Furthermore, a sinusoidal smooth start-up phase was used to the initiate the simulation and smoothly increase velocity from zero, the initial condition, in order to avoid pressure fluctuation artifacts at the inlet [50,51]. The total flow rate headed to the branches was calculated using the lumped-parameter model and then distributed to the branches based on the relative cross-sectional area of each branch at the inlet. Note: our lumped parameter model used a limited number of input parameters that can all be reliably measured using Doppler echocardiography and a sphygmomanometer. The no-slip boundary condition was applied at the solid walls as described above (Section: *Modeling surface curvature near the wall of complex geometries*). The arterial wall was

treated as solid and rigid. This can be justified by: 1) Jin et al. (2003) showed that rigid wall assumption for the aorta is realistic. Their results showed that the overall behavior for wall shear stress at each point is similar for the rigid and elastic walls with average root mean squared error of 1.23%[52]. Furthermore, their velocity distribution, computed in both elastic and rigid models, showed very strong agreement with MRI velocity measurements; 2) patients with COA do not have elastic aorta - they are highly hypertensive and characterized by highly reduced compliance and elevated stiffness index in both proximal and distal aorta[53-57]. 3) Keshavarz-Motamed et al. (2013) showed that there is very good agreement between numerical simulations, including rigid wall, and MRI velocity measurements, which includes elastic aorta, justified rigid wall as a quite well assumption[32]. 4) Keshavarz-Motamed et al. (2016) showed that there are very good agreements between numerical simulations, including rigid wall, and clinical Doppler echocardiography velocity measurements in 34 patients with coarctation (68 cases) in both pre and post intervention, which includes elastic aorta, justified rigid wall as a very well assumption[17]. Similar results were concluded by Sadeghi et al. (2020)[28] – there were very good agreements between computational results including rigid wall and clinical Doppler echocardiography velocity measurements in patient's aorta.

❖ **Reconstructed geometries in patients with coarctation**

3D geometries of the complete aorta including ascending aorta, aortic branches and descending aorta were reconstructed from segmented CT images of patients using ITK-

SNAP (version 3.8.0-BETA), a 3-D image processing and model generation software package (Figure 1).

❖ **Numerical strategy**

Multiple and single relaxation time LBM-based model were coupled with Smagorinsky's turbulent model in order to stabilize complex turbulent fluid flow across the domain. For treating complex geometry, we utilized the second order accuracy method proposed by Bouzidi et al. [45]. A smooth start-up phase was added to the inlet velocity condition to suppress the undesired pressure fluctuation. For turbulent modelling, Large Eddy Smagorinsky subgrid-scale model with constant $C_s = 0.1$ was applied [58]. Mesh sensitivity analysis was performed for maximum velocity and pressure drop at the coarctation of the aorta region (Table 1). Mesh definition was considered acceptable if no significant differences (lower than 2%) existed between successive mesh refinements in both quantities. The physical time step in this study was as low as 1.5 μs and physical lattice height adjacent to the wall was as low as $50\,\mu m$ to ensure that it is within the viscous sublayer.

3.3.4 Lumped parameter model

Our developed lumped-parameter model includes several sub-models allowing for the analysis of complex coarctation disease when coexistent with other valvular, vascular and ventricular disease including: 1) left atrium, 2) left ventricle, 3) aortic valve, 4) mitral valve, 5) coarctation of the aorta, 6) systemic circulation, and 7) pulmonary circulation

(Figure 1) [17,39]. This paper reports an innovative method to integrate the parameter-estimation algorithm, the lumped -parameter model and non-invasive clinical Doppler echocardiography and sphygmomanometer measurements to make a patient-specific, *in silico* model of the cardiovascular system[17,39]. The algorithm uses the following input parameters that all can be reliably measured using Doppler echocardiography: forward left ventricular outflow tract stroke volume, heart rate, ejection time, ascending aorta area, left ventricular outflow tract area, aortic valve effective orifice area, mitral valve effective orifice area, COA severity and grading of aortic and mitral valves regurgitation severity. Other input parameters of the model are systolic and diastolic blood pressures measured using sphygmomanometers. The calculations of the lumped-parameter model were validated against cardiac catheterization data (the instantaneous pressures in the aorta and LV) in patients with complex valvular, ventricular and vascular diseases with substantial inter- and intra-patient variability with a wide range of disease (N=49)[39]. The model has already been validated against *in vivo* cardiac catheterization in patients with coarctation (N=40)[17,28], some sub-models have been validated against *in vivo* MRI data (N=57)[17] and *in vivo* Doppler echocardiography[59,60]. In addition, some of the sub-models of C3VD-CMF have been used previously[18,37,38,61-65].

❖ **Cardiac-arterial model**

1) **Left Ventricle**

LV pressure and volume were coupled using a time varying elastance E(t), a measure of cardiac muscle stiffness.

$$E(t) = \frac{P_{LV}(t)}{V(t) - V_0} \tag{5}$$

where $P_{LV}(t)$, $V(t)$, and V_0 are the LV time-varying pressure, time-varying volume, and unloaded volume, respectively.

In order to generate a signal to model LV elastance, a double Hill function representation of a normalized elastance curve for human adults was used [66,67]. This elastance curve has similar shapes in the normal human heart with various inotropic conditions or diseased human hearts despite the presence of differences with regard to the etiology of cardiovascular diseases[39,68,69]. As explained by Keshavarz-Motamed [39], to represent the normalized elastance function of the LV, we observed that among summation of Gaussian functions [70,71], Boltzmann Distribution [72], and double Hill function [66,67], the latter provided the most physiologically accurate results for the pressure, flow, and volume waveforms. The double Hill function which is a cooperative process [73], as physiologically expected from myocyte recruitment during preload. The double-Hill LV time-varying elastance curves (E) is as follows [66,67]:

$$E(t) = N \left(\frac{\left(\frac{t}{\tau_1}\right)^{m_1}}{1 + \left(\frac{t}{\tau_1}\right)^{m_1}} \right) \left(\frac{1}{1 + \left(\frac{t}{\tau_2}\right)^{m_2}} \right) + E_{min} \tag{6}$$

$$N = \frac{E_{max} - E_{min}}{2} \tag{7}$$

where N, τ_1, τ_2, m_1, m_2, E_{min} and E_{max} are elastane normalization, ascending time translation, descending time translation, ascending gradient, descending gradient,

minimum elastance and maximum elastance, respectively (see Table 2). A double Hill function was deemed necessary to model the contraction and relaxation in the heart chambers: in equation 6, the first term in brackets corresponds to the contraction of the chamber and the second term in brackets corresponds to the relaxation of the chamber. τ_1, τ_2, m_1, m_2 govern the time translation and gradient of the elastance function, respectively: (1) τ_1 and τ_2 are parameters that are functions of the cardiac cycle duration (T) and are calculated in each patient using the equations provided in Table 2; (2) m_1, m_2 are constant for all patients (see Table 2 for more details). Parameter values used for the elastance function were adapted from [68,74-82] to obtain physiologically realistic waveforms for pressure, volume, and flow that can be found in Table 2.

2) Left Atrium

LA pressure and volume were coupled using time varying elastance E(t), following the same method described above for the LV model, and thus the elastance function used for LA is defined in equations 6 and 7 as well [66,67] (Table 2). Additionally, a phase lag was used in the LA elastance function to account for the relative onset of contractions between LA and LV [67]. Specifically, LV contraction was initiated at T = 0, and LA contraction was introduced at 0.85 T [67], resulting in a time delay of 0.15 T.

❖ Modeling heart valves

1) Aortic valve

The aortic valve was modeled using the net pressure gradient formulation (PG_{net}) through the aortic valve. This formulation explains the instantaneous net pressure gradient across the aortic valve as a function of the instantaneous flow rate and the energy loss coefficient which links the LV pressure to the ascending aorta pressure as follows[17,18,39] :

$$PG_{net}|_{AV} = \frac{2\pi\rho}{\sqrt{E_L Co|_{AV}}} \frac{\partial Q(t)}{\partial t} + \frac{\rho}{2E_L Co|^2_{AV}} Q^2(t) \tag{8}$$

and

$$E_L Co|_{AV} = \frac{(EOA|_{AV})A_{AO}}{A - EOA|_{AV}} \tag{9}$$

where $E_L Co|_{AV}$, $EOA|_{AV}$, A_{AO}, ρ and Q are the valvular energy loss coefficient, the effective orifice area, ascending aorta cross sectional area, fluid density and transvalvular flow rate, respectively.

2) **Aortic regurgitation**

Aortic regurgitation (AR) was modeled using the same analytical formulation as the aortic valve and is as follows[17,39,83] :

$$PG_{net}|_{AR} = \frac{2\pi\rho}{\sqrt{E_L Co|_{AR}}} \frac{\partial Q(t)}{\partial t} + \frac{\rho}{2E_L Co|^2_{AR}} Q^2(t) \tag{10}$$

and

$$E_L Co|_{AR} = \frac{EO A_{AR} A_{LVOT}}{A_{LVOT} - EO A_{AR}} \tag{11}$$

where $E_L Co|_{AR}$, EOA_{AR} and A_{LVOT} are regurgitation energy loss coefficient, regurgitant effective orifice area and LVOT area, respectively. The AR pressure gradient is calculated as the difference between aorta pressure and LV pressure during diastole.

3) Mitral valve

The mitral valve (MV) was modeled using the analytical formulation for the net pressure gradient ($PG_{net}|_{MV}$) across the MV during LA ejection[39,84]. Density remains constant and viscous effects are disregarded as this formulation expresses the instantaneous net pressure gradient across the LA and vena contracta as an unsteady, incompressible and inviscid flow. $PG_{net}|_{MV}$ was expressed as a function of ρ, Q_{MV}, EOA_{MV} and M_{MV}, where they represent the density of fluid, transvalvular flow rate, effective orifice area and inertance, respectively[39]. In this formulation (equation 12), the pressure recovery phenomenon was ignored as the effect is insignificant due to the large volume of the LV [84].

$$PG_{net}|_{MR} = \frac{M_{MV}}{EOA_{MV}}\frac{\partial Q_{MV}(t)}{\partial t} + \frac{\rho}{2EOA|_{MV}^2}Q_{MV}{}^2(t) \tag{12}$$

4) Mitral regurgitation

Mitral regurgitation (MR) was modeled using the following equation[39,84]. The MR pressure gradient is calculated as the difference between mitral pressure and LA pressure during systole.

$$PG_{net}|_{MR} = \frac{M_{MV}}{EOA_{MR}}\frac{\partial Q(t)}{\partial t} + \frac{\rho}{2EOA|_{MR}^2}Q^2(t) \tag{13}$$

where $EOA|_{MR}$ is MR effective orifice area.

❖ **Modeling coarctation of the aorta**

The characteristics of the arterial system are important when modeling COA as only a portion of total flow rate will cross the COA. To consider this, two parallel branches were considered: (1) the first branch simulates the flow towards the upper body, or the flow bypassing the COA (including aortic arch arteries and potential collaterals); (2) a second branch simulates the flow crossing COA and directed towards the descending aorta. This branch includes a resistance for the proximal descending aorta, and a time-varying resistance and an inductance which together represent the trans-coarctation net pressure gradient induced by the COA[17]:

$$TPG_{net}|_{coa} = \frac{2\pi\rho}{\sqrt{E_L Co|_{coa}}}\frac{\partial Q(t)}{\partial t} + \frac{\rho}{2E_L Co|_{coa}^2}Q^2(t) \tag{14}$$

$$E_L Co|_{COA} = \frac{(EOA|_{coa})A}{A - EOA|_{coa}} \tag{15}$$

where $E_L Co|_{coa}$, $EOA|_{coa}$, A, ρ and Q are the energy loss coefficient of the COA, the effective orifice area of the COA, aortic cross-sectional area downstream of the COA, the fluid density and the trans-coarctation flow rate, respectively.

❖ **Pulmonary flow**

The pulmonary valve flow waveform was simulated by a rectified sine curve with duration t_{ee} and amplitude Q_{MPV} as follows:

$$Q_{PV}(t) = Q_{MPV}\, sin\left(\frac{\pi t}{t_{ee}}\right), t \le t_{ee}\,; \quad Q_{PV}(t) = 0, t_{ee} < t \le T \tag{16}$$

where Q_{MPV}, t_{ee} and T are mean flow rate of the pulmonary valve, end-ejection time and cardiac cycle duration, respectively. Forward left ventricular outflow tract stroke volume (*Forward LVOT-SV*) was the sole input flow condition in this study. Indeed, the mean flow rate of the pulmonary valve (Q_{MPV}) was optimized so that the lump-parameter algorithm replicates the measured *Forward LVOT*-SV.

❖ **Computational algorithm**

The lumped-parameter model was analyzed numerically by creating and solving a system of ordinary differential equations in Matlab Simscape (MathWorks, Inc.), supplemented by additional functions written in Matlab and Simscape. Matlab's ode23t trapezoidal rule variable-step solver was used to solve the system of differential equations with an initial time step of 0.1 milliseconds. The convergence residual criterion was set to 10^{-6}. Initial voltages and currents of capacitors and inductors were set to zero. The model ran for numerous cycles (~ 150) to reach a steady state before starting the response optimization process described below. Simulations started at the onset of isovolumic contraction. The instantaneous LV volume, V(t), was calculated using the time varying elastance and LV pressure, P_{LV}. Subsequently, the LV flow rate was calculated as the time derivative of the instantaneous LV volume. The same approach was used to obtain the left-atrial volume,

pressure and flow rate. P_{LV} was initially calculated using the initial values of the model input parameters from Table 2. The *Forward LVOT-SV* was calculated using the lumped-parameter model and then fitted to the one measured by Doppler echocardiography by optimizing Q_{MPV}. Finally, for each patient R_{SA}, C_{SAC}, and C_{ao} were optimized to fit the aortic pressure from the model to the patient systolic and diastolic pressures measured using a sphygmomanometer. Blood was assumed to be a Newtonian and incompressible fluid with the dynamic viscosity of 0.0035 Pa·s and density of 1050 kg/m^3.

❖ Input parameters and patient-specific parameter estimation

Details about lumped parameter algorithm input parameters were described in Supplementary Material (Appendix A$_3$).

❖ Patient-specific response optimization

The parameters of the model are listed in Table 2. Some of the parameters were considered constant based on previous studies in the literature or shown in the rationale below and their values reported in Table 2. Additionally, the parameters that were measured in each patient can also be found in Table 2. In order to correctly simulate the conditions of the body for each patient, as described below, four parameters of the model were optimized so that the lumped-parameter model reproduced the physiological measurements performed in the patient. Simulink Design Optimization toolbox was used to optimize the response of the lumped-parameter model using the trust region reflective algorithm implemented in Matlab fmincon function. The response optimization was performed in two sequential automatic steps with tolerances of 10^{-6}.

The mean flow rate of the pulmonary valve, Q_{MPV}, could not be reliably measured using Doppler echocardiography. However, since *Forward LVOT-SV* can be measured reliably using Doppler echocardiography, in the first step of optimization, Q_{MPV} was optimized to minimize the error between the *Forward LVOT-SV* calculated by the lumped-parameter model and the one measured in each patient.

Physiologically, arterial hypertension is determined by two factors: the degree of reduction in the caliber of small arteries or arterioles, and the extent of reduction in the systemic arteries and veins compliance, C_{SAC}, and aortic compliance, C_{ao}. While the former is ensued by an increase in the systemic arteries resistance, R_{SA}, and the mean blood pressure, the latter results in an increase in the pulse pressure (systolic minus diastolic blood pressure). Therefore, in the second step of optimization, R_{SA}, C_{SAC}, and C_{ao} were optimized so that maximum and minimum values of aortic pressure were respectively equal to the systolic and diastolic pressures measured using a sphygmomanometer in each patient. Since the left ventricle faces the total systemic resistance and not the individual resistances, and the systemic arteries resistance, R_{SA}, is one order of magnitude greater than the aortic resistance, R_{ao}, systemic vein resistance, R_{SV}, and proximal descending aorta resistance, R_{pda}, for the sake of simplicity we considered R_{ao}, R_{SV} and R_{pda} as constants and optimized R_{SA} as the main contributor of the total systemic resistance in each patient[17,39,59,85].

Table 3-1. Grid sensitivity analysis. Velocity comparisons for different mesh resolutions in patient #2. We observed less than 2% variation in the maximum error in our mesh sensitivity study in the entire velocity domain for all 3 patients investigated in this study.
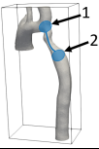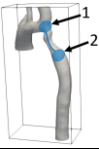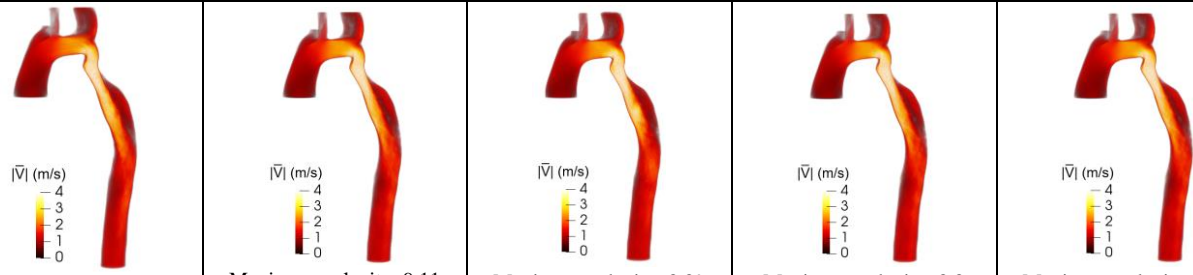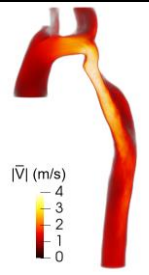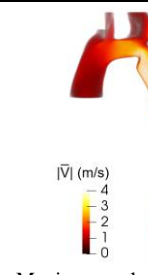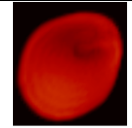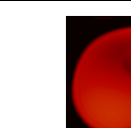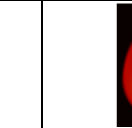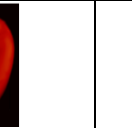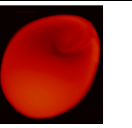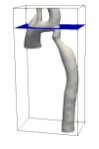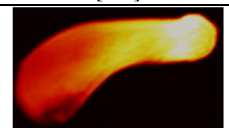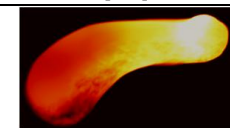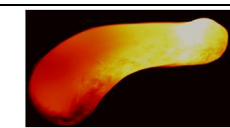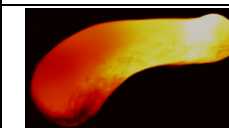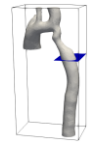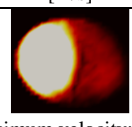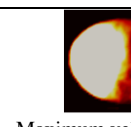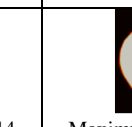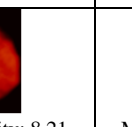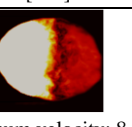
Name	Cell 1	Cell 2	Cell 3	Cell 4 (actual case)	Cell 5
Number of fluid cells	0.35 million	2.82 million	9.53 million	76.24 million	180.73 million
Peak pressure drop at COA $(P_1 - P_2)$	225.93 [mmHg]	219.12 [mmHg]	202.27 [mmHg]	201.98 [mmHg]	201.35 [mmHg]
3-D Velocity magnitude contour	Maximum velocity: 9.31[m/s] Average velocity: 1.55 [m/s]	Maximum velocity: 9.11 [m/s] Average velocity: 1.61 [m/s]	Maximum velocity: 8.89 [m/s] Average velocity: 1.65 [m/s]	Maximum velocity: 8.8 [m/s] Average velocity: 1.68 [m/s]	Maximum velocity: 8.77 [m/s] Average velocity: 1.69 [m/s]
Velocity (slice location A)	Maximum velocity: 1.78 [m/s] Average velocity: 1.24 [m/s]	Maximum velocity: 1.81 [m/s] Average velocity: 1.3 [m/s]	Maximum velocity: 1.82 [m/s] Average velocity:1.33 [m/s]	Maximum velocity: 1.86 [m/s] Average velocity:1.37 [m/s]	Maximum velocity: 1.86 [m/s] Average velocity:1.36 [m/s]
Velocity (slice location B)	Maximum velocity:4.87 [m/s] Average velocity: 2.12 [m/s]	Maximum velocity: 4.96 [m/s] Average velocity: 2.2 [m/s]	Maximum velocity: 4.95 [m/s] Average velocity:2.26 [m/s]	Maximum velocity: 4.97 [m/s] Average velocity: 2.27 [m/s]	Maximum velocity: 4.98 [m/s] Average velocity: 2.28 [m/s]
Velocity (slice location C)	Maximum velocity: 8.46 [m/s] Average velocity: 2.93 [m/s]	Maximum velocity: 8.14 [m/s] Average velocity: 3.27 [m/s]	Maximum velocity: 8.21 [m/s] Average velocity: 3.44 [m/s]	Maximum velocity: 8.35 [m/s] Average velocity: 3.46 [m/s]	Maximum velocity: 8.37 [m/s] Average velocity: 3.46 [m/s]

Table 3-2. Cardiovascular parameters. Summarized parameters used in the lumped parameter modeling to simulate all patient-specific cases with COA and MVD.

Description	Abbreviation	Value
Valve parameters		
Effective orifice area	EOA	Measured using DE
Inertance (mitral valve)	M_{MV}	Constant value: 0.53 gcm^{-2} gc m -2
Systematic circulation parameters		
Aortic resistance	R_{ao}	Constant value: 0.05 mmHg.s.mL^{-1}
Aortic compliance	C_{ao}	Initial value: 0.5 mL/mmHg Optimized based on brachial pressures *(Systolic and diastolic brachial pressures are optimization constraints)*
Systemic vein resistance	R_{SV}	0.05 mmHg.s.mL^{-1}
Systemic arteries and veins compliance	C_{SAC}	Initial value: 2 mL/mmHg Optimized based on brachial pressures *(Systolic and diastolic brachial pressures are optimization constraints)*
systemic arteries resistance (including arteries, arterioles and capillaries)	R_{SA}	Initial value: 0.8 mmHg.s.mL^{-1} Optimized based on brachial pressures *(Systolic and diastolic brachial pressures are optimization constraints)*
Upper body resistance	R_{ub}	Adjusted to have 15% of total flow rate in healthy case(94)
Proximal descending aorta resistance	R_{pda}	Constant value: 0.05 mmHg.s.mL^{-1}
Elastance Function[*]		
Maximum Elastance	E_{max}	2.1 (LV) 0.17 (LA)
Minimum Elastance	E_{min}	0.06 (LV, LA)
Elastance ascending gradient	m_1	1.32 (LV, LA)
Elastance descending gradient	m_2	27.4 (LV) 13.1 (LA)
Elastance ascending time translation	τ_1	0.269 T (LV) 0.110 T (LA)
Elastance descending time translation	τ_2	0.452 T (LV) 0.18 T (LA)
Pulmonary circulation parameters		
Pulmonary Vein Inertance	L_{PV}	Constant value:0.0005 mmHg·s^2·mL^{-1}
Pulmonary Vein Resistance	R_{PV}	Constant value: 0.002 mmHg·s·mL^{-1}
Pulmonary Vein and capillary Resistance	R_{PVC}	Constant value: 0.001 mmHg·s·mL^{-1}
Pulmonary Vein and Capillary Compliance	C_{PVC}	Constant value: 40 mL/mmHg
Pulmonary Capillary Inertance	L_{PC}	Constant value: 0.0003 mmHg·s^2·mL^{-1}
Pulmonary Capillary Resistance	R_{PC}	Constant value: 0.21 mmHg·s·mL^{-1}
Pulmonary Arterial Resistance	R_{PA}	Constant value: 0.01 mmHg·s·mL^{-1}
Pulmonary Arterial Compliance	C_{PA}	Constant value: 4 mL/mmHg
Mean Flow Rate of Pulmonary	Q_{MPV}	*Forward LVOT-SV is the only input flow condition*

Valve		(measured using DE). *Q_{MPV} is a flow parameter that was optimized so that the lump-parameter model could reproduce the desirable DE-measured Forward LVOT-SV.*
Input flow condition		
Forward left ventricular outflow tract stroke volume	*Forward LVOT-SV*	Measured using DE
Output condition		
Central venous pressure	P_{CV0}	Constant value: 4 mmHg
Other		
Constant blood density	ρ	Constant value: 1050 kg/m^3
Heart rate	HR	Measured using DE
Duration of cardiac cycle	T	Measured using DE
Systolic End Ejection time	T_{EJ}	Measured using DE

We conducted an extensive parameter sensitivity analysis that revealed negligible effects of changes in the pulmonary parameters (e.g., C_{PVC}) on the model output variables[17,39,59,85]. We, therefore, did not include these pulmonary parameters in the parameter-optimization process and considered them as constants given in Table 3.2.

3.4   Results

3.4.1 Validation: computational framework *vs.* 4-D flow MRI

The computational framework used in this study was validated against 4-D flow MRI measurements in COA patients (N=5). The level of qualitative agreement of the velocity field between 4D flow MRI data and LBM results, that we observed in this study, is comparable to those of previous observations made using other computational fluid dynamics methods [86-89]. Bland–Altman plots were graphed to describe the degree of concordance and agreement between LBM and 4-D flow MRI measurements [90]. Voxel-

by-voxel Bland-Altman analysis comparing the velocity fields resulted from the smooth down sampled low-resolution LBM and the 4-D flow MRI measurements on the entire flow domain at the early, peak and late systole, can be found in the Figure 2a & 2b. The middle blue solid line in the Bland-Altman chart indicates bias (mean difference) of the computed LBM velocity magnitude and the measured 4D flow MRI velocity magnitude ($\overline{\|u_{LBM}\| - \|u_{MRI}\|}$). This line is surrounded by the 95% limits of agreement illustrated with blue dashed lines (±1.96 SD). Here, SD is the standard deviation (the square root of variance) and it measures the random fluctuations around the mean difference value[90]. The results showed an agreement between the simulated and measured velocity fields in all five patients as follows. Mean of differences at early systole for patients #I, #II #III, #IV and #V were 0.12, -0.019, 0.051, -0.069 and -0.047 m/s, respectively, and the corresponding average limits of agreement (1.96 SD) were ±0.484, ±0.329, ±0.372, ±0.341 and ±0.196 m/s. Mean of differences at peak systole for patients #I, #II #III, #IV and #V were -0.008, -0.046, 0.057, -0.04 and -0.05 m/s, respectively, and the corresponding average limits of agreement (1.96 SD) were ±0.452, ±0.346, ±0.366, ±0.274 and ±0.188 m/s, respectively. Mean of differences at late systole for patients #I, #II #III, #IV and #V were -0.065, -0.094, 0.02, -0.04 and -0.082 m/s, respectively, and the corresponding average limits of agreement (1.96 SD) were ±0.411, ±0.350, ±0.217, ±0.284 and ±0.178 m/s, respectively. Furthermore, statistical analyses of the planar velocity differences between the resulting velocity fields from our computational framework and the 4-D flow MRI measurements at peak systole in three different planar aortic cross sections can be found in Figure 3a and 3b. Additionally, this figure compares

the 4-D flow MRI velocity field and the down sampled LBM-based velocity fields using linear regression and Bland-Altman analysis. In order to assess the correlation between the results from our computational framework and the 4-D flow MRI, the coefficient of determination (R^2) was used at the aforementioned planar sections. The resulting linear regression is shown with a blue dashed line. Mean of differences in the planar cross section at ascending aorta for patients #I, #II and #III, #IV and #V were -0.082, -0.061, -0.06, -0.08 and -0.2 m/s, respectively, corresponding limits of agreement (1.96 SD) were ±0.392, ±0.27, ±0.52, ±0.178, ±0.24 m/s, respectively and corresponding R^2 were 0.718, 0.8583, 0.558, 0.877 and 0.654, respectively. Mean of differences in the planar cross section at aortic arch for patients #I, #II and #III, #IV and #V were 0.033, 0.026, 0.001, -0.01 and -0.05 m/s, respectively, corresponding limits of agreement (1.96 SD) were ±0.212, ±0.206, ±0.448, ±0.324, ±0.082 m/s, respectively and R^2 were 0.876, 0.9511, 0.4194, 0.781 and 0.887, respectively. Mean of differences in the planar cross section at descending aorta for patients #I, #II and #III, #IV and #V were 0.082, -0.028, -0.07, 0.032 and -0.089 m/s, respectively, corresponding limits of agreement (1.96 SD) were ±0.17, ±0.368, ±0.294, ±0.186, ±0.066 m/s, respectively and corresponding R^2 were 0.912, 0.574, 0.5922, 0.93 and 0.95, respectively. All the statistical correlations observed between computational results versus 4D Flow MRI measurements are comparable and in the range of previous studies [87-89].
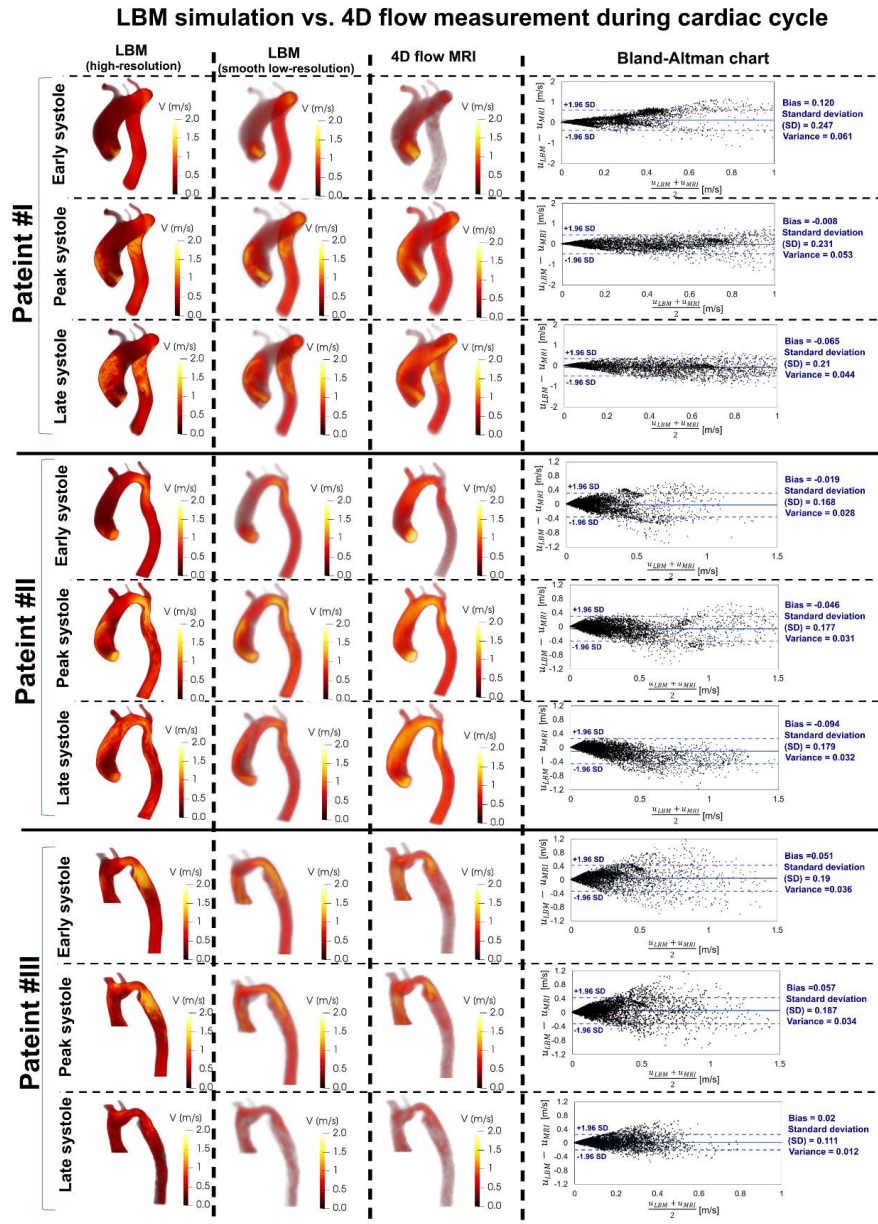
Figure 3-2. Panel A. Validation against 4-D flow MRI. We compared 4-D flow MRI data and results of the computational framework (based on lumped parameter model (LPM) and Lattice Boltzmann model (LBM)) in sample Patients #I to #III, qualitatively (revealed in velocity mapping) and quantitatively by performing Pearson's product moment correlation analysis on the entire domain during cardiac cycle between smooth down-sampled LBM and 4D flow MRI measurements.

Figure 3.2. Panel A. Validation against 4-D flow MRI. We compared 4-D flow MRI data and results of the computational framework (based on lumped parameter model (LPM) and Lattice Boltzmann model (LBM)) in sample Patients #I to #III, qualitatively (revealed in velocity mapping) and quantitatively by performing Pearson's product moment correlation analysis on the entire domain during cardiac cycle between smooth down-sampled LBM and 4D flow MRI measurements.

It is important to note that 4-D flow MRI itself is not error free and its measurements involves errors due to low temporal resolution (20 ms highest)[85] and patient motion artefacts. The differences between the computational results and 4-D flow MRI measurements can be partly due to the shortages of 4-D flow MRI. Weak correlation can be attributed to practical limitations of 4D flow MRI. Despite 4D flow MRI's potentials in providing invaluable in-vivo measurement of blood velocity, it is not free from

inaccuracies. The main sources of inherent and unavoidable inaccuracy in measurements are: (1) motion artifacts due to the unavoidable movements of heart and lungs (2) phase shift in voxels located at the boundary between stationary and moving tissue is noisy, which may result in unprecise velocity measurements (3) turbulent characteristics at the sub-voxel scale cannot be detected due to the low spatial resolution of MRI[89,91,92]. It was observed that the largest LBM/MRI velocity differences are mainly located where the MRI yielded fluctuating velocities. These fluctuations could be explained by the signal loss in 4D flow MRI measurements due to intravoxel dephasing and missing turbulent characteristics at the sub-voxel scale[89,91,92]. Since the shape and geometry of the aorta, as well as the blood flow velocity and regions of high convective acceleration, are different in each patient, the accuracy of measurements may be different for each case. All these inaccuracies affect similarity of the MRI and computational flow fields in some cases.

In addition, for all patients investigated in this study, we observed good agreements between the simulated and clinical Doppler echocardiography velocity magnitudes (mean relative error of 3.8%). Moreover, our patient-specific Doppler-based lumped-parameter model calculations were validated against clinical cardiac catheterization data (the instantaneous pressures in the aorta and LV) in patients with complex valvular, ventricular and vascular diseases with a substantial inter- and intra-patient variability with a wide range of disease (N=49)[39,85]. The model has already been validated against *in vivo* cardiac catheterization in patients with coarctation (N=40)[17,28] and some sub-models have been validated against *in vivo* MRI data (N=57)[64]. In addition, some of the sub-models of the lumped parameter model have been used and validated previously[18,37-39,59-65]. Indeed,

LBM simulation vs. 4D flow measurement at peak systole at different aortic sections
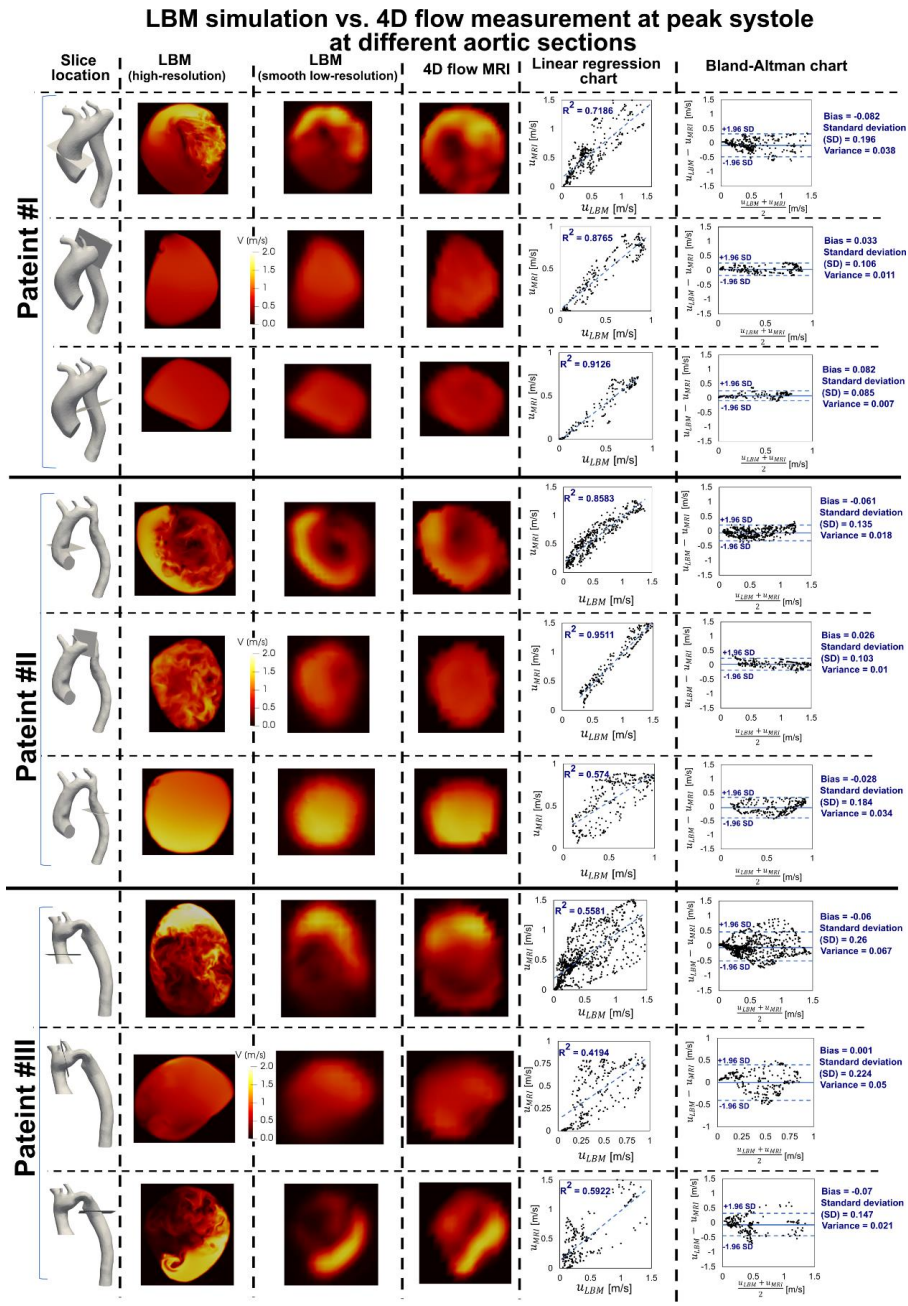
Figure 3-3. panel A. Validation against 4-D flow MRI. We compared 4-D flow MRI data and results of the computational framework (based on lumped parameter model (LPM) and Lattice Boltzmann model (LBM)) in sample Patients #I to #III, qualitatively (revealed in velocity mapping) and quantitatively by performing linear regression and Pearson's product moment correlation analysis at different sections at peak systole between smooth down-sampled LBM and PC-MRI measurements.
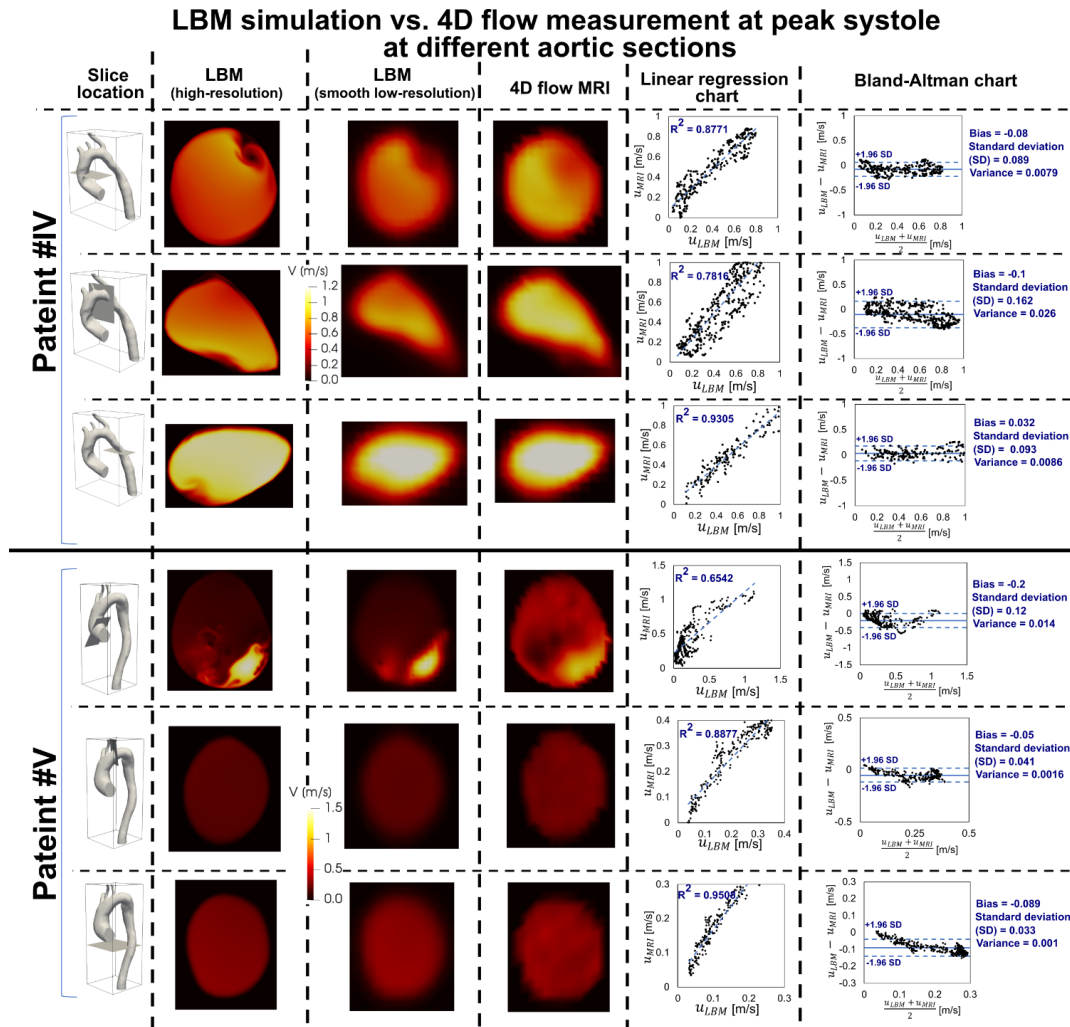
Figure 3-3. panel B. Validation against 4-D flow MRI. We compared 4-D flow MRI data and results of the computational framework (based on lumped parameter model (LPM) and Lattice Boltzmann model (LBM)) in sample Patients #I to #III, qualitatively (revealed in velocity mapping) and quantitatively by performing linear regression and Pearson's product moment correlation analysis at different sections at peak systole between smooth down-sampled LBM and PC-MRI measurements.

the beat-to-beat pressure calculations of the lumped-parameter model were compared

with cardiac catheter pressure measurements and very good qualitative and quantitative

agreements in terms of both shape of the waveform, and specific wave features such as
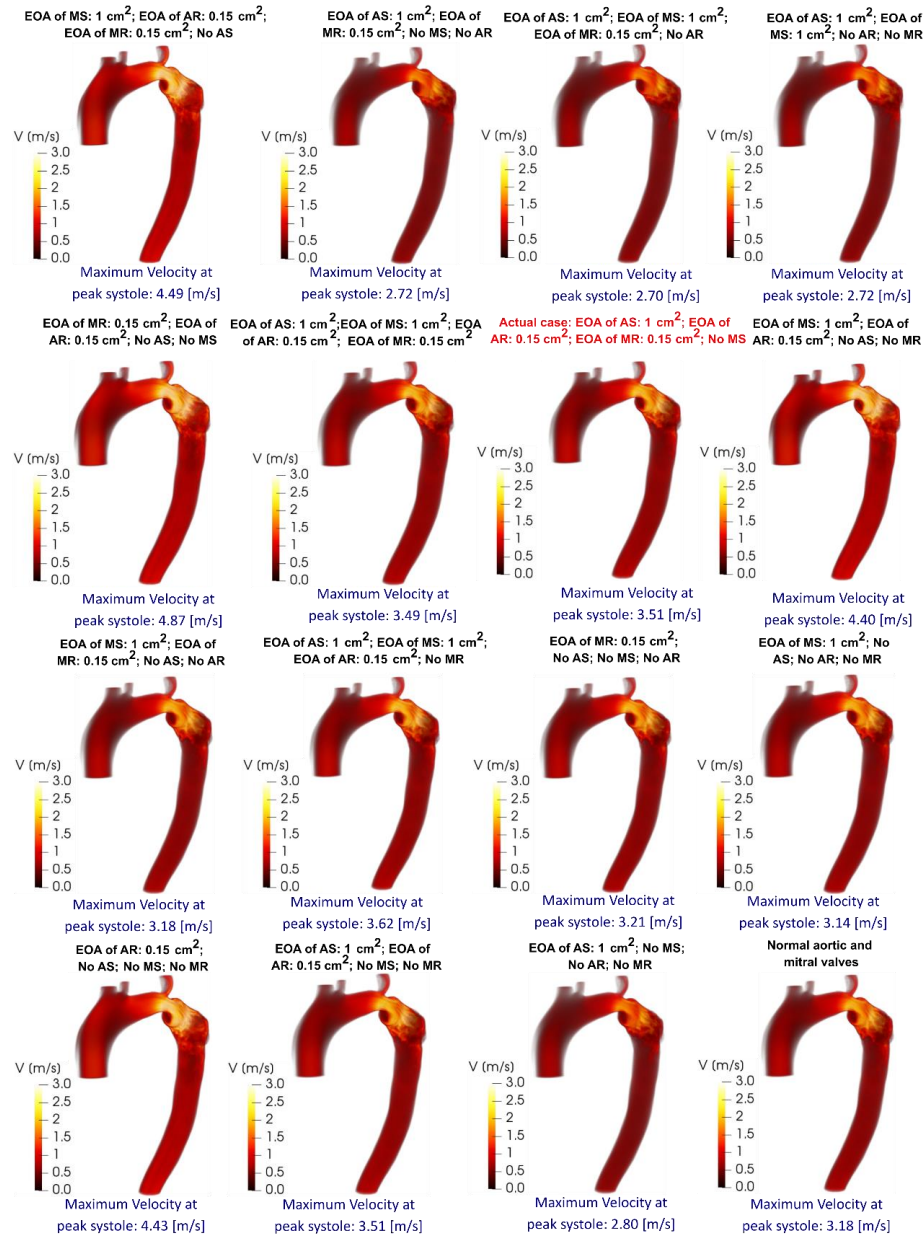
Figure 3-4. Flow modeling in Patient No. 1. Computed velocity magnitude using the computational framework (based on LPM and LBM) in sample Patient No. 1. *Actual patient* (in red text in this figure) has severe aortic stenosis ($EOA_{AS}=1$ cm^2), moderate aortic valve regurgitation ($EOA_{AR}=0.15$ cm^2), moderate mitral valve regurgitation ($EOA_{MR}=0.15$ cm^2) with no mitral stenosis. This patient has brachial pressures of 70 and 125 mmHg and forward LV stroke volume of 110 mL.

the amplitude and the timing of the systolic peak in the aorta. Note that cardiac catheterization is a gold standard in clinics to evaluate hemodynamics, e.g., pressures through the heart and circulatory system. Moreover, the entire patient-specific computational framework (Lattice Boltzmann method and lumped parameter model) was validated against clinical Doppler echocardiography previously[28].

The agreements between the results calculated using our computational framework with the ones measured from 4-D flow MRI and cardiac catheterization allow us to accept our computational results (Figures 4 to 13) with confidence to investigate the flow features.

3.4.2 Aortic fluid dynamics

COA alone largely modified the flow dynamics, this disturbed flow resulting from COA abruptly separated from the aortic walls and developed into a high-speed eccentric jet. Our data (Figures 4, 7 and 10) revealed that *the velocity downstream of the COA in all patients with AR alone was drastically increased. This situation deteriorates when COA and AR coexist alongside MR.* As examples, maximum velocity downstream of the COA in patients #1, #2 and #3 (Figures 4, 7 and 10) are as follows:

1. Patient #1: COA with normal valves: 3.18 m/s, COA with only AR: 4.43 m/s, COA with AR and MR: 4.87 m/s.

2. Patient #2: COA with normal valves: 5.27 m/s, COA with only AR: 8.8 m/s, COA with AR and MR: 9.36 m/s.

3. Patient #3: COA with normal valves: 6.3 m/s, COA with only AR: 9.33 m/s, COA with AR and MR: 10.15 m/s.

Indeed, *AR and MR, when coexistent with COA substantially alter the velocity magnitude downstream of the COA, create transitional to turbulent flow downstream of COA and may lead to significant progression of the disease at the COA region* (Figures 4, 7 and 10).

In order to investigate a fundamental component of the work performed by the heart resulting in the movement of the blood, we specifically selected the kinetic energy (KE). Both KE contours and volumetric integration of KE during the cardiac cycle revealed that MVD and COA have mechanical interactions with one another and alter the KE across the COA and through the aorta which likely leads to overestimating or underestimating the disease (Figures 5, 8 and 11). As examples, both maximum KE as well as volumetric integration of KE during the cardiac cycle were exacerbated significantly in the following cases: COA coexisting with MS, AR and MR; COA coexisting with MR and AR; COA coexisting with MS and AR and COA coexisting with AR (Figures 5, 8 and 11). Both maximum KE as well as volumetric integration of KE during the cardiac cycle in patients with COA and MVD confirmed the following findings (Figures 5, 8 and 11):

Mixed valvular disease and coarctation: patient #1
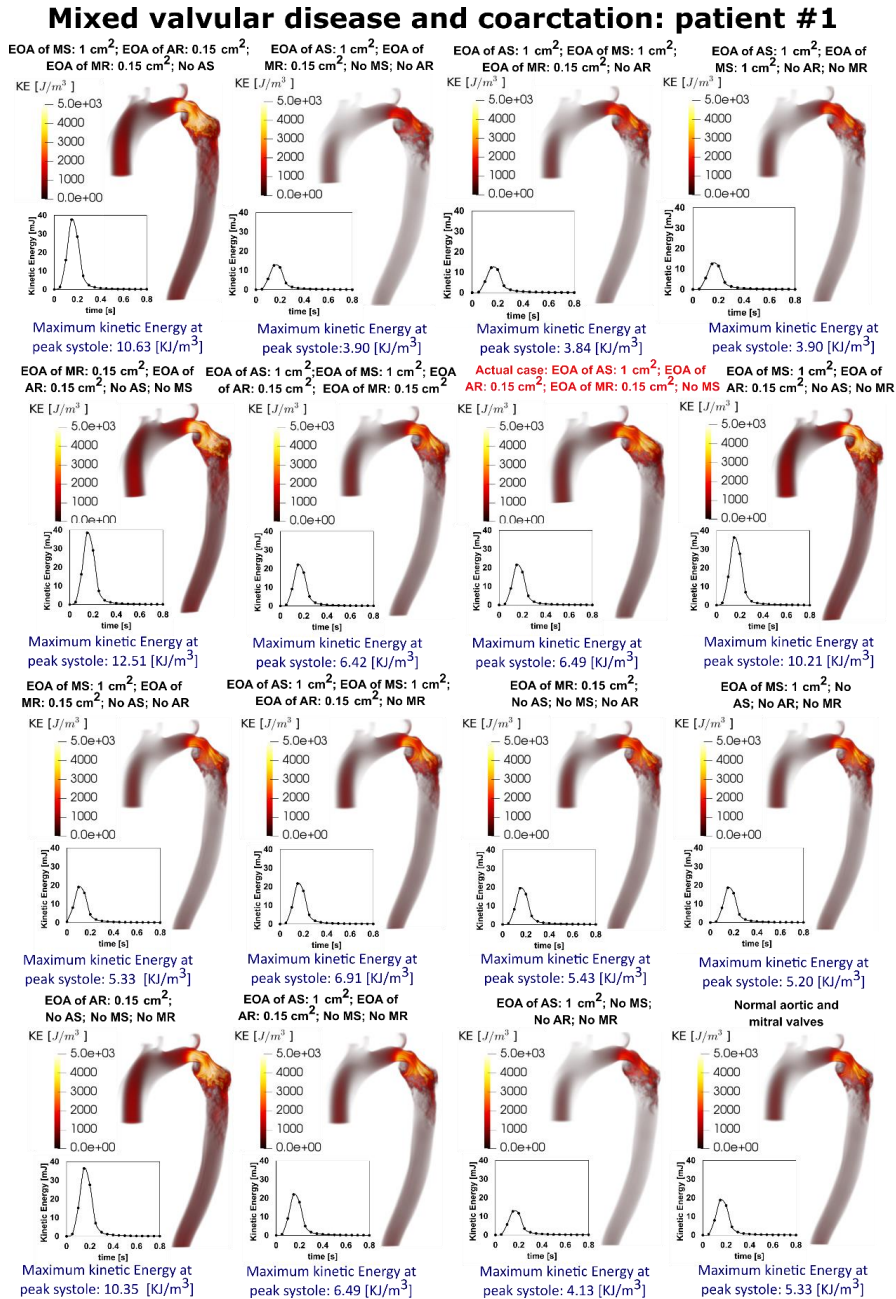
Figure 3-5. Flow modeling in Patient No. 1. Computed kinetic energy (KE) contours and volumetric integration of KE during cardiac cycle using the computational framework (based on LPM and LBM) in sample Patient No. 1 (*Actual patient* in red text in this figure). kinetic energy can be computed as $KE = \frac{1}{2}\rho(u^2 + v^2 + w^2)$. Here u, v, w and ρ correspond to the three components of the instantaneous velocity vector and density.

1. The presence of AS alone does not increase the KE across the COA in patients with COA and MVD (e.g., patient #2: COA with AS alone: 13.13 KJ/m^3 (max KE); COA with normal valves: 14.65 KJ/m^3 (max KE); Figure 8).

2. KE elevated in the presence of MR alone (e.g., patient #2: COA with MR alone:16.24 KJ/m^3 (max KE); COA with normal valves: 14.65 KJ/m^3 (max KE); Figure 8).

3. KE drastically increased in the presence of AR alone (e.g., patient #2: COA with AR alone: 40.84 KJ/m^3 (max KE); COA with normal valves: 14.65 KJ/m^3 (max KE); Figure 8).

4. The individual COA status remained unchanged in patients with MS alone (e.g., patient #2: COA with MS alone:15.32 KJ/m^3 (max KE); COA with normal valves: 14.65 KJ/m^3 (max KE); Figure 8).

Wall shear stress, as a force induced by blood flow has a major impact on regulating endothelial function and is a predeterminant biomarker of the disease progression. The flow alterations discussed previously contributed to elevated wall shear stress, mainly at the neck of the COA as well as distal to the COA. Our data explained that *MVD impacted WSS at the COA region, and can further increase the WSS (e.g., COA coexists with AR alone; COA coexists with MR alone; COA coexists with AR and MR; Figures 6, 9 and 12) or improve the WSS (e.g., COA coexists with AS alone; Figures 6, 9 and 12) at the COA region*. Local perturbation in shear stress exposes endothelial cells to high shear stress

which affects vessel distensibility and compliance which can potentially lead to vascular diseases. Although high WSS may act as a deterrent against formation of atherosclerosis, very high WSS can trigger endothelial cells to express a transcriptional profile which ultimately leads to arterial remodeling, rupture, and dissection. To evaluate temporal oscillations in wall shear stress, the oscillatory shear index (OSI) distribution was used (Figures 6, 9 and 12). OSI has a range between 0 and 0.5, where 0.5 indicates a purely oscillatory flow. Our results suggest MVD modifies OSI magnitude as well as its distribution through the aorta and revealed that areas of high OSI lie within the areas of low WSS, which can be more susceptible to atherosclerotic plaque formation. These results confirmed the following findings:

1. The presence of AS alone and MR alone intensifies OSI magnitude with a larger affected area in patients with COA and MVD.

2. The presence of AR alone reduced the OSI magnitude.

3. OSI were remained unchanged in patients presenting with MS alone.

A hemodynamically significant COA is often defined as a catheter pressure gradient or Doppler pressure gradient of 20 mmHg across the site of COA. Indeed, the COA pressure gradient greater than 20 mmHg warns of major COA and secures interventional/surgical repair. Our results revealed that MVD alter the simulated Doppler pressure gradient across the COA remarkably and can often lead to overestimating or underestimating the severity of the disease (Figure 13). As examples, Doppler pressure gradients were exacerbated significantly in the following cases: COA coexisting alongside MS, AR, and

MR; COA coexisting with MR and AR; COA coexisted with MS and AR; and COA coexisting solely with AR (Figure 13). These results are crucial since wall expansion, compression and collapse are caused by high pressure drops across the COA. Moreover, the pressure drops introduced by the presence of the COA and MVD must be compensated by the LV, this in turn can lead to heart failure. Doppler trans-coarctation pressure gradient in patients with COA and MVD confirmed the following findings (Patient #1, #2 and #3; Figure 13):

1. Pressure gradient across the COA drastically increased in the presence of AR alone (e.g., patient #2: COA with AR alone: 300.76 mmHg (max, DE); COA with normal valves: 110.09 mmHg (max, DE)).

2. COA pressure gradient elevated severely in the presence of MR and AR (e.g., patient #2: COA with MR and AR: 341.4 mmHg (max, DE); COA with normal valves: 110.09 mmHg (max, DE)).

3. COA pressure gradients were not dramatically changed in patients with MS or AS alone (e.g., patient #2: COA with MS alone:115 mmHg (DE); COA with AS alone: 98.6 mmHg (max, DE); COA with normal valves: 110.09 mmHg (DE)).

3.4.3 Discussions

As the prevalence of congenital heart disease continues to grow due to advances in diagnosis and treatment, it is essential to have a robust understanding of vascular changes

imparted by these pathologies, especially pertaining to long-term prognosis[93]. As the third most common congenital heart disease, COA is frequently seen in conjunction with other left ventricular outflow tract (LVOT) abnormalities, most notably BAV and AS[94,95]. Mutations of the *NOTCH1* gene have been linked to the BAV phenotype and recent genomic studies have demonstrated that COA likewise has associated *NOTCH1* variants, providing a potential mechanism for familial trends of COA and the co-development of these LVOT abnormalities[96-98]. BAV, which occurs in up to 85% of COA patients, is predisposed to calcific stenosis and can progress to AR, mainly through dilation of the ascending aorta[99-101]. Similar to COA, isolated AS causes an increased pressure load on the LV, leading to concentric hypertrophy and reduced compliance[102]. When compounded by AR, as seen in approximately 27% of severe AS cases, the stiff ventricle poorly tolerates the regurgitant volume load which ultimately leads to a worse prognosis and quicker progression rate than isolated AS or AR[103,104]. These aortic valve pathologies, together with mitral valve abnormalities which are present in 8% of COA cases, account for MVD commonly seen in conjunction with COA[105].

Mixed valvular disease and coarctation: patient #1

Figure 3-6. Flow modeling in Patient No. 1. Computed wall shear stress (WSS) and Oscillatory shear index (OSI) using the computational framework (based on LPM and LBM) in sample Patient No. 1 (Actual patient in red text in this figure). OSI can be computed as $\mathrm{OSI} = \frac{1}{2}\left(1 - \frac{\left|\int_0^T \tau dt\right|}{\int_0^T |\tau| dt}\right)$. Here, T and τ are the cardiac cycle period and instantaneous wall shear stress, respectively.

Mixed valvular disease and coarctation: patient #2
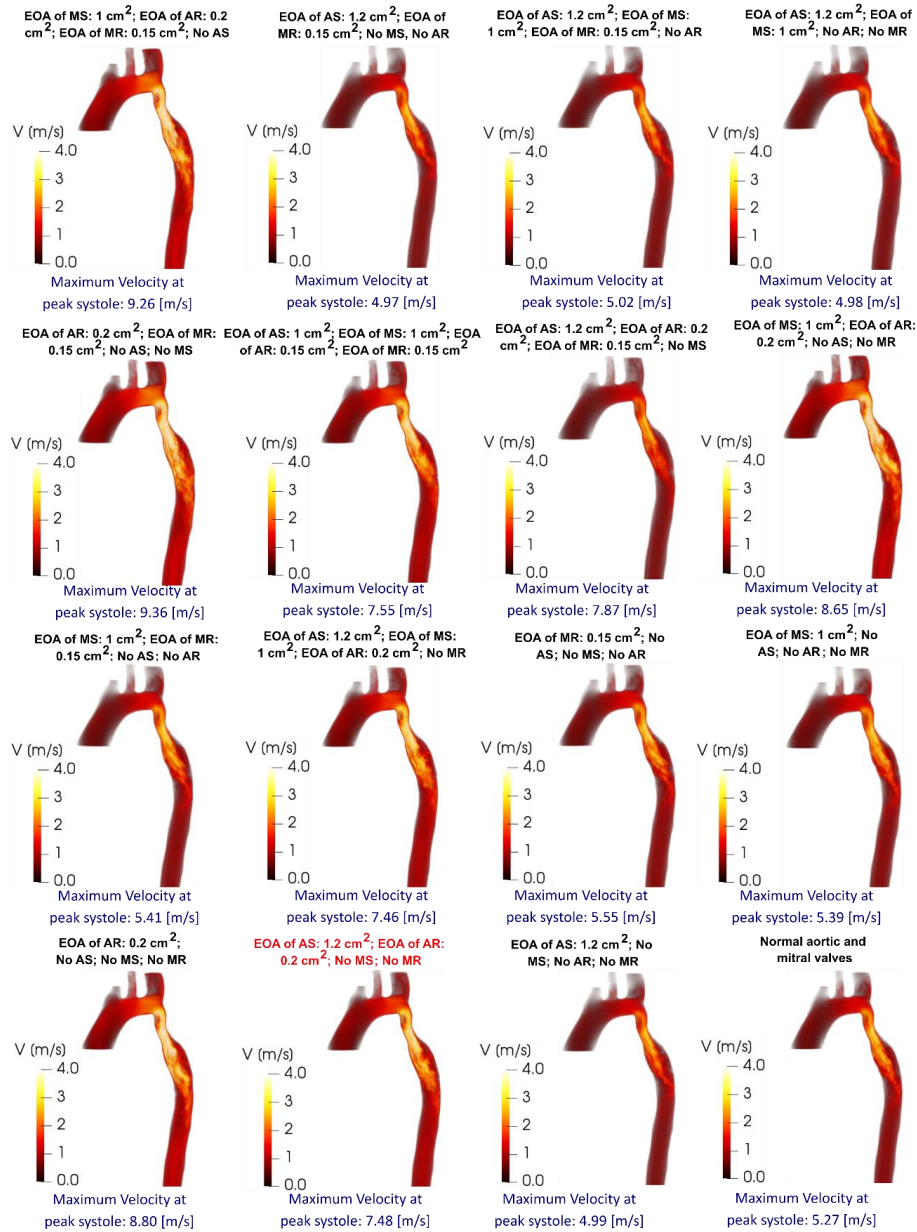
Figure 3-7. Flow modeling in Patient No. 2. Computed velocity magnitude using the computational framework (based on LPM and LBM) in sample Patient No. 1. Actual patient (in red text in this figure) has moderate aortic stenosis (EOA$_{AS}$=1.2 cm^2), moderate aortic valve regurgitation (EOA$_{AR}$=0.2 cm^2), with no mitral valve regurgitation and no mitral stenosis. This patient has brachial pressures of 60 and 131 mmHg and forward LV stroke volume of 124 mL.

Mixed valvular disease and coarctation: patient #2
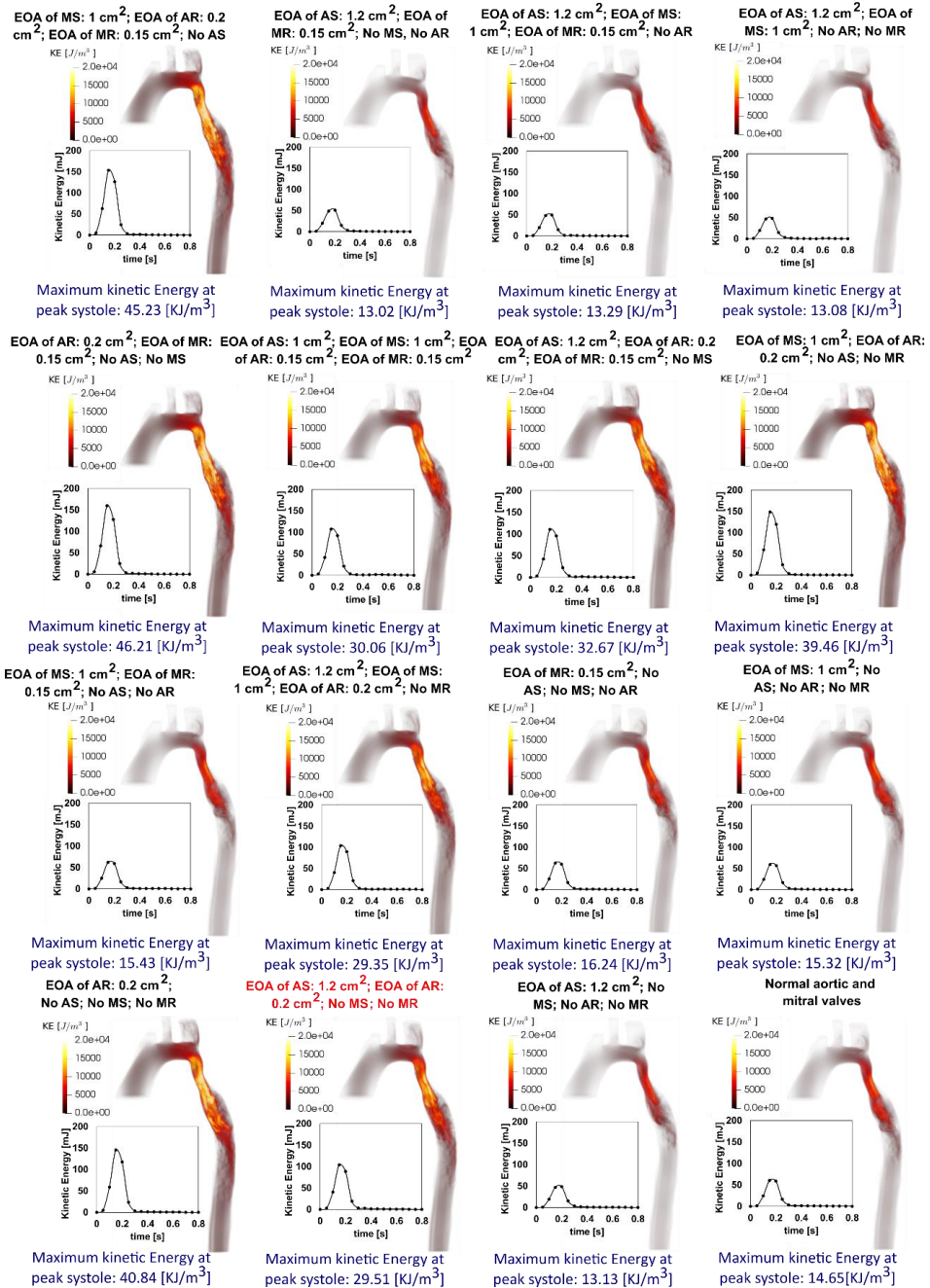
Figure 3-8. Flow modeling in Patient No. 2. Computed kinetic energy (KE) contours and volumetric integration of KE during cardiac cycle using the computational framework (based on LPM and LBM) in sample Patient No. 1 (Actual patient in red text in this figure). kinetic energy can be computed as $KE = \frac{1}{2}\rho(u^2 + v^2 + w^2)$. Here u, v, w and ρ correspond to the three components of the instantaneous velocity vector and density.

Mixed valvular disease and coarctation: patient #2

Figure 3-9. Flow modeling in Patient No. 2. Computed wall shear stress (WSS) and Oscillatory shear index (OSI) using the computational framework (based on LPM and LBM) in sample Patient No. 1 (Actual patient in red text in this figure). OSI can be computed as $OSI = \frac{1}{2}\left(1 - \frac{\left|\int_0^T \tau dt\right|}{\int_0^T |\tau| dt}\right)$. Here, T and τ are the cardiac cycle period and instantaneous wall shear stress, respectively.
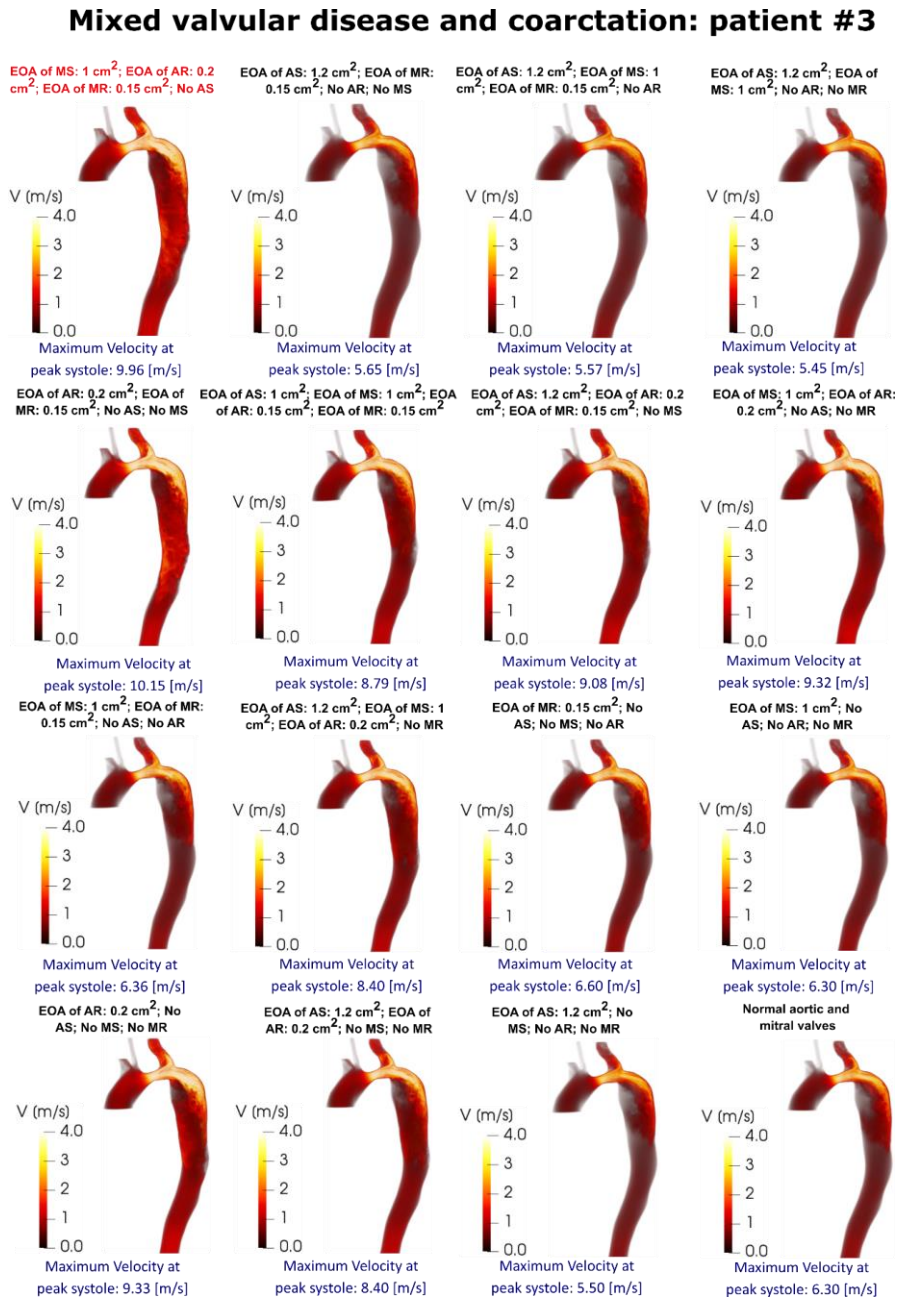
Figure 3-10. Flow modeling in Patient No. 3. Computed velocity magnitude using the computational framework (based on LPM and LBM) in sample Patient No. 1. Actual patient (in red text in this figure) has severe mitral stenosis ($EOA_{MS}=1$ cm^2), moderate aortic valve regurgitation ($EOA_{AR}=0.2$ cm^2), moderate mitral valve regurgitation ($EOA_{AR}=0.15$ cm^2) and no aortic stenosis. This patient has brachial pressures of 55 and 138 mmHg and forward LV stroke volume of 121 mL.

Mixed valvular disease and coarctation: patient #3
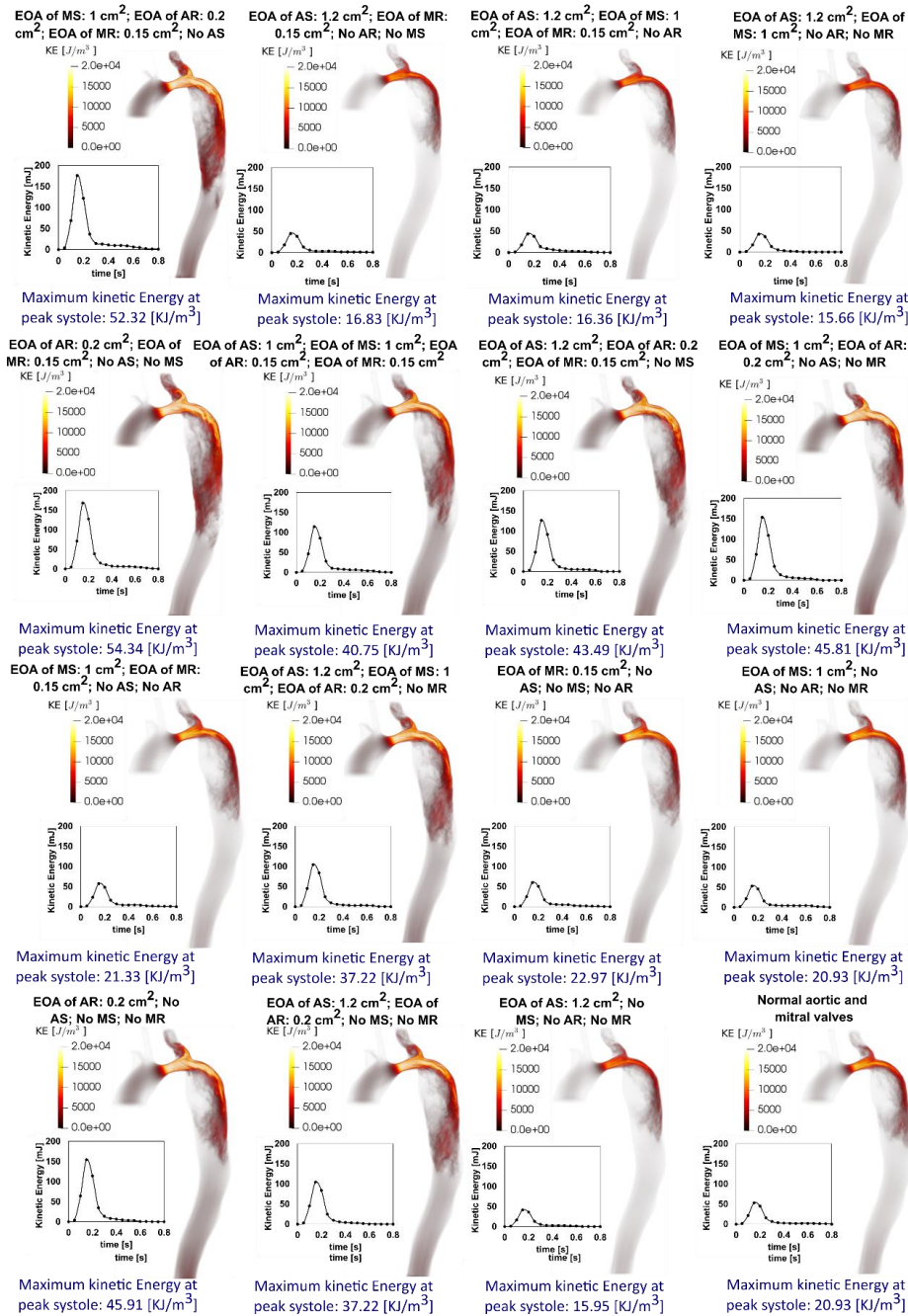
Figure 3-11. Flow modeling in Patient No. 3. Computed kinetic energy (KE) contours and volumetric integration of KE during cardiac cycle using the computational framework (based on LPM and LBM) in sample Patient No. 1 (Actual patient in red text in this figure). kinetic energy can be computed as $KE = \frac{1}{2}\rho(u^2 + v^2 + w^2)$. Here u, v, w and ρ correspond to the three components of the instantaneous velocity vector and density.

Clinical difficulties arise when a patient presents with COA and MVD, as the interactions between the hemodynamic alterations imparted by each lesion are not well characterized, hindering diagnosis and generating uncertainty regarding the best course of treatment. The choice of proceeding with a single or multiple-stage operation is at the discretion of the surgeon, as no standardized guidelines are currently in place[19]. Additionally, it is difficult to grade the severity of these pathologies, as the standard classifications were developed for isolated lesions, and do not allow for modification when two separate lesions impact the same parameter[103,106]. As these pathologies can rapidly progress, determination of clinical severity and optimal timing for intervention is critical to prevent the occurrence of further cardiovascular complications, such as aneurysms or dissections[17,104]. We set out to investigate the hemodynamic significance of MVD and COA to provide insight into the establishment of treatment protocols which address the patient-specific expression of these pathologies, and have several critical findings as follows:

- **MVD may exacerbate the COA hemodynamics**

1. *Presence of AR and MR in patients with COA and MVD:* Maximum velocity downstream of the COA in all patients with AR alone was drastically increased. The condition deteriorates when COA and AR coexist alongside MR. Indeed, AR and MR when coexistent with COA substantially alter the velocity magnitude downstream of the COA, create transitional to turbulent flow downstream of COA and may lead to significant progression of the disease at the COA region. Presence

of AR *impacted on WSS at COA region severely, presence of AR and MR can further increase the WSS.*

2. *Presence of AS and MS in patients with COA and MVD*: COA hemodynamics were not dramatically changed in patient with AS alone or MS alone, however, AS or MS may exacerbate the COA hemodynamics when they coexist with AR and/or MR.

These findings are essential since hemodynamic alterations caused by the COA and MVD can result in endothelial dysfunction, dedifferentiation of arterial smooth muscle and medial thickening. Moreover, local perturbation in shear stress exposes endothelial cells to high shear stress which affects vessel distensibility and compliance and may lead to vascular diseases.

- **When coexisting with MVD, Doppler pressure gradient across COA is a poor indicator of COA severity**

1. The pressure gradient across the site of COA, when measured using Doppler echocardiography is not heavily affected by the presence of AS or MS alone. The pressure gradient found in these patients was solely a result of the presence of the COA.

2. In the presence of MR, the COA pressure gradient was non-remarkably elevated.

3. The presence of AR had major effects on the COA pressure gradients – AR interacted with COA and amplified the COA pressure gradients measured by Doppler echocardiography.

4. COA pressure gradient elevated severely in the presence of MR and AR. *This reveals that COA pressure gradient may be overestimated in presence of MR and/or AR.*

- **To precisely assess the COA severity, both presence and severity of MVD matter**

The results of the current study demonstrate that MVD interacts with COA fluid dynamics, amplifying irregular flow patterns especially downstream of COA. As a result, MVD may contribute to speed up the progression of diseases in this region and may lead to major aortic wall complications such as aneurysm, rupture, and dissection[19,107-109]. Furthermore, when the COA coexists alongside MVD, the high-pressure loss downstream of the COA can augment the flow resistance and ultimately lead to collapse the aortic wall[32,110]. *Our results suggest that not only the severity of the COA, but also the presence and the severity of the MVD should be considered in the evaluation of risks in patients*

Mixed valvular disease and coarctation: patient #3

Figure 3-12. Flow modeling in Patient No. 3. Computed wall shear stress (WSS) and Oscillatory shear index (OSI) using the computational framework (based on LPM and LBM) in sample Patient No. 1 (Actual patient in red text in this figure). OSI can be computed as $\text{OSI} = \frac{1}{2}\left(1 - \frac{\left|\int_0^T \tau dt\right|}{\int_0^T |\tau| dt}\right)$. Here, T and τ are the cardiac cycle period and instantaneous wall shear stress, respectively.

Maximum Doppler echocardiography pressure gradient of coarctation (mmHg)
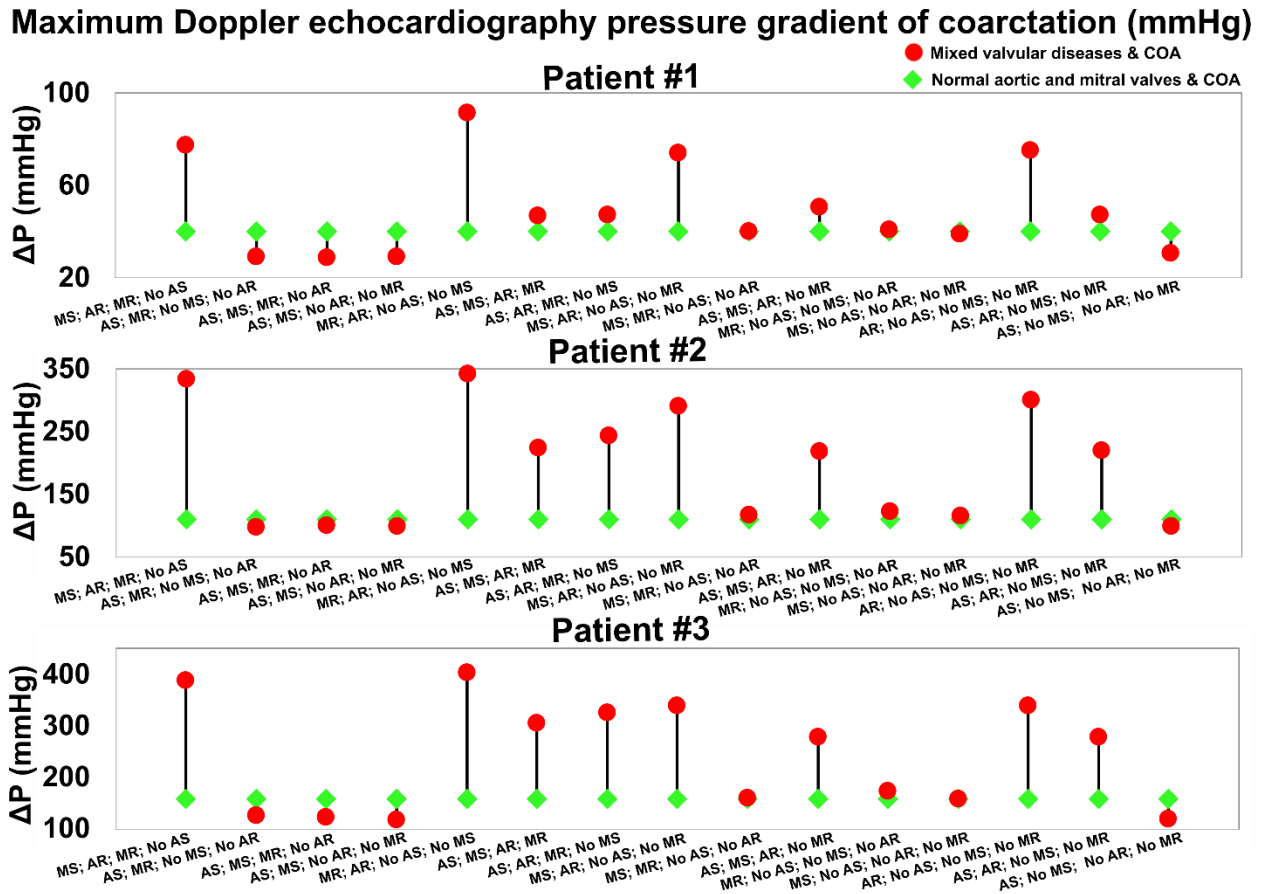
Figure 3-13. Simulated Doppler echocardiography pressure gradient of coarctation in Patients No. 1, 2 and 3. Doppler pressure gradient can be calculated as $\Delta P=4(V_D^2- V_U^2)$, where V_D and V_U are the maximum velocity upstream of the COA and minimum velocity downstream of the COA, respectively.

with COA. The results suggest that some more aggressive surgical approaches may be required as regularly chosen current surgical techniques may not be optimal for patients with both COA and MVD.

Due to the complex multiphysics nature of the aorta, the overall estimation of hemodynamics parameters is very dependent on the outputs of the lumped-parameter model that are in-turn depend on the parameters used in the lumped-parameter model.

Our patient-specific Doppler-based lumped-parameter algorithm, which provided boundary conditions, was validated against clinical catheterization data in forty-nine C3VD patients with a substantial inter- and intra-patient variability with a wide range of disease[39] as well as in 34 patients with coarctation[17]. We performed a comprehensive parameter sensitivity analysis on the outputs of the lumped-parameter model that are used in the present study to find hemodynamics parameters. We found that the outputs from the lumped-parameter model were most sensitive to the forward left ventricular outflow tract stroke volume (Forward LVOT-SV, an input parameter to the lumped parameter algorithm): LV pressure: 27%, LV Volume 19% by a ±20% change in the Forward LVOT-SV. The other input parameters affected the output to a much lower degree. We should point out that Forward LVOT-SV is measured reliably using Doppler echocardiography with high accuracy and sensitivity of the model to this parameter does not jeopardize the results obtained from the model. In addition, sensitivity analysis revealed negligible effects of changes (±20%) in the free parameters on the model output variables. Indeed, the results obtained with Lattice Boltzmann model and lumped-parameter algorithm were validated against clinical Doppler echocardiography and 4-D flow MRI (as shown in Figures 2 and 3 in this study) in patients. Our results show good agreements between velocity calculated using the computational framework and the ones measured using Doppler echocardiography and 4D flow MRI in all investigated patients in with COA.

3.5   Limitations

This study was performed on 3 COA patients with MVD. Future studies must consider further validation of the computational framework in a larger population of COA patients with MVD. However, our results in this study demonstrate the ability of the framework to track changes in both cardiac, and vascular states in these patients. However, we observed good agreements between the velocity fields calculated by our proposed framework, the MRI-measured velocity fields and Doppler echocardiography velocity fields in this study (N=3) as well as cardiac catheterization pressure gradients (N=82)[17,39]. These observations made us more confident that the limitation in the number of patients in this study does not affect our conclusions.

Conflict of Interest

The authors declare that they have no competing interests. The authors declare that the research was conducted in the absence of any commercial or financial relationships that could be construed as a potential conflict of interest.

Author Contributions

R.S. Computational development and modeling, image processing, data collection and analysis, interpretation of data and manuscript writing; N.G. & S. K. Data analysis and manuscript writing; J.G. clinical data collection, analysis and interpretation of data; Z.K.M. Conception and design, lumped parameter algorithm development, data analysis, interpretation of data, manuscript writing, critical revision, final approval of the

manuscript and supervised this research. All authors read and approved the final manuscript.

Funding

Acknowledgments

Data Availability Statement

The development and validation of the proposed method require the retrospective clinical data routinely measured in clinics and were transferred as the de-identified & anonymized data. The code and the optimization algorithms are available from the author upon request.

3.6   References

1   Paladini, D. *et al.* Aortic coarctation: prognostic indicators of survival in the fetus. *Heart* **90**, 1348-1349 (2004).

2   Sinning, C. *et al.* Bicuspid aortic valve and aortic coarctation in congenital heart disease—important aspects for treatment with focus on aortic vasculopathy. *Cardiovascular diagnosis and therapy* **8**, 780 (2018).

3   Kim, Y. Y., Andrade, L. & Cook, S. C. Aortic Coarctation. *Cardiology Clinics* **38**, 337-351 (2020).

4   Hamdan, M. A. Coarctation of the aorta: a comprehensive review. *Prevalence* **50**, 30 (2006).

5   Hager, A., Kanz, S., Kaemmerer, H., Schreiber, C. & Hess, J. Coarctation Long-term Assessment (COALA): significance of arterial hypertension in a cohort of 404 patients up to 27 years after surgical repair of isolated coarctation of the aorta, even in the absence of restenosis and prosthetic material. *The Journal of Thoracic and Cardiovascular Surgery* **134**, 738-745. e732 (2007).

6   Voges, I. *et al.* Aortic stiffening and its impact on left atrial volumes and function in patients after successful coarctation repair: a multiparametric cardiovascular magnetic resonance study. *Journal of Cardiovascular Magnetic Resonance* **18**, 1-11 (2016).

7   Dijkema, E. J., Leiner, T. & Grotenhuis, H. B. Diagnosis, imaging and clinical management of aortic coarctation. *Heart* **103**, 1148-1155 (2017).

8   Baumgartner, H. *et al.* 2020 ESC Guidelines for the management of adult congenital heart diseaseThe Task Force for the management of adult congenital heart disease of the European Society of Cardiology (ESC). *European Heart Journal*.

9   Menting, M. E. *et al.* Quantitative assessment of systolic left ventricular function with speckle-tracking echocardiography in adult patients with repaired aortic coarctation. *The international journal of cardiovascular imaging* **32**, 777-787 (2016).

10   Teo, L. L., Cannell, T., Babu-Narayan, S. V., Hughes, M. & Mohiaddin, R. H. Prevalence of associated cardiovascular abnormalities in 500 patients with aortic coarctation referred for cardiovascular magnetic resonance imaging to a tertiary center. *Pediatric cardiology* **32**, 1120-1127 (2011).

11   Rao, P. S. Coarctation of the aorta. *Current cardiology reports* **7**, 425-434 (2005).

12   Shone, J. D. *et al.* The developmental complex of "parachute mitral valve," supravalvular ring of left atrium, subaortic stenosis, and coarctation of aorta. *The American journal of cardiology* **11**, 714-725 (1963).

13   Wood, W. C., Wood, J. C., Lower, R. R., Bosher Jr, L. H. & McCue, C. M. Associated coarctation of the aorta and mitral valve disease: Nine cases with surgical correction of both lesions in three. *The Journal of pediatrics* **87**, 217-220 (1975).

14   Swan, H., Trapnell, J. & Denst, J. Congenital mitral stenosis and systemic right ventricle with associated pulmonary vascular changes frustrating surgical repair of patent ductus arteriosus and coarctation of the aorta. *American heart journal* **38**, 914-923 (1949).

15   Hamdan, M. A., Maheshwari, S., Fahey, J. T. & Hellenbrand, W. E. Endovascular stents for coarctation of the aorta: initial results and intermediate-term follow-up. *Journal of the American College of Cardiology* **38**, 1518-1523 (2001).

16   Goldman, L. & Schafer, A. I. *Goldman's cecil medicine E-book*. (Elsevier Health Sciences, 2011).

17   Keshavarz-Motamed, Z. *et al.* Elimination of transcoarctation pressure gradients has no impact on left ventricular function or aortic shear stress after intervention in patients with mild coarctation. *JACC: Cardiovascular Interventions* **9**, 1953-1965 (2016).

18   Keshavarz-Motamed, Z., Garcia, J., Pibarot, P., Larose, E. & Kadem, L. Modeling the impact of concomitant aortic stenosis and coarctation of the aorta on left ventricular workload. *Journal of biomechanics* **44**, 2817-2825 (2011).

19   Zhang, H. *et al.* Bicuspid aortic valve with critical coarctation of the aorta: single- or two-stage operation? *Journal of thoracic disease* **10**, 4353 (2018).

20   Mulay, A. V., Ashraf, S. & Watterson, K. G. Two-stage repair of adult coarctation of the aorta with congenital valvular lesions. *The Annals of thoracic surgery* **64**, 1309-1311 (1997).

21   Bartoccioni, S. *et al.* Aortic Coarctation, Aortic Valvular Stenosis, and Coronary Artery Disease: Combined One-Stage Surgical Therapy Operation. *Journal of cardiac surgery* **10**, 594-596 (1995).

22   Rivera, P. C., Gadboys, H. L. & Glover, R. P. Simultaneous surgical treatment of coexistent coarctation of the aorta and aortic valvular stenosis∗. *The American journal of cardiology* **5**, 551-555 (1960).

23   Kumar, S., Goud, A., Versha, F., Mukherjee, A. & Pai, R. Coarctation of aorta in an adult with severe aortic stenosis: deciding on the optimal approach. *Journal of the American College of Cardiology* **71**, A2160-A2160 (2018).

24   Massey, R. & Shore, D. F. Surgery for complex coarctation of the aorta. *International journal of cardiology* **97**, 67-73 (2004).

25   Kutty, S. *et al.* Reduced global longitudinal and radial strain with normal left ventricular ejection fraction late after effective repair of aortic coarctation: a CMR

feature tracking study. *The international journal of cardiovascular imaging* **29**, 141-150 (2013).

26   Gardiner, H. M. *et al.* Arterial reactivity is significantly impaired in normotensive young adults after successful repair of aortic coarctation in childhood. *Circulation* **89**, 1745-1750 (1994).

27   Wendell, D. C., Friehs, I., Samyn, M. M., Harmann, L. M. & LaDisa Jr, J. F. Treating a 20 mm Hg gradient alleviates myocardial hypertrophy in experimental aortic coarctation. *journal of surgical research* **218**, 194-201 (2017).

28   Sadeghi, R., Khodaei, S., Ganame, J. & Keshavarz-Motamed, Z. towards non-invasive computational-mechanics and imaging-based diagnostic framework for personalized cardiology for coarctation. *Scientific Reports* **10**, 1-19 (2020).

29   Andersson, M., Lantz, J., Ebbers, T. & Karlsson, M. Multidirectional WSS disturbances in stenotic turbulent flows: A pre-and post-intervention study in an aortic coarctation. *Journal of biomechanics* **51**, 8-16 (2017).

30   Arzani, A., Dyverfeldt, P., Ebbers, T. & Shadden, S. C. In vivo validation of numerical prediction for turbulence intensity in an aortic coarctation. *Annals of biomedical engineering* **40**, 860-870 (2012).

31   Coogan, J. S., Humphrey, J. D. & Figueroa, C. A. Computational simulations of hemodynamic changes within thoracic, coronary, and cerebral arteries following early wall remodeling in response to distal aortic coarctation. *Biomechanics and modeling in mechanobiology* **12**, 79-93 (2013).

32   Keshavarz-Motamed, Z., Garcia, J. & Kadem, L. Fluid dynamics of coarctation of the aorta and effect of bicuspid aortic valve. *PLoS one* **8**, e72394 (2013).

33   Kim, H. J. *et al.* On coupling a lumped parameter heart model and a three-dimensional finite element aorta model. *Annals of biomedical engineering* **37**, 2153-2169 (2009).

34   LaDisa, J. F. *et al.* Computational simulations for aortic coarctation: representative results from a sampling of patients. (2011).

35   Tossas-Betancourt, C. *et al.* Computational analysis of renal artery flow characteristics by modeling aortoplasty and aortic bypass interventions for abdominal aortic coarctation. *Journal of vascular surgery* **71**, 505-516. e504 (2020).

36   Youssefi, P. *et al.* Impact of patient-specific inflow velocity profile on hemodynamics of the thoracic aorta. *Journal of biomechanical engineering* **140** (2018).

37   Keshavarz-Motamed, Z. *et al.* Effect of coarctation of the aorta and bicuspid aortic valve on flow dynamics and turbulence in the aorta using particle image velocimetry. *Experiments in fluids* **55**, 1-16 (2014).

38   Keshavarz-Motamed, Z. *et al.* A new approach for the evaluation of the severity of coarctation of the aorta using Doppler velocity index and effective orifice area: in vitro validation and clinical implications. *Journal of biomechanics* **45**, 1239-1245 (2012).

39   Keshavarz-Motamed, Z. A diagnostic, monitoring, and predictive tool for patients with complex valvular, vascular and ventricular diseases. *Scientific Reports* **10**, 1-19 (2020).

40   Marlevi, D. *et al.* Estimation of cardiovascular relative pressure using virtual work-energy. *Scientific reports* **9**, 1-16 (2019).

41   Hassanabad, A. F. *et al.* Pressure drop mapping using 4D flow MRI in patients with bicuspid aortic valve disease: A novel marker of valvular obstruction. *Magnetic resonance imaging* **65**, 175-182 (2020).

42   Garcia, J., Barker, A. J. & Markl, M. The role of imaging of flow patterns by 4D flow MRI in aortic stenosis. *JACC: Cardiovascular Imaging* **12**, 252-266 (2019).

43   Garcia, D. A fast all-in-one method for automated post-processing of PIV data. *Experiments in fluids* **50**, 1247-1259 (2011).

44   Garcia, D. Robust smoothing of gridded data in one and higher dimensions with missing values. *Computational statistics & data analysis* **54**, 1167-1178 (2010).

45   Bouzidi, M. h., Firdaouss, M. & Lallemand, P. Momentum transfer of a Boltzmann-lattice fluid with boundaries. *Physics of fluids* **13**, 3452-3459 (2001).

46   Porter, B., Zauel, R., Stockman, H., Guldberg, R. & Fyhrie, D. 3-D computational modeling of media flow through scaffolds in a perfusion bioreactor. *Journal of biomechanics* **38**, 543-549 (2005).

47   LaDisa Jr, J. F. *et al.* Circumferential vascular deformation after stent implantation alters wall shear stress evaluated with time-dependent 3D computational fluid dynamics models. *Journal of applied physiology* **98**, 947-957 (2005).

48   Skordos, P. Initial and boundary conditions for the lattice Boltzmann method. *Physical Review E* **48**, 4823 (1993).

49   Heuveline, V., Krause, M. J. & Latt, J. Towards a hybrid parallelization of lattice Boltzmann methods. *Computers & Mathematics with Applications* **58**, 1071-1080 (2009).

50   Henn, T., Heuveline, V., Krause, M. J. & Ritterbusch, S. in *International Workshop on Statistical Atlases and Computational Models of the Heart.* 34-43 (Springer).

51   Mirzaee, H. *et al.* MRI-based computational hemodynamics in patients with aortic coarctation using the lattice Boltzmann methods: clinical validation study. *Journal of Magnetic Resonance Imaging* **45**, 139-146 (2017).

52   Jin, S., Oshinski, J. & Giddens, D. P. Effects of wall motion and compliance on flow patterns in the ascending aorta. *J. Biomech. Eng.* **125**, 347-354 (2003).

53   Senzaki, H. *et al.* Ventricular–vascular stiffening in patients with repaired coarctation of aorta: integrated pathophysiology of hypertension. *Circulation* **118**, S191-S198 (2008).

54   Vitarelli, A. *et al.* Assessment of ascending aorta distensibility after successful coarctation repair by strain Doppler echocardiography. *Journal of the American Society of Echocardiography* **21**, 729-736 (2008).

55   Vogt, M. *et al.* Impaired elastic properties of the ascending aorta in newborns before and early after successful coarctation repair: proof of a systemic vascular disease of the prestenotic arteries? *Circulation* **111**, 3269-3273 (2005).

56   Brili, S. *et al.* Aortic elastic properties in patients with repaired coarctation of aorta. *Journal of the American College of Cardiology* **31**, 401-401 (1998).

57   Xu, J. *et al.* Intravascular ultrasound assessment of regional aortic wall stiffness, distensibility, and compliance in patients with coarctation of the aorta. *American heart journal* **134**, 93-98 (1997).

58   Nathen, P., Gaudlitz, D., Krause, M. & Kratzke, J. in *21st AIAA Computational Fluid Dynamics Conference. American Institute of Aeronautics and Astronautics.*

59   Khodaei, S. *et al.* Towards a non-invasive computational diagnostic framework for personalized cardiology of transcatheter aortic valve replacement in interactions with complex valvular, ventricular and vascular disease. *International Journal of Mechanical Sciences* **202**, 106506 (2021).

60   Khodaei, S. *et al.* Personalized intervention cardiology with transcatheter aortic valve replacement made possible with a non-invasive monitoring and diagnostic framework. *Scientific Reports* **11**, 1-28 (2021).

61   Ben-Assa, E. *et al.* Ventricular stroke work and vascular impedance refine the characterization of patients with aortic stenosis. *Science translational medicine* **11**, eaaw0181 (2019).

62   Benevento, E., Djebbari, A., Keshavarz-Motamed, Z., Cecere, R. & Kadem, L. Hemodynamic changes following aortic valve bypass: a mathematical approach. *PloS one* **10**, e0123000 (2015).

63   Keshavarz-Motamed, Z. *et al.* The role of aortic compliance in determination of coarctation severity: lumped parameter modeling, in vitro study and clinical evaluation. *Journal of biomechanics* **48**, 4229-4237 (2015).

64   Keshavarz-Motamed, Z. *et al.* Non-invasive determination of left ventricular workload in patients with aortic stenosis using magnetic resonance imaging and Doppler echocardiography. *PLoS One* **9** (2014).

65   Keshavarz-Motamed, Z. *et al.* Mixed valvular disease following transcatheter aortic valve replacement: quantification and systematic differentiation using clinical measurements and image-based patient-specific in silico modeling. *Journal of American Heart Association* **9**, e015063 (2020).

66   Broomé, M., Maksuti, E., Bjällmark, A., Frenckner, B. & Janerot-Sjöberg, B. Closed-loop real-time simulation model of hemodynamics and oxygen transport in the cardiovascular system. *Biomedical engineering online* **12**, 1-20 (2013).

67   Mynard, J., Davidson, M., Penny, D. & Smolich, J. A simple, versatile valve model for use in lumped parameter and one-dimensional cardiovascular models. *International Journal for Numerical Methods in Biomedical Engineering* **28**, 626-641 (2012).

68   Senzaki, H., Chen, C.-H. & Kass, D. A. Single-beat estimation of end-systolic pressure-volume relation in humans: a new method with the potential for noninvasive application. *Circulation* **94**, 2497-2506 (1996).

69   Suga, H., Sagawa, K. & Shoukas, A. A. Load independence of the instantaneous pressure-volume ratio of the canine left ventricle and effects of epinephrine and heart rate on the ratio. *Circulation research* **32**, 314-322 (1973).

70   Pironet, A. *et al.* Simulation of left atrial function using a multi-scale model of the cardiovascular system. *PloS one* **8**, e65146 (2013).

71   Chaudhry, Q. A. A Gaussian function model for simulation of complex environmental sensing. *Complex Adaptive Systems Modeling* **3**, 1-4 (2015).

72   McDowell, S. A. A simple derivation of the Boltzmann distribution. *Journal of chemical education* **76**, 1393 (1999).

73   Moss, R. L., Razumova, M. & Fitzsimons, D. P. Myosin crossbridge activation of cardiac thin filaments: implications for myocardial function in health and disease. *Circulation research* **94**, 1290-1300 (2004).

74   Brown, K. A. & Ditchey, R. V. Human right ventricular end-systolic pressure-volume relation defined by maximal elastance. *Circulation* **78**, 81-91 (1988).

75   Dell'italia, L. J. & Walsh, R. A. Application of a time varying elastance model to right ventricular performance in man. *Cardiovascular research* **22**, 864-874 (1988).

76   Gleason, W. L. & Braunwald, E. Studies on the first derivative of the ventricular pressure pulse in man. *The Journal of clinical investigation* **41**, 80-91 (1962).

77   Kass, D. A., Md, M. M., Phd, W. G., Brinker Fsca, J. A., Md & Maughan, W. L. Use of a conductance (volume) catheter and transient inferior vena caval occlusion for rapid determination of pressure-volume relationships in man. *Catheterization and cardiovascular diagnosis* **15**, 192-202 (1988).

78   Liang, F., Takagi, S., Himeno, R. & Liu, H. Multi-scale modeling of the human cardiovascular system with applications to aortic valvular and arterial stenoses. *Medical & biological engineering & computing* **47**, 743-755 (2009).

79   Maniar, H. S. *et al.* Impact of pericardial restraint on right atrial mechanics during acute right ventricular pressure load. *American Journal of Physiology-Heart and Circulatory Physiology* **284**, H350-H357 (2003).

80   Stergiopulos, N., Meister, J.-J. & Westerhof, N. Determinants of stroke volume and systolic and diastolic aortic pressure. *American Journal of Physiology-Heart and Circulatory Physiology* **270**, H2050-H2059 (1996).

81   Takeuchi, M., Odake, M., Takaoka, H., Hayashi, Y. & Yokoyama, M. Comparison between preload recruitable stroke work and the end-systolic pressure–volume relationship in man. *European heart journal* **13**, 80-84 (1992).

82   Van de Werf, F. *et al.* Diastolic properties of the left ventricle in normal adults and in patients with third heart sounds. *Circulation* **69**, 1070-1078 (1984).

83   Asaadi, M. *et al.* On Left Ventricle Stroke Work Efficiency in Children with Moderate Aortic Valve Regurgitation or Moderate Aortic Valve Stenosis. *Pediatric Cardiology*, 1-9 (2021).

84   Tanné, D., Kadem, L., Rieu, R. & Pibarot, P. Hemodynamic impact of mitral prosthesis-patient mismatch on pulmonary hypertension: an in silico study. *Journal of Applied Physiology* **105**, 1916-1926 (2008).

85   Baiocchi, M. *et al.* Effects of Choice of Medical Imaging Modalities on a Non-invasive Diagnostic and Monitoring Computational Framework for Patients With Complex Valvular, Vascular, and Ventricular Diseases Who Undergo Transcatheter Aortic Valve Replacement. *Frontiers in Bioengineering and Biotechnology*, 389 (2021).

86   Nannini, G. *et al.* Aortic Hemodynamics Assessment prior and after Valve Sparing Reconstruction: A Patient-Specific 4D flow-based FSI Model. *Computers in Biology and Medicine*, 104581 (2021).

87   Biglino, G. *et al.* Using 4D cardiovascular magnetic resonance imaging to validate computational fluid dynamics: a case study. *Frontiers in pediatrics* **3**, 107 (2015).

88   Gao, Q. *et al.* Optimization of 4D flow MRI velocity field in the aorta with divergence-free smoothing. *Medical & Biological Engineering & Computing*, 1-16 (2021).

89   Miyazaki, S. *et al.* Validation of numerical simulation methods in aortic arch using 4D Flow MRI. *Heart and vessels* **32**, 1032-1044 (2017).

90   Giavarina, D. Understanding bland altman analysis. *Biochemia medica* **25**, 141-151 (2015).

91   Stankovic, Z., Allen, B. D., Garcia, J., Jarvis, K. B. & Markl, M. 4D flow imaging with MRI. *Cardiovascular diagnosis and therapy* **4**, 173 (2014).

92   Puiseux, T. *et al.* Reconciling PC-MRI and CFD: An in-vitro study. *NMR in Biomedicine* **32**, e4063 (2019).

93   Rapoff, M. A. *Adherence to pediatric medical regimens*. (Springer Science & Business Media, 2009).

94   Riehle, T. J. *et al.* Velocity-encoded magnetic resonance image assessment of regional aortic flow in coarctation patients. *The Annals of thoracic surgery* **81**, 1002-1007 (2006).

95   Al Akhfash, A. A. *et al.* Two-dimensional echocardiographic predictors of coarctation of the aorta. *Cardiology in the Young* **25**, 87 (2015).

96   McBride, K. L. *et al.* Linkage analysis of left ventricular outflow tract malformations (aortic valve stenosis, coarctation of the aorta, and hypoplastic left heart syndrome). *European journal of human genetics* **17**, 811-819 (2009).

97   Moss, A. J. Coarctation of the aorta in siblings. *The Journal of pediatrics* **46**, 707-709 (1955).

98   Freylikhman, O. *et al.* Variants in the NOTCH1 gene in patients with aortic coarctation. *Congenital heart disease* **9**, 391-396 (2014).

99   Mordi, I. & Tzemos, N. Bicuspid aortic valve disease: a comprehensive review. *Cardiology research and practice* **2012** (2012).

100   Tawes Jr, R., Berry, C. & Aberdeen, E. Congenital bicuspid aortic valves associated with coarctation of the aorta in children. *British heart journal* **31**, 127 (1969).

101   Lilly, L. S. *Pathophysiology of heart disease: a collaborative project of medical students and faculty*. (Lippincott Williams & Wilkins, 2012).

102   Jashari, H., Rydberg, A., Ibrahimi, P., Bajraktari, G. & Henein, M. Y. Left ventricular response to pressure afterload in children: aortic stenosis and coarctation: a systematic review of the current evidence. *International journal of cardiology* **178**, 203-209 (2015).

103   Honda, S. *et al.* Impact of aortic regurgitation on the prognosis of severe aortic stenosis. *Heart* **98**, 1591-1594 (2012).

104   Ong, G. & Pibarot, P. Combined aortic stenosis and regurgitation: double the trouble. *Heart* **105**, 1515-1522 (2019).

105   Muhll, I. F. V., Sehgal, T. & Paterson, D. I. The adult with repaired coarctation: need for lifelong surveillance. *Canadian Journal of Cardiology* **32**, 1038. e1011-1038. e1015 (2016).

106   Unger, P. *et al.* Multiple and mixed valvular heart diseases: pathophysiology, imaging, and management. *Circulation: Cardiovascular Imaging* **11**, e007862 (2018).

107   Liu, T. *et al.* Bicuspid aortic valve: an update in morphology, genetics, biomarker, complications, imaging diagnosis and treatment. *Frontiers in physiology* **9**, 1921 (2019).

108   Keane, M. G. *et al.* Bicuspid aortic valves are associated with aortic dilatation out of proportion to coexistent valvular lesions. *Circulation* **102**, Iii-35-Iii-39 (2000).

109   Oliver, J. M. *et al.* Risk of aortic root or ascending aorta complications in patients with bicuspid aortic valve with and without coarctation of the aorta. *The American journal of cardiology* **104**, 1001-1006 (2009).

110   Oliver, J. M. *et al.* Risk factors for aortic complications in adults with coarctation of the aorta. *Journal of the American College of Cardiology* **44**, 1641-1647 (2004).

Chapter 4: Reducing morbidity and mortality in patients with coarctation requires systematic differentiation of impacts of mixed valvular disease on coarctation hemodynamics

Reza Sadeghi[1], Benjamin Tomka[1], Seyedvahid Khodaei[1], Julio Garcia[2,3,4,5], Javier Ganame[6], Zahra Keshavarz-Motamed*[1,7,8,9]

1. Department of Mechanical Engineering, McMaster University, Hamilton, ON, Canada
2. Stephenson Cardiac Imaging Centre, Libin Cardiovascular Institute of Alberta, Calgary, AB, Canada
3. Department of Radiology, University of Calgary, Calgary, AB, Canada
4. Department of Cardiac Sciences, University of Calgary, Calgary, AB, Canada
5. Alberta Children's Hospital Research Institute, Calgary, AB, Canada
6. Division of Cardiology, Department of Medicine, McMaster University, Hamilton, ON, Canada
7. School of Biomedical Engineering, McMaster University, Hamilton, ON, Canada
8. School of Computational Science and Engineering, McMaster University, Hamilton, ON, Canada
9. The Thrombosis & Atherosclerosis Research Institute, McMaster University, Hamilton, ON, Canada

This paper was submitted and is under review.

* Correspondence author

4.1 Structured abstract

Background: Despite ongoing advances in surgical techniques for coarctation of the aorta (COA) repair, the long-term results are not always benign. Associated mixed valvular diseases (MVD; various combinations of aortic and mitral valvular pathologies) are responsible for considerable postoperative morbidity and mortality. We investigated the impact of COA and MVD on hemodynamics.

Methods and Results: We developed a patient-specific computational framework. Our results demonstrate that MVD interacts with COA fluid dynamics and contributes to speed up the progression of the disease by amplifying the irregular flow patterns downstream of COA (local) and exacerbating the left ventricular function (global) (N=26). Velocity downstream of COA with aortic regurgitation alone was increased and the situation got worsen when COA and aortic regurgitation coexist with mitral regurgitation (COA with normal valves: 5.27 m/s, COA with only aortic regurgitation: 8.8 m/s, COA with aortic and mitral regurgitation: 9.36 m/s; patient #2). Workload in these patients was increased due to the presence of aortic stenosis alone, aortic regurgitation alone, mitral regurgitation alone and when they coexist (COA with normal valves: 1.0617 J; COA with only aortic stenosis: 1.225 J; COA with only aortic regurgitation: 1.6512 J; COA with only mitral regurgitation: 1.3599 J; patient #1).

Conclusions: Not only the severity of COA, but also the presence and the severity of MVD should be considered in the evaluation of risks in patients. The results suggest that

more aggressive surgical approaches may be required as regularly chosen current surgical techniques may not be optimal for such patients.

Keywords: Coarctation, mixed valvular disease, aortic fluid dynamics, local hemodynamics, global hemodynamics, left ventricle metrics, aortic stenosis, aortic regurgitation, mitral regurgitation, mitral stenosis

4.2 Clinical perspective

➢ **What is new?**

- Doppler echocardiography pressure gradient across coarctation is a poor indicator to assess the diseases severity when coexisting with mixed valvular disease (various combinations of aortic and mitral valvular pathologies).
- Catheter pressure gradient fails to reflect the effect of mixed valvular disease on the clinical assessment of coarctation hemodynamics.
- Mixed valvular disease exacerbates the coarctation hemodynamics (local) and contributes to speed up the progression of the disease by amplifying the irregular flow patterns downstream of coarctation.
- Mixed valvular disease exacerbated the left ventricular function and hemodynamics (global).

➢ **What are the clinical implications?**

To assess risks in patient with coarctation of the aorta, not only the severity of coarctation, but also the presence and the severity of mixed valvular disease (various

combinations of aortic and mitral valvular pathologies) should be considered. The results suggest that more aggressive surgical approaches may be required as regularly chosen current surgical techniques may not be optimal for such patients.

4.3   Introduction

Coarctation of the aorta (COA) is one of the most common congenital heart defects, accounting for 5-8% of all congenital heart defects, occurring in approximately 3/10000 of live births[1-3]. COA is often present in conjunction with other cardiac pathologies, mainly alongside mixed valvular diseases[4-8]. Mixed valvular diseases (MVD) are classified as various combinations of aortic and mitral valvular pathologies occurring simultaneously. COA is commonly associated with bicuspid aortic valve as up to 85% of COA patients suffer from both pathologies[1, 4, 9]. Additionally, aortic stenosis (AS) and aortic regurgitation (AR) are commonly found alongside COA occurring in 5-15% and 2-4% of cases, respectively[10-15]. Furthermore, COA is frequently found alongside mitral valve diseases, presenting itself in 20-59% of all patients with mitral pathologies[16-18]. The common mitral valve diseases found to coexist with COA include mitral stenosis (MS) and mitral regurgitation (MR) occurring in 3% and 2-5% of COA patients respectively[19-25]. COA and MVD have significant effects on the left ventricle (LV), and if not treated promptly are likely to result in LV dysfunction, cardiac failure, and death[26-31].

While COA is readily diagnosed and interventional/surgical therapies are implemented, areas of contention and uncertainty remain. The coexistence of MVD alongside COA poses many clinical challenges for diagnosis and assessment. A

hemodynamically significant COA is often defined as a catheter pressure gradient or resting or exercise Doppler pressure gradient of 20 mmHg across the site of coarctation. While most cardiologists agree that a pressure gradient greater than 20 mmHg warns of severe COA and warrants interventional/surgical repair, it has yet to be determined whether MVD has any impact on the pressure gradient across the site of COA. The severity of COA may be masked by the hemodynamic effects of MVD, and vice versa, ultimately resulting in clinical challenges for accurate diagnosis and assessment[21, 32-34]. The optimal method and timing of intervention often remains unclear when MVD are present, given the balance of risks for early and late mortality and reoperation[23, 35-38]. Due to the complexity of treatment for COA and MVD, there are increased rates of post-operative mortality[16, 39]. Moreover, when COA and MVD are present, surgery is often performed in a multiple-stage approach as higher morbidity rates have been recorded if multiple pathologies are repaired simultaneously[23, 37]. Treatment strategies for patients with COA and MVD are quite unclear and differ on an individualized basis, some groups suggest that treatment strategies for patients with COA and MVD may need to be redefined[35, 38]. Before updating the current treatment recommendations, the quantitative understanding of the interplay between valvular pathologies and COA, and the breakdown of effects of each disease constituents on the cardiac function of the cardiovascular system is crucial[40-42].

"Cardiology is flow"[43] and therefore the essential sources of cardiovascular mortality and morbidity can be explained on the basis of adverse hemodynamics: abnormal biomechanical forces and flow patterns, leading to the development and progression of

cardiovascular disease[9, 44-47] Precise and effective diagnosis hinges on the quantification of the following requirements: **global** hemodynamics: (1) *Metrics of cardiac function*, e.g., heart workload and its contribution breakdown of each component of the cardiovascular diseases and of the **local** hemodynamics: (2) *Aortic fluid dynamics*, e.g., details of the instantaneous 3-D flow. In this study, we developed a patient-specific, imaged-based, computational-mechanics framework that dynamically couples the local hemodynamics with the global circulatory cardiovascular system using 3-D Lattice Boltzmann method (LBM) and lumped parameter modeling (LPM) to investigate the impact of COA and MVD on both local and global hemodynamics (Figure 1) in 26 patients. The developed computational framework was validated against clinical cardiac catheterization data, Doppler echocardiography and four-dimensional flow magnetic resonance imaging (4-D flow MRI) (Figures 2 and 3). To the best of our knowledge, this is the first study that investigates the effects of MVD on COA in terms of both local and global hemodynamic (Figures 4 to 14).

4.4   Methods

4.4.1 Study population

Thirty-six deidentified and anonymous patients with COA and MVD (see Table 1 for patients' characteristics) between 2008 and 2019 at Stephenson Cardiac Imaging Centre, Libin Cardiovascular Institute of Alberta (Calgary, AB, Canada) and St. Joseph's Healthcare (Hamilton, ON, Canada) were considered. Informed consent was obtained

from all participants. The selections were done by operators blinded to the objectives and contents of this study at each institution and the protocols were reviewed and approved by the Institutional Review Boards of each institution. All methods and measurements were performed in accordance with relevant guidelines and regulations including guidelines of the American College of Cardiology and American Heart Association. Senior cardiologists reviewed the echocardiograms and reports using OsiriX imaging software (version 8.0.2; Pixmeo, Switzerland). Cardiac catheterization was performed to determine the pressure gradient and exact morphology of the COA in all patients. Computed tomography (CT) data was collected, including images and documented reports. CT images were segmented, and the 3-D geometries of the complete aorta were reconstructed to be used for our computational model.

4.4.2 Numerical study

We developed a computational fluid dynamics framework using 3-D Lattice Boltzmann method (large eddy simulation, Smagorinsky subgrid scale model) and lumped parameter modeling to simulate both the local and global hemodynamics in patients with MVD and COA (Figure 1, Panel A, schematic diagram):

  Global hemodynamics (Cardiac function metrics and hemodynamics). Our developed patient-specific Doppler-based lumped-parameter algorithm includes several sub-models allowing for the analysis of complex coarctation disease, e.g. when COA coexists with the other valvular, vascular and ventricular disease: 1) left atrium, 2) left ventricle, 3) aortic valve, 4) mitral valve, 5) coarctation of the aorta, 6) systemic circulation, and 7)

pulmonary circulation (Figure 1). Our Doppler-based lumped parameter algorithm uses the following input parameters that all can be reliably measured using Doppler echocardiography: forward left ventricular outflow tract stroke volume, heart rate, ejection time, ascending aorta area, left ventricular outflow tract area, aortic valve effective orifice area, mitral valve effective orifice area, COA severity, and grading of aortic and mitral valves regurgitation severity. Note that the proposed method does not need catheter data or any invasive data for estimating the cardiac function metrics (e.g., workload). Other input parameters of the lumped parameter algorithm include systolic and diastolic blood pressures measured using sphygmomanometers. The calculations of the lumped-parameter model were validated against cardiac catheterization data (the instantaneous pressures in the aorta and left ventricle) in patients with complex valvular, ventricular and vascular diseases with a wide range of cardiovascular diseases[46, 48].

Local hemodynamics (3-D blood flow dynamics). We developed a computational fluid dynamics framework to simulate the local hemodynamics in patients with COA in pre- and post-intervention states (Figure 1). This framework is based on lumped parameter modeling[46, 48] and 3-D lattice Boltzmann method (LBM; Smagorinsky subgrid scale model) as implemented in the open-source OpenLB library with some supplements as explained in Sadeghi et al. (2021)[45]. Reynolds-averaged Navier Stokes equations are very common to model blood low, however, there are limitations to model pulsatile flows [49]. Direct numerical simulations put a burden on computing resources and are limited to low Reynolds numbers. Large eddy simulation (LES), which falls between Direct numerical simulations and Reynolds-averaged Navier Stokes, is well suited for computational

modeling of turbulent vascular flows with a great potential in modeling the physiological

low-Reynolds pulsatile flows[46]. We used a 3-D LBM-based computational fluid dynamics

approach using LES (Smagorinsky subgrid scale model) to simulate blood flow through

the vascular system[45]. Calculations of this computational fluid dynamics framework were

validated against 4-D flow MRI measurements (Figures 2 and 3).

Model properties & Boundary conditions

Aortic local flow dynamics are greatly influenced by upstream and downstream flow

conditions which must be accounted for. Additionally, the proper choice of boundary

conditions is critical as they influence the accuracy of flow simulations. Blood was

assumed to be a Newtonian and incompressible fluid with dynamic viscosity of 0.0035

Pa·s and density of 1050 kg/m^3. A lumped-parameter model (Figure 1) simulated the

function of the left side of the heart in the presence of COA and MVD and was used to

impose the time-dependent inlet flow at the ascending aorta cross section and the outlet

pressure at the descending aorta cross section. The time-dependent flow rate obtained

from the lumped-parameter model was used to scale this profile in order to observe this

time-varying inlet boundary condition (Figure 1). The inlet velocity boundary condition

in lattice Boltzmann was implemented using the method suggested by Skordos[50] which

uses a second-order finite difference scheme to compute the velocity gradient of the

boundary nodes and extrapolates the pressure distribution at the inlet from bulk nodes[51].

Furthermore, a sinusoidal smooth start-up phase was used to begin the simulation and

smoothly increase the initial condition for the velocity from zero in order to avoid

pressure fluctuation artifacts at the inlet [52, 53]. The total flow rate headed to the branches was calculated using the lumped-parameter model and then distributed to the branches based on the relative cross-sectional area of each branch. No-slip boundary condition was applied at the solid walls as described above (Section: *Modeling surface curvature near the wall of complex geometries*). Patients with COA are typically hypertensive and characterized by reduced compliance and elevated stiffness in both the proximal and distal aorta, e.g., Jin et al. [54] and Keshavarz-Motamed et al.[9, 46, 55] showed that a rigid-wall assumption for the aorta is acceptable and thus, the aortic wall in this study was treated as such.

Due to the complex multi-physics nature of the aorta and the valves, the overall estimation of cardiac parameters is very reliant on the outputs of the lumped-parameter algorithm that are in-turn depend on input parameters used in the lumped-parameter algorithm. Our patient-specific Doppler-based lumped-parameter algorithm, which provided boundary conditions, was validated against clinical catheterization data in patients with a wide range of cardiovascular diseases[45, 46, 48]. We used the validated lumped-parameter algorithm[45, 46, 48] to obtain the boundary conditions. Moreover, our performed sensitivity analysis revealed negligible effects of changes ($\pm20\%$) in the free parameters on the model output variables[56].

Reconstructed geometries in patients with coarctation

3D geometries of the complete aorta including ascending aorta, aortic branches and descending aorta were reconstructed from segmented CT images of patients using ITK-

SNAP (version 3.8.0-BETA) (Figure 1). We used smoothing procedure for the surfaces to overcome the challenges of computational convergence and stability. Change in the volume due to smoothing was less than 1% in all patients.
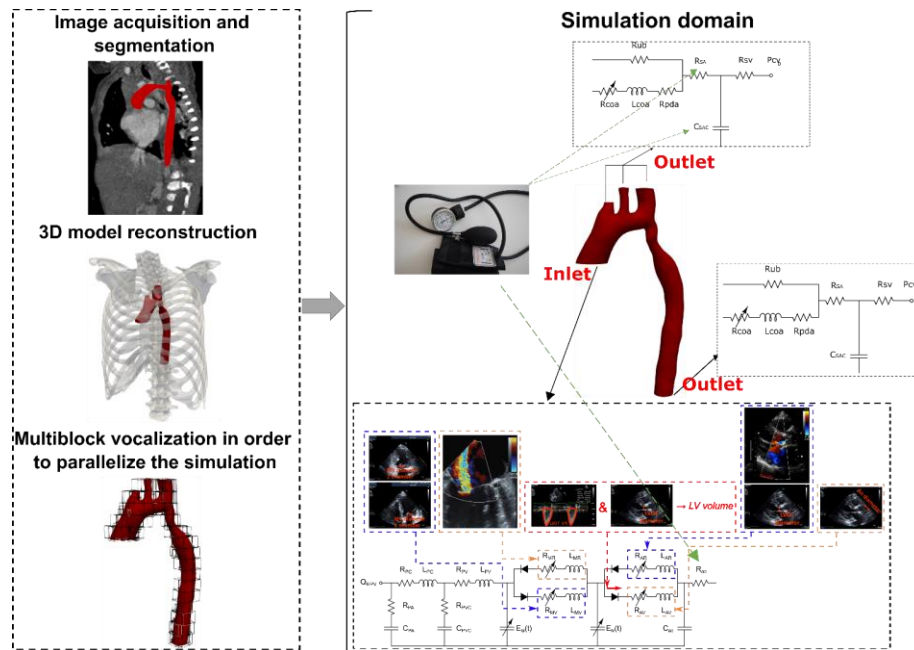
(a)
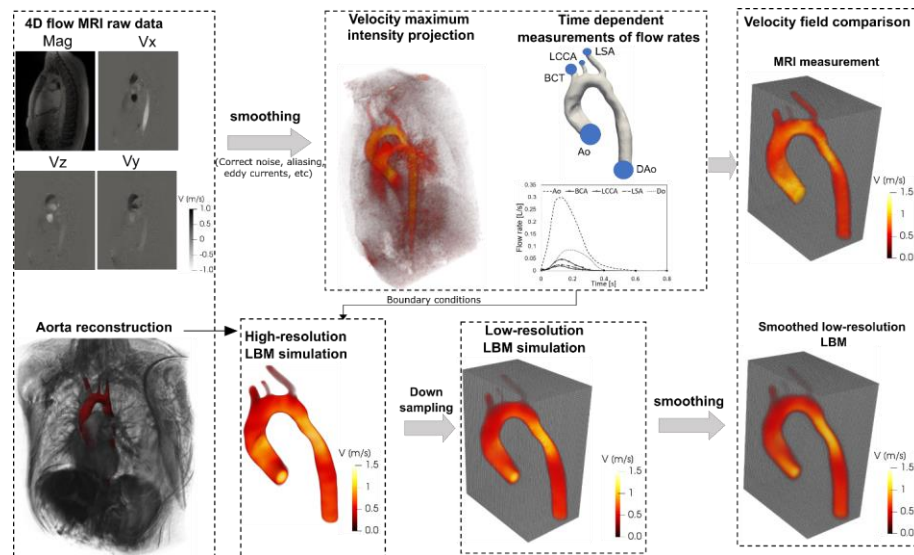
(b)

Figure 4-1 Reconstructed geometry and simulation domain. (a) In this study, we developed a patient-specific, imaged-based, computational-mechanics framework that dynamically couples the local hemodynamics with the global circulatory cardiovascular system to investigate the impact of COA and MVD on both local and global hemodynamics in these patients. We used CT images from patients to segment and reconstruct the 3D geometries of the complete aorta. These 3-D geometries were used for investigating hemodynamic using computational fluid dynamics. Local flow dynamics is greatly influenced by upstream and downstream flow conditions that are absent in the flow simulation domain. A lumped-parameter model simulates the function of the left side of the heart[47]. Time-dependent inlet flow at ascending aorta and outlet pressure at descending aorta position were obtained from lumped parameter modeling and applied as boundary conditions. Boundary conditions of the aortic branches were adjusted to match the flow distribution. (b) We compared 4-D flow MRI data and results of our computational framework. The 3-D geometry of the complete aorta was reconstructed using MRI images and the entire volume of Down-sampled LBM data was smoothed[52,53] (see *Four-dimensional flow magnetic resonance imaging (4-D flow MRI* section for more details).

Numerical strategy

Multiple and single relaxation time LBM-based model were coupled with Smagorinsky's turbulent model in order to stabilize complex turbulent fluid flow across the domain. For treating complex geometry, we utilized second order accuracy method proposed by Bouzidi et al. [57]. A smooth startup phase was added to the inlet velocity condition to suppress the undesired pressure fluctuation. For turbulent modelling, Large Eddy Smagorinsky subgrid-scale model with constant $C_s = 0.1$ was applied [58]. Mesh sensitivity analysis was performed for maximum velocity and pressure drop at the coarctation region. Mesh definition was considered acceptable if no significant differences (lower than 5%) existed between successive mesh refinements in both quantities. The physical time step in this study was as low as 1.5 μs and physical lattice height adjacent to the wall was as low as 50 μm to ensure that it is within the viscous sublayer.

4.4.3 Four-dimensional flow magnetic resonance imaging (4-D flow MRI)

Four-dimensional flow magnetic resonance imaging (4-D flow MRI) is a recent development of phase-contrast MRI (PC-MRI) with the capability of comprehensive blood flow assessment in three spatial dimensions over the cardiac cycle[59]. 4-D flow MRI provides visualization of the vascular territory of interest and allows for the estimation of hemodynamic biomarkers such as wall shear forces[60] and pressure gradients[61, 62]. Additionally, 4-D flow MRI provides comprehensive information regarding complex flow patterns in vascular diseases[63]. *In this* study, acquisition of 4-D flow MRI data in patients with COA and valvular diseases was performed (Figure 1, Panel B, data acquisition and analysis workflow of 4-D flow MRI) by standard Cartesian 4-D flow sequence using 1.5T MRI scanners (Philips Achieva; Philips Medical Systems, Best, the Netherlands). Electrocardiogram gating synchronized and diaphragm navigator gated 4-D flow MRI were performed during free breathing. Acquisition parameters were as follows: spatial resolution of (1.97–2.62, 1.97–2.62, 2.5–4 mm^3), temporal resolution of 36–40 ms. Velocity encoding was set to the range (1.5–4.5 m/s), the total scan time for each measurement varied from 8 to 15 min. All 4-D flow data was corrected for multiple sources of phase offset errors and noises such as velocity aliasing, Maxwell terms, and eddy currents using an in-house MATLAB-based code (MathWorks, Inc.). Data smoothing algorithm proposed by Garcia[64, 65] was used to eliminate random errors of the velocity vectors. Garcia[64, 65] proposed a fully automated smoothing procedure based on a

penalized least squares approach that allows fast smoothing of the data and can replace spurious or missing vectors with the smoothed one.

The 3-D segmentation of thoracic aorta geometry and orifice shape of aortic stenosis or bicuspid valve was performed by ITK-SNAP (Yushkevich et al., 2006; http://www.itksnap.org) and an in-house MATLAB-based code. Fusion 3-D (Autodesk, Inc) and Meshmixer (Autodesk, Inc) were used to smooth the geometry and fix the defects. Finally, the Stereolithography (STL) format of the geometry (domain) was extracted for our computational simulation. Time-varying flow velocity information extracted from patient-specific 4-D flow MRI data was imposed at the inlet and outlets of each LBM computational model. To study the effect of resolution and comparing LBM to 4-D flow MRI velocity fields on identical grids, we down sampled the high-resolution LBM velocities into PC-MRI resolution by linear interpolation of LBM velocity on MRI sub grid. Moreover, down-sampled LBM data subjected to an imitation of the smoothing inherent in the 4-D flow MRI measurement to have the closest LBM approximation to the 4-D flow MRI data. The down-sampling and smoothing procedures are schematically shown in Figure 1 (Panel B).

Velocity field extracted from 4-D flow MRI measurements was smoothed through a multidimensional spline smoothing technique proposed by Garcia[64, 65]. The algorithm deals with occurrences of missing and outlying values and eliminates random errors automatically. The mathematics behind algorithm structure is based on penalized least squares approach that allows fast smoothing of the data and can replace spurious or

missing vectors with the smoothed one. The algorithm allows fast unsupervised smoothing that combines the use of the discrete cosine transform and the generalized cross-validation score. Garcia's algorithm was compared with conventional methods, including the normalized median test, and experimental raw particle image velocimetry velocity fields and it was shown that it can easily deal with a large amount of missing data and reduce the experimental noise while keeping the most important characteristics of a dataset[64].

In the current study, to investigate the effect of resolution and to compare LBM and 4-D flow MRI velocity fields on identical grids, we down sampled the high-resolution LBM velocity fields by linear interpolation on the 4D flow MRI grid. The down-sampling and smoothing procedures are schematically shown in Figure 1.

4.4.4 Statistical analysis

All results were expressed as mean ± standard deviations (SD). Statistical analyses were performed using SigmaStat software (Version 3.1, Systat Software, San Jose, CA, USA). Coefficient of determination, R^2, was used to quantify the quality of linear regressions. Statistically significant differences between two datasets were assessed using two-sample t-test at 1% significance level.

Table 4-1. Baseline patient characteristics. DE: Doppler echocardiography, NYHA: New York Heart Association

	Pre intervention Mean ± SD (n=36)
Ventricular indices – DE findings	
Ejection fraction, %	59.5 ± 11.5
Heart rate, bpm	65.8 ± 10.6
Stroke volume, mL	62.3 ± 10.4
NYHA classifications ≥ grade 2	39%
Valvular indices – DE findings	
Mean aortic valve gradient, mmHg	26 ± 7.3
Maximum aortic valve gradient, mmHg	46 ± 19.5
Aortic valve disease type	Tricuspid: 22; Bicuspid: 14
Aortic valve Regurgitation ≥ grade 2	36%
Mitral valve Regurgitation ≥ grade 2	21%
Vascular indices – Sphygmomanometer	
Brachial systolic blood pressure, mmHg	145 ± 25.4
Brachial diastolic blood pressure, mmHg	78 ± 11.9
Patient description	
Mean age, years; Gender	34 ± 11.5; (Female: 42%)
Mean weight, kg; Mean height, cm	78 ± 14.6; 169.3 ± 7.9
Body surface area, m^2	1.8 ± 0.31
Associated cardiovascular lesions	
Bicuspid aortic valve	14
Tricuspid aortic valve stenosis	6
Aortic valve regurgitation	12
Mitral valve stenosis	4
Heart failure	11
Mitral valve regurgitation	10
Descending aorta aneurysms	5

4.5 Results

4.5.1 Validation: computational framework vs. 4-D flow MRI

In this study, we developed a patient-specific, imaged-based, computational-mechanics framework that dynamically couples the local hemodynamics with the global circulatory cardiovascular system to investigate the impact of COA and MVD on both local and global hemodynamics in these patients. The entire computational framework was validated against 4-D flow MRI measurements in five patients with COA. Figure 2 describes sample cases of voxel-by-voxel Bland-Altman analysis between the velocity fields resulted from the smooth down sampled low-resolution LBM and 4-D flow MRI measurements on the entire flow domain at the early systole, the peak systole as well as the late systole. The simulated velocity fields were in agreement with the velocity fields measured using 4-D flow MRI in patients: as examples, average biases (means of differences) were -0.049, -0.059 and 0.0426 [m/s] and corresponding average limits of agreement (1.96 SD) were also ±0.302, ±0.191 and ±0.325 [m/s] for patients #I, #II and #III, respectively. Moreover, Figure 3 shows the statistical analyses of the planar velocity differences between velocity field resulted from our computational framework and 4-D flow MRI measurements in sample cases at the peak of systole. As this figure shows, the 4-D flow MRI velocity field and the down sampled LBM-based velocity fields were compared using Pearson's correlation and Bland-Altman analysis. The coefficient of determination (R^2) was used to assess the linearity between the results from 4-D flow MRI and our computational framework at these planar sections. The average of

coefficients of determination were 0.863, 0.830, 0.526 for patients #I, #II and #III, respectively. Average lateral section Biases (means of differences) were also -0.049, -0.0113 and -0.042 m/s and the corresponding limits of agreement (1.96 standard deviation of differences) were ±0.229, ±0.129 and ±0.420 m/s for patients #I, #II and #III, respectively, which shows agreements between the data resulted from 4-D flow MRI and our computational framework. We observed similar agreement (computational results *vs.* 4-D flow MRI measurement) in the other patients with COA investigated in this study. It is important to note that 4-D flow MRI itself has some limitations and its measurements involves errors due to low temporal resolution (20 ms highest)[56, 66]. The differences between the computational results and 4-D flow MRI measurements can be partly due to the shortages of 4-D flow MRI.

In addition, our developed patient-specific Doppler-based lumped-parameter model calculations were validated against clinical cardiac catheterization data (the instantaneous pressures in the aorta and LV) in patients with complex valvular, ventricular and vascular diseases with a substantial inter- and intra-patient variability with a wide range of disease (N=49)[48, 56]. The model has already been validated against *in vivo* cardiac catheterization in patients with coarctation (N=40)[45, 46] and some sub-models have been validated against *in vivo* MRI data (N=57)[67]. In addition, some of the sub-models of the lumped parameter model have been used and validated previously[42, 48, 55, 67-75]. Moreover, the entire patient-specific computational framework (Lattice Boltzmann method and lumped parameter model) was validated against clinical Doppler echocardiography previously[45]. Moreover, for all 26 patients investigated in this study, we observed good agreements between the

simulated and experimental Doppler echocardiography pressure gradients (Mean relative error: 3.9%).

The good agreements between results calculated using our computational framework with the results measured using clinical 4-D flow MRI, Doppler echocardiography and cardiac catheterization allows us to accept our computational results with confidence to investigate the flow features.

4.5.2 Clinical measure of hemodynamics: Doppler echocardiography and catheter pressure gradients

Currently, clinical assessment of COA for management and intervention decisions are achieved based on the symptoms and hemodynamics metrics, focused only on COA. A hemodynamically significant COA is often defined as a catheter pressure gradient or Doppler pressure gradient of 20 mmHg across the COA. Indeed, the COA pressure gradient greater than 20 mmHg warns of major COA and secures interventional/surgical repair. Our data revealed that MVD and COA have mechanical interactions with one another, alter the pressure gradient across the COA and lead to overestimating or underestimating the disease (Figures 5, 7, 9, 12 and 14). As examples, Doppler and catheter pressure gradients were exacerbated significantly in the following cases: COA coexisting with MS, AR, and MR; COA coexisting alongside MR and AR; COA coexisting with MS and AR and COA coexisting with AR (Figures 5, 7, 9, 12 and 14). This is very important since wall expansion, compression and collapse are caused by high

pressure drops in the COA. Moreover, the pressure drops introduced by the presence of the COA and MVD must be compensated for by the LV, this in turn can lead to heart failure. Both Doppler and catheter measures documented a trans-coarctation pressure gradient in patients with COA and MVD confirmed the following findings (Figures 5, 7, 9, 12 and 14):

(1) *The presence of AS alone does not increase the pressure gradient across the COA in patients with COA and MVD* (e.g., patient #2: COA with AS alone: 98.60 mmHg (max, DE), 59 mmHg (max, catheter); COA with normal valves: 110 mmHg (max, DE), 78.7 mmHg (max, catheter); Figure 7).

(2) *COA pressure gradient elevated in the presence of MR alone* (e.g., patient #2: COA with MR alone:122.4 mmHg (max, DE), 85.2 mmHg (max, catheter); COA with normal valves: 110 mmHg (max, DE), 78.7 mmHg (max, catheter); Figure 7).

(3) *Pressure gradient across the COA drastically increased in the presence of AR alone* (e.g., patient #2: COA with AR alone: 300.76 mmHg (max, DE), 182.17 mmHg (max, catheter); COA with normal valves: 110 mmHg (max, DE), 78.7 mmHg (max, catheter); Figure 7).

(4) *The individual COA status remained unchanged in patients with MS alone* (e.g., patient #2: COA with MS alone:115 mmHg (DE), 78.8 mmHg (max, catheter); COA with normal valves: 110 mmHg (DE), 78.7 mmHg (max, catheter); Figure 7).

We observed similar pressure gradient characteristics in the other patients with COA and MVD investigated in this study.
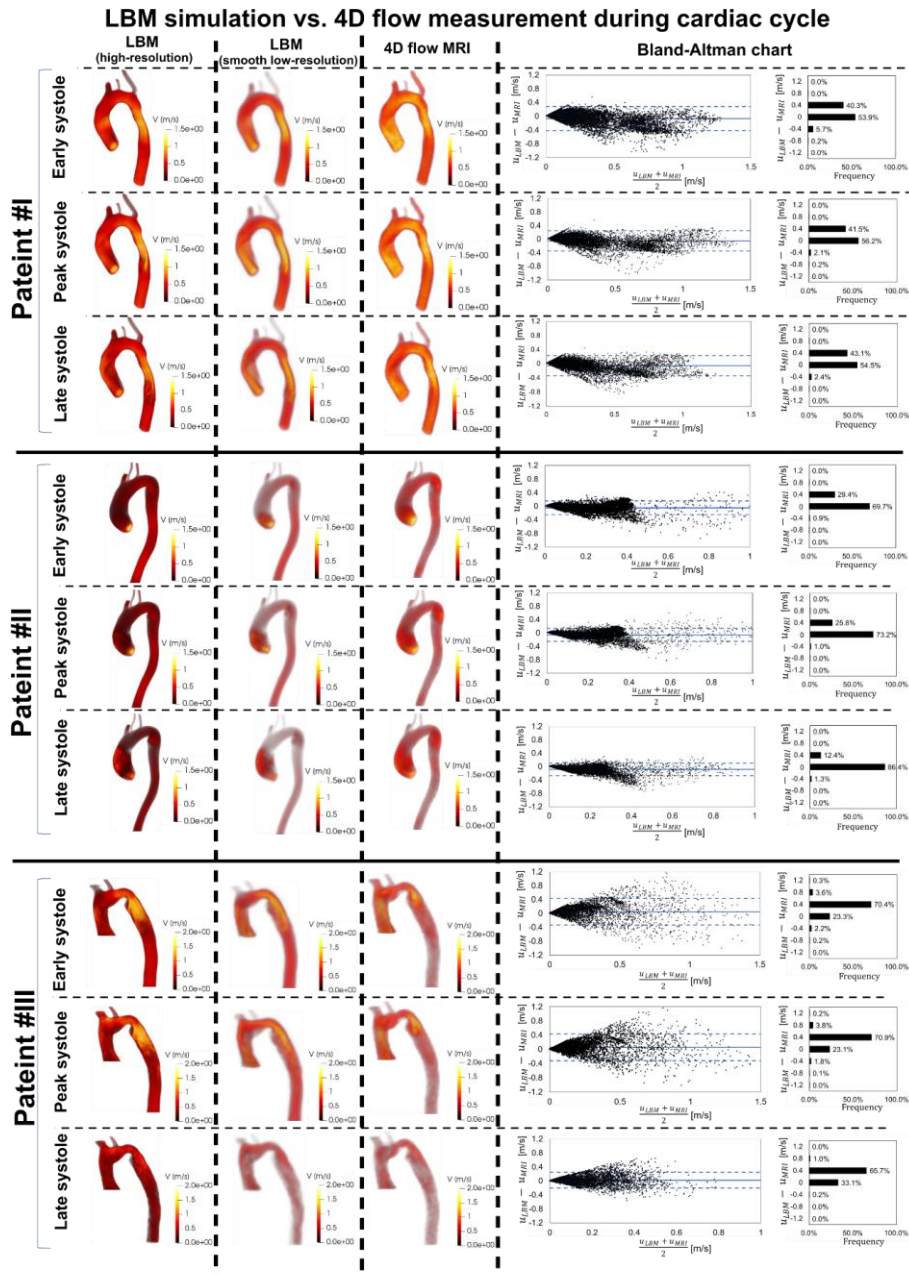
Figure 4-2. Validation against 4-D flow MRI (part I). We compared 4-D flow MRI data and results of the computational framework (based on lumped parameter model (LPM) and Lattice Boltzmann model (LBM)) in sample Patients #I to #III, qualitatively (revealed in velocity mapping) and quantitatively by performing Pearson's product moment correlation analysis on the entire domain during cardiac cycle between smooth down-sampled LBM and 4D flow MRI measurements.
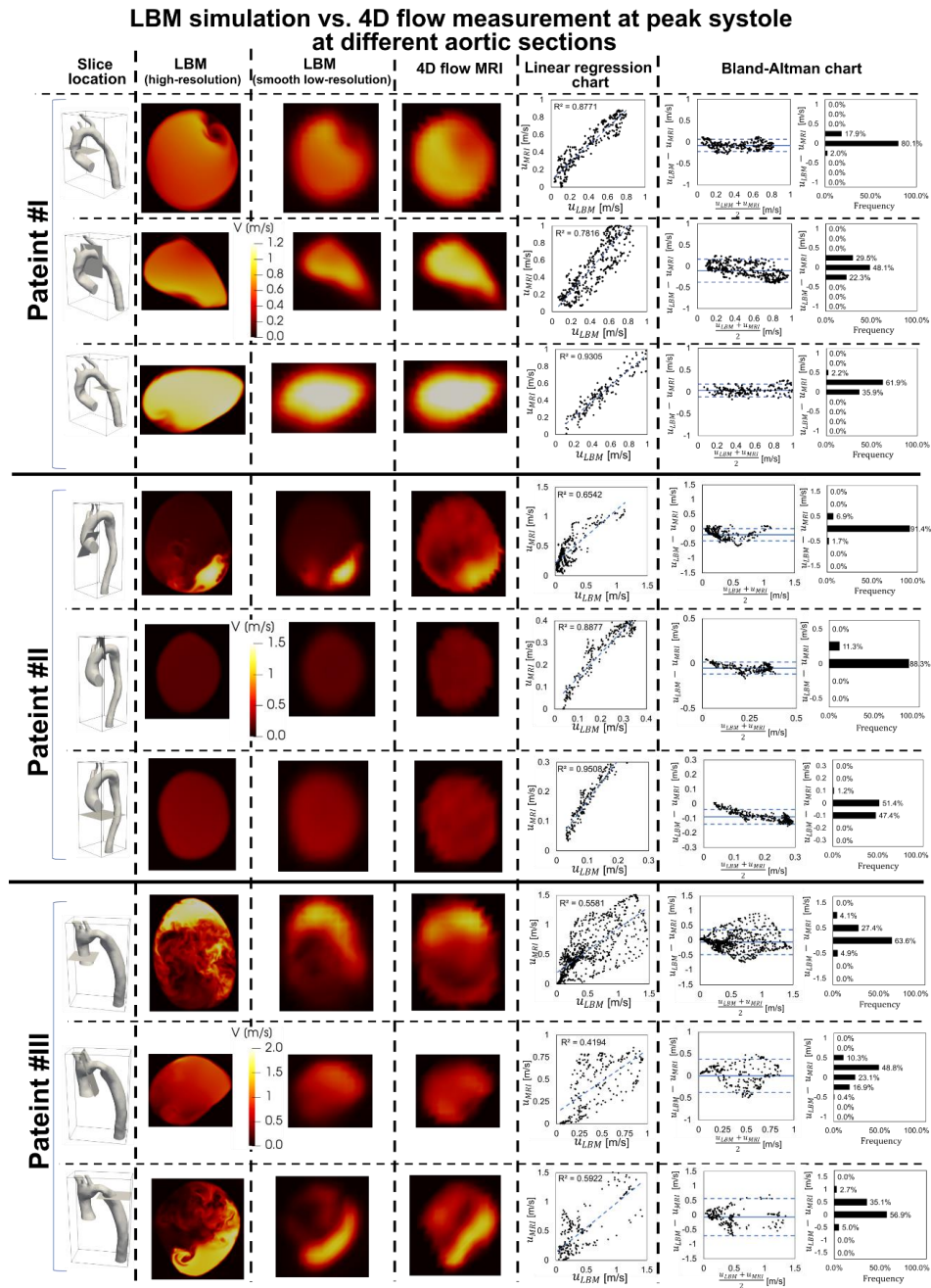
Figure 4-3. Validation against 4-D flow MRI (part II). We compared 4-D flow MRI data and results of the computational framework (based on lumped parameter model (LPM) and Lattice Boltzmann model (LBM)) in sample Patients #I to #III, qualitatively (revealed in velocity mapping) and quantitatively by performing linear regression and Pearson's product moment correlation analysis at different sections at peak systole between smooth down-sampled LBM and PC-MRI measurements.

4.5.3 Simulated global and local hemodynamics

Global hemodynamics (cardiac function). The LV workload is an effective metric of the LV function and its clinical state and is calculated as the area encompassed by the LV pressure–volume loop. Our results revealed that LV function parameters, e.g., LV pressure and workload, are dramatically different in patients with MVD (Figures 5, 7 and 9 show examples of LV pressure and workload in 3 patients with COA and MVD). Our data showed (Figures 5, 7, 9, 10, 11 and 14) that *the LV workload in all COA patients with MVD was universally increased due to the presence of AS alone, AR alone, MR alone and when they coexist. MS alone does not have a remarkable impact on LV workload in these patients*. As examples, LV workload and LV pressure in patient #1 are as follows (Figure 5): COA with normal valves: LV workload: 1.0617 J, LV peak pressure: 122.51 mmHg; COA with only AS: LV workload: 1.225 J, LV peak pressure: 143.43 mmHg; COA with only AR: LV workload: 1.6512 J, LV peak pressure: 136.74 mmHg; COA with only MR: LV workload: 1.3599 J, LV peak pressure: 123.48 mmHg; COA with only MS: LV workload: 1.0472 J, LV peak pressure: 122.07 mmHg. We observed similar cardiac function characteristics in the other patients with COA and MVD.

Local hemodynamics (aortic dynamics). The presence of the COA itself modified largely the flow dynamics: the disturbed flow resulting from COA detached from the walls and developed into a high-speed eccentric jet. Our data (Figures 4, 6 and 8) described that *the velocity downstream of the COA in all patients with AR alone was*

drastically increased. This situation got worsen when COA and AR coexist with MR. As an example, maximum velocity downstream of the COA in patient #2 (Figure 6) are as follows: COA with normal valves: 5.27 m/s, COA with only AR: 8.8 m/s, COA with AR and MR: 9.36 m/s. Indeed, *AR and MR when coexistent with COA substantially alter the velocity magnitude downstream of the COA, further encouraging turbulent flow downstream of COA and may lead to significant progression of the disease at the COA region* (Figures 4, 6 and 8). We observed similar characteristics in the other patients with COA and MVD investigated in this study.

Such flow alterations contributed to elevated wall shear stress mainly at the neck of the COA as well as distal to the COA. Wall shear stress, as a force induced by blood flow, has a major impact on regulating endothelial function and is a predeterminant biomarker of disease progression. In this study, the total shear stress exerted on the aorta wall was evaluated using time-averaged wall shear stress (TAWSS). Our data explained that *MVD impacted TAWSS at COA region, and can further increase the TAWSS (e.g., COA coexists with AR alone; COA coexists with MR alone; COA coexists with AR and MR; Figures 4, 6 and 8) or improve the TAWSS (e.g., COA coexists with AS alone; Figures 4, 6 and 8) at the COA region*. Local perturbation in shear stress exposes endothelial cells to high shear stress which affects vessel distensibility and compliance and potentially lead to vascular diseases. Although high WSS may act as a deterrent against formation of atherosclerosis, very high WSS can trigger endothelial cells to express a transcriptional profile which ultimately leads to arterial remodeling, rupture and dissection.

In addition, systemic arterial compliance (SAC = stroke volume (SV)/pulse pressure (PP)) was obtained as an index of arterial hemodynamics. Patients with COA usually have upper extremity hypertension and are characterized by reduced systemic arterial compliance. Our results suggest that any combination of MVD along with COA substantially alters the SAC magnitudes (Figures 13 and 14).

4.6   Discussion

MVD, which are classified as various combinations of different aortic and mitral valvular pathologies such as AS, AR, bicuspid aortic valve, MR, and MS, are often present in conjunction with COA. We sought that in patients with COA and MVD, the interactions between MVD and COA have dramatic impacts on both the local and global hemodynamics. It is important to note that in current clinical practice, proper treatment is difficult to administer when COA and MVD are present. Treatment is often performed in a multiple-stage approach as higher morbidity rates have been recorded if several pathologies are repaired simultaneously[23, 33, 37]. Indeed, it is often unclear what the effects of each pathology are on the cardiovascular system and which pathology is more life-threatening. Furthermore, timing of intervention is crucial as the overload on the LV due to the COA and MVD is likely to lead to LV dysfunction, cardiac failure, and death if not treated promptly[23, 29, 76]. To date, there are no standardized guidelines and the ideal treatment methods are often unclear for individuals suffering from COA and MVD[35, 38]. Hemodynamic significance of MVD and COA must be analyzed carefully to establish

proper treatment methods since an individualized treatment approach is crucial for the optimal recovery of each patient[41, 42]. In the present work, there are several findings which should be individually discussed:

Doppler echocardiography COA pressure gradient is a poor indicator of COA severity when coexisting with MVD

Our results demonstrate that in patients who suffered from COA and MVD (one or a combination of AS, AR, MS and MR):

1. The presence of AS alone or MS had no major effects on the pressure gradients across the COA measured by Doppler echocardiography. In these patients, the pressure gradient was due to COA itself.

2. Moreover, COA pressure gradient was non-remarkably elevated in the presence of MR.

3. In contrast, the presence of AR had major effects on the COA pressure gradients – AR interacted with COA and amplified the COA pressure gradients measured by Doppler echocardiography. This is crucial because the high-pressure loss due to COA can be exacerbated by AR, speeding up the collapse of the aorta wall[9, 77-81].

As one example, in the case of COA patient #1 with actual status of severe AS, mild-moderate AR and mild-moderate MR, the DE COA pressure gradients (47.3 mmHg (maximum) and 21.50 mmHg (mean)) were almost as if this patient had normal valves (39.8 mmHg (maximum) and 19.09 mmHg (mean)) (Figure 5). This is extremely critical for the two following reasons:

Figure 4-4. Flow modeling (local) in Patient No. 1. Computed velocity magnitude and time-averaged wall shear stress (TAWSS) using the computational framework (Lattice Boltzmann method and lumped parameter model) in sample Patient No. 1. Actual patient (in red font in this figure) has severe aortic stenosis (EOA_{AS}=1 cm^2), moderate aortic valve regurgitation (EOA_{AR}=0.15 cm^2), moderate mitral valve regurgitation (EOA_{MR}=0.15 cm^2) with no mitral stenosis. This patient has brachial pressures of 70 and 125 mmHg, forward LV stroke volume of 110 mL, maximum LV pressure of 170 mmHg and LV workload of 2.4923 J. The total shear stress exerted on the wall throughout the cardiac cycle was evaluated using the time-averaged wall shear stress (TAWSS) which is obtained as $TAWSS = \frac{1}{T}\int_0^T |\tau|\, dt$. Here, T and τ are the cardiac cycle period and instantaneous wall shear stress, respectively.

Mixed valvular disease and coarctation: patient #1
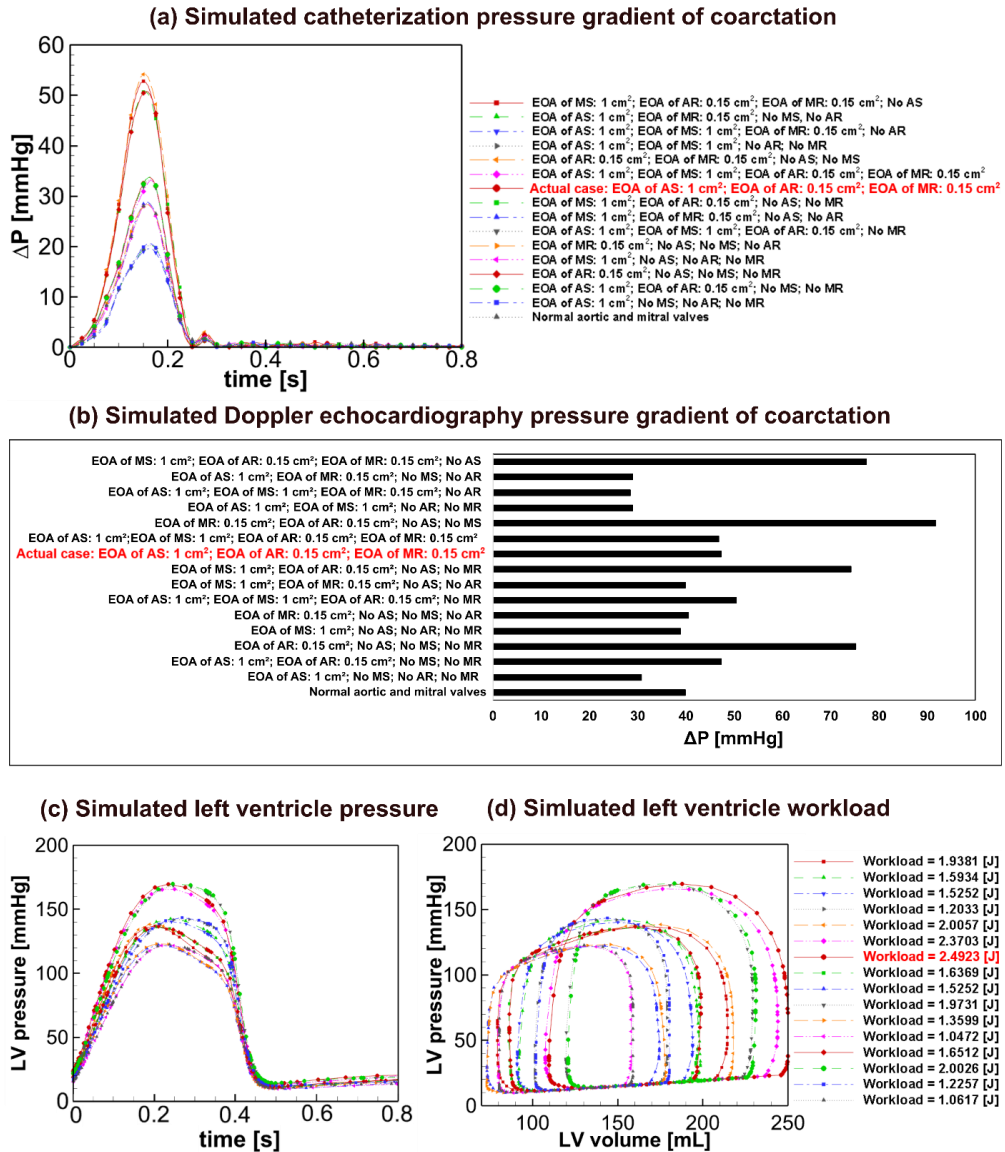
Figure 4-5. Flow modeling (global) in Patient No. 1. (a) simulated catheter pressure gradient of coarctation which is the difference between the tabulated pressures of the neck and upstream of COA, using the computational framework, Lattice Boltzmann method and lumped parameter model ($\Delta P = P_2 - P_1$; P_2: pressure at the neck of COA; P_1: pressure upstream of COA); (b) simulated peak Doppler echocardiography pressure gradient of coarctation using the computational framework, Lattice Boltzmann method and lumped parameter model ($\Delta P = 4V_{max}^2$; V_{max}: maximum velocity downstream of COA during systole); (c) simulated left ventricle pressure using lumped parameter model; (d) simulated left ventricle workload using lumped parameter model.

172

Mixed valvular disease and coarctation: patient #2

Figure 4-6. Flow modeling (local) in Patient No. 2. Computed velocity magnitude and time-averaged wall shear stress (TAWSS) using the computational framework (Lattice Boltzmann method and lumped parameter model) in sample Patient No. 1. Actual patient (in red font in this figure) has moderate aortic stenosis (EOA$_{AS}$=1.2 cm^2), moderate aortic valve regurgitation (EOA$_{AR}$=0.2 cm^2), with no mitral valve regurgitation and no mitral stenosis. This patient has brachial pressures of 60 and 131 mmHg, forward LV stroke volume of 124 mL, maximum LV pressure of 156.5 mmHg and LV workload of 2.022 J.

Mixed valvular disease and coarctation: patient #2

(a) Simulated catheterization pressure gradient of coarctation

(b) Simulated Doppler echocardiography pressure gradient of coarctation

(c) Simulated left ventricle pressure

(d) Simulated left ventricle workload
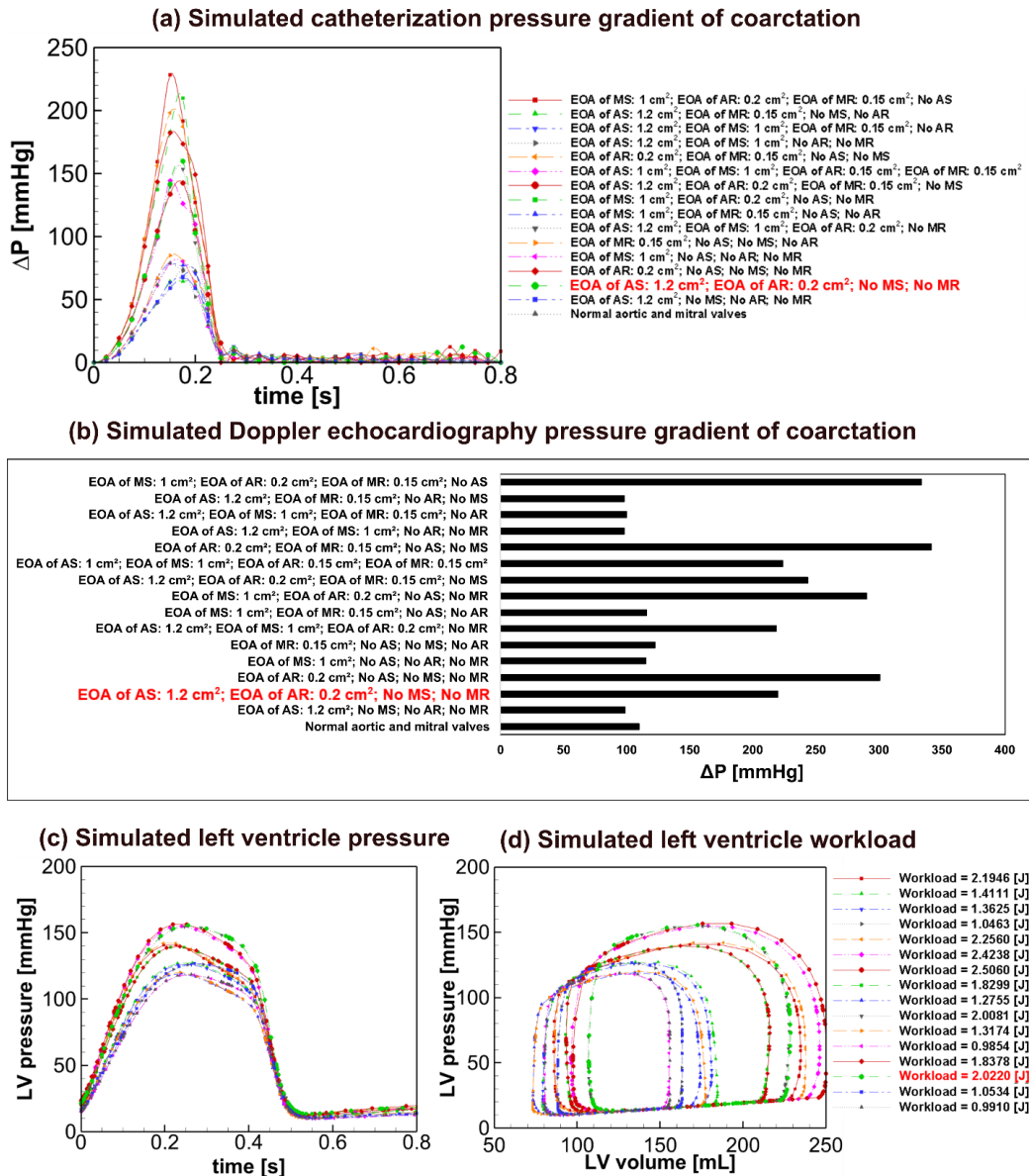
Figure 4-7. Flow modeling (global) in Patient No. 2. (a) simulated catheter pressure gradient of coarctation which is the difference between the tabulated pressures of the neck and upstream of COA, using the computational framework, Lattice Boltzmann method and lumped parameter model ($\Delta P = P_2 - P_1$; P_2: pressure at the neck of COA; P_1: pressure upstream of COA); (b) simulated peak Doppler echocardiography pressure gradient of coarctation using the computational framework, Lattice Boltzmann method and lumped parameter model ($\Delta P = 4V_{max}^2$; V_{max}: maximum velocity downstream of COA during systole); (c) simulated left ventricle pressure using lumped parameter model; (d) simulated left ventricle workload using lumped parameter model.

Figure 4-8. Flow modeling (local) in Patient No. 3. Computed velocity magnitude and time-averaged wall shear stress (TAWSS) using the computational framework (Lattice Boltzmann method and lumped parameter model) in sample Patient No. 1. Actual patient (in red font in this figure) has severe mitral stenosis (EOA$_{MS}$=1 cm^2), moderate aortic valve regurgitation (EOA$_{AR}$=0.2 cm^2), moderate mitral valve regurgitation (EOA$_{AR}$=0.15 cm^2) and no aortic stenosis. This patient has brachial pressures of 55 and 138 mmHg, forward LV stroke volume of 121 mL, maximum LV pressure of 142 mmHg and LV workload of 2.2599.

Mixed valvular disease and coarctation: patient #3
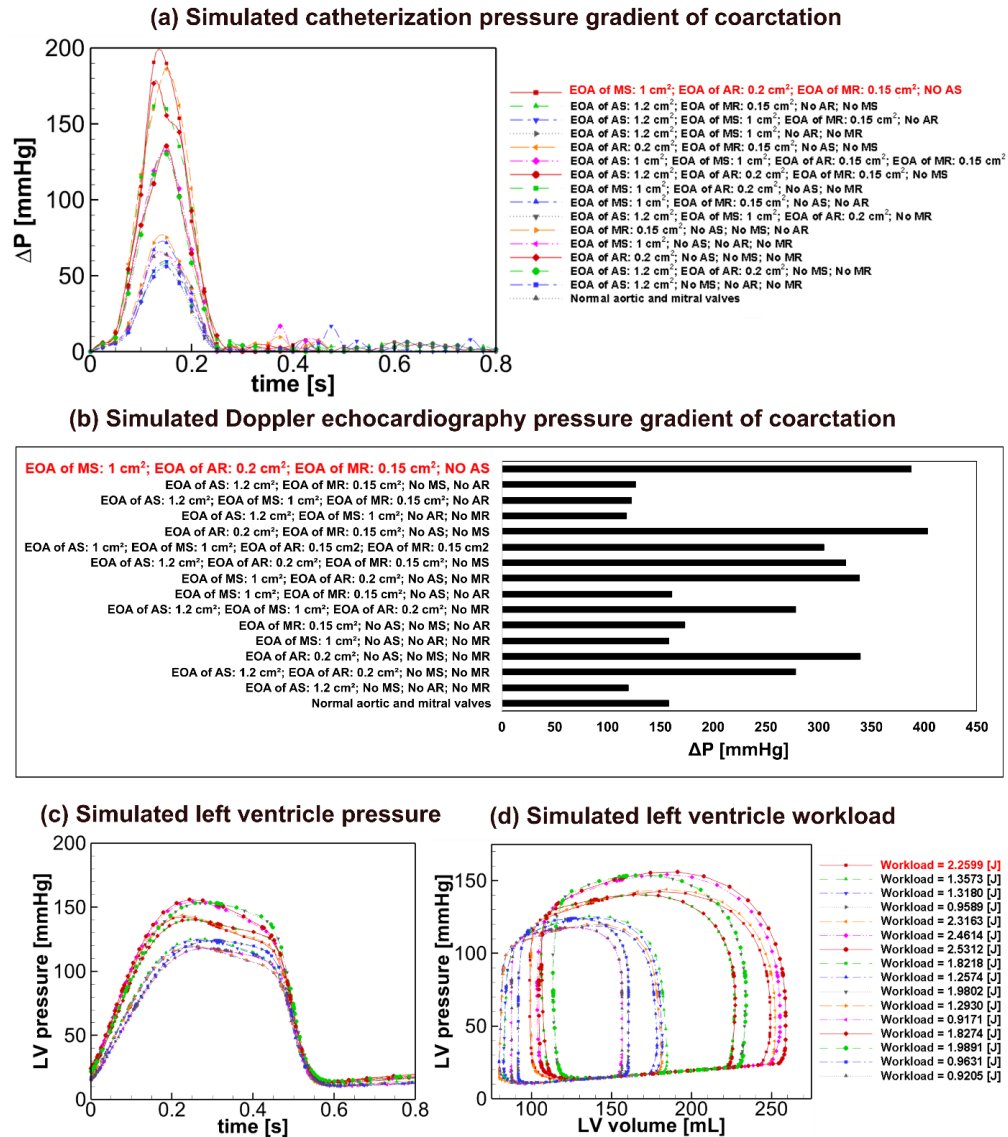
Figure 4-9. Flow modeling (global) in Patient No. 3. (a) simulated catheter pressure gradient of coarctation which is the difference between the tabulated pressures of the neck and upstream of COA, using the computational framework, Lattice Boltzmann method and lumped parameter model ($\Delta P = P_2 - P_1$; P_2: pressure at the neck of COA; P_1: pressure upstream of COA); (b) simulated peak Doppler echocardiography pressure gradient of coarctation using the computational framework, Lattice Boltzmann method and lumped parameter model ($\Delta P = 4V_{max}^2$; V_{max}: maximum velocity downstream of COA during systole); (c) simulated left ventricle pressure using lumped parameter model; (d) simulated left ventricle workload using lumped parameter model.

Figure 4-10. Differences in the simulated LV workloads between (mixed valvular disease & COA) and (normal aortic and mitral valves & COA) in individual patients (N=26).

**Changes in simulated LV peak pressure (mmHg)
in patients with COA and MVD (N=26)
(Mixed valvular diseases & COA − Normal aortic and mitral valves & COA)**
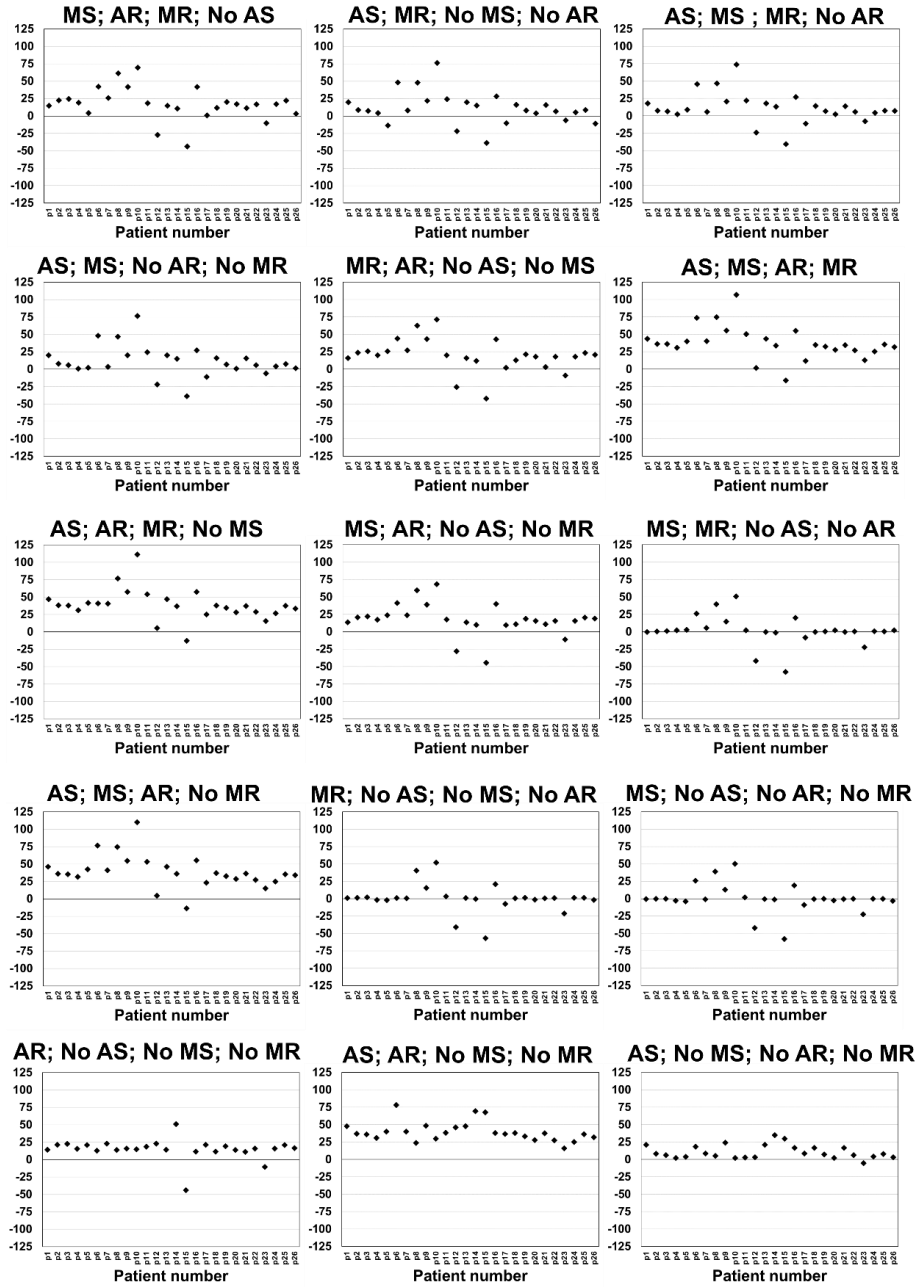
Figure 4-11. Differences in the simulated LV peak pressure between (mixed valvular disease & COA) and (normal aortic and mitral valves & COA) in individual patients (N=26).

Figure 4-12. Differences in the simulated catheter pressure gradient between (mixed valvular disease & COA) and (normal aortic and mitral valves & COA) in individual patients (N=26).

Changes in simulated systemic arterial compliance (mL/mmHg)
in patients with COA and MVD (N=26)
(Mixed valvular diseases & COA − Normal aortic and mitral valves & COA)
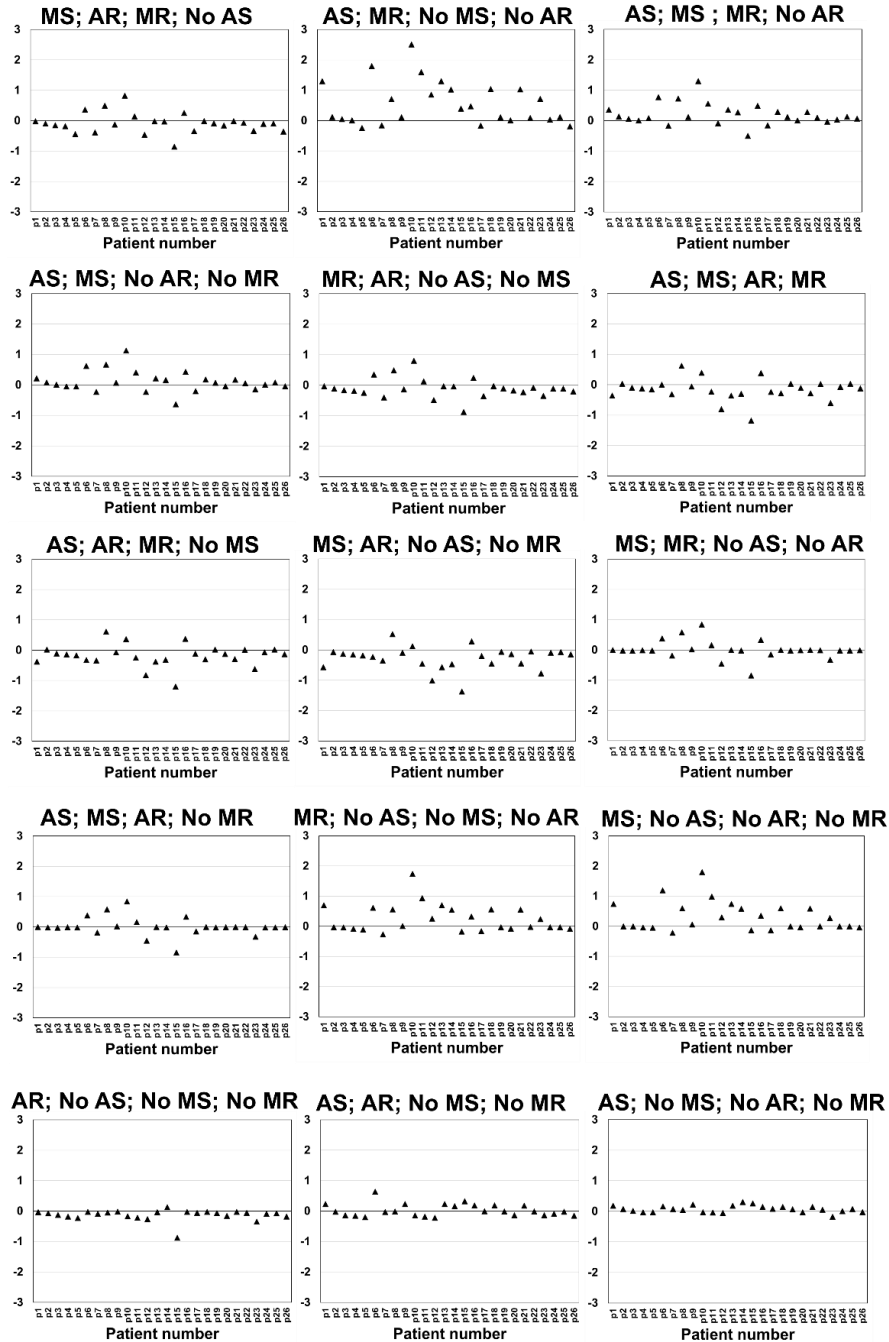
Figure 4-13. Differences in the simulated systemic arterial compliance between (mixed valvular disease & COA) and (normal aortic and mitral valves & COA) in individual patients (N=26).

Box and whiskers diagram of changes in patients with COA and MVD (N=26)
(Mixed valvular diseases & COA − Normal aortic and mitral valves & COA)

(a) Changes in simulated LV workload (J)

(b) Changes in simulated LV peak pressure (mmHg)

(c) Changes in simulated catheter pressure gradient (mmHg)

(d) Changes in simulated systemic arterial compliance (mL/mmHg)
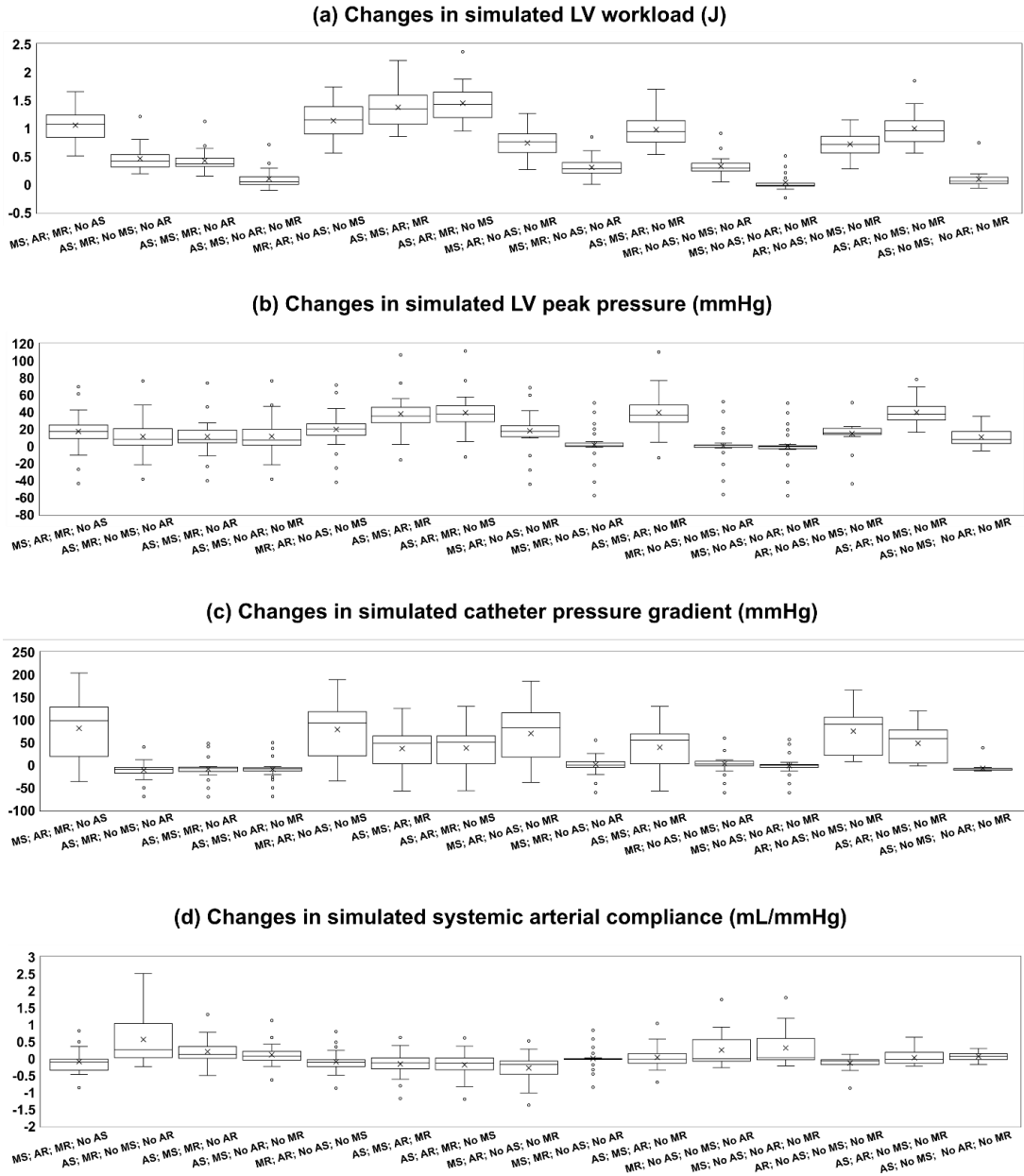
Figure 4-14. Difference in the simulated hemodynamics parameters between (mixed valvular disease & COA) and (normal aortic and mitral valves & COA) in all patients (N=26) using Box and Whisker diagram: (a) simulated LV workload; (b) simulated LV peak pressure; (c) simulated catheter pressure gradient; (d) simulated systemic arterial compliance.

1. In the case that COA coexists with AS alone in this patient (no AR, MR or MS), DE COA pressure gradients dropped from 47.3 to 30.7 mmHg (maximum) and from 21.50 to 12.04 mmHg (mean). This shows that COA pressure gradient may be masked and underestimated in presence of AS.

2. In the case that COA coexists with AR alone in this patient (no AS, MR or MS), DE COA pressure gradients elevated from 47.3 to 75.2 mmHg (maximum) and from 21.50 to 30.50 mmHg (mean). This reveals that COA pressure gradient may be overestimated in presence of AR alone.

Catheter pressure gradient fails to reflect the effect of MVD on the clinical assessment of COA hemodynamics

The gold standard for diagnosis and grading of coarctation of the aorta is the measurement of the pressure gradient across the site of coarctation by cardiac catheterization[82]. As precise positioning of the probe in the vena contracta is difficult, probes are typically placed 1-2 cm distal to the coarctation, where velocity is reduced and the flow is influenced by the pressure recovery phenomenon, decreasing the accuracy of the measurement[72, 83]. In addition to the invasive nature of the procedure that hinders follow-up, and sedation, which is frequently required, can reduce cardiac activity and lead to an underestimation of the pressure gradient[84]. For patients with COA who also suffer from AS, MS, MR, or a combination, we did not observe major effects due to these valvular diseases on the catheter pressure gradient, and the measured COA gradient was produced by COA itself (similar to DE pressure gradients). In contrast, similar to observations about DE pressure gradients, the coexistence of AR with COA greatly

amplified the catheter COA pressure gradient, leading to an overestimation of the severity of coarctation. Furthermore, catheter (and Doppler) COA pressure gradients are highly influenced by the flow rate - they are nonlinearly reduced when the flow rate is decreased. In fact, the relief of the pressure gradient through COA does not correlate with the relief of symptoms or functional improvements[83].

MVD exacerbated the COA hemodynamics (local)

The jets emerging from the COA orifice substantially alters the vortical structure in the aorta, creating disturbed flow, leading to high shear stress mainly downstream of the COA[9, 71, 85]. Our results demonstrate that MVD interacts with COA fluid dynamics, amplifies irregular flow patterns, and consequently increase TAWSS especially downstream of COA. In patients with COA who also suffered from AS, MS or a combination, the presence of these valvular diseases had modest effects on the COA. However, the presence of AR and/or MR, compared to the other valvular diseases (AS and MS), had major impacts on the COA hemodynamics as they interacted with COA and through increasing TAWSS, they may contribute to speeding up the progression of the COA more than other valvular diseases do. These progressions may include endothelial dysfunction, dedifferentiation of the arterial smooth muscle and medial thickening all of which can lead to major aortic wall complications such as aortic aneurysm, rupture and dissection at the COA region.

MVD exacerbated the left ventricular function and hemodynamics (global)

Our results reveal that COA and some components of MVD increase the burden on the LV (e.g., AS alone, AR alone, MR alone and when they coexist). Compared to the other valvular diseases, the presence of AR and/or MR, when coexistent with COA, elevates the heart workload significantly due to the increased stroke volume causing LV volume overload. Therefore, uncorrected COA along with AR and/or MR cause an overloaded LV, resulting in faster deterioration or failure of the LV. In order to plan interventions as well as their sequence, our findings suggest that not only the severity of the COA and MVD should be considered but the breakdown of the effects of each disease constituent on the global function of the heart should also be considered. It is crucial to identify patients in whom AR and/or MR coexists with COA; in these patients the increased risk of a double procedure may be justified since correcting one pathology at a time has limited utility in reducing myocardial strain and causes persistent increased LV mass and hypertrophy.

4.7   Limitations

We developed a computational fluid dynamics framework using 3-D Lattice Boltzmann method (Large eddy simulation, Smagorinsky subgrid scale model) and lumped parameter model to simulate both the local and global hemodynamics in patients with MVD and COA. One limitation of our simulations is lack of modeling of the aortic and mitral valves. Diseased aortic valve (e.g., bicuspid aortic valve or aortic stenosis) create complex blood flow patterns in the thoracic aorta that influence the local hemodynamics in the coarctation region[71, 86, 87]. However, the good agreements between results calculated

using our computational framework with the results measured using clinical 4-D flow MRI, Doppler echocardiography and cardiac catheterization, which include moving aortic and mitral valves, show that this limitation does not significantly modify the conclusions of this study. Please note that considering moving aortic and mitral valve leaflets as well as modeling the left ventricle are computationally expensive and complicated. Future numerical studies should consider the interactions between the fluid and structure and investigate the effect of dynamical opening and closing of the aortic valve leaflets on the vortex dynamics in the aorta.

Competing interest

The authors declare that they have no competing interests.

Authors contributions

R.S. Computational modeling, image processing, data collection and analysis, interpretation of data and manuscript writing; B.T. & S.K. Data collection and analysis and manuscript writing; J.G. & J.G. clinical data collection, analysis and interpretation of data; Z.K.M. Conception and design, lumped parameter algorithm development, data analysis, interpretation of data, manuscript writing, critical revision, final approval of the manuscript and supervised this research. All authors read and approved the final manuscript.

Data availability

The development and validation of the proposed method require the retrospective clinical data routinely measured in clinics (Doppler ultrasound and catheter data) and were transferred as the de-identified & anonymized data. The code and the optimization algorithms are available from the author upon request.

4.8   References

1.   Sinning C, Zengin E, Kozlik-Feldmann R, Blankenberg S, Rickers C, von Kodolitsch Y, Girdauskas E. Bicuspid aortic valve and aortic coarctation in congenital heart disease—important aspects for treatment with focus on aortic vasculopathy. *Cardiovascular diagnosis and therapy*. 2018;8:780

2.   Ma L, Gu Q, Ni B, Sun H, Zhen X, Zhang S, Shao Y. Simultaneously surgical management of adult complex coarctation of aorta concomitant with intracardiac abnormality. *Journal of Thoracic Disease*. 2018;10:5842

3.   Endorsed by the Association for European Paediatric Cardiology, Authors/Task Force Members, Baumgartner H, Bonhoeffer P, De Groot NM, de Haan F, Deanfield JE, Galie N, Gatzoulis MA, Gohlke-Baerwolf C. Esc guidelines for the management of grown-up congenital heart disease (new version 2010) the task force on the management of grown-up congenital heart disease of the european society of cardiology (esc). *European heart journal*. 2010;31:2915-2957

4.   Roos-Hesselink J, Schölzel B, Heijdra R, Spitaels S, Meijboom F, Boersma E, Bogers A, Simoons M. Aortic valve and aortic arch pathology after coarctation repair. *Heart*. 2003;89:1074-1077

5.   Perloff J. Survival pattern without cardiac surgery or interventional catheterization: A narrowing base. *Congenital heart disease in adults*. 1998;23

6.   Mazzanti L, Prandstraller D, Tassinari D, Rubino I, Santucci S, Picchio F, Forabosco A, Cacciari E. Heart disease in turner's syndrome. *Helvetica paediatrica acta*. 1988;43:25-31

7.   Brickner ME, Hillis LD, Lange RA. Congenital heart disease in adults. *New England Journal of Medicine*. 2000;342:256-263

8.   Braverman AC, Güven H, Beardslee MA, Makan M, Kates AM, Moon MR. The bicuspid aortic valve. *Current problems in cardiology*. 2005;30:470-522

9.   Keshavarz-Motamed Z, Garcia J, Kadem L. Fluid dynamics of coarctation of the aorta and effect of bicuspid aortic valve. *PLoS one*. 2013;8:e72394

10.   Smith D, Matthews M. Aortic valvular stenosis with coarctation of the aorta: With special reference to the development of aortic stenosis upon congenital bicuspid valves. *British Heart Journal*. 1955;17:198

11.   Simon AB, Zloto AE. Coarctation of the aorta: Longitudinal assessment of operated patients. *Circulation*. 1974;50:456-464

12.   Liberthson RR, Pennington DG, Jacobs ML, Daggett WM. Coarctation of the aorta: Review of 234 patients and clarification of management problems. *The American journal of cardiology*. 1979;43:835-840

13.   Koller M, Rothlin M, Senning Å. Coarctation of the aorta: Review of 362 operated patients. Long-term follow-up and assessment of prognostic variables. *European heart journal*. 1987;8:670-679

14.   Jost CHA, Schaff HV, Connolly HM, Danielson GK, Dearani JA, Puga FJ, Warnes CA. Spectrum of reoperations after repair of aortic coarctation: Importance of an individualized approach because of coexistent cardiovascular disease. *Mayo Clinic Proceedings*. 2002;77:646-653

15.   Hamdan MA. Coarctation of the aorta: A comprehensive review. *Prevalence*. 2006;50:30

16.   Popescu BA, Jurcut R, Serban M, Parascan L, Ginghina C. Shone's syndrome diagnosed with echocardiography and confirmed at pathology. *European Journal of Echocardiography*. 2008;9:865-867

17.   Ganju NK, Kandoria A, Thakur S, Ganju SA. A constellation of cardiac anomalies: Beyond shone's complex. *Heart views: the official journal of the Gulf Heart Association*. 2016;17:23

18.   Celano V, Pieroni DR, Morera JA, Roland J-M, Gingell R. Two-dimensional echocardiographic examination of mitral valve abnormalities associated with coarctation of the aorta. *Circulation*. 1984;69:924-932

19.   Rosenquist GC. Congenital mitral valve disease associated with coarctation of the aorta: A spectrum that includes parachute deformity of the mitral valve. *Circulation*. 1974;49:985-993

20.   Omran A, Arifi AA, Mohamed A. Echocardiography in mitral stenosis. *Journal of the Saudi Heart Association*. 2011;23:51-58

21.   Ludman P, Yacoub M, Dancy M. Mitral valve prolapse and occult aortic coarctation. *Postgraduate medical journal*. 1990;66:834-837

22.   Easthope R, Tawes Jr RL, Bonham-Carter R, Aberdeen E, Waterston D. Congenital mitral valve disease associated with coarctation of the aorta: A report of 39 cases. *American heart journal*. 1969;77:743-754

23.   Cartier R, Ugolini P, Paquet E. Severe aortic insufficiency associated with left ventricular dysfunction and aortic coarctation. *Canadian journal of surgery*. 2002;45:213

24.   Becker AE, Becker MJ, Edwards JE. Anomalies associated with coarctation of aorta particular reference to infancy. *Circulation*. 1970;41:1067-1075

25.   Baumgartner H, Hung J, Bermejo J, Chambers JB, Evangelista A, Griffin BP, Iung B, Otto CM, Pellikka PA, Quiñones M. Echocardiographic assessment of valve stenosis: Eae/ase recommendations for clinical practice. *Journal of the American Society of Echocardiography*. 2009;22:1-23

26.   Wood WC, Wood JC, Lower RR, Bosher Jr LH, McCue CM. Associated coarctation of the aorta and mitral valve disease: Nine cases with surgical correction of both lesions in three. *The Journal of pediatrics*. 1975;87:217-220

27.   Warnes C. Bicuspid aortic valve and coarctation: Two villains part of a diffuse problem. 2003

28.   Mangoni AA, Koelling TM, Meyer GS, Akins CW, Fifer MA. Outcome following mitral valve replacement in patients with mitral stenosis and moderately reduced left ventricular ejection fraction. *European journal of cardio-thoracic surgery*. 2002;22:90-94

29.   Jashari H, Rydberg A, Ibrahimi P, Bajraktari G, Henein MY. Left ventricular response to pressure afterload in children: Aortic stenosis and coarctation: A

systematic review of the current evidence. *International journal of cardiology*. 2015;178:203-209

30.   Enriquez-Sarano M, Avierinos J-F, Messika-Zeitoun D, Detaint D, Capps M, Nkomo V, Scott C, Schaff HV, Tajik AJ. Quantitative determinants of the outcome of asymptomatic mitral regurgitation. *New England Journal of Medicine*. 2005;352:875-883

31.   Bekeredjian R, Grayburn PA. Valvular heart disease: Aortic regurgitation. *Circulation*. 2005;112:125-134

32.   Terzaki AK, Leachman RD, Ali MK, Hallman GL, Cooley DA. Congenital mitral incompetence and coarctation of aorta: Report of two cases treated surgically. *Thorax*. 1972;27:729-737

33.   Brown JW, Dunn JM, Brymer JF, Kirsh MM. Simultaneous treatment of aortic stenosis and coarctation by left thoracotomy with apical aortic conduit. *The Annals of thoracic surgery*. 1978;25:364-367

34.   Brauner RA, Laks H, Drinkwater Jr DC, Scholl F, McCaffery S. Multiple left heart obstructions (shone's anomaly) with mitral valve involvement: Long-term surgical outcome. *The Annals of thoracic surgery*. 1997;64:721-729

35.   Velinović M, Karan R, Kovačević-Kostić N, Obrenović-Kirćanski B, Stojimirov M, Milićević V, Nikolić D, Milić D. Aortic coarctation and associated cardiac lesions: Optimal therapeutic approach: Report of 2 cases. *Vojnosanitetski pregled*. 2019;76:1197-1202

36.   Teixeira AM, Reis-Santos K, Anjos R. Hybrid approach to severe coarctation and aortic regurgitation. *Cardiology in the Young*. 2005;15:525

37.   Mulay AV, Ashraf S, Watterson KG. Two-stage repair of adult coarctation of the aorta with congenital valvular lesions. *The Annals of thoracic surgery*. 1997;64:1309-1311

38.   Koletsis E, Ekonomidis S, Panagopoulos N, Tsaousis G, Crockett J, Panagiotou M. Two stage hybrid approach for complex aortic coarctation repair. *Journal of Cardiothoracic Surgery*. 2009;4:10

39.   Bolling SF, Iannettoni MD, Dick II M, Rosenthal A, Bove EL. Shone's anomaly: Operative results and late outcome. *The Annals of thoracic surgery*. 1990;49:887-893

40.   Zhang H, Zhu K, Yang S, Zhai J, Zhou T, Sun X, Wang C. Bicuspid aortic valve with critical coarctation of the aorta: Single-or two-stage operation? *Journal of thoracic disease*. 2018;10:4353

41.   Kumar S, Goud A, Versha F, Mukherjee A, Pai R. Coarctation of aorta in an adult with severe aortic stenosis: Deciding on the optimal approach. *Journal of the American College of Cardiology*. 2018;71:A2160-A2160

42.   Keshavarz-Motamed Z, Garcia J, Pibarot P, Larose E, Kadem L. Modeling the impact of concomitant aortic stenosis and coarctation of the aorta on left ventricular workload. *Journal of biomechanics*. 2011;44:2817-2825

43.   Richter Y, Edelman ER. Cardiology is flow. 2006

44.   Anvari S, Nambiar S, Pang J, Maftoon N. Computational models and simulations of cancer metastasis. *Archives of Computational Methods in Engineering*. 2021:1-23

45.   Sadeghi R, Khodaei S, Ganame J, Keshavarz-Motamed Z. Towards non-invasive computational-mechanics and imaging-based diagnostic framework for personalized cardiology for coarctation. *Scientific Reports*. 2020;10:1-19

46.   Keshavarz-Motamed Z, Rikhtegar Nezami F, Partida RA, Nakamura K, Staziaki PV, Ben-Assa E, Ghoshhajra B, Bhatt AB, Edelman ER. Elimination of transcoarctation pressure gradients has no impact on left ventricular function or aortic shear stress after intervention in patients with mild coarctation. *JACC: Cardiovascular Interventions*. 2016;9:1953-1965

47.   Karaosmanoglu AD, Khawaja RDA, Onur MR, Kalra MK. Ct and mri of aortic coarctation: Pre-and postsurgical findings. *American Journal of Roentgenology*. 2015;204:W224-W233

48.   Keshavarz-Motamed Z. A diagnostic, monitoring, and predictive tool for patients with complex valvular, vascular and ventricular diseases. *Scientific Reports*. 2020;10:1-19

49.   Mittal R, Simmons S, Udaykumar H. Application of large-eddy simulation to the study of pulsatile flow in a modeled arterial stenosis. *Journal of biomechanical engineering*. 2001;123:325-332

50.   Skordos P. Initial and boundary conditions for the lattice boltzmann method. *Physical Review E*. 1993;48:4823

51.   Heuveline V, Krause MJ, Latt J. Towards a hybrid parallelization of lattice boltzmann methods. *Computers & Mathematics with Applications*. 2009;58:1071-1080

52.   Henn T, Heuveline V, Krause MJ, Ritterbusch S. Aortic coarctation simulation based on the lattice boltzmann method: Benchmark results. *International Workshop on Statistical Atlases and Computational Models of the Heart*. 2012:34-43

53. Mirzaee H, Henn T, Krause MJ, Goubergrits L, Schumann C, Neugebauer M, Kuehne T, Preusser T, Hennemuth A. Mri-based computational hemodynamics in patients with aortic coarctation using the lattice boltzmann methods: Clinical validation study. *Journal of Magnetic Resonance Imaging*. 2017;45:139-146

54. Jin S, Oshinski J, Giddens DP. Effects of wall motion and compliance on flow patterns in the ascending aorta. *Journal of biomechanical engineering*. 2003;125:347-354

55. Keshavarz-Motamed Z, Edelman ER, Motamed PK, Garcia J, Dahdah N, Kadem L. The role of aortic compliance in determination of coarctation severity: Lumped parameter modeling, in vitro study and clinical evaluation. *Journal of biomechanics*. 2015;48:4229-4237

56. Baiocchi M, Barsoum S, Khodaei S, de la Torre Hernandez JM, Valentino SE, Dunford EC, MacDonald MJ, Keshavarz-Motamed Z. Effects of choice of medical imaging modalities on a non-invasive diagnostic and monitoring computational framework for patients with complex valvular, vascular, and ventricular diseases who undergo transcatheter aortic valve replacement. *Frontiers in Bioengineering and Biotechnology*. 2021:389

57. Bouzidi Mh, Firdaouss M, Lallemand P. Momentum transfer of a boltzmann-lattice fluid with boundaries. *Physics of fluids*. 2001;13:3452-3459

58. Nathen P, Gaudlitz D, Krause M, Kratzke J. An extension of the lattice boltzmann method for simulating turbulent flows around rotating geometries of arbitrary shape. *21st AIAA Computational Fluid Dynamics Conference. American Institute of Aeronautics and Astronautics*. 2013

59. Stankovic Z, Allen BD, Garcia J, Jarvis KB, Markl M. 4d flow imaging with mri. *Cardiovascular diagnosis and therapy*. 2014;4:173

60. Van Ooij P, Garcia J, Potters WV, Malaisrie SC, Collins JD, Carr JC, Markl M, Barker AJ. Age-related changes in aortic 3d blood flow velocities and wall shear stress: Implications for the identification of altered hemodynamics in patients with aortic valve disease. *Journal of Magnetic Resonance Imaging*. 2016;43:1239-1249

61. Marlevi D, Ruijsink B, Balmus M, Dillon-Murphy D, Fovargue D, Pushparajah K, Bertoglio C, Colarieti-Tosti M, Larsson M, Lamata P. Estimation of cardiovascular relative pressure using virtual work-energy. *Scientific reports*. 2019;9:1-16

62. Hassanabad AF, Burns F, Bristow MS, Lydell C, Howarth AG, Heydari B, Gao X, Fedak PW, White JA, Garcia J. Pressure drop mapping using 4d flow mri in patients with bicuspid aortic valve disease: A novel marker of valvular obstruction. *Magnetic resonance imaging*. 2020;65:175-182

63. Garcia J, Barker AJ, Markl M. The role of imaging of flow patterns by 4d flow mri in aortic stenosis. *JACC: Cardiovascular Imaging*. 2019;12:252-266

64. Garcia D. A fast all-in-one method for automated post-processing of piv data. *Experiments in fluids*. 2011;50:1247-1259

65. Garcia D. Robust smoothing of gridded data in one and higher dimensions with missing values. *Computational statistics & data analysis*. 2010;54:1167-1178

66. Shen J, Faruqi AH, Jiang Y, Maftoon N. Mathematical reconstruction of patient-specific vascular networks based on clinical images and global optimization. *IEEE Access*. 2021;9:20648-20661

67. Keshavarz-Motamed Z, Garcia J, Gaillard E, Capoulade R, Le Ven F, Cloutier G, Kadem L, Pibarot P. Non-invasive determination of left ventricular workload in patients with aortic stenosis using magnetic resonance imaging and doppler echocardiography. *PLoS One*. 2014;9

68. Asaadi M, Mawad W, Djebbari A, Keshavardz-Motamed Z, Dahdah N, Kadem L. On left ventricle stroke work efficiency in children with moderate aortic valve regurgitation or moderate aortic valve stenosis. *Pediatric Cardiology*. 2021:1-9

69. Ben-Assa E, Brown J, Keshavarz-Motamed Z, Jose M, Leiden B, Olender M, Kallel F, Palacios IF, Inglessis I, Passeri JJ. Ventricular stroke work and vascular impedance refine the characterization of patients with aortic stenosis. *Science translational medicine*. 2019;11:eaaw0181

70. Benevento E, Djebbari A, Keshavarz-Motamed Z, Cecere R, Kadem L. Hemodynamic changes following aortic valve bypass: A mathematical approach. *PloS one*. 2015;10:e0123000

71. Keshavarz-Motamed Z, Garcia J, Gaillard E, Maftoon N, Di Labbio G, Cloutier G, Kadem L. Effect of coarctation of the aorta and bicuspid aortic valve on flow dynamics and turbulence in the aorta using particle image velocimetry. *Experiments in fluids*. 2014;55:1-16

72. Keshavarz-Motamed Z, Garcia J, Maftoon N, Bedard E, Chetaille P, Kadem L. A new approach for the evaluation of the severity of coarctation of the aorta using doppler velocity index and effective orifice area: In vitro validation and clinical implications. *Journal of biomechanics*. 2012;45:1239-1245

73. Keshavarz-Motamed Z, Khodaei S, Rikhtegar Nezami F, Amrute JM, Lee SJ, Brown J, Ben-Assa E, Garcia Camarero T, Ruano Calvo J, Sellers S. Mixed valvular disease following transcatheter aortic valve replacement: Quantification and systematic differentiation using clinical measurements and image-based patient-specific in silico modeling. *Journal of American Heart Association*. 2020;9:e015063

74. Khodaei S, Henstock A, Sadeghi R, Sellers S, Blanke P, Leipsic J, Emadi A, Keshavarz-Motamed Z. Personalized intervention cardiology with transcatheter aortic valve replacement made possible with a non-invasive monitoring and diagnostic framework. *Scientific Reports*. 2021;11:1-28

75. Khodaei S, Sadeghi R, Blanke P, Leipsic J, Emadi A, Keshavarz-Motamed Z. Towards a non-invasive computational diagnostic framework for personalized cardiology of transcatheter aortic valve replacement in interactions with complex valvular, ventricular and vascular disease. *International Journal of Mechanical Sciences*. 2021;202:106506

76. Spain MG, Smith MD, Grayburn PA, Harlamert EA, Demaria AN, O'Brien M, Kwan OL. Quantitative assessment of mitral regurgitation by doppler color flow imaging: Angiographic and hemodynamic correlations. *Journal of the American College of Cardiology*. 1989;13:585-590

77. Wendell DC, Samyn MM, Cava JR, Ellwein LM, Krolikowski MM, Gandy KL, Pelech AN, Shadden SC, LaDisa Jr JF. Including aortic valve morphology in computational fluid dynamics simulations: Initial findings and application to aortic coarctation. *Medical engineering & physics*. 2013;35:723-735

78. Siu SC, Silversides CK. Bicuspid aortic valve disease. *Journal of the American College of Cardiology*. 2010;55:2789-2800

79. Hope MD, Meadows AK, Hope TA, Ordovas KG, Reddy GP, Alley MT, Higgins CB. Evaluation of bicuspid aortic valve and aortic coarctation with 4d flow magnetic resonance imaging. *Circulation*. 2008;117:2818-2819

80. Davies RR, Kaple RK, Mandapati D, Gallo A, Botta Jr DM, Elefteriades JA, Coady MA. Natural history of ascending aortic aneurysms in the setting of an unreplaced bicuspid aortic valve. *The Annals of thoracic surgery*. 2007;83:1338-1344

81. Ayad RF, Grayburn PA, Ko JM, Filardo G, Roberts WC. Accuracy of two-dimensional echocardiography in determining aortic valve structure in patients> 50 years of age having aortic valve replacement for aortic stenosis. *The American journal of cardiology*. 2011;108:1589-1599

82. Kim YY, Andrade L, Cook SC. Aortic coarctation. *Cardiology Clinics*. 2020;38:337-351

83. Seifert BL, DesRochers K, Ta M, Giraud G, Zarandi M, Gharib M, Sahn DJ. Accuracy of doppler methods for estimating peak-to-peak and peak instantaneous gradients across coarctation of the aorta: An in vitro study. *Journal of the American Society of Echocardiography*. 1999;12:744-753

84. Brüning J, Hellmeier F, Yevtushenko P, Kühne T, Goubergrits L. Uncertainty quantification for non-invasive assessment of pressure drop across a coarctation of the aorta using cfd. *Cardiovascular engineering and technology*. 2018;9:582-596

85. Keshavarz-Motamed Z, Kadem L. 3d pulsatile flow in a curved tube with coexisting model of aortic stenosis and coarctation of the aorta. *Medical engineering & physics*. 2011;33:315-324

86. Lavon K, Halevi R, Marom G, Ben Zekry S, Hamdan A, Joachim Schäfers H, Raanani E, Haj-Ali R. Fluid–structure interaction models of bicuspid aortic valves: The effects of nonfused cusp angles. *Journal of biomechanical engineering*. 2018;140:031010

87. de Oliveira DM, Abdullah N, Green NC, Espino DM. Biomechanical assessment of bicuspid aortic valve phenotypes: A fluid–structure interaction modelling approach. *Cardiovascular Engineering and Technology*. 2020;11:431-447

Chapter 5: Impact of extra-anatomical bypass on coarctation fluid dynamics using patient-specific lumped parameter and Lattice Boltzmann modeling

Reza Sadeghi[1], Benjamin Tomka[1], Krishna Gandhi[1], Julia Garcia[2,3,4,5], Zahra Keshavarz-Motamed*[1,6,7]

1. Department of Mechanical Engineering, McMaster University, Hamilton, ON, Canada
2. Stephenson Cardiac Imaging Centre, Libin Cardiovascular Institute of Alberta, Calgary, AB, Canada
3. Department of Radiology, University of Calgary, Calgary, AB, Canada
4. Department of Cardiac Sciences, University of Calgary, Calgary, AB, Canada
5. Alberta Children's Hospital Research Institute, Calgary, AB, Canada
6. School of Biomedical Engineering, McMaster University, Hamilton, ON, Canada
7. School of Computational Science and Engineering, McMaster University, Hamilton, ON, Canada

This paper was submitted and is under review.

* Correspondence author

5.1   Abstract

Background: Accurate hemodynamic analysis is not only crucial for successful diagnosis of coarctation of the aorta (COA), but intervention decisions also heavily rely on the hemodynamics assessment in both pre and post intervention states to minimize patient risks. Despite ongoing advances in surgical techniques for COA treatments, the impacts of extra-anatomic bypass grafting, a surgical technique to treat COA, on the aorta are not always benign. Our objective was to investigate the impact of bypass grafting on aortic hemodynamics.

Methods: To investigate hemodynamics, we developed a patient-specific computational-mechanics framework, validated against clinical cardiac catheterization data and 4-D flow magnetic resonance imaging.

Results: Our results demonstrate that bypass grafting improved hemodynamic metrics (e.g., reduction in flow velocities, and turbulent characteristics) in some patients, however, the hemodynamic conditions worsened in others (e.g., patient #1; maximum velocity, pre-intervention: 1.9 m/s; post-intervention: 1.74 m/s; maximum turbulent kinetic energy, pre-intervention: 0.81 mJ, post-intervention: 1.15 mJ). Moreover, bypass grafting does not always alleviate high wall shear stress through the aorta (e.g., patient #1; maximum surface integral of wall shear stress, pre-intervention: 0.0222 N/m^2, post-intervention: 0.0319 N/m^2).

Conclusions: We concluded that bypass graft may lead to pseudoaneurysm formation and potential aortic rupture as well as intimal hyperplasia due to the persistent abnormal and

irregular aortic hemodynamics. Moreover, post-intervention, exposures of endothelial cells to high shear stress may lead to arterial remodeling, aneurysm, rupture and dissection.

Keywords: Coarctation, bypass graft, aortic fluid dynamics, hemodynamic metrics, turbulent characteristics

5.2   Introduction

Coarctation of the aorta (COA) is a common congenital heart defect (CHD) which is recognized as a general arteriopathy involving a discrete stenosis or a longer, hypoplastic segment of the aortic isthmus[1,2]. COA is the 6th most prevalent CHD, occurring in 5-8% of all cases with an approximate incidence of 3/10000 livebirths[1-6]. COA imposes significant afterload on the left ventricle (LV) which results in elevated wall stress, LV hypertrophy, LV dysfunction, the development of arterial collaterals, upper body hypertension, flow disturbance in the thoracic aorta, and decreased perfusion to the lower body[2,5]. Further impacts of COA include aortic dissection, aortic rupture, myocardial infarction, and heart failure[5,7]. If left untreated, COA carries dismal prognosis, several studies have shown an average survival age of 30-35 years, with a mortality rate of 75% by age 46[3,8,9]. The appropriate surgical technique for COA repair often remains unclear for adult patients[10]. Surgical techniques to treat COA include resection with end-to-end anastomosis, prosthetic patch aortoplasty, subclavian flap aortoplasty, interposition grafting and extra-anatomic bypass grafting[2,4,11,12].

Extra-anatomical bypass grafting has been recommended in some of these complex cases and may represent a viable option for a single-stage approach[4,5,10,12-15]. Extra-anatomic bypass grafting is a surgical technique typically performed via median sternotomy and can be performed for isolated cases of COA as well as cases where additional cardiovascular pathologies are present[11,12]. Furthermore, surgical treatment for COA carries some risk for spinal cord injury, occurring in approximately 0.5% of patients being operated on for coarctation[16], studies have shown that extra-anatomic bypass minimizes the risk of paraplegia[2,15]. When performing bypass grafting, proximally, the prosthetic conduit is anastomosed to the ascending aorta or the subclavian artery, distally the conduit is attached to the descending aorta[4,14,17]. This technique leaves the stenosed aorta in situ, but is able to provide adequate blood flow to the distal aorta[14]. While extra-anatomic bypass can be performed with low risk[15], some adverse cases do exist and include prosthetic graft pseudoaneurysm, intimal hyperplasia and potential re-COA, all of which may require reoperation[18-24].

The development and progression of cardiovascular diseases can often be explained by abnormal hemodynamics characterized by disturbed or turbulent flow, and adverse vascular biomechanics[25-31]. Blood flow often determines the form and function of the heart and surrounding vascular network and can dictate the functional and structural response of repair [29,31,32]. Blood flow analysis can be greatly useful for diagnostic and monitoring purposes as disturbed flow strongly influences vascular pathologies[27,32]. Moreover, there is currently no consensus on the ideal treatment method for isolated,

complex, or recurrent COA[33,34], and hemodynamics may provide insight to the optimal treatment method on a patient-specific basis.

A clinically useful tool that can be used to accurately assess fluid dynamics in COA patients pre- and post- bypass grafting should satisfy the following requirements:

(4) The local fluid dynamics are influenced by the conditions downstream and upstream of coarctation. Therefore, in addition to performing the 3-D blood flow calculations in the patient-specific geometry, imposing accurate patient-specific flow and pressure boundary conditions is critically important for a computational diagnostic framework. This not only gives patient-specific flow and pressure conditions to the local flow, but also enables providing diagnostic information about the global circulatory physiology.

(5) The patient-specific boundary conditions should be obtained *non-invasively* in each patient because obtaining them invasively (e.g., with catheterization) contradicts the whole purpose of the computational framework.

(6) To reliably augment the current clinical diagnostics capabilities with calculations of blood flow through COA, the computational diagnostic framework should be fast enough to provide results in a matter of minutes rather than days.

There have been attempts for quantifying blood flow through artery bypass grafts using conventional macroscopic numerical methods based on the discretization of Navier–Stokes equations (finite difference method, finite volume method, finite element method, etc.)[18,19,35-39]. However, none of these models can satisfy Requirements #1 & #2 as they

do not have patient-specific boundary conditions, patient-specific geometry etc[18,19,35-39]. Moreover, none of these models can satisfy Requirement #3 above because the conventional methods need days of calculations and therefore, they are not feasible for clinical diagnosis[18,19,35-39].

"Cardiology is flow"[32] and indeed the essential sources of cardiovascular mortality and morbidity can be explained on the basis of abnormal fluid dynamics, leading to the development and progression of cardiovascular disease[25,26,31,40]. To effectively evaluate risk status and create guidelines for intervention, precise quantification of a*ortic fluid dynamics*, is required. For this purpose and to satisfy Requirements #1 to #3, we developed an innovative patient-specific, image-based, computational-mechanics framework that integrates the local hemodynamics with the global circulatory cardiovascular system using the Lattice Boltzmann method (LBM) along with Doppler-based lumped parameter modeling (LPM) to investigate the impact of bypass grafts on aortic fluid dynamics in 3 patients with COA. Our lumped parameter algorithm uses a limited number of parameters that can be reliably and non-invasively measured using Doppler echocardiography and sphygmomanometer and calculates patient-specific Boundary conditions (Requirements #1 & #2). Lattice Boltzmann method (LBM), rooted in mesoscopic kinetic equations, has been developed as a powerful and fast alternative to computationally intensive conventional methods for fluid dynamics simulations because of its simplicity, handling of complex flow phenomena, efficient executions, and the fact that LBM equations are intrinsically parallelizable (Requirement #3)[31,41].

5.3   Methods

In this study, we simulated the 3-D blood flow dynamics in patients with COA pre- and post-intervention using our developed patient-specific, image-based, computational fluid dynamics framework using 3-D Lattice Boltzmann method (large eddy simulation, Smagorinsky subgrid scale model) and Doppler-based lumped parameter modeling (Figure 5-1, Panel A, schematic diagram). This framework is based on 3-D lattice Boltzmann method (LBM; Smagorinsky subgrid scale model) and Doppler-based, patient-specific, lumped parameter modeling[29,42] as implemented in the open-source OpenLB library with some supplements as explained below. Our developed patient-specific Doppler-based lumped-parameter algorithm includes several sub-models which allow for the analysis of complex coarctation disease when coexistent with the other valvular, vascular and ventricular disease including the following: 1) left atrium, 2) left ventricle, 3) aortic valve, 4) mitral valve, 5) coarctation of the aorta, 6) systemic circulation, and 7) pulmonary circulation (Figure 5-1, Panel A). The input parameters for our patient-specific Doppler-based lumped parameter algorithm can all be reliably measured using two non-invasive techniques: Doppler echocardiography and sphygmomanometers. All input parameters are as follows: forward left ventricular outflow tract stroke volume, heart rate, ejection time, ascending aorta area, left ventricular outflow tract area, aortic valve effective orifice area, mitral valve effective orifice area, COA severity, grading of aortic and mitral valves regurgitation severity, and systolic and diastolic blood pressures. Calculations of this computational fluid dynamics framework
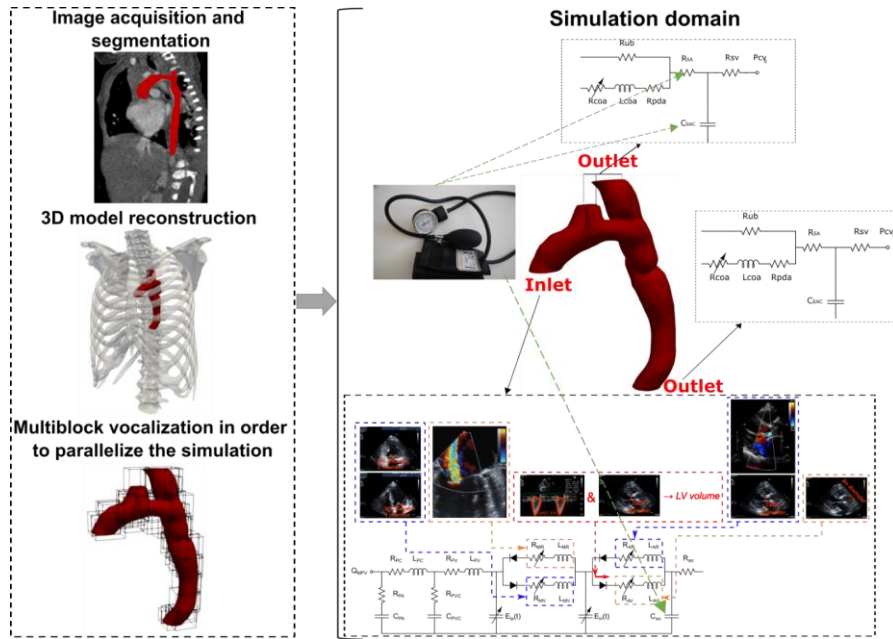
(a)
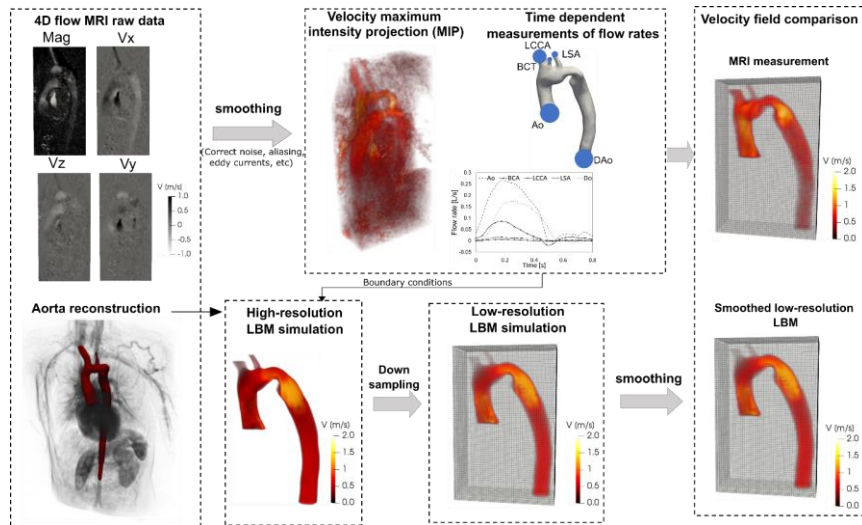
(b)

Figure 5-1. Reconstructed geometry and simulation domain. Schematic diagram of our developed patient-specific, image-based, computational-mechanics framework that dynamically couples the local hemodynamics with the global circulatory cardiovascular system to investigate the impact of COA and bypass grafting on fluid dynamics in these patients. We used CT images from patients to segment and reconstruct the 3D geometries of the complete aorta. These 3-D geometries were used for investigating hemodynamics using computational fluid dynamics. Local flow dynamics are greatly influenced by

upstream and downstream flow conditions that are absent in the flow simulation domain. A lumped-parameter model simulates the function of the left side of the heart. Time-dependent inlet flow at ascending aorta and outlet pressure at descending aorta position were obtained from lumped parameter modeling and applied as boundary conditions. Boundary conditions of the aortic branches were adjusted to match the flow distribution; (b) We compared 4-D flow MRI data and results of our computational framework. The 3-D geometry of the complete aorta was reconstructed using MRI images and the entire volume of Down-sampled LBM data was smoothed (see *Four-dimensional flow magnetic resonance imaging (4-D flow MRI* section for more details).

were validated against 4-D flow MRI measurements (Figure 5-1, Panel A, schematic diagram; Figures 5-2, Panels A & B, results).

5.3.1 Lattice Boltzmann method (LBM)

In a healthy vascular system, blood flow is mostly laminar, however, blood flow becomes distally turbulent under pathophysiological conditions. Modelling blood flow is typically performed based on the Reynolds-averaged Navier Stokes (RANS) equations, however, this method has noticeable limitations when modelling pulsatile flows [43]. Direct numerical simulations (DNS) are limited to a low Reynolds number and put a major burden on computing. Large eddy simulation (LES) is an additional approach between DNS and RANS that well suited for computational modeling of turbulent vascular flows with a high potential in modeling the physiological low-Reynolds transitional flows [29]. In this study, we used a 3-D LBM-based computational fluid dynamics approach using LES (Smagorinsky subgrid scale model) to simulate blood flow through the vascular system.

❖ *Governing equations*

The simplest form of LBM equations are based on the *Bhatnagar-Gross-Krook* (BGK) approximation with single relaxation time (SRT) [44]. The discretized form of Boltzmann equation based on BGK approximation is as follows [45]:

$$f_\alpha(x + e_\alpha \delta t, t + \delta t) - f_\alpha(x, t) = -1/\tau \ (f_\alpha(x, t) - f_\alpha^{eq}(x, t)) \tag{1}$$

For the BGK-LBM model with Q velocities, a set of distribution functions $\{f_\alpha | \alpha = 0, 1, ..., Q - 1\}$ is defined on each lattice node (x). τ, t and f^{eq} represent the relaxation time, discrete time and Maxwell-Boltzmann equilibrium distribution function, respectively. The subscript α depends on the number of lattice vectors.

The LBM follows D_xQ_y reference in which x represents the number of dimensions and y is the number of particle velocities. In order to simulate blood flow across the aorta, we considered the three-dimensional nineteen-velocity model, D_3Q_{19} [31]. The discrete velocity vectors in D_3Q_{19} are as follows [31]:

$$e_0, e_1, e_2, e_3, e_4, e_5, e_6, e_7, e_8, e_9, e_{10}, e_{11}, e_{12}, e_{13}, e_{14}, e_{15}, e_{16}, e_{17}, e_{18} =$$

$$\begin{bmatrix} 0 & 1 & 0 & -1 & 0 & 0 & 0 & 1 & -1 & -1 & 1 & 1 & 1 & -1 & -1 & 0 & 0 & 0 & 0 \\ 0 & 0 & 1 & 0 & -1 & 0 & 0 & 1 & 1 & -1 & -1 & 0 & 0 & 0 & 0 & 1 & 1 & -1 & -1 \\ 0 & 0 & 0 & 0 & 0 & 1 & -1 & 0 & 0 & 0 & 0 & 1 & -1 & -1 & 1 & 1 & -1 & -1 & 1 \end{bmatrix}^{(2)}$$

The Maxwell–Boltzmann distribution function (f_α^{eq}) for the lattice speed of sound $c_s = 1/\sqrt{3}$ is defined as follows [31]:

$$f_\alpha^{eq} = w_\alpha \rho \left[1 + \frac{e_\alpha \cdot u}{c_s^2} + \frac{(e_\alpha \cdot u)^2}{2c_s^4} - \frac{(u \cdot u)}{2c_s^2} \right] \tag{3}$$

In Equation (3), u is defined as the velocity, w_α represents the weighting coefficients given by $w_0 = 1/3$, $w_{1\sim6} = 2/36$ and $w_{7\sim18} = 1/36$ for D$_3$Q$_{19}$ model, e_α is the discrete velocity vector in α direction ($\alpha= 0, \dots, 18$), and ρ represents the lattice density.

Various defects of BGK models exist including fixed ratio of kinematic, bulk viscosities and a fixed Prandtl number which cause instabilities at high Reynolds numbers [46]. To overcome these limitations, a multi-relaxation time (MRT), LBM-based model was implemented. In this regard, Equation (1) was modified to Equation (4) considering MRT scheme as follows:

$$f_\alpha(x + e_\alpha \delta t, t + \delta t) - f_\alpha(x, t) = -M_{\alpha\gamma}^{-1}\hat{S}_{\gamma k}(m_k(x, t) - m_k^{eq}(x, t)) \tag{4}$$

where $m_k(x, t)$ represents vectors of moments and their equilibrium functions $m_k^{eq}(x, t)$. M and $\hat{S}$ are the transform matrix and collision matrix, respectively.

Mappings between moment and distribution functions were performed by linear transformation as follows:

$$m = M.\,[f_0, f_2, \dots, f_{18}]^T \text{ and } [f_0, f_2, \dots, f_{18}] = M^{-1}m \tag{5}$$

The Equilibrium distribution function must satisfy conservation of mass and momentum leading to Equations (6) and (7), respectively[47]:

$$\rho = \sum_{\alpha=0}^{\alpha=18} f_\alpha^{eq} = \sum_{\alpha=0}^{\alpha=18} f_\alpha \tag{6}$$

$$Pu = \sum_{\alpha=0}^{\alpha=18} f_\alpha^{eq} \, e_\alpha = \sum_{\alpha=0}^{\alpha=18} f_\alpha \, e_\alpha \tag{7}$$

The transformation matrix M for D3Q19 is defined as the following:

$$(8)$$

$$
M =
\begin{bmatrix}
1 & 1 & 1 & 1 & 1 & 1 & 1 & 1 & 1 & 1 & 1 & 1 & 1 & 1 & 1 & 1 \\
-3 & -11 & -11 & -11 & -11 & -11 & -11 & 8 & 8 & 8 & 8 & 8 & 8 & 8 & 8 & 8 \\
12 & -4 & -4 & -4 & -4 & -4 & -4 & 1 & 1 & 1 & 1 & 1 & 1 & 1 & 1 & 1 \\
0 & 1 & -1 & 0 & 0 & 0 & 0 & 1 & -1 & 1 & -1 & 1 & -1 & 1 & -1 & 0 \\
0 & -4 & 4 & 0 & 0 & 0 & 0 & 1 & -1 & 1 & -1 & 1 & -1 & 1 & -1 & 0 \\
0 & 0 & 0 & 1 & -1 & 0 & 0 & 1 & 1 & -1 & -1 & 0 & 0 & 0 & 0 & 1 \\
0 & 0 & 0 & -4 & 4 & 0 & 0 & 1 & 1 & -1 & -1 & 0 & 0 & 0 & 0 & 1 \\
0 & 0 & 0 & 0 & 0 & 1 & -1 & 0 & 0 & 0 & 0 & 1 & 1 & -1 & -1 & 1 \\
0 & 0 & 0 & 0 & 0 & -4 & 4 & 0 & 0 & 0 & 0 & 1 & 1 & -1 & -1 & 1 \\
0 & 2 & 2 & -1 & -1 & -1 & -1 & 1 & 1 & 1 & 1 & 1 & 1 & 1 & 1 & -2 \\
0 & -4 & -4 & 2 & 2 & 2 & 2 & 1 & 1 & 1 & 1 & 1 & 1 & 1 & 1 & -2 \\
0 & 0 & 0 & 1 & 1 & -1 & -1 & 1 & 1 & 1 & 1 & -1 & -1 & -1 & -1 & 0 \\
0 & 0 & 0 & -2 & -2 & 2 & 2 & 1 & 1 & 1 & 1 & -1 & -1 & -1 & -1 & 0 \\
0 & 0 & 0 & 0 & 0 & 0 & 0 & 1 & -1 & -1 & 1 & 0 & 0 & 0 & 0 & 0 \\
0 & 0 & 0 & 0 & 0 & 0 & 0 & 0 & 0 & 0 & 0 & 0 & 0 & 0 & 0 & 1 \\
0 & 0 & 0 & 0 & 0 & 0 & 0 & 0 & 0 & 0 & 0 & 1 & -1 & -1 & 1 & 0 \\
0 & 0 & 0 & 0 & 0 & 0 & 0 & 1 & -1 & 1 & -1 & -1 & 1 & -1 & 1 & 0 \\
0 & 0 & 0 & 0 & 0 & 0 & 0 & -1 & -1 & 0 & 1 & 0 & 0 & 0 & 0 & 1 \\
0 & 0 & 0 & 0 & 0 & 0 & 0 & 0 & 0 & 0 & 0 & 1 & 1 & -1 & -1 & -1 \\
\end{bmatrix}
$$

The corresponding macroscopic moments vector are:

$$(9)$$

$$m_\alpha = (m_0, m_1, \ldots, m_{18})^\mathsf{T}$$

Diagonal matrix $\hat{S}$ in Equation (4) is defined as follows:

$$(10)$$

$$\hat{S} = \mathrm{diag}\,(0, 1.19, 1.4, 0, 1.2, 0, 1.2, v, 1.4, v, v, v, 1.98, 1.98, 1.98)$$

where v is physical viscosity and (m^{eq}) is equilibrium moments matrix, as shown below:

$$(11)$$

$$m_k^{eq} = \left(m_0{}^{eq}, m_1{}^{eq}, \ldots, m_{18}^{eq}\right)^\mathsf{T}$$

The equilibrium moments in Equation (11) were obtained as follows:

$$m_0^{eq} = \rho, m_1^{eq} = -11\rho + \frac{19}{\rho}\left(j_x{}^2 + j_y{}^2 + j_z{}^2\right), m_2^{eq} = \frac{-475}{63}\frac{1}{\rho}\left(j_x{}^2 + j_y{}^2 + j_z{}^2\right) \tag{12}$$

$$m_3^{eq} = j_x, m_4^{eq} = -\frac{2}{3}j_x, m_5^{eq} = j_y, m_6^{eq} = -\frac{2}{3}j_y, m_7^{eq} = j_z, \tag{13}$$

$$m_8^{eq} = -\frac{2}{3}j_z, m_9^{eq} = \frac{1}{\rho}\left[2j_x^2 - \left(j_y^2 + j_z^2\right)\right], \tag{14}$$

$$m_{10}^{eq} = 0, , m_{11}^{eq} = \frac{1}{\rho}\left[j_y^2 - j_z^2\right], m_{12}^{eq} = 0, \tag{15}$$

$$m_{13}^{eq} = \frac{1}{\rho}j_x j_y, m_{14}^{eq} = \frac{1}{\rho}j_y j_z, m_{15}^{eq} = \frac{1}{\rho}j_x j_z, \tag{16}$$

$$m_{16}^{eq} = m_{17}^{eq} = m_{18}^{eq} = 0, \tag{17}$$

The momentum $j = \left(j_x, j_y, j_z\right)$ was defined as follows:

$$j_x = \rho u_x, j_y = \rho u_y, j_z = \rho u_z \tag{18}$$

❖ *Lattice Boltzmann method & Large Eddy simulation*

Turbulent modeling was performed via Large Eddy Simulation employing the Smagorinsky subgrid scale model. The physical viscosity is a superposition of the molecular kinematic viscosity (v_{mol}) and turbulent viscosity (v_{turb}), related to the length scale or lattice size (Δ_x). Collision time (τ) was therefore altered as follows [48]:

$$\tau = \tau_{mol} + \tau_{turb} \tag{19}$$

The molecular and turbulent collision time in equation (19) were obtained as follows:

$$\tau_{mol} = 3v_{mol} + 0.5 \tag{20}$$

$$\tau_{turb} = 0.5(\sqrt{\tau_{mol}^2 + \left((C_s\Delta_x)^2 \frac{\Delta t}{C_s} 4\sqrt{2\tau\overline{\Pi}}\right)} - \tau_{mol} \tag{21}$$

C_s represents the Smagorinsky constant and $\overline{\Pi}$ is the magnitude of second-order non equilibrium moment. Total viscosity, v, is given as [48]:

$$v = v_{mol} + v_{turb} = \frac{1}{3}\left(\tau - \frac{1}{2}\right)c^2\delta_t = \frac{1}{3}\left(\tau_{mol} + \tau_{turb} - \frac{1}{2}\right)c^2\delta_t \tag{22}$$

❖ *Modeling surface curvature near the wall of complex geometries*

An interpolated bounce-back scheme proposed by Bouzidi et al. [49] was used in order to treat boundaries of inclined and complicated geometry. To evaluate the post-propagation state of fluid node A next to a curved solid wall, the distribution function used for this technique [31] was defined as follows:

$$f_{\overline{\alpha}}(x_A, t + \Delta t) = \begin{cases} 2qf_\alpha^c(x_A, t) - (1 - 2q)f_\alpha^c(x_E, t) & q < \frac{1}{2} \\ \frac{1}{2q}f_\alpha^c(x_A, t) + \frac{(2q-1)}{2q}f_\alpha^c(x_A, t) & q \geq \frac{1}{2} \end{cases} \tag{23}$$

where $f_{\overline{\alpha}}(x_A, t + \Delta t)$ represents the post-collision and post-propagation state of the distribution function at time $(t + \Delta t)$ and the point x_A. f_α^c is the value of the distribution function after a collision and before propagation state of the fluid node; the factor q represents the normalized distance from the wall [31].

❖ *Wall shear stress*

Wall shear stress (WSS) is defined as the frictional force induced by fluid moving along a solid wall. The total stress tensor for the fluid is as follows:

$$T_{ij} = -p.\delta_{ij} + \sigma_{ij} \tag{24}$$

where p, δ_{ij} and σ_{ij} represent pressure, Kronecker symbol and contribution from the viscous force, respectively. $T_{ij}n_j$ represents the stress on the boundary surface element with normal vector $\vec{n}$. The wall stress vector, $\vec{\tau}$, is computed as:

$$\tau_i = T_{ij}n_j - (n_j T_{kj} n_k)n_i \tag{25}$$

The total stress T_{ij} can be replaced by σ_{ij} since the projection of normal stress $(p.\delta_{ij})$ on the tangential plane is zero. The viscouse stress for a Newtonian fluid is proportional to the strain rate tensor $(\sigma_{ij} = 2\mu\varepsilon_{ij})$[50,51] and is as follows:

$$\varepsilon_{ij} = -\frac{1}{2\rho\tau c_s^2}\Pi_{ij} \tag{26}$$

where Π_{ij} represents a second order non equilibrium moment that can be computed locally from the particle distribution *functions*.

❖ *Model properties and boundary conditions*

Flow conditions upstream and downstream to the local aortic region are heavily influential on local flow dynamics and must be accounted for. Additionally, the proper

choice of boundary conditions is crucial as they are also influential on the accuracy of flow simulations. Blood was assumed to be a Newtonian and incompressible fluid with dynamic viscosity and density of 0.0035 Pa·s and 1050 kg/m^3, respectively. A lumped-parameter model (Figure 5-1) that simulated the function of the left side of the heart was used to impose the time-dependent inlet flow at the ascending aorta cross section and the outlet pressure at the descending aorta cross section. In order to scale this profile in order to observe this time-varying inlet boundary condition, the time-dependent flow rate obtained from the lumped-parameter model was used (Figure 5-1). The inlet velocity boundary condition in lattice Boltzmann was implemented using the method suggested by Skordos[52] which involves the use of a second-order finite difference scheme to compute the velocity gradient of the boundary nodes and extrapolates the pressure distribution at the inlet from bulk nodes[53]. Furthermore, in order to avoid pressure fluctuation artifacts at the inlet, a sinusoidal smooth start-up phase was used to initiate the simulation and smoothly increase the initial condition for the velocity from zero [54,55]. Moreover, the lumped-parameter model calculated the total flow rate headed and distributed to the branches based on the relative cross-sectional area of each branch. A no-slip boundary condition was applied at the solid walls as described in the section above (*Modeling surface curvature near the wall of complex geometries*). Based on the knowledge that patients with COA are typically hypertensive and characterized by reduced compliance and elevated stiffness in both the proximal and distal aorta, e.g., Jin et al. [56], Keshavarz-Motamed et al. [26,29,57] showed that a rigid-wall assumption for the aorta is reasonable and thus, the aortic wall in this study was treated as such.

The overall estimation of cardiac parameters is very dependent on the outputs of the lumped-parameter model due to the complex multiphysics nature of the aorta and heart valves. These lumped-parameter model outputs in-turn depend on the input parameters used in the lumped-parameter model. Our patient-specific, Doppler-based, lumped-parameter algorithm, which provided boundary conditions, has been validated against clinical catheterization data in patients with a substantial inter- and intra-patient variability with a wide range of disease[29,31,42]. We used the validated lumped-parameter model[29,31,42] to obtain the boundary conditions in the present study. In addition, to find cardiac parameters we performed a comprehensive parameter sensitivity analysis on the outputs of the lumped-parameter model. Our findings demonstrate that the outputs from the lumped-parameter model were most sensitive to the forward left ventricular outflow tract stroke volume (Forward LVOT-SV, an input parameter to the lumped parameter algorithm): LV pressure: 27%, LV Volume 19% by a ±20% change in the Forward LVOT-SV. The other input parameters affected the output to a much lesser degree. It should be noted that Forward LVOT-SV is measured reliably using Doppler echocardiography with high precision. The sensitivity of the model to this parameter does not endanger the results obtained from the lumped parameter model. In addition, sensitivity analysis revealed negligible effects of changes (±20%) in the free parameters on the model output variables.

❖ *Reconstructed geometries in patients with coarctation*

The 3D geometries of the complete aorta (ascending aorta, aortic branches and descending aorta) were reconstructed from segmented CT images of patients using a 3-D image processing and model generation software package (Figure 5-1), ITK-SNAP (version 3.8.0-BETA). In order to parallelize the simulation, these 3-D reconstructions were voxelized into multiblocks which were distributed between computer processor units.

❖ *Numerical strategy*

In order to stabilize complex turbulent fluid flow across the domain, single and multiple relaxation time LBM-based models were coupled with Smagorinsky's turbulent model. We utilized second order accuracy method proposed by Bouzidi et al. [49] to treat complex geometry. A smooth startup phase was added to the inlet velocity condition to suppress any undesired pressure fluctuation. Large Eddy Smagorinsky subgrid-scale model with constant $C_s = 0.1$ was applied [48] for turbulent modelling. Mesh sensitivity analysis was performed for maximum velocity and pressure drop at the coarctation region. Mesh definition was considered acceptable if no significant differences (lower than 5%) existed between successive mesh refinements in both quantities. In this study, the physical time step and physical lattice height adjacent to the wall were as low as $1.5\,\mu s$ and $50\,\mu m$, respectively. The minimal lattice height was to ensure that it is within the viscous sublayer.

5.3.2 Lumped parameter model

❖ *Cardiac-arterial model*

1) Left ventricle. LV pressure and volume were coupled using a measure of cardiac muscle stiffness, a time varying elastance E(t) calculated as follows:

$$E(t) = \frac{P_{LV}(t)}{V(t) - V_0}$$

(27)

where $P_{LV}(t)$, $V(t)$, and V_0 represent the LV time-varying pressure, time-varying volume, and unloaded volume, respectively.

As explained by Keshavarz-Motamed [42], to represent the normalized elastance function of the LV, we observed that among the summation of Gaussian functions [58,59], Boltzmann Distribution [60], and double Hill function [61,62], the latter provided the most physiologically accurate results for the pressure, flow, and volume waveforms. The double Hill function, as motivated by myocyte recruitment during preload, is a cooperative process [63]. The double-Hill LV normalized time-varying elastance curves (E$_N$) is calculated as follows [61,62]:

$$E_N(t) = N \left(\frac{\left(\frac{t}{\tau_1}\right)^{m1}}{1 + \left(\frac{t}{\tau_1}\right)^{m1}} \right) \left(\frac{1}{1 + \left(\frac{t}{\tau_2}\right)^{m2}} \right) + E_{min}$$

(28)

$$N = \frac{E_{max} - E_{min}}{2}$$

(29)

where N, τ_1, τ_2, m_1, m_2, E_{max} and E_{min} represent the elastane normalization, ascending time translation, descending time translation, ascending gradient, descending

gradient, maximum elastance and minimum elastance, respectively (see Table 5-1). It was necessary to use a double Hill function to model the contraction and relaxation in the heart chambers as shown in Equation 28 above. In this equation, the first term In brackets corresponds to the contraction of the chamber and the second term corresponds to the relaxation of the chamber. τ_1 and τ_2 govern the time translation of the elastance function as both parameters are functions of the cardiac cycle duration (T) and are calculated in each patient using the equations provided in Table 5-1. m_1 and m_2 govern the gradient of the elastance function and are constant for all patients (see Table 5-1 for more details). In order to obtain physiologically realistic waveforms for pressure, volume, and flow, parameter values used for the elastance function were adapted from [64-73] and can be found in Table 5-1.

2) Left atrium. Following the same method described above for the LV model, LA pressure and volume were coupled using time varying elastance E(t), and thus the elastance function used for LA is defined in equations 28 and 29 as well [61,62] (Table 5-1). A phase lag was also used in the LA elastance function in order to account for the relative offset of contractions between LA and LV [61]. Specifically, LV contraction was initiated at T = 0, and LA contraction was introduced at 0.85 T [61], resulting in a time delay of 0.15 T.

❖ *Modeling heart valves*

Aortic valve. The aortic valve was modeled using the analytical formulation for the net pressure gradient (PG_{net}) through the aortic valve. This formulation explains the instantaneous net pressure gradient across the aortic valve as a function of the

instantaneous flow rate and the energy loss coefficient. This links the LV pressure to the ascending aorta pressure as follows:

$$PG_{net}|_{AV} = \frac{2\pi\rho}{\sqrt{E_L Co|_{AV}}} \frac{\partial Q(t)}{\partial t} + \frac{\rho}{2E_L Co|_{AV}^2} Q^2(t) \tag{30A}$$

and

$$E_L Co|_{AV} = \frac{(EOA|_{AV})A_{AO}}{A - EOA|_{AV}} \tag{30B}$$

where $E_L Co|_{AV}$, $EOA|_{AV}$, A_{AO}, ρ and Q represent the valvular energy loss coefficient, the effective orifice area, ascending aorta cross sectional area, fluid density and transvalvular flow rate, respectively. $E_L Co|_{AV}$, represents the 'recovered EOA', which is the valve effective orifice area adjusted for the area of the aorta at the level of sinotubular junction.

Aortic regurgitation. Aortic regurgitation (AR) was modeled using the same analytical formulation as the aortic valve and is as follows:

$$PG_{net}|_{AR} = \frac{2\pi\rho}{\sqrt{E_L Co|_{AR}}} \frac{\partial Q(t)}{\partial t} + \frac{\rho}{2E_L Co|_{AR}^2} Q^2(t) \tag{31A}$$

and

$$E_L Co|_{AR} = \frac{EOA_{AR} A_{LVOT}}{A_{LVOT} - EOA_{AR}} \tag{31B}$$

where $E_L Co|_{AR}$, EOA_{AR} and A_{LVOT} represent regurgitation energy loss coefficient, regurgitant effective orifice area and LVOT area, respectively. AR pressure gradient is calculated as the difference between aorta pressure and LV pressure during diastole.

Mitral valve. The mitral valve (MV) was modeled using the net pressure gradient ($PG_{net}|_{MV}$) across the MV during LA ejection. This formulation expresses the instantaneous net pressure gradient across the LA and vena contracta as an unsteady, incompressible, and inviscid flow and therefore density is kept constant and viscous effects are disregarded. $PG_{net}|_{MV}$ was expressed as a function of ρ, Q_{MV}, EOA_{MV} and M_{MV}, which represent the density of fluid, transvalvular flow rate, effective orifice area and inertance, respectively. In this formulation as shown in equation 32, the large volume of the LV negates the pressure recovery phenomenon and it was therefore ignored [74].

$$PG_{net}|_{MR} = \frac{M_{MV}}{EOA_{MV}}\frac{\partial Q_{MV}(t)}{\partial t} + \frac{\rho}{2EOA|_{MV}^2}Q_{MV}{}^2(t) \tag{32}$$

Mitral regurgitation. Mitral regurgitation (MR) was modeled using the following equation where the MR pressure gradient is calculated as the difference between mitral and LA pressure during systole.

$$PG_{net}|_{MR} = \frac{M_{MV}}{EOA_{MR}}\frac{\partial Q(t)}{\partial t} + \frac{\rho}{2EOA|_{MR}^2}Q^2(t) \tag{33}$$

where $EOA|_{MR}$ represents the MR effective orifice area.

❖ *Modeling coarctation of the aorta*

When modelling COA, it is important to consider the characteristics of the arterial system as only a portion of total flow rate will cross the COA. In order to account for this, two parallel branches were considered: (1) the first branch simulates the flow towards the upper body, or the flow bypassing the COA (including aortic arch arteries and potential collaterals); (2) a second branch simulates the flow crossing COA and directed towards the descending aorta. The second branch includes a resistance for the proximal descending aorta as well as a time-varying resistance and an inductance, together they represent the trans-coarctation net pressure gradient induced by the COA[29]:

$$TPG_{net}|_{coa} = \frac{2\pi\rho}{\sqrt{E_L Co|_{coa}}} \frac{\partial Q(t)}{\partial t} + \frac{\rho}{2E_L Co|_{coa}^2} Q^2(t) \tag{34}$$

$$E_L Co|_{COA} = \frac{(EOA|_{coa})A}{A - EOA|_{coa}} \tag{35}$$

where $E_L Co|_{coa}$ and $EOA|_{coa}$ represent the energy loss coefficient of the COA and the effective orifice area of the COA, respectively. A, ρ, and Q are the aortic cross-sectional area downstream of the COA, the fluid density and the trans-coarctation flow rate, respectively. Based on equation (35), the energy loss coefficient is described in terms of the aortic cross section just downstream of the COA and the effective orifice area of the COA.

❖ *Pulmonary flow*

The pulmonary valve flow waveform was simulated by a rectified sine curve with duration t_{ee} and amplitude Q_{MPV} as follows:

$$Q_{PV}(t) = Q_{MPV}\, sin\left(\frac{\pi t}{t_{ee}}\right), t \leq t_{ee}\,; \quad Q_{PV}(t) = 0, t_{ee} < t \leq T \tag{36}$$

where Q_{MPV}, t_{ee} and T represent the mean flow rate of the pulmonary valve, end-ejection time and cardiac cycle duration, respectively. The only input flow condition in this study was Forward LVOT-SV. Indeed, in order for the lump-parameter algorithm to reproduce the measured Forward LVOT-SV, the mean flow rate of the pulmonary valve (Q_{MPV}) was optimized.

❖ *Computational algorithm*

The lumped-parameter model was analyzed numerically by creating and solving a system of ordinary differential equations in Matlab Simscape (MathWorks, Inc.), supplemented by additional functions written in Matlab and Simscape. To solve the system of differential equations, Matlab's ode23t trapezoidal rule variable-step solver was used with an initial time step of 0.1 milliseconds. The convergence residual criterion was set to 10^{-6} while initial voltages and currents of capacitors and inductors were set to zero. The model ran for ~150 cycles to reach a steady state before initiating the response optimization process as described below. A double Hill function representation of a normalized elastance curve for human adults was used in order to generate a signal to model LV elastance [61,62]. This elastance formulation was shown to completely represent the LV function independent of its pathological condition.

Simulations started at the onset of isovolumic contraction. The instantaneous LV volume, V(t), was calculated using the time varying elastance and LV pressure, P_{LV}. P_{LV}

was initially calculated using the initial values of the model input parameters from Table 5-1. Subsequently, the LV flow rate was calculated as the time derivative of the instantaneous LV volume. This approach was also used to obtain the left-atrium volume, pressure, and flow rate. The Forward LVOT-SV was calculated using the lumped-parameter model and then fitted to the one measured (Equation 37) by optimizing Q_{MPV} (as detailed below).

Forward LVOT-SV measured using DE is defined as the following:

$$Forward\ LVOT\text{-}SV_{DE} = ESV - EDV = A_{LVOT} \times VTI_{LVOT} = \frac{\pi \times (D_{LVOT})^2}{4} \times VTI_{LVOT}$$

(37)

where D_{LVOT}, A_{LVOT}, and VTI_{LVOT} represent the LVOT diameter, LVOT area, and LVOT velocity-time integral, respectively.

Finally, R_{SA}, C_{SAC}, and C_{ao} were optimized for each patient so that the aortic pressure from the model fit the sphygmomanometer measurements of patient systolic and diastolic pressures.

❖ *Input parameters*

The developed algorithm uses the following input parameters measured using Doppler echocardiography: LV stroke volume, cardiac cycle duration, ascending aorta area, LVOT area, aortic valve effective orifice area, mitral valve effective orifice area, the effective orifice area of the COA, aortic cross-sectional area downstream of the COA, and

grading of the severity of aortic and mitral valves regurgitation. Parameters measured using a sphygmomanometer include systolic and diastolic blood pressures which are additional input parameters for the developed algorithm.

❖ *Patient-specific response optimization*

The parameters of the model are listed in Table 5-1. Also reported in Table 5-1 are some parameters that were considered constant based on previous studies in literature or based on the rationale given below. Additionally, the parameters that were measured in each patient are also indicated in Table 5-1. Four parameters of the model were optimized so that the lumped-parameter model reproduced the physiological measurements performed in the patient. Simulink Design Optimization toolbox was used to optimize the response of the lumped-parameter model using the trust region reflective algorithm implemented in Matlab fmincon function. The response optimization was performed in two sequential steps with tolerances of 10^{-6}.

The mean flow rate of the pulmonary valve, Q_{MPV}, could not be reliably measured using Doppler echocardiography. In the first step of optimization, Q_{MPV} was optimized to minimize the error between the Forward LVOT-SV calculated by the lumped-parameter model and the one measured in each patient since Forward LVOT-SV can be measured reliably using Doppler echocardiography.

In the second step of optimization, R_{SA}, C_{SAC}, and C_{ao} were optimized so that the maximum and minimum values of the aorta pressure were equal to the systolic and diastolic pressures, respectively, measured using a sphygmomanometer in each patient.

For the sake of simplicity, we considered the aortic resistance, R_{ao}, and the systemic vein resistance, R_{SV}, as constants and optimized the systemic arteries resistance, R_{SA}, as the main contributor of the total systemic resistance. This is reasonable since the left ventricle faces the total systemic resistance rather than the individual resistances, and the systemic arteries resistance is one order of magnitude greater than both the aortic resistance and systemic vein resistance. C_{ao} was considered to be 0.6 of C_{SAC} because 60% of the total arterial compliance resides in the proximal aorta [75].

In addition, we conducted an extensive parameter sensitivity analysis that concluded the pulmonary parameters (e.g., C_{PVC}) have negligible effects on the model output variables. Therefore, we did not include these pulmonary parameters in the parameter-optimization process and considered them as constants given in Table 5-1.

5.3.3 Four-dimensional flow magnetic resonance imaging (4-D flow MRI)

Four-dimensional flow magnetic resonance imaging (4-D flow MRI) is a recent development of phase-contrast MRI (PC-MRI) with the capability to comprehensively assess blood flow in three spatial dimensions over the cardiac cycle[76]. 4-D flow MRI provides visualization of the vascular territory of interest and allows for the estimation of hemodynamic biomarkers such as wall shear forces[77] and pressure gradients[78,79]. Furthermore, 4-D flow MRI provides comprehensive information regarding complex flow patterns in vascular diseases[80]. *In this* study, acquisition of 4-D flow MRI data in patients with COA and valvular diseases was performed (Figure 5-1, Panel B, data acquisition and

analysis workflow of 4-D flow MRI) by standard Cartesian 4-D flow sequence using 1.5T MRI scanners (Philips Achieva; Philips Medical Systems, Best, the Netherlands). Electrocardiogram gating synchronized and diaphragm navigator gated 4-D flow MRI were performed during free breathing. Acquisition parameters were as follows: spatial resolution of (1.97–2.62, 1.97–2.62, 2.5–4 mm^3), temporal resolution of 36–40 ms. Velocity encoding was set to the range (1.5–4.5 m/s), the total scan time for each measurement varied from 8-15 min. All 4-D flow data was corrected for multiple sources of phase offset errors and noises such as velocity aliasing, Maxwell terms, and eddy currents using an in-house MATLAB-based code (MathWorks, Inc.). The data smoothing algorithm proposed by Garcia[81,82] was used to eliminate random errors of the velocity vectors. Garcia[81,82] proposed a fully automated smoothing procedure based on a penalized least squares approach that allows fast smoothing of the data and can replace spurious or missing vectors with the smoothed one.

Using ITK-SNAP (Yushkevich et al., 2006; http://www.itksnap.org) and an in-house MATLAB-based code, the 3-D segmentation of the thoracic aorta geometry and orifice shape of aortic stenosis or bicuspid valve was performed. In order to smooth the geometry and fix any defects, Fusion 360 (Autodesk, Inc) and Meshmixer (Autodesk, Inc) were used. Finally, the Stereolithography (STL) format of the geometry (domain) was extracted for the us in our computational simulation. Time-varying flow velocity information extracted from patient-specific 4-D flow MRI data was imposed at the inlet and outlets of each LBM computational model. We down sampled the high-resolution LBM velocities into PC-MRI resolution by linear interpolation of LBM velocity on MRI

sub grid in order to study the effect of resolution and comparing LBM to 4-D flow MRI velocity fields on identical grids. Moreover, the down-sampled LBM data was subjected to an imitation of the smoothing inherent in the 4-D flow MRI measurement in order to have the closest LBM approximation to the 4-D flow MRI data. The down-sampling and smoothing procedures are schematically shown in Figure 5-1 (Panel B).

Deidentified and anonymous patients at Stephenson Cardiac Imaging Centre, Libin Cardiovascular Institute of Alberta (Calgary, AB, Canada) were considered. Informed consent was obtained from all patients. The selections were done by operators blinded to the objectives and contents of this study at each institution and the protocols were reviewed and approved by the Institutional Review Boards of each institution. All methods and measurements were performed in accordance with relevant guidelines and regulations including guidelines of the American College of Cardiology and American Heart Association. Senior cardiologists reviewed the echocardiograms and reports using OsiriX imaging software (version 8.0.2; Pixmeo, Switzerland).

5.4   Results

5.4.1 Validation: computational framework vs. 4-D flow MRI

In this study, we developed a patient-specific, imaged-based, computational-mechanics framework that dynamically couples the local hemodynamics with the global circulatory cardiovascular system to investigate the impact of COA and MVD on both local and global hemodynamics in these patients. The entire computational framework was

validated against 4-D flow MRI measurements in five patients with COA. Figure 5-2 (Panel A) describes sample cases of voxel-by-voxel Bland-Altman analysis between the velocity fields resulted from the smooth down sampled low-resolution LBM and 4-D flow MRI measurements on the entire flow domain at the peak systole. The simulated velocity fields were in agreement with the velocity fields measured using 4-D flow MRI in patients: as examples, biases (means of differences) were -0.05, -0.04, -0.0087, -0.046 and 0.057 [m/s] and corresponding limits of agreement (1.96 SD) were also ±0.192, ±0.28, ±0.46, ±0.35 and ±0.374 [m/s] for patients #1, #2, #3, #4 and #5, respectively.

Moreover, Figure 5-2 (Panel B) shows the statistical analyses of the planar velocity differences between velocity field resulted from our computational framework and 4-D flow MRI measurements in sample cases at the peak of systole. As this figure shows, the 4-D flow MRI velocity field and the down sampled LBM-based velocity fields were compared using Pearson's correlation and Bland-Altman analysis. The coefficient of determination (R^2) was used to assess the linearity between the results from 4-D flow MRI and our computational framework at these planar sections. The coefficients of determination were 0.9508, 0.9305, 0.9126, 0.574 and 0.592 for patients #1, #2, #3, #4 and #5, respectively. Lateral section Biases (means of differences) were also -0.089, -0.032, 0.082, -0.028 and -0.07 m/s and the corresponding limits of agreement (1.96 SD) were ±0.066, ±0.186, ±0.171, ±0.369 and ±0.294 m/s for patients #1, #2, #3, #4 and #5, respectively, which shows agreements between the data resulted from 4-D flow MRI and our computational framework. We observed similar agreement (computational results *vs.* 4-D flow MRI measurement) in the other patients with COA investigated in this study. It

is important to note that 4-D flow MRI itself has some limitations and its measurements involves errors due to low temporal resolution (20 ms highest)[83]. The differences between the computational results and 4-D flow MRI measurements can be partly due to the shortages of 4-D flow MRI.

In addition, our developed patient-specific Doppler-based lumped-parameter model calculations were validated against clinical cardiac catheterization data (the instantaneous pressures in the aorta and LV) in patients with complex valvular, ventricular and vascular diseases with a substantial inter- and intra-patient variability with a wide range of disease (N=49)[42,83]. The model has already been validated against *in vivo* cardiac catheterization in patients with coarctation (N=40)[29,31] and some sub-models have been validated against *in vivo* MRI data (N=57)[84]. In addition, some of the sub-models of the lumped parameter model have been used previously[27,42,57,84-91]. Moreover, the entire patient-specific computational framework (Lattice Boltzmann method and lumped parameter model) was validated against clinical Doppler echocardiography previously[31]. Moreover, for all 26 patients investigated in this study, we observed good agreements between the simulated and experimental Doppler echocardiography pressure gradients (Mean relative error: 3.9%).
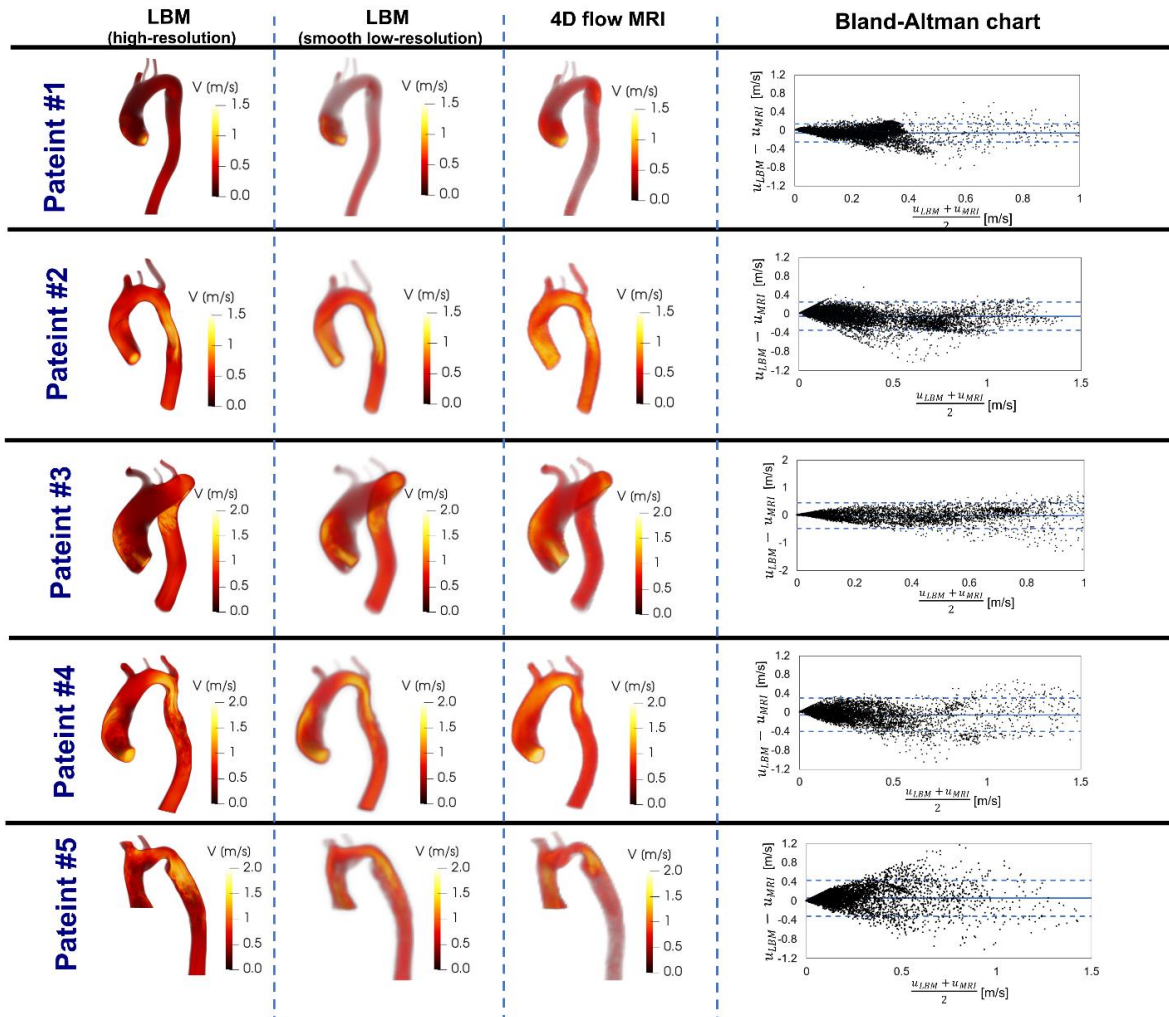
Figure 5-2. Validation against 4-D flow MRI. (a) We compared 4-D flow MRI data and results of the computational framework (based on lumped parameter model (LPM) and Lattice Boltzmann model (LBM)) in Patients #I to #V. (a) qualitatively (revealed in velocity mapping) and quantitatively by performing Pearson's product moment correlation analysis on the entire domain at peak systole between smooth down-sampled LBM and 4D flow MRI measurements; (b) qualitatively (revealed in velocity mapping) and quantitatively by performing linear regression and Pearson's product moment correlation analysis at sample cross sections at peak systole between smooth down-sampled LBM and PC-MRI measurements.

Figure 5-3. Flow modeling in Patient No. 1 in pre and post intervention status. (a) & (b) Time-evolving velocity magnitude; (c) & (d) Flow patterns and 3-D streamlines through the aorta

The good agreements between results calculated using our computational framework with the results measured using clinical 4-D flow MRI, Doppler echocardiography and cardiac catheterization allows us to accept our computational results with confidence to investigate the flow features.

5.4.2 Velocity

Figures 5-3, 5-5, and 5-7, panels A and B show the velocity mappings of the aorta in both pre- and post-intervention status for patients #1, #2, and #3, respectively. Patient #1 (Fig. 5-3, panels A & B) exhibits elevated velocity strictly at the neck of COA pre-intervention reaching a maximum of 1.9 [m/s] which drops slightly to 1.74 [m/s] post-intervention. Furthermore, increased velocity magnitudes are observed at the inlet of the graft as well as at the neck of COA post-intervention. The velocity through the graft appears to reach a maximum of approximately 1.4 [m/s]. Overall, the bypass graft slightly reduced the maximum observed velocity in patient #1, however, there is no substantial improvement. In contrast to the isolated regions of elevated velocity in patient #1, patient #2 (Figure. 5-5, panels A & B) exhibits an elevated velocity at the sight of COA, reaching a maximum of 1.59 [m/s] pre-intervention. Post-intervention, the condition is critically improved as the maximum recorded velocity is 1.03 [m/s] with a maximum of 0.6 [m/s] through the graft. Elevated velocities post-intervention are mainly visualized at the inlet and outlet of the graft as well as distal to the outlet. Patient #3 (Figure. 5-7, panels A & B) exhibits elevated velocities in nearly all regions of the aorta pre-intervention, with a maximum velocity of 1.47 [m/s] recorded at the neck of COA. The condition is substantially improved as the maximum velocity post-intervention decreases to 1.05 [m/s] with a maximum of 0.7 [m/s] through the graft, however, elevated velocities are observed in most regions of the aorta, similar to pre-intervention.

Table 5-1. Summarized parameters used in the lumped parameter modeling to simulate all cases.

Description	Abbreviation	Value
Valve parameters		
Effective orifice area	EOA	Measured using DE
Inertance (mitral valve)	M_{MV}	Constant value: 0.53 gcm^{-2}
Systematic circulation parameters		
Aortic resistance	R_{ao}	Constant value: 0.05 mmHg.s.mL^{-1}
Aortic compliance	C_{ao}	Initial value: 0.5 mL/mmHg Optimized based on brachial pressures *(Systolic and diastolic brachial pressures are optimization constraints)*
Systemic vein resistance	R_{SV}	0.05 mmHg.s.mL^{-1}
Systemic arteries and veins compliance	C_{SAC}	Initial value: 2 mL/mmHg Optimized based on brachial pressures *(Systolic and diastolic brachial pressures are optimization constraints)*
systemic arteries resistance (including arteries, arterioles and capillaries)	R_{SA}	Initial value: 0.8 mmHg.s.mL^{-1} Optimized based on brachial pressures *(Systolic and diastolic brachial pressures are optimization constraints)*
Upper body resistance	R_{ub}	Adjusted to have 15% of total flow rate in healthy case
Proximal descending aorta resistance	R_{pda}	Constant value: 0.05 mmHg.s.mL^{-1}
Elastance Function[*]		
Maximum Elastance	E_{max}	2.1 (LV) 0.17 (LA)
Minimum Elastance	E_{min}	0.06 (LV, LA)
Elastance ascending gradient	m_1	1.32 (LV, LA)
Elastance descending gradient	m_2	27.4 (LV) 13.1 (LA)
Elastance ascending time translation	τ_1	0.269 T (LV) 0.110 T (LA)
Elastance descending time translation	τ_2	0.452 T (LV) 0.18 T (LA)
Pulmonary circulation parameters		
Pulmonary Vein Inertance	L_{PV}	Constant value:0.0005 mmHg·s^2·mL^{-1}
Pulmonary Vein Resistance	R_{PV}	Constant value: 0.002 mmHg·s·mL^{-1}
Pulmonary Vein and capillary Resistance	R_{PVC}	Constant value: 0.001 mmHg·s·mL^{-1}
Pulmonary Vein and Capillary Compliance	C_{PVC}	Constant value: 40 mL/mmHg
Pulmonary Capillary Inertance	L_{PC}	Constant value: 0.0003 mmHg·s^2·mL^{-1}
Pulmonary Capillary Resistance	R_{PC}	Constant value: 0.21 mmHg·s·mL^{-1}
Pulmonary Arterial Resistance	R_{PA}	Constant value: 0.01 mmHg·s·mL^{-1}
Pulmonary Arterial Compliance	C_{PA}	Constant value: 4 mL/mmHg
Mean Flow Rate of	Q_{MPV}	*Forward LVOT-SV is the only input flow condition (measured using*

Pulmonary Valve		DE).
		Q_{MPV} is a flow parameter that was optimized so that the lump-parameter model could reproduce the desirable DE-measured Forward LVOT-SV.
Input flow condition		
Forward left ventricular outflow tract stroke volume	Forward LVOT-SV	Measured using DE
Output condition		
Central venous pressure	P_{CV0}	Constant value: 4 mmHg
Other		
Constant blood density	ρ	Constant value: 1050 kg/m^3
Heart rate	HR	Measured using DE
Duration of cardiac cycle	T	Measured using DE
Systolic End Ejection time	T_{EJ}	Measured using DE
End diastolic volume	EDV	Measured using DE
End systolic volume	ESV	Measured using DE

5.4.3 Streamlines and evolution of flow patterns

Figures 5-3, 5-5, and 5-7, panels C illustrate the velocity streamlines and time evolving flow patterns in the central plane pre-intervention for patients #1, #2, and #3, respectively. All patients exhibited relatively smooth flow patterns throughout the acceleration phase. In all three examined patients, chaotic flow ensues throughout peak systole. A small vortex appears directly downstream to the COA in patient #1 (Figure 5-3, panel C), which later dissipates in deceleration. Similarly, a strong vortex appears downstream to the COA in patient #3 (Figure 5-7, panel C) which also dissipates in the deceleration phase. Both vortices lead to recirculation and reversed flow during deceleration. The flow patterns remain relatively smooth in all systolic phases for patient #2 (Figure 5-5, panel C) with some slightly disturbed flow in the descending aorta during deceleration. No recirculation or reversed flow was observed in any phase for patient #2.
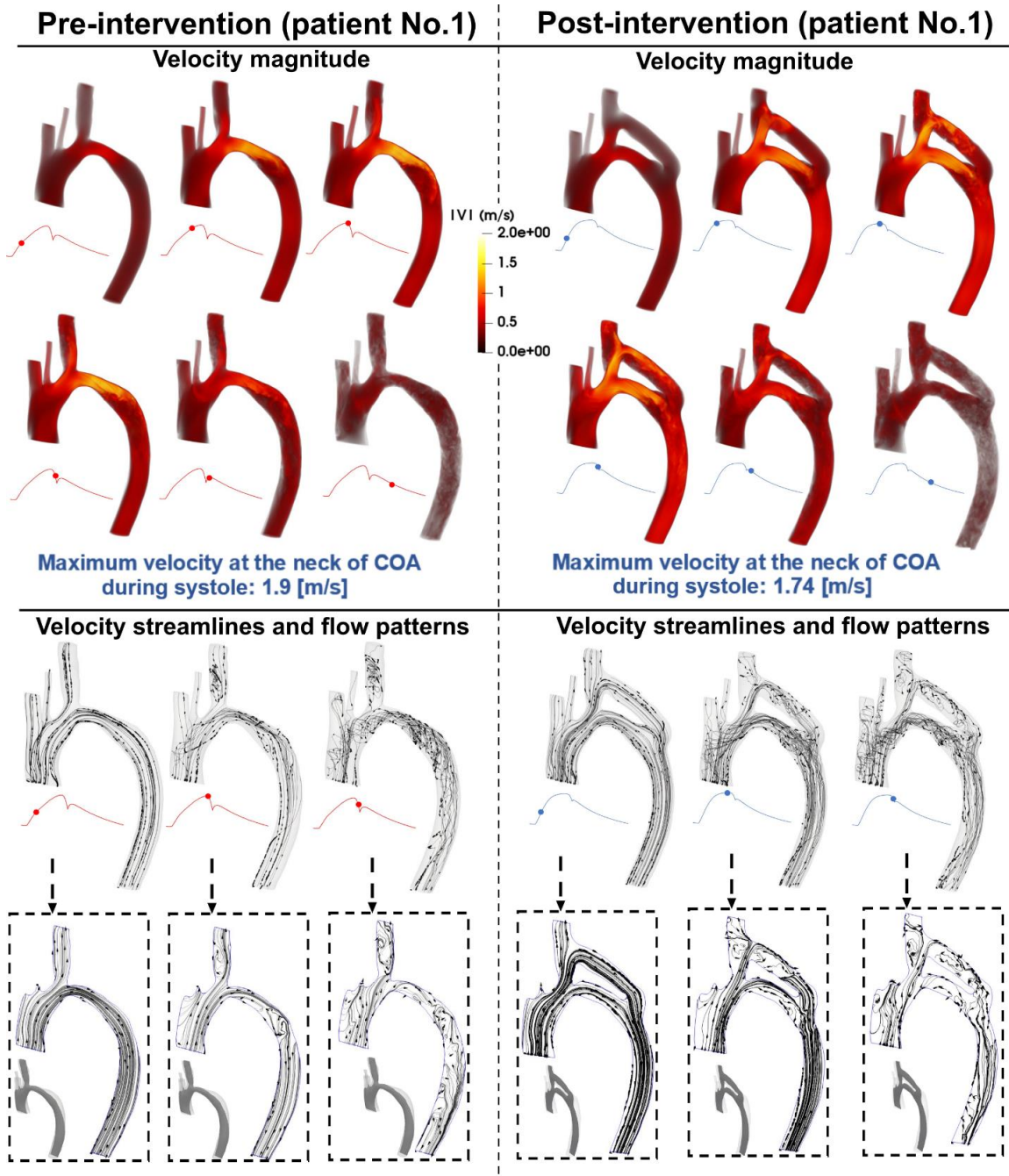
Figure 5-4. Flow modeling in Patient No. 1 in pre and post intervention status. (a) & (b) Time-evolving velocity magnitude; (c) & (d) Flow patterns and 3-D streamlines through the aorta
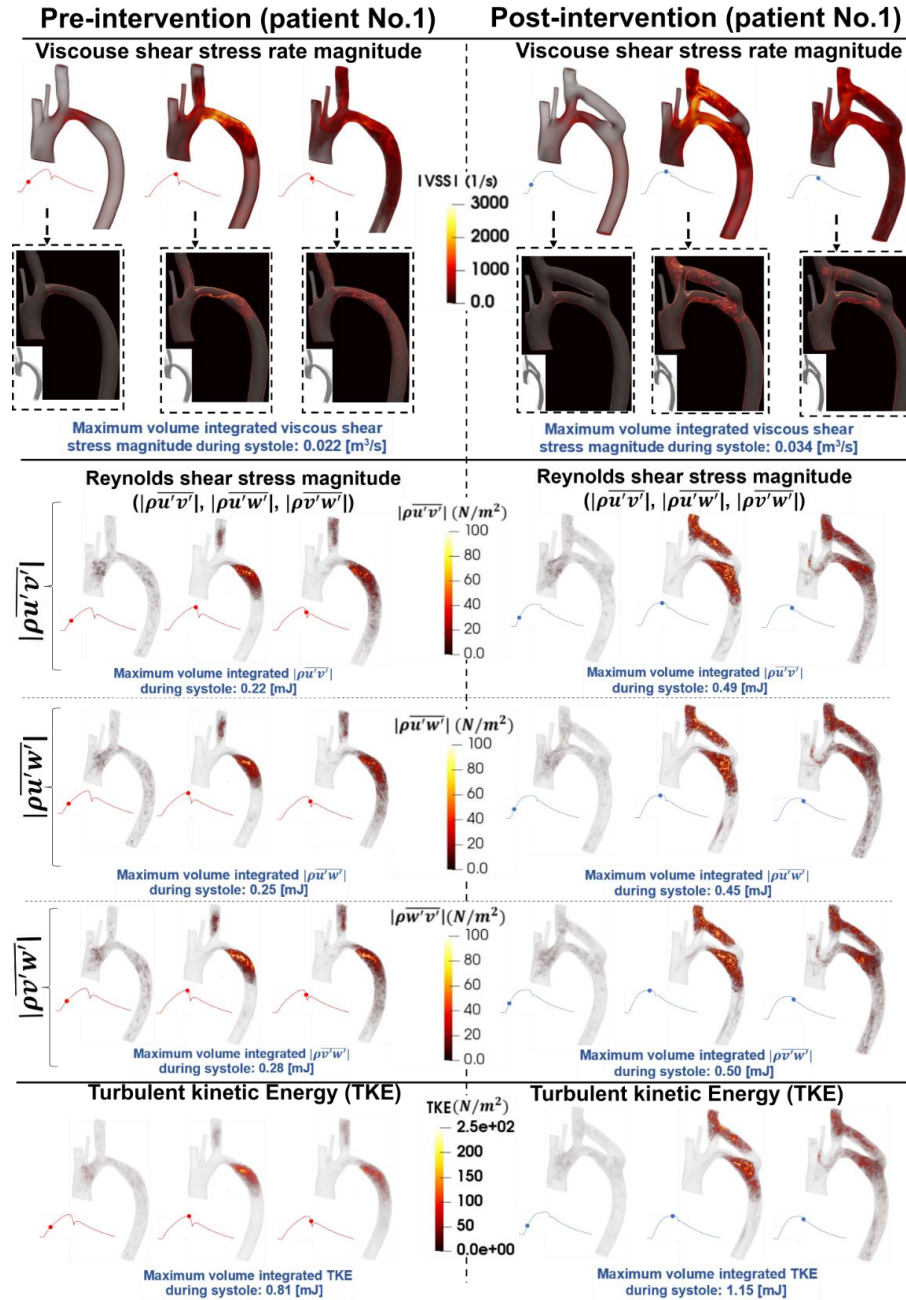
Figure 5-5. Flow modeling in Patient No. 1 in pre and post intervention status. (a) & (b) Viscous shear stress (VSS) magnitude; (c) & (d) Computed Reynolds Shear stress ($\rho\overline{u'v'}, \rho\overline{u'w'}$ and $\rho\overline{w'v'}$) magnitude; (e) & (f) Turbulent kinetic energy (TKE), computed as $\frac{1}{2}\rho(\overline{u'^2} + \overline{v'^2} + \overline{w'^2})$, where u, v, w and ρ correspond to the three components of the instantaneous velocity vector and density. The bar and prime denote the ensemble averaged and fluctuating components, respectively.
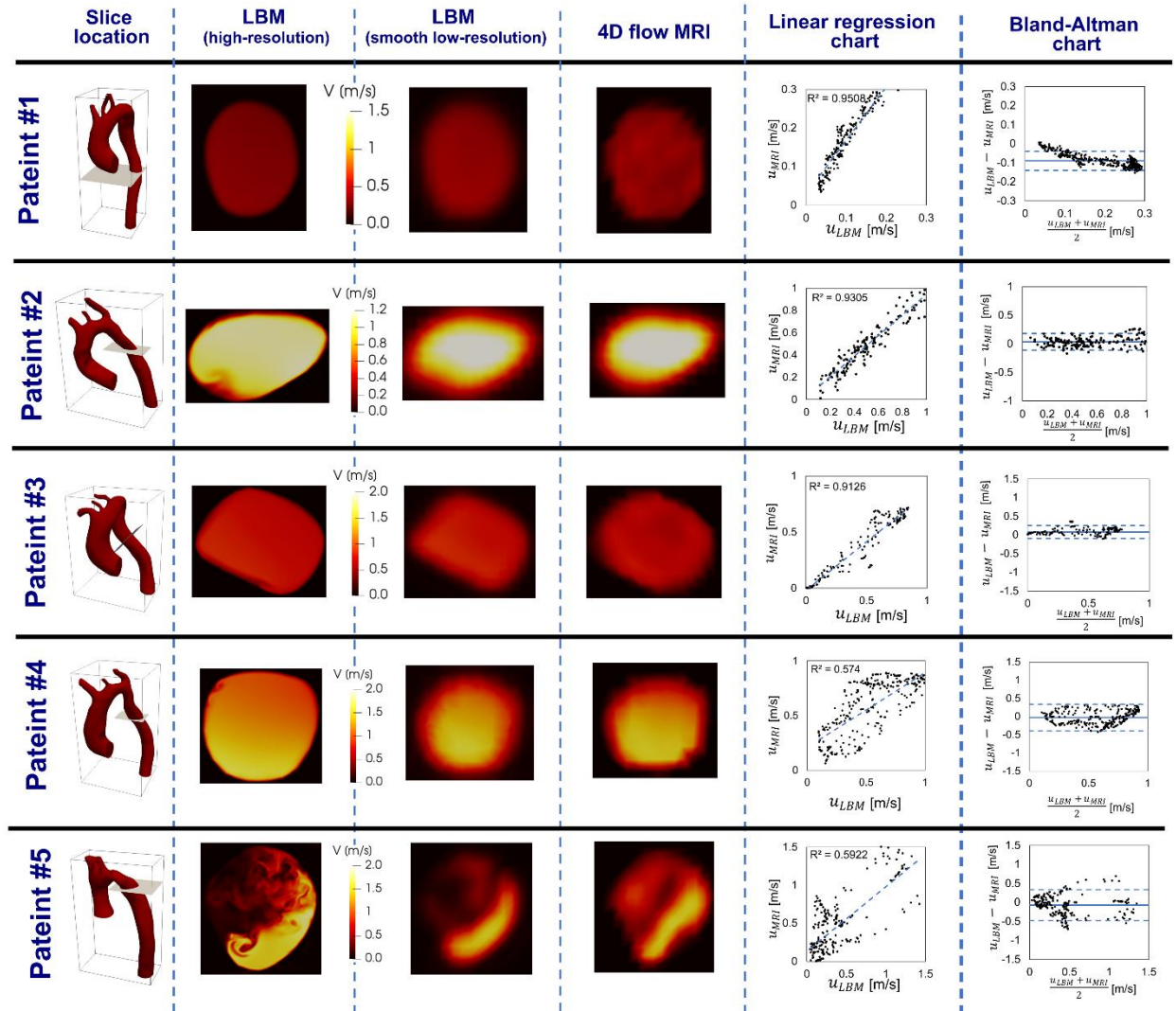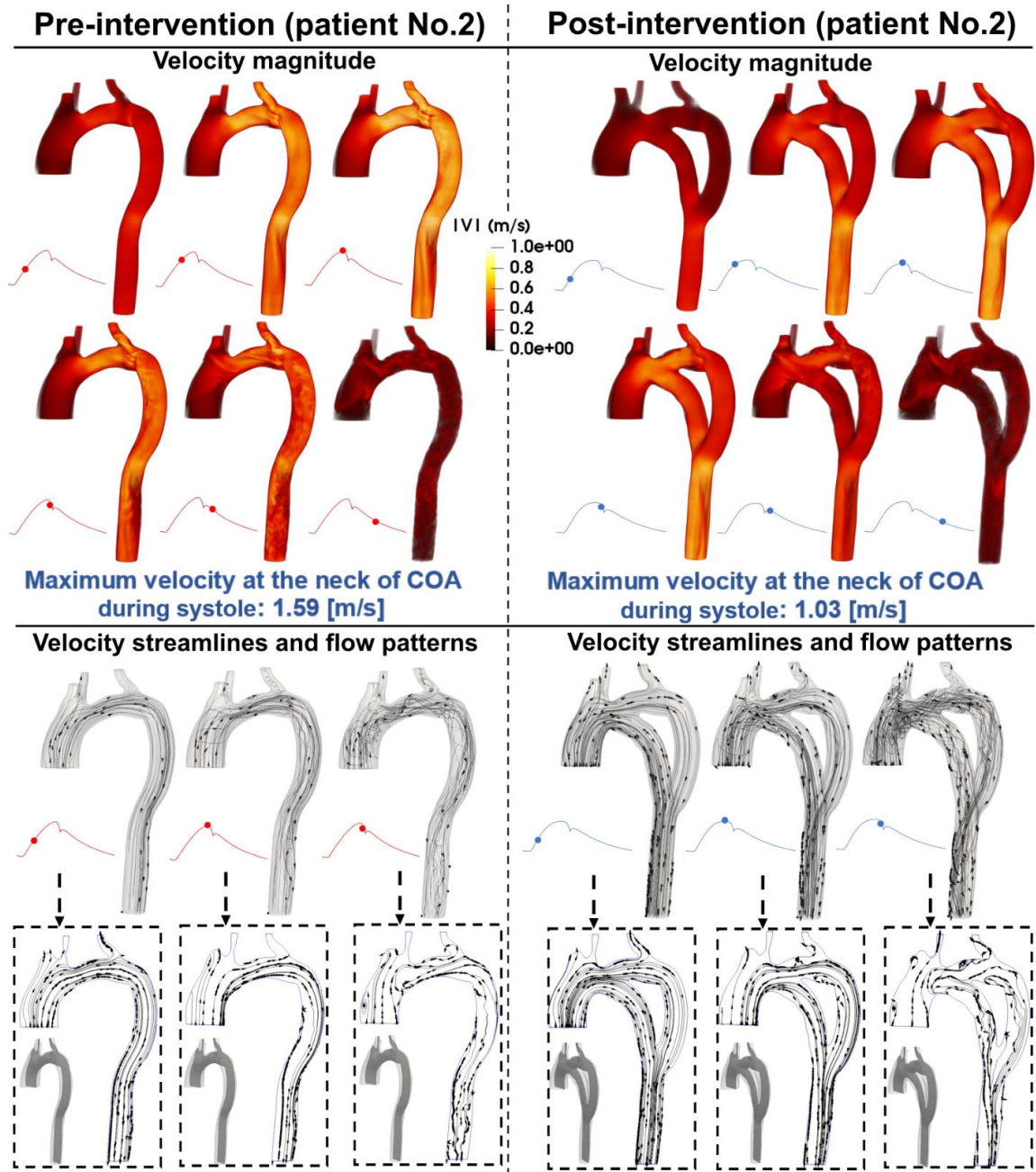
Figure 5-6. Flow modeling in Patient No. 2 in pre and post intervention status. (a) & (b) Time-evolving velocity magnitude; (c) & (d) Flow patterns and 3-D streamlines through the aorta
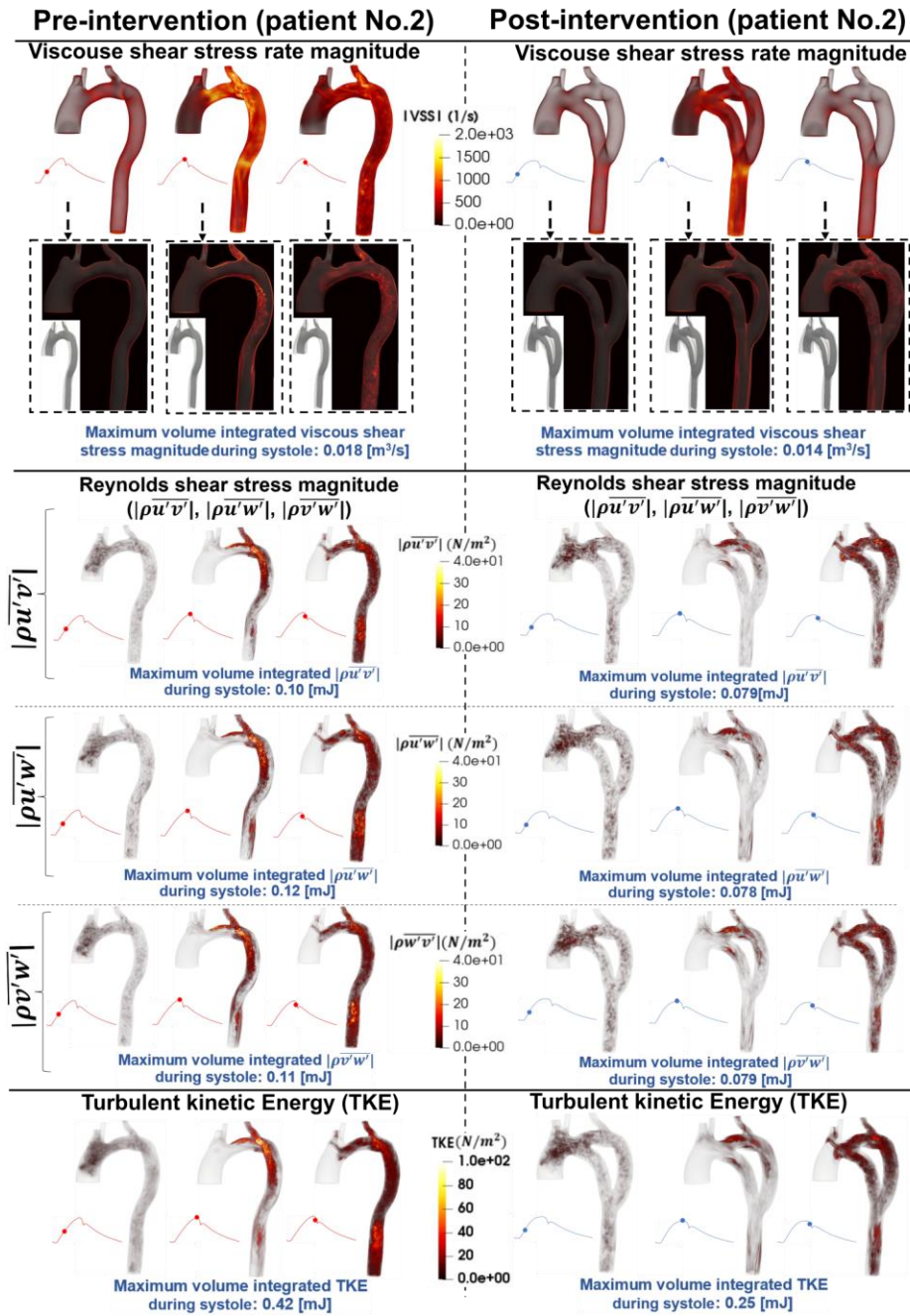
Figure 5-7. Flow modeling in Patient No. 2 in pre and post intervention status. (a) & (b) Viscous shear stress (VSS) magnitude; (c) & (d) Computed Reynolds Shear stress ($\rho\overline{u'v'}, \rho\overline{u'w'}$ and $\rho\overline{w'v'}$) magnitude; (e) & (f) Turbulent kinetic energy (TKE), computed as $\frac{1}{2}\rho(\overline{u'^2} + \overline{v'^2} + \overline{w'^2})$, where u, v, w and ρ correspond to the three components of the instantaneous velocity vector and density. The bar and prime denote the ensemble averaged and fluctuating components, respectively.

Figures 5-3, 5-5, and 5-7, panels D illustrate the velocity streamlines and time evolving flow patterns post-intervention for patients #1, #2, and #3, respectively. In all three patients, flow is very smooth through all regions of the graft and examined aorta during the acceleration phase. The flow patterns in all three patients exhibited different behaviors in the remaining systolic phases. The flow patterns in patient #1 (Figure 5-3. Panel D) become more chaotic through the graft and at the outlet during peak systole leading to some recirculation and reversed flow. In the deceleration phase, the flow throughout the entire aorta and bypass graft is not smooth with a large amount of reversed flow and recirculation. Patient #2 (Figure 5-5, panel D) exhibits smooth flow patterns throughout peak systole with increased disturbed flow in deceleration. Again, no recirculation or reversed flow was observed in patient #2. In patient #3 (Figure 5-7, panel D), a large vortex forms at the inlet of the graft and an additional vortex is observed downstream to the COA. Flow remains chaotic in the deceleration phase upstream to the COA, the vortex at the inlet of the graft dissipates and laminar flow is mostly restored throughout the graft, however, the vortex downstream to the COA expands circumferentially and collects all flow from the graft.

Overall, the bypass graft in patient #1 does not seem to improve flow patterns with the exception of resolving the vortex in peak systole, the behavior of the velocity streamlines is similar in each phase of pre-intervention compared to post-intervention. Intervention in patient #2 did not seem to have a significant effect on the velocity streamlines and flow patterns, however, it did not worsen the condition for the patient who already exhibited smooth flow patterns. In patient #3, although the graft appears to slightly improve the

flow patterns in the acceleration phase by evenly distributing the flow across the aorta, the flow becomes more chaotic with larger vortices in the other phases of systole compared to pre-intervention.
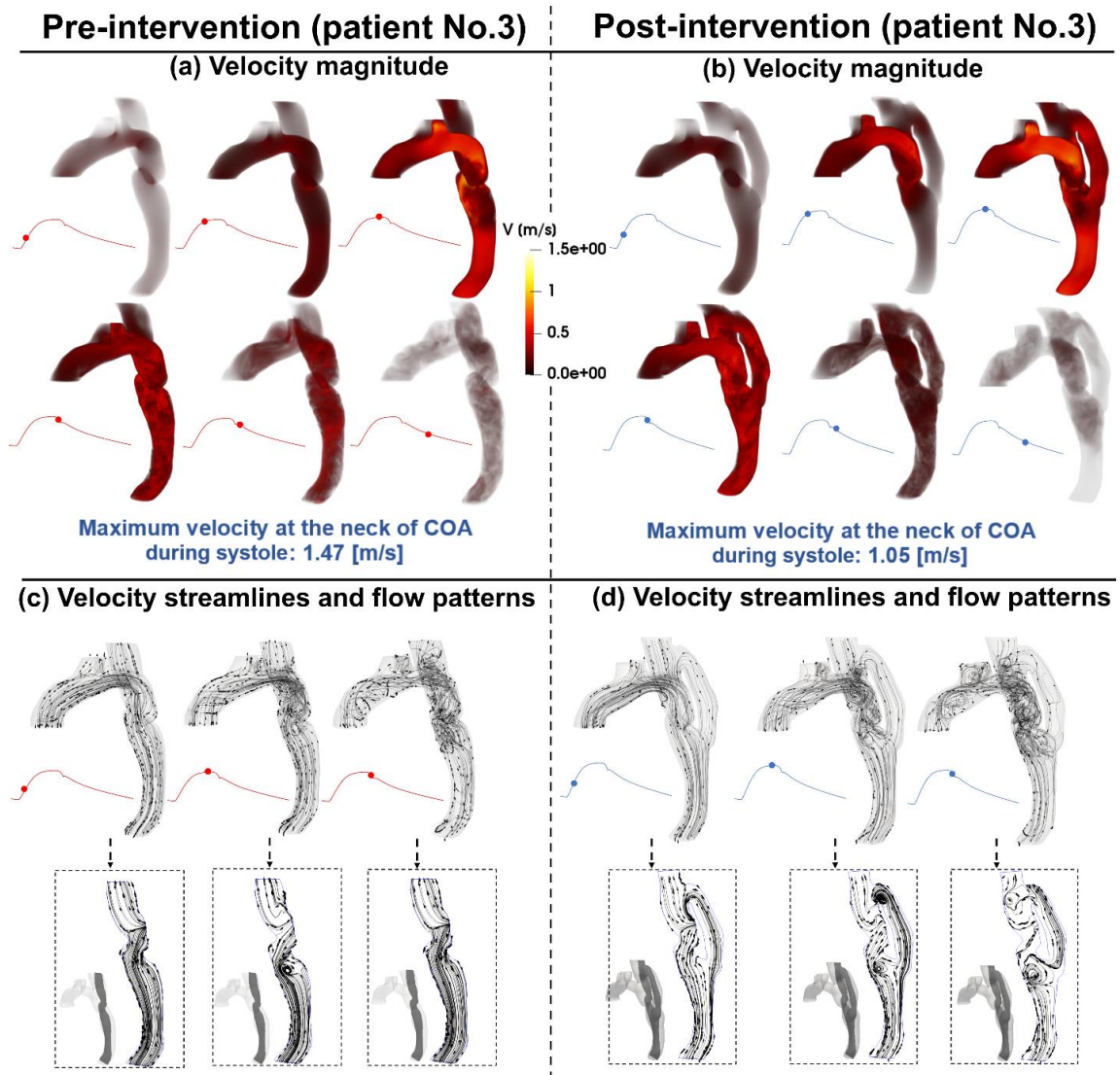
Figure 5-8. Flow modeling in Patient No. 3 in pre and post intervention status. (a) & (b) Time-evolving velocity magnitude; (c) & (d) Flow patterns and 3-D streamlines through the aorta

5.4.4 Viscous Shear Stress

The streamlines and velocity profile presented above clearly demonstrate the main features of the flow, but do not highlight the intensity of the spatial velocity gradients. Viscous shear stress (VSS) quantifies the effect of shearing between adjacent layers of fluid. In Figures 5-4, 5-6, and 8, panels A, VSS contours are shown in pre-intervention status for patients #1, #2, and #3, respectively. Slightly elevated VSS is observed directly at the neck of COA with negligible VSS values in all other regions for all three patients throughout the acceleration phase. During peak systole, VSS rapidly increases upstream, at the neck, and downstream of the COA, reaching a maximum magnitude of 0.022 $[m^3/s]$, 0.018 $[m^3/s]$, and 0.030 $[m^3/s]$ pre-intervention in patients 1-3, respectively. VSS slightly dissipates throughout deceleration, however, elevated levels do remain through all regions of the examined aorta.

Figures 5-4, 5-6, and 5-8, panels B, illustrates the VSS contours in patients #1, #2, and #3 post-intervention, respectively. The acceleration phase has a similar behavior as the pre-interventional state, with slightly elevated VSS around the neck of COA. In patient #1 (Figure 5-3, panel B), substantially elevated VSS is observed at the inlet of the graft and through the neck of COA reaching a maximum of 0.034 $[m^3/s]$ at peak systole, which is much greater than pre-intervention (0.022 $[m^3/s]$ at peak systole). Patient #2 (Figure 5-5, panel B) displayed slightly elevated VSS in all regions of the aorta at peak systole compared to acceleration, with a more substantial increase at the outlet of the graft.
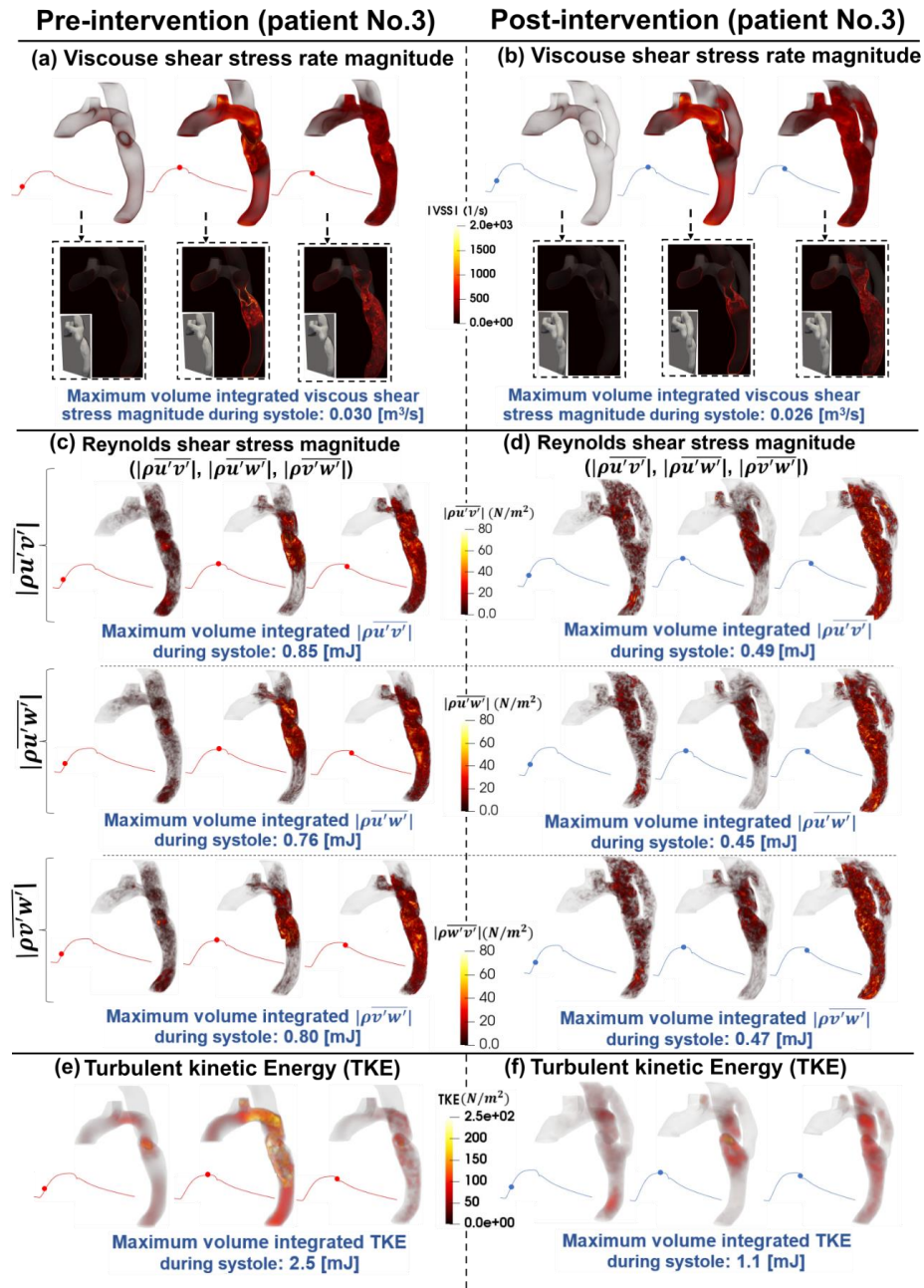
Figure 5-9. Flow modeling in Patient No. 3 in pre and post intervention status. (a) & (b) Viscous shear stress (VSS) magnitude; (c) & (d) Computed Reynolds Shear stress ($\rho\overline{u'v'}, \rho\overline{u'w'}$ and $\rho\overline{w'v'}$) magnitude; (e) & (f) Turbulent kinetic energy (TKE), computed as $\frac{1}{2}\rho(\overline{u'^2} + \overline{v'^2} + \overline{w'^2})$, where u, v, w and ρ correspond to the three components of the instantaneous velocity vector and density. The bar and prime denote the ensemble averaged and fluctuating components, respectively.

Maximum VSS recorded for patient #2 was 0.014 [m^3/s] which is slightly improved when compared to the pre-intervention status (0.018 [m^3/s]). Patient #3 (Figure 5-7, panel B) exhibits similar VSS patterns to pre-intervention, with increased VSS upstream, at the neck, and downstream of the COA reaching a maximum of 0.026 [m^3/s] in post-intervention status at peak systole which is slightly improved from pre-intervention (0.030 [m^3/s]). All three patients exhibited a similar behavior with regards to VSS in the deceleration phase as the patterns remained similar to peak systole with smaller magnitudes.

5.4.5 Turbulent characteristics

In healthy vessels, blood flow is usually laminar and does not experience transition to turbulence. Under physiological conditions, mainly in the presence of flow obstruction, turbulence develops in the aorta. In order to investigate the occurrence of turbulence and the intensity of fluctuations in the fluid flow environment, we choose the turbulent kinetic energy (TKE) and Reynolds shear stress (RSS) in particular, which are both derived using fluctuating components of the velocities. The TKE is a sum of the normal fluctuating stresses, whereas the RSS represents the ensemble averaged correlation between the two in-plane velocity components. These quantities characterize the level of fluctuations in the flow field through the aorta and give insight into the onset of instability and the intensity of turbulence.
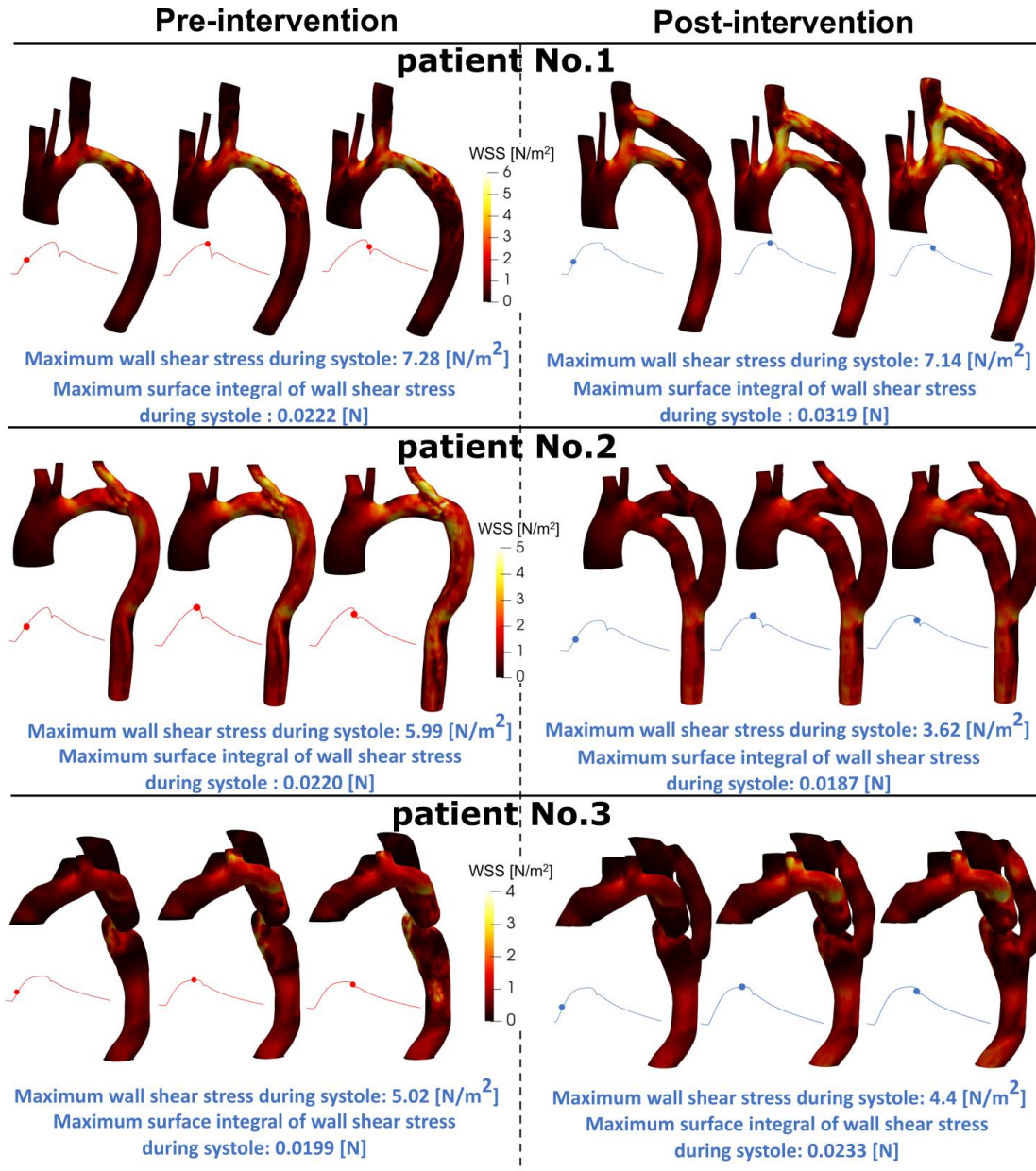
Figure 5-10. Flow modeling in Patient No. 1, 2 and 3 in pre and post intervention status. (a) Computed wall shear stress in patient #1; (b) Computed wall shear stress in patient #2; (c) Computed wall shear stress in patient #3.

5.4.6 Reynolds Shear Stress

In Figures 5-4, 5-6, and 5-8, panels C, the RSS mapping is shown pre-intervention for patients #1, #2, and #3, respectively. Consistently low or negligible RSS was observed in the acceleration phase for all patients. In peak systole, patients #1 (Figure 5-4, panel C) and #2 (Figure 5-6, panel C) exhibit RSS isolated to the neck of COA and slightly downstream whereas patient #3 (Figure 5-8, panel C) exhibits increased RSS upstream from the COA as well. Throughout deceleration, the RSS remains in the same regions as during peak systole for patient #1 with a decrease in magnitude, however, for patients #2 and #3, the regions of RSS expand down the descending aorta. Maximum RSS values observed in patients #1, #2, and #3 were 0.22-0.28 [mJ], 0.10-0.12 [mJ], and 0.76-0.85 [mJ], respectively.

Figures 5-4, 5-6, and 5-8, panels D illustrate the RSS post-intervention for patients #1, #2, and #3, respectively. Similar to pre-intervention, RSS levels during the acceleration phase are very low for all patients. Patient #1 (Figure 5-4, panel D) displays increased RSS (significant worsening) at peak systole compared to pre-intervention (with a maximum range of 0.22-0.28 [mJ]) with elevated levels at the neck of COA along with the inlet and outlet of the graft achieving a maximum range of 0.45-0.50 [mJ] in post-intervention status. The regions of elevated RSS remain constant through deceleration with decreased magnitudes. Unlike patient #1, patient #2 (Figure 5-6, panel D) displays reduced RSS at peak systole with a maximum range of 0.078-0.079 [mJ] in post-intervention status, compared to pre-intervention (with a maximum range of 0.10-0.12 [mJ]). Patient #3

(Figure 5-8, panel D) has a significant reduction (improvement) in RSS post-intervention (maximum RSS observed ranges: pre-intervention: 0.76 to 0.85 [mJ]; post-intervention: 0.45 to 0.49 [mJ]).

Overall, the condition for patient #1 worsens post-intervention as there are more observed regions of elevated RSS. In contrast, the condition for patient #2 greatly improves post-intervention, not only the maximum magnitudes of RSS decrease, but the regions of elevated RSS do not cover as much area. The RSS patterns for patient #3 and contours remained very similar post-intervention, however, the magnitudes were greatly decreased resulting in improved fluid dynamics with regards to RSS.

5.4.7 Turbulent Kinetic Energy

Figures 5-4, 5-6, and 5-8, panels E illustrate the TKE contours throughout the aorta pre-intervention for patients #1, #2, and #3, respectively. In the acceleration phase for all patients, there are negligible amounts of TKE throughout the examined regions of the aorta. In patients #1 (Figure 5-4, panel E) and #2 (Figure 5-6, panel E), the TKE observed at peak systole is isolated to the neck of COA and directly downstream, reaching a maximum of 0.81 [mJ] and 0.42 [mJ], respectively. The elevated levels of TKE dissipate in patient #1, however, in patient #2 the TKE appears to expand to the majority of the examined aorta with slightly decreased magnitude from peak systole. In contrast to the isolated peak systolic TKE of patient #1 and #2, the TKE contours observed in patient #3 (Figure 5-8, panel E) are observed upstream, at the neck, and downstream to the COA

reaching a maximum of 2.5 [mJ]. In the deceleration phase, nearly all TKE dissipates for this patient.

The post-intervention TKE contours are shown in Figures 5-4, 5-6, 5-8, panels F for patients #1, #2, and #3, respectively. Similar to pre-intervention, all three patients displayed very low TKE in the acceleration phase. The behavior of TKE for the three patients varies significantly throughout peak systole and deceleration. Patient #1 (Figure 5-4, panel F) exhibits elevated TKE at the neck of COA as well as at the inlet and outlets of the graft reaching a maximum of 1.15 [mJ] in post-intervention compared to pre-intervention (0.81 [mJ]). Throughout deceleration, TKE remains present in the same regions with decreased magnitudes. In patient #2 (Figure 5-6, panel F), TKE is very low throughout peak systole with slightly elevated levels at the proximal section of the bypassed aorta. TKE slightly increases throughout the majority of the aorta and graft in the deceleration phase, however, magnitudes in post-intervention status (with a maximum of 0.25 [mJ]) are much lower than in pre-intervention status (with a maximum of 0.42 [mJ]). TKE contours shown for patient #3 (Figure 5-8, panel F) exhibit slightly elevated levels directly around and at the neck of COA during peak systole, with negligible levels in the graft. In the deceleration phase, elevated TKE expands throughout more of the graft, while remaining at a low magnitude compared to pre-intervention. The maximum recorded TKEs were 2.5 [mJ] and 1.1 [mJ] in pre and post-intervention status, respectively, in patient #3 throughout systole.

It is evident that the TKE values are significantly higher post-intervention for patient #1 which may have negative implications in the future. It is important to note that high levels of TKE were recorded at both the inlet and outlet of the graft. The condition for patient #2 improved with a great reduction in TKE, and minimal levels through the graft. Furthermore, for patient #3, the implemented bypass graft greatly improves the condition with regards to the TKE expressed in the regions around COA, maximum values greatly decreased, and the flow is much less turbulent compared to pre-intervention with negligible turbulence detected through the graft.

5.5   Discussions

Accurate hemodynamic analysis is not only crucial for the successful diagnosis of COA, but treatment decisions also heavily rely on the hemodynamics assessment in both pre and post intervention states to minimize patient risks. Our results can provide insights about possible reasons for graft failure as follows:

❖ *Bypass grafting may not improve the aorta hemodynamics*

The presence of the COA itself alter largely the flow dynamics. Such flow alterations contributed to elevated wall shear stress mainly at the COA region as well as distal to the COA. Wall shear stress, as a force induced by blood flow, has a major impact on regulating endothelial function and is a predeterminant biomarker of disease progression. High abnormal stresses (e.g., elevated wall shear stress) can result in endothelial dysfunction, dedifferentiation of arterial smooth muscle and medial thickening[26,28,29,86,92-95]. We observed that bypass graft exacerbated aortic wall shear stress near the junctions

of anastomoses for all 3 patients investigated in this study (Figure 5-9). In addition, bypass grafting does not always alleviate high wall shear stress significantly. As one example, in patient #1, maximum wall shear stress during systole did not improve post intervention (pre-intervention: 7.28 N/m^2; post-intervention: 7.14 N/m^2) and maximum surface integral of wall shear stress during systole increased significantly post intervention (pre-intervention: 0.0222 N/m^2; post-intervention: 0.0319 N/m^2). Such exposures of endothelial cells to high shear stress affects vessel distensibility and compliance and potentially lead to arterial remodeling, aneurysm, rupture and dissection.

❖ *Bypass graft may lead to intimal hyperplasia due to the persistent abnormal aortic hemodynamics*

Intimal hyperplasia is a common cause for graft failure which involves the abnormal layering of cells on a blood vessel membrane across a vascular reconstruction (e.g., a bypass graft)[18,19,96]. This phenomenon is supposed to be an adaptation process following an intervention; however, the cell proliferation and differentiation process causes the region of connection between the vessel and graft to narrow, *causing recurrent COA*, typically near the junctions of anastomoses[18,19,96,97]. Moreover, graft implementation can result in local turbulence which may contribute to the progression of intimal hyperplasia near the junctions of anastomoses, specifically at the outlet[18,97-99]. In response to abnormal fluid dynamics, the vessel wall attempts to correct the flow disruption by intimal thickening, causing the narrowing of the vessel[18,97-99]. It has also been shown that abnormal flow velocity has been linked with high cell turnover, leaky cell junctions,

platelet aggregation and smooth muscle proliferation, all of which contribute to intimal hyperplasia[38]. Once this process begins post-intervention, it is difficult to control, leading to a significant risk for any vascular reconstructive surgery[96].

Our findings suggest that bypass grafting improved hemodynamic metrics (reduction in shear stresses, flow velocities, and turbulent characteristics)[18,38,97-99] in some patients, however, the hemodynamic conditions worsened in others which has previously been linked to the onset and progression of intimal hyperplasia. In addition, the geometry of the bypass graft can significantly impact blood flow parameters such as the flow field and wall shear stress (Figure 5-9) which often lead to the development and progression of intimal hyperplasia near the junctions of anastomoses[37-39,97]. Based on the results of this study, it is evident that patient #1 is at risk of intimal hyperplasia post-intervention. The flow velocity magnitude did not significantly improve in patient #1 post-intervention and indeed, elevated flow velocity can lead to arterial wall complications. Furthermore, viscous shear stress as well as turbulence characteristics (such as Reynold's shear and turbulent kinetic energy) increased post-intervention significantly, leading to an increased risk of graft failure in patient #1. The hemodynamic conditions improved for patients #2 and #3 for most of the analyzed hemodynamic metrics. Despite this, both patients are at risk for developing intimal hyperplasia due to the elevated abnormal hemodynamics near the junctions of anastomoses.

❖ *Bypass graft may lead to pseudoaneurysm formation and potential aortic rupture due to aortic wall disruptions*

A pseudoaneurysm, or false aneurysm, is a common long-term complication following a bypass graft surgery for COA and occurs in 11-24% of cases[21,24,100,101]. Although infrequent early after intervention, pseudoaneurysm incidence increases over-time and are commonly diagnosed during long-term follow-up[24] occurring near the junctions of anastomoses[24,102-104]. Aortic pseudoaneurysms are often the result of a disruption of at least one layer of the aortic wall, which is contained within the remaining vascular layers and surrounding structures[103]. Disturbed flow conditions, including elevated velocity flow, high wall shear stresses and vortical flow[105], may lead to wall complications and pseudoaneurysm[103,106]. If left untreated, pseudoaneurysms are likely to result in mortality or loss of a limb[24,107]. Indeed, monitoring of fluid dynamics at the inlet and outlet of bypass grafts is crucial to prevent potential pseudoaneurysm rupture. Our findings in this study show that all patients investigated in this study exhibit at least some of the following abnormal hemodynamics parameters: elevated velocity magnitude, persistence of vortical flow structure, elevated turbulence characteristics, and elevated wall shear stress (Figure 5-3 to 5-9) at the bypass graft junction regions[105]. All the mentioned abnormal hemodynamic metrics may lead to the formation and potential rupture of pseudoaneurysm.

Conflict of interest

The authors declare that they have no competing interests. The authors declare that the research was conducted in the absence of any commercial or financial relationships that could be construed as a potential conflict of interest.

Data availability statement

The development and validation of the proposed method require the retrospective clinical data routinely measured in clinics and were transferred as the de-identified & anonymized data. The code and the optimization algorithms are available from the author upon request.

5.6   References

1   Sinning, C. *et al.* Bicuspid aortic valve and aortic coarctation in congenital heart disease—important aspects for treatment with focus on aortic vasculopathy. *Cardiovascular diagnosis and therapy* **8**, 780 (2018).

2   Endorsed by the Association for European Paediatric Cardiology *et al.* ESC Guidelines for the management of grown-up congenital heart disease (new version 2010) The Task Force on the Management of Grown-up Congenital Heart Disease of the European Society of Cardiology (ESC). *European heart journal* **31**, 2915-2957 (2010).

3   Suradi, H. & Hijazi, Z. M. Current management of coarctation of the aorta. *Global Cardiology Science and Practice* **2015**, 44 (2015).

4   Ma, L. *et al.* Simultaneously surgical management of adult complex coarctation of aorta concomitant with intracardiac abnormality. *Journal of thoracic disease* **10**, 5842 (2018).

5   Kaya, U., Colak, A., Becit, N., Ceviz, M. & Kocak, H. Surgical management of aortic coarctation from infant to adult. *The Eurasian journal of medicine* **50**, 14 (2018).

6   Yin, K. *et al.* Surgical management of aortic coarctation in adolescents and adults. *Interactive cardiovascular and thoracic surgery* **24**, 430-435 (2017).

7   Shih, M.-C. P., Tholpady, A., Kramer, C. M., Sydnor, M. K. & Hagspiel, K. D. Surgical and endovascular repair of aortic coarctation: normal findings and appearance of complications on CT angiography and MR angiography. *American Journal of Roentgenology* **187**, W302-W312 (2006).

8   Bouchart, F. *et al.* Coarctation of the aorta in adults: surgical results and long-term follow-up. *The Annals of thoracic surgery* **70**, 1483-1488 (2000).

9   Campbell, M. Natural history of coarctation of the aorta. *Heart* **32**, 633-640 (1970).

10   Yamashita, K. *et al.* Surgical treatment for isolated coarctation of the aorta in an adult patient. *General thoracic and cardiovascular surgery* **56**, 340-343 (2008).

11   Al-Husayni, F., Samman, A., Althobaiti, M., Alghamdi, A. & Alkashkari, W. Late Complications After Previous Surgical Repair for Coarctation With Extra-Anatomic Bypass Graft: Report on Two Cases. *Cureus* **13** (2021).

12   Nakamura, E., Nakamura, K., Furukawa, K., Ishii, H. & Kawagoe, K. Selection of a surgical treatment approach for aortic coarctation in adolescents and adults. *Annals of Thoracic and Cardiovascular Surgery* **24**, 97-102 (2018).

13   Delmo Walter, E. M., Javier, M. F. d. M. & Hetzer, R. Extra-anatomical bypass in complex and recurrent aortic coarctation and hypoplastic arch. *Interactive cardiovascular and thoracic surgery* **25**, 400-406 (2017).

14   Beckmann, E. & Jassar, A. S. Coarctation repair—redo challenges in the adults: what to do? *Journal of visualized surgery* **4** (2018).

15　　Said, S. M., Burkhart, H. M., Dearani, J. A., Connolly, H. M. & Schaff, H. V. Ascending-to-descending aortic bypass: a simple solution to a complex problem. *The Annals of thoracic surgery* **97**, 2041-2048 (2014).

16　　Raina, T. *et al.* Extra Anatomic Bypass of Coarctation of the Aorta in an Adolescent: Avoiding Spinal Cord Ischemia. *MAMC Journal of Medical Sciences* **1**, 31 (2015).

17　　Grinda, J.-M., Macé, L., Dervanian, P., Folliguet, T. A. & Neveux, J.-Y. Bypass graft for complex forms of isthmic aortic coarctation in adults. *The Annals of thoracic surgery* **60**, 1299-1302 (1995).

18　　Su, C., Lee, D., Tran-Son-Tay, R. & Shyy, W. Fluid flow structure in arterial bypass anastomosis. (2005).

19　　Dey, S., Ibtida, T., Roy, C. K. & Sakib, N. in *2020 IEEE Region 10 Symposium (TENSYMP).* 1494-1497 (IEEE).

20　　Alkashkari, W., Al-Husayni, F., Alfouti, M., Alsofyani, R. & Alfawaz, S. Endovascular treatment for pseudoaneurysms after the surgical repair of aortic coarctation. *Cureus* **12** (2020).

21　　Alnasser, S. A., Vunnamadala, K. C., Preventza, O. A., Coselli, J. S. & de la Cruz, K. I. Endovascular repair of a pseudoaneurysm after multiple open repairs of aortic coarctation. *Texas Heart Institute Journal* **47**, 149-151 (2020).

22　　Khavandi, A. *et al.* Transcatheter and endovascular stent graft management of coarctation-related pseudoaneurysms. *Heart* **99**, 1275-1281 (2013).

23　　Bianco, V., Aranda-Michel, E., Kilic, A., Serna-Gallegos, D. & Sultan, I. Endovascular Repair of an Extra-Anatomic Bypass Graft Pseudoaneurysm in a Patient With Congenital Coarctation of the Aorta. *Circulation: Cardiovascular Imaging* **14**, e011403 (2021).

24　　Mulder, E. J., Van Bockel, J. H., Maas, J., van den Akker, P. J. & Hermans, J. Morbidity and mortality of reconstructive surgery of noninfected false aneurysms detected long after aortic prosthetic reconstruction. *Archives of Surgery* **133**, 45-49 (1998).

25　　Karaosmanoglu, A. D., Khawaja, R. D. A., Onur, M. R. & Kalra, M. K. CT and MRI of aortic coarctation: pre-and postsurgical findings. *American Journal of Roentgenology* **204**, W224-W233 (2015).

26　　Keshavarz-Motamed, Z., Garcia, J. & Kadem, L. Fluid dynamics of coarctation of the aorta and effect of bicuspid aortic valve. *PLoS one* **8**, e72394 (2013).

27　　Keshavarz-Motamed, Z., Garcia, J., Pibarot, P., Larose, E. & Kadem, L. Modeling the impact of concomitant aortic stenosis and coarctation of the aorta on left ventricular workload. *Journal of biomechanics* **44**, 2817-2825 (2011).

28　　Keshavarz-Motamed, Z. & Kadem, L. 3D pulsatile flow in a curved tube with coexisting model of aortic stenosis and coarctation of the aorta. *Medical engineering & physics* **33**, 315-324 (2011).

29　　Keshavarz-Motamed, Z. *et al.* Elimination of transcoarctation pressure gradients has no impact on left ventricular function or aortic shear stress after intervention

in patients with mild coarctation. *JACC: Cardiovascular Interventions* **9**, 1953-1965 (2016).

30   Marsden, A. L. & Esmaily-Moghadam, M. Multiscale modeling of cardiovascular flows for clinical decision support. *Applied Mechanics Reviews* **67**, 030804 (2015).

31   Sadeghi, R., Khodaei, S., Ganame, J. & Keshavarz-Motamed, Z. towards non-invasive computational-mechanics and imaging-based diagnostic framework for personalized cardiology for coarctation. *Scientific Reports* **10**, 1-19 (2020).

32   Richter, Y. & Edelman, E. R.   (Am Heart Assoc, 2006).

33   Barron, D. J., Lamb, R. K., Ogilvie, B. C. & Monro, J. L. Technique for extraanatomic bypass in complex aortic coarctation. *The Annals of thoracic surgery* **61**, 241-244 (1996).

34   Wang, R. *et al.* Treatment of complex coarctation and coarctation with cardiac lesions using extra-anatomic aortic bypass. *Journal of vascular surgery* **51**, 1203-1208 (2010).

35   Dutra, R. F., Zinani, F. S., Rocha, L. A. & Biserni, C. Constructal design of an arterial bypass graft. *Heat Transfer* **49**, 4019-4039 (2020).

36   Ramachandra, A. B., Kahn, A. M. & Marsden, A. L. Patient-specific simulations reveal significant differences in mechanical stimuli in venous and arterial coronary grafts. *Journal of cardiovascular translational research* **9**, 279-290 (2016).

37   Impiombato, A. N., Zinani, F. S. F., Rocha, L. A. O. & Biserni, C. Constructal Design of an Idealize Arterial Bypass Graft: Effect of the Bypass Attachment Pointon Resistance to Flow. *Journal of Applied and Computational Mechanics* (2020).

38   Lee, D., Su, J. & Liang, H. A numerical simulation of steady flow fields in a bypass tube. *Journal of Biomechanics* **34**, 1407-1416 (2001).

39   Ku, J. P., Elkins, C. J. & Taylor, C. A. Comparison of CFD and MRI flow and velocities in an in vitro large artery bypass graft model. *Annals of Biomedical engineering* **33**, 257-269 (2005).

40   Marsden, A. L. Simulation based planning of surgical interventions in pediatric cardiology. *Physics of fluids* **25**, 101303 (2013).

41   Succi, S. *The lattice Boltzmann equation: for fluid dynamics and beyond*. (Oxford university press, 2001).

42   Keshavarz-Motamed, Z. A diagnostic, monitoring, and predictive tool for patients with complex valvular, vascular and ventricular diseases. *Scientific reports* **10**, 1-19 (2020).

43   Mittal, R., Simmons, S. & Udaykumar, H. Application of large-eddy simulation to the study of pulsatile flow in a modeled arterial stenosis. *Journal of biomechanical engineering* **123**, 325-332 (2001).

44   Bhatnagar, P. L., Gross, E. P. & Krook, M. A model for collision processes in gases. I. Small amplitude processes in charged and neutral one-component systems. *Physical review* **94**, 511 (1954).

45   Mohamad, A. A. *Lattice Boltzmann method: fundamentals and engineering applications with computer codes*. (Springer Science & Business Media, 2011).

46   d'Humieres, D. Generalized lattice-Boltzmann equations. *Progress in Astronautics and Aeronautics* **159**, 450-450 (1994).

47   Sukop, M. & DT Thorne, J. *Lattice Boltzmann Modeling* (Springer, Berlin, Heidelberg, 2006).

48   Nathen, P., Gaudlitz, D., Krause, M. & Kratzke, J. in *21st AIAA Computational Fluid Dynamics Conference. American Institute of Aeronautics and Astronautics.*

49   Bouzidi, M. h., Firdaouss, M. & Lallemand, P. Momentum transfer of a Boltzmann-lattice fluid with boundaries. *Physics of fluids* **13**, 3452-3459 (2001).

50   Porter, B., Zauel, R., Stockman, H., Guldberg, R. & Fyhrie, D. 3-D computational modeling of media flow through scaffolds in a perfusion bioreactor. *Journal of biomechanics* **38**, 543-549 (2005).

51   LaDisa Jr, J. F. *et al.* Circumferential vascular deformation after stent implantation alters wall shear stress evaluated with time-dependent 3D computational fluid dynamics models. *Journal of applied physiology* **98**, 947-957 (2005).

52   Skordos, P. Initial and boundary conditions for the lattice Boltzmann method. *Physical Review E* **48**, 4823 (1993).

53   Heuveline, V., Krause, M. J. & Latt, J. Towards a hybrid parallelization of lattice Boltzmann methods. *Computers & Mathematics with Applications* **58**, 1071-1080 (2009).

54   Henn, T., Heuveline, V., Krause, M. J. & Ritterbusch, S. in *International Workshop on Statistical Atlases and Computational Models of the Heart.* 34-43 (Springer).

55   Mirzaee, H. *et al.* MRI-based computational hemodynamics in patients with aortic coarctation using the lattice Boltzmann methods: clinical validation study. *Journal of Magnetic Resonance Imaging* **45**, 139-146 (2017).

56   Jin, S., Oshinski, J. & Giddens, D. P. Effects of wall motion and compliance on flow patterns in the ascending aorta. *Journal of biomechanical engineering* **125**, 347-354 (2003).

57   Keshavarz-Motamed, Z. *et al.* The role of aortic compliance in determination of coarctation severity: lumped parameter modeling, in vitro study and clinical evaluation. *Journal of biomechanics* **48**, 4229-4237 (2015).

58   Pironet, A. *et al.* Simulation of left atrial function using a multi-scale model of the cardiovascular system. *PloS one* **8**, e65146 (2013).

59   Chaudhry, Q. A. A Gaussian function model for simulation of complex environmental sensing. *Complex Adaptive Systems Modeling* **3**, 1-4 (2015).

60   McDowell, S. A. A simple derivation of the Boltzmann distribution. *Journal of chemical education* **76**, 1393 (1999).

61   Mynard, J., Davidson, M., Penny, D. & Smolich, J. A simple, versatile valve model for use in lumped parameter and one-dimensional cardiovascular models.

International Journal for Numerical Methods in Biomedical Engineering **28**, 626-641 (2012).

62   Broomé, M., Maksuti, E., Bjällmark, A., Frenckner, B. & Janerot-Sjöberg, B. Closed-loop real-time simulation model of hemodynamics and oxygen transport in the cardiovascular system. *Biomedical engineering online* **12**, 1-20 (2013).

63   Moss, R. L., Razumova, M. & Fitzsimons, D. P. Myosin crossbridge activation of cardiac thin filaments: implications for myocardial function in health and disease. *Circulation research* **94**, 1290-1300 (2004).

64   Brown, K. A. & Ditchey, R. V. Human right ventricular end-systolic pressure-volume relation defined by maximal elastance. *Circulation* **78**, 81-91 (1988).

65   Dell'italia, L. J. & Walsh, R. A. Application of a time varying elastance model to right ventricular performance in man. *Cardiovascular research* **22**, 864-874 (1988).

66   Gleason, W. L. & Braunwald, E. Studies on the first derivative of the ventricular pressure pulse in man. *The Journal of clinical investigation* **41**, 80-91 (1962).

67   Kass, D. A., Md, M. M., Phd, W. G., Brinker Fsca, J. A., Md & Maughan, W. L. Use of a conductance (volume) catheter and transient inferior vena caval occlusion for rapid determination of pressure-volume relationships in man. *Catheterization and cardiovascular diagnosis* **15**, 192-202 (1988).

68   Liang, F., Takagi, S., Himeno, R. & Liu, H. Multi-scale modeling of the human cardiovascular system with applications to aortic valvular and arterial stenoses. *Medical & biological engineering & computing* **47**, 743-755 (2009).

69   Maniar, H. S. *et al.* Impact of pericardial restraint on right atrial mechanics during acute right ventricular pressure load. *American Journal of Physiology-Heart and Circulatory Physiology* **284**, H350-H357 (2003).

70   Senzaki, H., Chen, C.-H. & Kass, D. A. Single-beat estimation of end-systolic pressure-volume relation in humans: a new method with the potential for noninvasive application. *Circulation* **94**, 2497-2506 (1996).

71   Stergiopulos, N., Meister, J.-J. & Westerhof, N. Determinants of stroke volume and systolic and diastolic aortic pressure. *American Journal of Physiology-Heart and Circulatory Physiology* **270**, H2050-H2059 (1996).

72   Takeuchi, M., Odake, M., Takaoka, H., Hayashi, Y. & Yokoyama, M. Comparison between preload recruitable stroke work and the end-systolic pressure–volume relationship in man. *European heart journal* **13**, 80-84 (1992).

73   Van de Werf, F. *et al.* Diastolic properties of the left ventricle in normal adults and in patients with third heart sounds. *Circulation* **69**, 1070-1078 (1984).

74   Tanné, D., Kadem, L., Rieu, R. & Pibarot, P. Hemodynamic impact of mitral prosthesis-patient mismatch on pulmonary hypertension: an in silico study. *Journal of Applied Physiology* **105**, 1916-1926 (2008).

75   Stergiopulos, N., Segers, P. & Westerhof, N. Use of pulse pressure method for estimating total arterial compliance in vivo. *American Journal of Physiology-Heart and Circulatory Physiology* **276**, H424-H428 (1999).

76   Stankovic, Z., Allen, B. D., Garcia, J., Jarvis, K. B. & Markl, M. 4D flow imaging with MRI. *Cardiovascular diagnosis and therapy* **4**, 173 (2014).

77   Van Ooij, P. *et al.* Age-related changes in aortic 3D blood flow velocities and wall shear stress: implications for the identification of altered hemodynamics in patients with aortic valve disease. *Journal of Magnetic Resonance Imaging* **43**, 1239-1249 (2016).

78   Marlevi, D. *et al.* Estimation of cardiovascular relative pressure using virtual work-energy. *Scientific reports* **9**, 1-16 (2019).

79   Hassanabad, A. F. *et al.* Pressure drop mapping using 4D flow MRI in patients with bicuspid aortic valve disease: A novel marker of valvular obstruction. *Magnetic resonance imaging* **65**, 175-182 (2020).

80   Garcia, J., Barker, A. J. & Markl, M. The role of imaging of flow patterns by 4D flow MRI in aortic stenosis. *JACC: Cardiovascular Imaging* **12**, 252-266 (2019).

81   Garcia, D. A fast all-in-one method for automated post-processing of PIV data. *Experiments in fluids* **50**, 1247-1259 (2011).

82   Garcia, D. Robust smoothing of gridded data in one and higher dimensions with missing values. *Computational statistics & data analysis* **54**, 1167-1178 (2010).

83   Baiocchi, M. *et al.* Effects of Choice of Medical Imaging Modalities on a Non-invasive Diagnostic and Monitoring Computational Framework for Patients With Complex Valvular, Vascular, and Ventricular Diseases Who Undergo Transcatheter Aortic Valve Replacement. *Frontiers in Bioengineering and Biotechnology*, 389 (2021).

84   Keshavarz-Motamed, Z. *et al.* Non-invasive determination of left ventricular workload in patients with aortic stenosis using magnetic resonance imaging and Doppler echocardiography. *PLoS One* **9** (2014).

85   Keshavarz-Motamed, Z. *et al.* A new approach for the evaluation of the severity of coarctation of the aorta using Doppler velocity index and effective orifice area: in vitro validation and clinical implications. *Journal of biomechanics* **45**, 1239-1245 (2012).

86   Keshavarz-Motamed, Z. *et al.* Effect of coarctation of the aorta and bicuspid aortic valve on flow dynamics and turbulence in the aorta using particle image velocimetry. *Experiments in fluids* **55**, 1-16 (2014).

87   Benevento, E., Djebbari, A., Keshavarz-Motamed, Z., Cecere, R. & Kadem, L. Hemodynamic changes following aortic valve bypass: a mathematical approach. *PloS one* **10**, e0123000 (2015).

88   Ben-Assa, E. *et al.* Ventricular stroke work and vascular impedance refine the characterization of patients with aortic stenosis. *Science translational medicine* **11**, eaaw0181 (2019).

89   Keshavarz-Motamed, Z. *et al.* Mixed valvular disease following transcatheter aortic valve replacement: quantification and systematic differentiation using clinical measurements and image-based patient-specific in silico modeling. *Journal of American Heart Association* **9**, e015063 (2020).

90   Khodaei, S. *et al.* Personalized intervention cardiology with transcatheter aortic valve replacement made possible with a non-invasive monitoring and diagnostic framework. *Scientific Reports* **11**, 1-28 (2021).

91   Khodaei, S. *et al.* Towards a non-invasive computational diagnostic framework for personalized cardiology of transcatheter aortic valve replacement in interactions with complex valvular, ventricular and vascular disease. *International Journal of Mechanical Sciences* **202**, 106506 (2021).

92   Liu, S. Q., Tang, D., Tieche, C. & Alkema, P. K. Pattern formation of vascular smooth muscle cells subject to nonuniform fluid shear stress: mediation by gradient of cell density. *American Journal of Physiology-Heart and Circulatory Physiology* **285**, H1072-H1080 (2003).

93   Menon, A. *et al.* Altered hemodynamics, endothelial function, and protein expression occur with aortic coarctation and persist after repair. *American Journal of Physiology-Heart and Circulatory Physiology* **303**, H1304-H1318 (2012).

94   Oliver, J. M. *et al.* Risk factors for aortic complications in adults with coarctation of the aorta. *Journal of the American College of Cardiology* **44**, 1641-1647 (2004).

95   Parks, W. J. *et al.* Incidence of aneurysm formation after Dacron patch aortoplasty repair for coarctation of the aorta: long-term results and assessment utilizing magnetic resonance angiography with three-dimensional surface rendering. *Journal of the American College of Cardiology* **26**, 266-271 (1995).

96   Subbotin, V. M. Analysis of arterial intimal hyperplasia: review and hypothesis. *Theoretical Biology and Medical Modelling* **4**, 1-20 (2007).

97   Haruguchi, H. & Teraoka, S. Intimal hyperplasia and hemodynamic factors in arterial bypass and arteriovenous grafts: a review. *Journal of Artificial Organs* **6**, 227-235 (2003).

98   Post, A. *et al.* Elucidating the role of graft compliance mismatch on intimal hyperplasia using an ex vivo organ culture model. *Acta biomaterialia* **89**, 84-94 (2019).

99   Lemson, M., Tordoir, J., Daemen, M. & Kitslaar, P. Intimal hyperplasia in vascular grafts. *European Journal of Vascular and Endovascular Surgery* **19**, 336-350 (2000).

100   Kotelis, D. *et al.* Endovascular repair of pseudoaneurysms after open surgery for aortic coarctation. *Interactive cardiovascular and thoracic surgery* **22**, 26-31 (2016).

101   Goto, T., Nishi, H., Kitahara, M., Sakakibara, S. & Kakizawa, Y. Successful hybrid TEVAR for distal anastomotic pseudoaneurysm and coarctation following previous palliative left subclavian artery to descending aorta bypass: A case report. *International Journal of Surgery Case Reports* **74**, 124-127 (2020).

102   Ashizawa, N. *et al.* A rare case of aortic tube graft occlusion 35 years after coarctectomy. *The Annals of thoracic surgery* **75**, 1961-1963 (2003).

103   Tochii, M. *et al.* Pseudoaneurysm of ascending aorta 16 years after coronary artery bypass grafting. *Annals of Thoracic and Cardiovascular Surgery* **17**, 323-325 (2011).

104   Mojadidi, M. K. *et al.* Coronary artery bypass graft pseudoaneurysm from saphenous vein graft stent fracture. *Journal of cardiology cases* **15**, 206-208 (2017).

105   Hope, M. D., Hope, T. A., Urbania, T. H. & Higgins, C. B. Four-dimensional flow magnetic resonance imaging with wall shear stress analysis before and after repair of aortopulmonary fistula. *Circulation: Cardiovascular Imaging* **3**, 766-768 (2010).

106   Lu, Y.-Q., Yao, F., Shang, A.-D. & Pan, J. Pseudoaneurysm of the aortic arch: A rare case report of pulmonary cancer complication. *Medicine* **95** (2016).

107   Frances, C., Romero, A. & Grady, D. Left ventricular pseudoaneurysm. *Journal of the American College of Cardiology* **32**, 557-561 (1998).

Chapter 6: Conclusion and future directions

6.1   Conclusion

Flow pattern in COA plays an important role in accurate and early diagnosis and it may help the clinician optimize the plan treatment. However, diagnostic tools in clinics are not well developed yet. Currently, clinical decisions are largely made based on the anatomy. Moreover, clinics mainly relies on cardiac catheterization data to evaluate pressure and flow through heart and circulatory system which is not only invasive, expensive, and high risk but also not practical in routine daily clinical practice or serial follow-up examinations. Other diagnosis methods including Echo-PIV, phase contrast MRI and Echocardiography, although there are promising imaging modality techniques, suffer from low temporal and spatial resolution. In this study, we developed a non-invasive method for assessing the CoA physiology, using lattice Boltzmann method, lumped parameter modelling and personalized medical images modalities, that can numerically compute the blood flow fields. The diagnostic information, that framework can provide, is vitally needed to improve clinical outcomes, to assess patient risk and to plan treatment. We validated this framework against clinical cardiac catheterization data, calculation using conventional finite-volume method, clinical Doppler echocardiography measurements and finally 4D flow MRI measurements.

The other line of current study was to investigate the impact of COA and mixed valvular diseases (MVD) on aortic fluid dynamics in patients with COA and MVD. A complicating factor of COA is its common association with mixed valvular diseases which include varying combinations of aortic and mitral valve pathologies, e.g., aortic

stenosis (AS), aortic regurgitations (AR), mitral stenosis (MS) and mitral regurgitation (MR). Although COA is readily diagnosed and interventional and surgical treatments are employed, argument and uncertainty persist when COA coexists with MVD. The optimal course of intervention for a patient with coexisting MVD and COA is an area of contention and uncertainty. Our observations summarized as follows:

- *To precisely assess the COA severity, both presence and severity of MVD matter:* Our results show that interaction of MVD with COA is amplifying irregular flow patterns, especially downstream of COA and it may contribute to speed up the progression of diseases (e.g. aneurysm, rupture, and dissection) in this region. In addition, high-pressure loss downstream of the COA because of COA and MVD Coexistence can augment the flow resistance and ultimately lead to collapse the aortic wall. The results suggest that not only the severity of the COA, but also the presence and the severity of the MVD should be considered in the evaluation of risk factors in patients with COA. It seems that some more aggressive surgical approaches may be required as regularly chosen current surgical techniques may not be optimal for patients with both COA

- *Catheter pressure gradient fails to reflect the effect of MVD on the clinical assessment of COA hemodynamics:* For patients with COA who also suffer from AS, MS, MR, or a combination, we did not observe major effects due to these valvular diseases on the catheter pressure gradient. In contrast, similar to observations about DE pressure gradients, the coexistence of AR with COA

greatly amplified the catheter COA pressure gradient, leading to an overestimation of the severity of coarctation.

- *Doppler echocardiography COA pressure gradient is a poor indicator of COA severity:* We observed that the pressure gradient across the site of COA, when measured using Doppler echocardiography is not heavily affected by the presence of AS or MS alone and it was solely a result of the presence of the COA. Moreover, COA pressure gradient elevated severely in the presence of MR and AR. This reveals that COA pressure gradient may be overestimated in presence of MR and/or AR.

- *MVD may exacerbate the COA hemodynamics:* COA hemodynamics were not dramatically changed in patient with AS alone or MS alone, however, AS or MS may exacerbate the COA hemodynamics when they coexist with AR and/or MR. In addition, maximum velocity downstream, kinetic energy and wall shear stress of the COA in all patients with AR alone was drastically increased. The condition deteriorates when COA and AR coexist alongside MR.

The other intention of current study was investigation of hemodynamics after bypass grafts surgery. The mortality rate during the first year after bypass graft surgery is quite high, well above the normal threshold. Our results can provide unique insights about possible reasons for graft failure summarized as follows:

- *Bypass grafting may not improve the aorta hemodynamics:* Bypass graft exacerbated aortic wall shear stress near the junctions of anastomoses. It may

result in vessel distensibility and compliance and potentially lead to arterial remodeling, aneurysm, rupture and dissection.

- *Bypass graft may lead to intimal hyperplasia due to the persistent abnormal aortic hemodynamics:* Our findings suggest that bypass grafting improved hemodynamic metrics (reduction in shear stresses, flow velocities, and turbulent characteristics) in some patients however, the hemodynamic conditions worsened in others depending on the geometry of the bypass graft. As a result of abnormal fluid dynamics caused by bypass graft, the vessel wall attempts to correct the flow disruption by intimal thickening, may causing the narrowing of the vessel.

- *Bypass graft may lead to pseudoaneurysm formation and potential aortic rupture due to aortic wall disruptions:* pseudoaneurysm is a common long-term complication following a bypass graft surgery for COA. Disturbed flow conditions, including elevated velocity flow, high wall shear stresses and vortical flow, may lead to wall complications and pseudoaneurysm. Our findings in this study show that all patients investigated in this study exhibit at least some of the following abnormal hemodynamics parameters: elevated velocity magnitude, elevated turbulence characteristics, and elevated wall shear stress, at the bypass graft junction regions. All the mentioned abnormal hemodynamic metrics may lead to the formation of pseudoaneurysm.

In conclusion, our individualized image-based framework may serve as a valuable tool to non-invasively investigate the flow dynamics of COA before and after the intervention/surgeries, and in coexistence of mixed valvular diseases. The diagnostic

information, that the framework can provide, is vitally needed to improve clinical outcomes, to assess patient risk and to plan treatment.

6.2   Future directions

- We developed a computational fluid dynamics framework using 3-D Lattice Boltzmann method (Large eddy simulation, Smagorinsky subgrid scale model) and lumped parameter model to simulate both the local and global hemodynamics in patients with valvular diseases and COA. One limitation of our simulations is lack of modeling of the aortic valves. Diseased aortic valve (e.g., bicuspid aortic valve or aortic stenosis) create complex blood flow patterns in the thoracic aorta that influence the local hemodynamics in the coarctation region. Future Lattice Boltzmann simulations should consider the interactions between the fluid and structure and investigate the effect of dynamical opening and closing of the aortic valve leaflets on the vortex dynamics in the aorta.

- Our models were formulated under the assumption of rigid walls. Fluid-structure interaction (FSI) analysis would address this limitation by taking into account displacements, deformations and elasticity of the aorta. This would come at a higher computational cost. This assumption is proved to be a realistic one in literature, especially in CoA patients who are usually subject to hypertension and reduced compliance in the aorta. However, it would be important to investigate how much the results seen in this study would be altered.

- Augmentation of 4D flow MRI data with CFD training machine learning networks can produce noise-free super resolution 4D flow images. Compared to 4D flow MRI, CFD can achieve higher temporal and spatial resolutions. Using high resolution patient specific CFD data to train a convolutional neural network, and then using the trained neural network to enhance 4D flow MRI velocity fields could be another interesting future work.

References

(Used in Chapter 1 and Chapter 6)

1   Sinning, C. *et al.* Bicuspid aortic valve and aortic coarctation in congenital heart disease—important aspects for treatment with focus on aortic vasculopathy. *Cardiovascular diagnosis and therapy* **8**, 780 (2018).

2   Mostefa-Kara, M., Houyel, L. & Bonnet, D. Anatomy of the ventricular septal defect in congenital heart defects: a random association? *Orphanet journal of rare diseases* **13**, 1-8 (2018).

3   Miettinen, O. S., Reiner, M. L. & Nadas, A. S. Seasonal incidence of coarctation of the aorta. *British heart journal* **32**, 103 (1970).

4   Elseed, A., Shinebourne, E. A. & Paneth, M. Manifestation of juxtaductal coarctation after surgical ligation of persistent ductus arteriosus in infancy. *British heart journal* **36**, 687 (1974).

5   Teo, L. L., Cannell, T., Babu-Narayan, S. V., Hughes, M. & Mohiaddin, R. H. Prevalence of associated cardiovascular abnormalities in 500 patients with aortic coarctation referred for cardiovascular magnetic resonance imaging to a tertiary center. *Pediatric cardiology* **32**, 1120-1127 (2011).

6   Rinnström, D. *Coarctation of the aorta: register and imaging studies*, Umeå universitet, (2016).

7   Gatzoulis, M. A., Webb, G. D. & Daubeney, P. E. *Diagnosis and Management of Adult Congenital Heart Disease E-Book*. (Elsevier Health Sciences, 2010).

8   Sievers, H.-H. & Schmidtke, C. A classification system for the bicuspid aortic valve from 304 surgical specimens. *The Journal of thoracic and cardiovascular surgery* **133**, 1226-1233 (2007).

9   Schaefer, B. M. *et al.* The bicuspid aortic valve: an integrated phenotypic classification of leaflet morphology and aortic root shape. *Heart* **94**, 1634-1638 (2008).

10   Siu, S. C. & Silversides, C. K. Bicuspid aortic valve disease. *Journal of the American College of Cardiology* **55**, 2789-2800 (2010).

11   Penny, D. J. & Vick III, G. W. Ventricular septal defect. *The Lancet* **377**, 1103-1112 (2011).

12   Schneider, D. J. & Moore, J. W. Patent ductus arteriosus. *Circulation* **114**, 1873-1882 (2006).

13   Crafoord, C. & Nylin, G. Congenital coarctation of the aorta and its surgical treatment. *Journal of Thoracic Surgery* **14**, 347-361 (1945).

14   Covella, M. *et al.* Echocardiographic aortic root dilatation in hypertensive patients: a systematic review and meta-analysis. *Journal of hypertension* **32**, 1928-1935 (2014).

15   Koller, M., Rothlin, M. & Senning, Å. Coarctation of the aorta: review of 362 operated patients. Long-term follow-up and assessment of prognostic variables. *European heart journal* **8**, 670-679 (1987).

16   Cohen, M., Fuster, V., Steele, P., Driscoll, D. & McGoon, D. Coarctation of the aorta. Long-term follow-up and prediction of outcome after surgical correction. *Circulation* **80**, 840-845 (1989).

17   Ong, C. M., Canter, C. E., Gutierrez, F. R., Sekarski, D. R. & Goldring, D. R. Increased stiffness and persistent narrowing of the aorta after successful repair of coarctation of the aorta: relationship to left ventricular mass and blood pressure at rest and with exercise. *American heart journal* **123**, 1594-1600 (1992).

18   Chen, S. *et al.* Prevalence and prognostic implication of restenosis or dilatation at the aortic coarctation repair site assessed by cardiovascular MRI in adult patients late after coarctation repair. *International journal of cardiology* **173**, 209-215 (2014).

19   Rubay, J. *et al.* Surgical repair of coarctation of the aorta in infants under one year of age. Long-term results in 146 patients comparing subclavian flap angioplasty and modified end-to-end anastomosis. *The Journal of cardiovascular surgery* **33**, 216-222 (1992).

20   Cramer, J. W. *et al.* Aortic aneurysms remain a significant source of morbidity and mortality after use of Dacron® patch aortoplasty to repair coarctation of the aorta: results from a single center. *Pediatric cardiology* **34**, 296-301 (2013).

21   Rinnström, D., Engström, K. G. & Johansson, B. Subtypes of bicuspid aortic valves in coarctation of the aorta. *Heart and vessels* **29**, 354-363 (2014).

22   Thanassoulis, G. *et al.* Retrospective study to identify predictors of the presence and rapid progression of aortic dilatation in patients with bicuspid aortic valves. *Nature clinical practice Cardiovascular medicine* **5**, 821-828 (2008).

23   Ergin, M. A. *et al.* Surgical treatment of the dilated ascending aorta: when and how? *The Annals of thoracic surgery* **67**, 1834-1839 (1999).

24   Kearney, P. M. *et al.* Global burden of hypertension: analysis of worldwide data. *The lancet* **365**, 217-223 (2005).

25   Nelson, J. S., Stone, M. L. & Gangemi, J. J. in *Critical heart disease in infants and children*   551-564. e553 (Elsevier, 2019).

26   Rinnstrom, D., Engstrom, K.-G., Ugander, M. & Johansson, B. Factors associated with left ventricular hypertrophy in adults with surgically repaired coarctation of the aorta. *European Heart Journal* **34** (2013).

27   Opio, J., Kiguli-Malwadde, E. & Byanyima, R. Coarctation of aorta presenting as acute haemorrhagic stroke in a 14-year old. A case report. *African health sciences* **8**, 256-258 (2008).

28   Leandro, J. *et al.* Ambulatory blood pressure monitoring and left ventricular mass and function after successful surgical repair of coarctation of the aorta. *Journal of the American College of Cardiology* **20**, 197-204 (1992).

29   Khouri, M. G., Peshock, R. M., Ayers, C. R., de Lemos, J. A. & Drazner, M. H. A 4-tiered classification of left ventricular hypertrophy based on left ventricular geometry: the Dallas heart study. *Circulation: Cardiovascular Imaging* **3**, 164-171 (2010).

30   Brown, M. L. *et al.* Coarctation of the aorta: lifelong surveillance is mandatory following surgical repair. *Journal of the American College of Cardiology* **62**, 1020-1025 (2013).

31   Gross, R. E. Coarctation of the aorta. *Circulation* **7**, 757-768 (1953).

32   Crossland, D., Furness, J., Abu-Harb, M., Sadagopan, S. & Wren, C. Variability of four limb blood pressure in normal neonates. *Archives of Disease in Childhood-Fetal and Neonatal Edition* **89**, F325-F327 (2004).

33   Keshavarz-Motamed, Z. *Flow Dynamics in Human Aorta with Coexisting Models of Bicuspid Aortic Stenosis and Coarctation of the Aorta*, Concordia University, (2011).

34   Budoff, M. J., Shittu, A. & Roy, S.   (Elsevier, 2013).

35   Stankovic, Z., Allen, B. D., Garcia, J., Jarvis, K. B. & Markl, M. 4D flow imaging with MRI. *Cardiovascular diagnosis and therapy* **4**, 173 (2014).

36   Rose-Felker, K. *et al.* Preoperative use of CT angiography in infants with coarctation of the aorta. *World Journal for Pediatric and Congenital Heart Surgery* **8**, 196-202 (2017).

37   Muzzarelli, S. *et al.* Diagnostic value of the flow profile in the distal descending aorta by phase-contrast magnetic resonance for predicting severe coarctation of the aorta. *Journal of Magnetic Resonance Imaging* **33**, 1440-1446 (2011).

38   Dijkema, E. J., Leiner, T. & Grotenhuis, H. B. Diagnosis, imaging and clinical management of aortic coarctation. *Heart* **103**, 1148-1155 (2017).

39   Waldhausen, J. A. Repair of coarctation of the aorta with a subclavian flap. *J Thorac Cardiovasc Surg* **51**, 532-533 (1966).

40   Beckmann, E. & Jassar, A. S. Coarctation repair—redo challenges in the adults: what to do? *Journal of visualized surgery* **4** (2018).

41   Backer, C. L., Paape, K., Zales, V. R., Weigel, T. J. & Mavroudis, C. Coarctation of the aorta: repair with polytetrafluoroethylene patch aortoplasty. *Circulation* **92**, 132-136 (1995).

42   Diemont, F. F., Chemla, E. S., Julia, P. L., Sirieix, D. & Fabiani, J.-N. Upper limb ischemia after subclavian flap aortoplasty: unusual long-term complication. *The Annals of thoracic surgery* **69**, 1576-1578 (2000).

43   Krasuski, R. A. & Fouad-Tarazi, F. in *Comprehensive Hypertension*   923-930 (Elsevier, 2007).

44   Grinda, J.-M., Macé, L., Dervanian, P., Folliguet, T. A. & Neveux, J.-Y. Bypass graft for complex forms of isthmic aortic coarctation in adults. *The Annals of thoracic surgery* **60**, 1299-1302 (1995).

45   Ma, L. *et al.* Simultaneously surgical management of adult complex coarctation of aorta concomitant with intracardiac abnormality. *Journal of thoracic disease* **10**, 5842 (2018).

46   Said, S. M., Burkhart, H. M., Dearani, J. A., Connolly, H. M. & Schaff, H. V. Ascending-to-descending aortic bypass: a simple solution to a complex problem. *The Annals of thoracic surgery* **97**, 2041-2048 (2014).

47   Su, C., Lee, D., Tran-Son-Tay, R. & Shyy, W. Fluid flow structure in arterial bypass anastomosis. (2005).

48   Dey, S., Ibtida, T., Roy, C. K. & Sakib, N. in *2020 IEEE Region 10 Symposium (TENSYMP).* 1494-1497 (IEEE).

49   Alkashkari, W., Al-Husayni, F., Alfouti, M., Alsofyani, R. & Alfawaz, S. Endovascular treatment for pseudoaneurysms after the surgical repair of aortic coarctation. *Cureus* **12** (2020).

50   Alnasser, S. A., Vunnamadala, K. C., Preventza, O. A., Coselli, J. S. & de la Cruz, K. I. Endovascular repair of a pseudoaneurysm after multiple open repairs of aortic coarctation. *Texas Heart Institute Journal* **47**, 149-151 (2020).

51   Khavandi, A. *et al.* Transcatheter and endovascular stent graft management of coarctation-related pseudoaneurysms. *Heart* **99**, 1275-1281 (2013).

52   Bianco, V., Aranda-Michel, E., Kilic, A., Serna-Gallegos, D. & Sultan, I. Endovascular Repair of an Extra-Anatomic Bypass Graft Pseudoaneurysm in a Patient With Congenital Coarctation of the Aorta. *Circulation: Cardiovascular Imaging* **14**, e011403 (2021).

53   Mulder, E. J., Van Bockel, J. H., Maas, J., van den Akker, P. J. & Hermans, J. Morbidity and mortality of reconstructive surgery of noninfected false aneurysms detected long after aortic prosthetic reconstruction. *Archives of Surgery* **133**, 45-49 (1998).

54   Bourassa, M. G. The history of cardiac catheterization. *The Canadian journal of cardiology* **21**, 1011-1014 (2005).

55   Singer, M. I., MI, S. & TJ, D. Transluminal aortic balloon angioplasty for coarctation of the aorta in the newborn. (1982).

56   Meliota, G., Lombardi, M., Zaza, P., Tagliente, M. R. & Vairo, U. Balloon angioplasty of aortic coarctation in critically ill newborns using axillary artery access. *Annals of pediatric cardiology* **13**, 67 (2020).

57   Gewillig, M., Boshoff, D. & Budts, W. Catheter-based interventions of the aorta. *Pediatric and congenital cardiology, cardiac surgery and intensive care. London: Springer*, 1101-1125 (2014).

58   O'Laughlin, M. P., Perry, S. B., Lock, J. E. & Mullins, C. E. Use of endovascular stents in congenital heart disease. *Circulation* **83**, 1923-1939 (1991).

59   Taylor, C. A., Fonte, T. A. & Min, J. K. Computational fluid dynamics applied to cardiac computed tomography for noninvasive quantification of fractional flow reserve: scientific basis. *Journal of the American College of Cardiology* **61**, 2233-2241 (2013).

60   Randles, A., Frakes, D. H. & Leopold, J. A. Computational fluid dynamics and additive manufacturing to diagnose and treat cardiovascular disease. *Trends in biotechnology* **35**, 1049-1061 (2017).

61   Taylor, C. A. & Draney, M. T. Experimental and computational methods in cardiovascular fluid mechanics. *Annu. Rev. Fluid Mech.* **36**, 197-231 (2004).

62   Clough, R. E., Waltham, M., Giese, D., Taylor, P. R. & Schaeffter, T. A new imaging method for assessment of aortic dissection using four-dimensional phase contrast magnetic resonance imaging. *Journal of vascular surgery* **55**, 914-923 (2012).

63   Tsai, T. T. *et al.* Tear size and location impacts false lumen pressure in an ex vivo model of chronic type B aortic dissection. *Journal of vascular surgery* **47**, 844-851 (2008).

64   Kwon, S., Feinstein, J. A., Dholakia, R. J. & LaDisa, J. F. Quantification of local hemodynamic alterations caused by virtual implantation of three commercially available stents for the treatment of aortic coarctation. *Pediatric cardiology* **35**, 732-740 (2014).

65   Yoganathan, A. Fluid mechanics of aortic stenosis. *European heart journal* **9**, 13-17 (1988).

66   Ong, C. W. *et al.* Computational fluid dynamics modeling of hemodynamic parameters in the human diseased aorta: a systematic review. *Annals of vascular surgery* **63**, 336-381 (2020).

67   Keshavarz-Motamed, Z., Garcia, J. & Kadem, L. Fluid dynamics of coarctation of the aorta and effect of bicuspid aortic valve. *PLoS one* **8**, e72394 (2013).

68   Keshavarz-Motamed, Z. & Kadem, L. 3D pulsatile flow in a curved tube with coexisting model of aortic stenosis and coarctation of the aorta. *Medical engineering & physics* **33**, 315-324 (2011).

69   Qiao, A., Yin, W. & Chu, B. Numerical simulation of fluid–structure interaction in bypassed DeBakey III aortic dissection. *Computer methods in biomechanics and biomedical engineering* **18**, 1173-1180 (2015).

70   Cheng, Z. *et al.* Analysis of flow patterns in a patient-specific aortic dissection model. (2010).

71   Brown, A. G. *et al.* Accuracy vs. computational time: translating aortic simulations to the clinic. *Journal of biomechanics* **45**, 516-523 (2012).

72   Kim, H. J. *et al.* On coupling a lumped parameter heart model and a three-dimensional finite element aorta model. *Annals of biomedical engineering* **37**, 2153-2169 (2009).

73   Alimohammadi, M. *Aortic dissection: simulation tools for disease management and understanding*. (Springer, 2018).

74   Abraham, J., Sparrow, E. M. & Lovik, R. Unsteady, three-dimensional fluid mechanic analysis of blood flow in plaque-narrowed and plaque-freed arteries. *International Journal of Heat and Mass Transfer* **51**, 5633-5641 (2008).

75   Berthier, B., Bouzerar, R. & Legallais, C. Blood flow patterns in an anatomically realistic coronary vessel: influence of three different reconstruction methods. *Journal of biomechanics* **35**, 1347-1356 (2002).

76   Xiao, N. *Simulation of 3-D blood flow in the full systemic arterial tree and computational frameworks for efficient parameter estimation*. (Stanford University, 2014).

77   van Bakel, T. *Computational modeling of hemodynamics for surgical planning and device development*, Utrecht University, (2019).

78   McCullough, J. *et al.* Towards blood flow in the virtual human: efficient self-coupling of HemeLB. *Interface focus* **11**, 20190119 (2021).

79   Steinman, D. A. Assumptions in modelling of large artery hemodynamics. *Modeling of physiological flows*, 1-18 (2012).

80   Hager, A., Kanz, S., Kaemmerer, H., Schreiber, C. & Hess, J. Coarctation Long-term Assessment (COALA): significance of arterial hypertension in a cohort of 404 patients up to 27 years after surgical repair of isolated coarctation of the aorta, even in the absence of restenosis and prosthetic material. *The Journal of Thoracic and Cardiovascular Surgery* **134**, 738-745. e732 (2007).

81   Taelman, L. *Fluid-structure interaction simulation of (repaired) aortic coarctation*, Ghent University, (2014).

82   Segers, P., Taelman, L., Degroote, J., Bols, J. & Vierendeels, J. The aortic reservoir-wave as a paradigm for arterial haemodynamics: insights from three-dimensional fluid–structure interaction simulations in a model of aortic coarctation. *Journal of hypertension* **33**, 554-563 (2015).

83   Arzani, A., Dyverfeldt, P., Ebbers, T. & Shadden, S. C. In vivo validation of numerical prediction for turbulence intensity in an aortic coarctation. *Annals of biomedical engineering* **40**, 860-870 (2012).

84   Keshavarz-Motamed, Z. *et al.* Elimination of transcoarctation pressure gradients has no impact on left ventricular function or aortic shear stress after intervention in patients with mild coarctation. *JACC: Cardiovascular Interventions* **9**, 1953-1965 (2016).

85   Goubergrits, L. *et al.* The impact of MRI-based inflow for the hemodynamic evaluation of aortic coarctation. *Annals of biomedical engineering* **41**, 2575-2587 (2013).

86   Gallo, D. *et al.* On the use of in vivo measured flow rates as boundary conditions for image-based hemodynamic models of the human aorta: implications for

indicators of abnormal flow. *Annals of biomedical engineering* **40**, 729-741 (2012).

87   Kousera, C. *et al.* A numerical study of aortic flow stability and comparison with in vivo flow measurements. *Journal of biomechanical engineering* **135**, 011003 (2013).

88   LaDisa, J. F. *et al.* Computational simulations for aortic coarctation: representative results from a sampling of patients. (2011).

89   Taylor, C. A. & Steinman, D. A. Image-based modeling of blood flow and vessel wall dynamics: applications, methods and future directions. *Annals of biomedical engineering* **38**, 1188-1203 (2010).

90   Mirzaee, H. *et al.* MRI-based computational hemodynamics in patients with aortic coarctation using the lattice Boltzmann methods: clinical validation study. *Journal of Magnetic Resonance Imaging* **45**, 139-146 (2017).

91   Wendell, D. C. *et al.* Including aortic valve morphology in computational fluid dynamics simulations: initial findings and application to aortic coarctation. *Medical engineering & physics* **35**, 723-735 (2013).

92   Andersson, M. *Turbulence Descriptors in Arterial Flows: Patient-Specific Computational Hemodynamics*, Linköping University Electronic Press, (2021).

93   Chen, D. *et al.* A longitudinal study of Type-B aortic dissection and endovascular repair scenarios: computational analyses. *Medical engineering & physics* **35**, 1321-1330 (2013).

94   Updegrove, A. *et al.* SimVascular: an open source pipeline for cardiovascular simulation. *Annals of biomedical engineering* **45**, 525-541 (2017).

95   Mirramezani, M. & Shadden, S. C. A distributed lumped parameter model of blood flow. *Annals of Biomedical Engineering* **48**, 2870-2886 (2020).

96   Liu, X., Fan, Y., Deng, X. & Zhan, F. Effect of non-Newtonian and pulsatile blood flow on mass transport in the human aorta. *Journal of biomechanics* **44**, 1123-1131 (2011).

97   Molla, M. M. & Paul, M. LES of non-Newtonian physiological blood flow in a model of arterial stenosis. *Medical engineering & physics* **34**, 1079-1087 (2012).

98   Razavi, A., Shirani, E. & Sadeghi, M. Numerical simulation of blood pulsatile flow in a stenosed carotid artery using different rheological models. *Journal of biomechanics* **44**, 2021-2030 (2011).

99   Lantz, J. *On Aortic Blood Flow Simulations: Scale-Resolved Image-Based CFD*, Linköping University Electronic Press, (2013).

100   Lee, S.-W. & Steinman, D. A. On the relative importance of rheology for image-based CFD models of the carotid bifurcation. (2007).

101   Tse, K. M., Chiu, P., Lee, H. P. & Ho, P. Investigation of hemodynamics in the development of dissecting aneurysm within patient-specific dissecting aneurismal aortas using computational fluid dynamics (CFD) simulations. *Journal of biomechanics* **44**, 827-836 (2011).

102   Fung, G. S., Lam, S., Cheng, S. W. & Chow, K. On stent-graft models in thoracic aortic endovascular repair: a computational investigation of the hemodynamic factors. *Computers in biology and medicine* **38**, 484-489 (2008).

103   Albal, P. G., Montidoro, T. A., Dur, O. & Menon, P. G. in *International Workshop on Statistical Atlases and Computational Models of the Heart.* 83-93 (Springer).

104   Feiger, B. *et al.* Accelerating massively parallel hemodynamic models of coarctation of the aorta using neural networks. *Scientific reports* **10**, 1-13 (2020).

105   Andersson, M., Lantz, J., Ebbers, T. & Karlsson, M. Quantitative assessment of turbulence and flow eccentricity in an aortic coarctation: impact of virtual interventions. *Cardiovascular engineering and technology* **6**, 281-293 (2015).

106   Lantz, J., Ebbers, T., Engvall, J. & Karlsson, M. Numerical and experimental assessment of turbulent kinetic energy in an aortic coarctation. *Journal of biomechanics* **46**, 1851-1858 (2013).

107   Lantz, J., Gårdhagen, R. & Karlsson, M. Quantifying turbulent wall shear stress in a subject specific human aorta using large eddy simulation. *Medical engineering & physics* **34**, 1139-1148 (2012).

108   Gårdhagen, R., Carlsson, F. & Karlsson, M. Large eddy simulation of pulsating flow before and after CoA repair: CFD for intervention planning. *Advances in Mechanical Engineering* **7**, 971418 (2015).

109   Mittal, R., Simmons, S. & Udaykumar, H. Application of large-eddy simulation to the study of pulsatile flow in a modeled arterial stenosis. *J. Biomech. Eng.* **123**, 325-332 (2001).

110   Keshavarz-Motamed, Z., Garcia, J. & Kadem, L. in *2011 Annual International Conference of the IEEE Engineering in Medicine and Biology Society.* 182-185 (IEEE).

111   Lantz, J., Renner, J. & Karlsson, M. Wall shear stress in a subject specific human aorta—influence of fluid-structure interaction. *International Journal of Applied Mechanics* **3**, 759-778 (2011).

112   Ghalichi, F. *et al.* Low Reynolds number turbulence modeling of blood flow in arterial stenoses. *Biorheology* **35**, 281-294 (1998).

113   Schubert, C. *et al.* Assessment of hemodynamic responses to exercise in aortic coarctation using MRI-ergometry in combination with computational fluid dynamics. *Scientific Reports* **10**, 1-12 (2020).

114   Mazzeo, M. D. & Coveney, P. V. HemeLB: A high performance parallel lattice-Boltzmann code for large scale fluid flow in complex geometries. *Computer Physics Communications* **178**, 894-914 (2008).

115   Sadeghi, R., Khodaei, S., Ganame, J. & Keshavarz-Motamed, Z. Towards non-invasive computational-mechanics and imaging-based diagnostic framework for personalized cardiology for coarctation. *Scientific Reports* **10**, 1-19 (2020).

Appendix

❖ Appendix A$_1$: Summary of smoothing algorithm

The smoothing algorithm DCT-PLS proposed by Garcia allows robust smoothing of multidimensional gridded data. This algorithm is based on a penalized least squares (PLS) approach, combined with the discrete cosine transform (DCT). Consider a noisy signal $y = \hat{y} + \varepsilon$, where ε represents a Gaussian noise with zero mean and unknown variance and, $\hat{y}$ is velocity field supposed to be smooth. This velocity field contains some noise and outliers. Moreover, the de-aliasing process may have misclassified isolated pixels, which induces the presence of additional outlying values. Robust spline smoother DCT-PLS allows robust smoothing of multidimensional gridded data. the DCT-PLS algorithm is written as the following fixed-point iteration formula[1]:

$$\hat{y}_{\{k+1\}} = IDCT\left(\Gamma\, DCT\left(W(y - \hat{y}_{\{k\}}) + \hat{y}_{\{k\}}\right)\right) \tag{1}$$

where $\hat{y}$ represents the smoothed blood velocity field and $\hat{y}_{\{k\}}$ stands for $\hat{y}$ at the kth iteration step. The matrix W in Eq. (1) contains weight factors which make the smoothing algorithm robust and minimize the side effects of high leverage points and outliers. The filtering array Γ is derived from the eigenvalues of the DCT matrix. In 2-dimensions fields (m × n), it is obtained using[1-3]:

$$\Gamma_{i,j} = \left(1 + s\left(4 - 2\cos\frac{(i-1)\pi}{m} - 2\cos\frac{(j-1)\pi}{n}\right)^2\right)^{-1} \tag{2}$$

Real positive scalar s in equation (2) controls the degree of smoothing. To have unsupervised process and avoid any subjectivity in the choice of the amount of smoothness, the value of s was determined by minimizing the generalized cross-validation (GCV) score[1-4]. Detailed information on the algorithm structure and higher dimension fields could be found at original paper[1].

❖ Appendix A₂: Lattice Boltzmann model

➢ Governing equations

The simplest form of LBM equations is based on *Bhatnagar-Gross-Krook* (BGK) approximation with single relaxation time (SRT) [5] with the following discretized form [6]:

$$f_\alpha(x + e_\alpha \delta t, t + \delta t) - f_\alpha(x, t) = -1/\tau \ (f_\alpha(x, t) - f_\alpha^{eq}(x, t)) \tag{3}$$

For the BGK-LBM model with Q velocities, a set of distribution functions $\{f_\alpha | \alpha = 0, 1, \ldots, Q - 1\}$ is defined on each lattice node (x). Relaxation time, discrete time and Maxwell-Boltzmann equilibrium distribution function is represented by τ, t and f^{eq}, respectively. Note that the subscript α depends on the number of lattice vectors.

The LBM follows $D_x Q_y$ reference in which x and y are the number of dimensions and number of particle velocities, respectively. We considered the three-dimensional nineteen-velocity model, $D_3 Q_{19}$, to simulate blood flow across the aorta[7] with the discrete velocity vectors as follows [7]:

$$e_0, e_1, e_2, e_3, e_4, e_5, e_6, e_7, e_8, e_9, e_{10}, e_{11}, e_{12}, e_{13}, e_{14}, e_{15}, e_{16}, e_{17}, e_{18} = \tag{4}$$

$$\begin{bmatrix} 0 & 1 & 0 & -1 & 0 & 0 & 0 & 1 & -1 & -1 & 1 & 1 & 1 & -1 & -1 & 0 & 0 & 0 & 0 \\ 0 & 0 & 1 & 0 & -1 & 0 & 0 & 1 & 1 & -1 & -1 & 0 & 0 & 0 & 0 & 1 & 1 & -1 & -1 \\ 0 & 0 & 0 & 0 & 0 & 1 & -1 & 0 & 0 & 0 & 0 & 1 & -1 & -1 & 1 & 1 & -1 & -1 & 1 \end{bmatrix}$$

For the lattice speed of sound $c_s = 1/\sqrt{3}$, Maxwell–Boltzmann distribution function (f_α^{eq}) is defined as follows [7]:

$$f_\alpha^{eq} = w_\alpha \rho \left[1 + \frac{e_\alpha \cdot u}{c_s^2} + \frac{(e_\alpha \cdot u)^2}{2c_s^4} - \frac{(u \cdot u)}{2c_s^2} \right] \tag{5}$$

u is defined as the velocity, w_α is the weighting coefficients given by $w_0 = 1/3$, $w_{1\sim6} = 2/36$ and $w_{7\sim18} = 1/36$ for D3Q19 model, e_α is the discrete velocity vector in α direction ($\alpha = 0, \ldots, 18$), and ρ is the lattice density.

In this study, a multi-relaxation time (MRT), LBM-based model was implemented to overcome some defects of BGK model including fixed ratio of kinematic, bulk viscosities and a fixed Prandtl number which cause instabilities at high Reynolds numbers [8]. In this regard, Equation (3) was modified to Equation (6) considering MRT scheme as follows:

$$f_\alpha(x + e_\alpha \delta t, t + \delta t) - f_\alpha(x, t) = -M_{\alpha\gamma}^{-1} \hat{S}_{\gamma k}(m_k(x, t) - m_k^{eq}(x, t)) \tag{6}$$

where $m_k(x, t)$, $m_k^{eq}(x, t)$, M and $\hat{S}$ indicate vectors of moments, their equilibrium functions, the transform matrix and collision matrix, respectively.

Mappings between moment and distribution functions were performed by linear transformation as follows:

$$m = M. [f_0, f_2, \ldots, f_{18}]^T \text{ and } [f_0, f_2, \ldots, f_{18}] = M^{-1}m \tag{7}$$

The Equilibrium distribution function must satisfy conservation of mass and momentum [9]. Therefore, mass and momentum were conserved by Equations (8) and (9), respectively:

$$\rho = \sum_{\alpha=0}^{\alpha=18} f_\alpha^{eq} = \sum_{\alpha=0}^{\alpha=18} f_\alpha \tag{8}$$

$$Pu = \sum_{\alpha=0}^{\alpha=18} f_\alpha^{eq} e_\alpha = \sum_{\alpha=0}^{\alpha=18} f_\alpha e_\alpha \tag{9}$$

The transformation matrix M for D3Q19 is defined as the following:

$$\tag{10}$$

M

$$
M = \begin{bmatrix}
1 & 1 & 1 & 1 & 1 & 1 & 1 & 1 & 1 & 1 & 1 & 1 & 1 & 1 & 1 & 1 & 1 & 1 & 1 \\
-3 & -11 & -11 & -11 & -11 & -11 & -11 & 8 & 8 & 8 & 8 & 8 & 8 & 8 & 8 & 8 & 8 & 8 & 8 \\
12 & -4 & -4 & -4 & -4 & -4 & -4 & 1 & 1 & 1 & 1 & 1 & 1 & 1 & 1 & 1 & 1 & 1 & 1 \\
0 & 1 & -1 & 0 & 0 & 0 & 0 & 1 & -1 & 1 & -1 & 1 & -1 & 1 & -1 & 0 & 0 & 0 & 0 \\
0 & -4 & 4 & 0 & 0 & 0 & 0 & 1 & -1 & 1 & -1 & 1 & -1 & 1 & -1 & 0 & 0 & 0 & 0 \\
0 & 0 & 0 & 1 & -1 & 0 & 0 & 1 & 1 & -1 & -1 & 0 & 0 & 0 & 0 & 1 & -1 & -1 & -1 \\
0 & 0 & 0 & -4 & 4 & 0 & 0 & 1 & 1 & -1 & -1 & 0 & 0 & 0 & 0 & 1 & -1 & -1 & -1 \\
0 & 0 & 0 & 0 & 0 & 1 & -1 & 0 & 0 & 0 & 0 & 1 & 1 & -1 & -1 & 1 & 1 & -1 & -1 \\
0 & 0 & 0 & 0 & 0 & -4 & 4 & 0 & 0 & 0 & 0 & 1 & 1 & -1 & -1 & 1 & 1 & -1 & -1 \\
0 & 2 & 2 & -1 & -1 & -1 & -1 & 1 & 1 & 1 & 1 & 1 & 1 & 1 & 1 & -2 & -2 & -2 & -2 \\
0 & -4 & -4 & 2 & 2 & 2 & 2 & 1 & 1 & 1 & 1 & 1 & 1 & 1 & 1 & -2 & -2 & -2 & -2 \\
0 & 0 & 0 & 1 & 1 & -1 & -1 & 1 & 1 & 1 & 1 & -1 & -1 & -1 & -1 & 0 & 0 & 0 & 0 \\
0 & 0 & 0 & -2 & -2 & 2 & 2 & 1 & 1 & 1 & 1 & -1 & -1 & -1 & -1 & 0 & 0 & 0 & 0 \\
0 & 0 & 0 & 0 & 0 & 0 & 0 & 1 & -1 & -1 & 1 & 0 & 0 & 0 & 0 & 0 & 0 & 0 & 0 \\
0 & 0 & 0 & 0 & 0 & 0 & 0 & 0 & 0 & 0 & 0 & 0 & 0 & 0 & 0 & 1 & -1 & 1 & 1 \\
0 & 0 & 0 & 0 & 0 & 0 & 0 & 0 & 0 & 0 & 0 & 1 & -1 & -1 & 1 & 0 & 0 & 0 & 0 \\
0 & 0 & 0 & 0 & 0 & 0 & 0 & 1 & -1 & 1 & -1 & -1 & 1 & -1 & 1 & 0 & 0 & 0 & 0 \\
0 & 0 & 0 & 0 & 0 & 0 & 0 & -1 & -1 & 0 & 1 & 0 & 0 & 0 & 0 & 1 & -1 & -1 & -1 \\
0 & 0 & 0 & 0 & 0 & 0 & 0 & 0 & 0 & 0 & 0 & 1 & 1 & -1 & -1 & -1 & -1 & 1 & 1
\end{bmatrix}
$$

The corresponding macroscopic moments vector are:

$$m_\alpha = (m_0, m_1, \dots, m_{18})^T \tag{11}$$

Diagonal matrix $\hat{S}$ is defined as follows:

$$\hat{S} = \text{diag}\,(0, 1.19, 1.4, 0, 1.2, 0, 1.2, v, 1.4, v, v, v, 1.98, 1.98, 1.98) \tag{12}$$

where v is physical viscosity and (m^{eq}) is equilibrium moments matrix, as shown below:

$$m_k^{eq} = \left(m_0{}^{eq},\ m_1{}^{eq}, \dots, m_{18}^{eq} \right)^T \tag{13}$$

The equilibrium moments in Equation (13) were obtained as follows:

$$m_0^{eq} = \rho,\ m_1^{eq} = -11\rho + \frac{19}{\rho}\left(j_x{}^2 + j_y{}^2 + j_z{}^2 \right),\ m_2^{eq} = \frac{-475}{63}\frac{1}{\rho}\left(j_x{}^2 + j_y{}^2 + j_z{}^2 \right) \tag{14}$$

$$m_3^{eq} = j_x,\ m_4^{eq} = -\frac{2}{3}j_x,\ m_5^{eq} = j_y,\ m_6^{eq} = -\frac{2}{3}j_y,\ m_7^{eq} = j_z, \tag{15}$$

$$m_8^{eq} = -\frac{2}{3}j_z,\ m_9^{eq} = \frac{1}{\rho}\left[2j_x^2 - \left(j_y^2 + j_z^2 \right) \right], \tag{16}$$

$$m_{10}^{eq} = 0,,\ m_{11}^{eq} = \frac{1}{\rho}\left[j_y^2 - j_z^2 \right],\ m_{12}^{eq} = 0, \tag{17}$$

$$m_{13}^{eq} = \frac{1}{\rho} j_x j_y, \; m_{14}^{eq} = \frac{1}{\rho} j_y j_z, \; m_{15}^{eq} = \frac{1}{\rho} j_x j_z \;, \tag{18}$$

$$m_{16}^{eq} = m_{17}^{eq} = m_{18}^{eq} = 0 \;, \tag{19}$$

The momentum $j = (j_x, j_y, j_z)$ was defined as follows:

$$j_x = \rho u_x, j_y = \rho u_y, j_z = \rho u_z \tag{20}$$

> ➤ **Lattice Boltzmann method & Large Eddy simulation**

In this study, turbulent modeling was performed via Large Eddy Simulation employing the Smagorinsky subgrid scale model. The physical viscosity is a superposition of the molecular kinematic viscosity (v_{mol}) and turbulent viscosity (v_{turb}), related to the length scale or lattice size (Δ_x). Therefore, collision time (τ) was altered as the following [10]:

$$\tau = \tau_{mol} + \tau_{turb} \tag{21}$$

The molecular and turbulent collision time in equation (21) were obtained as the following[11,12].

$$\tau_{mol} = 3v_{mol} + 0.5 \tag{22}$$

$$\tau_{turb} = 0.5 \left(\sqrt{\tau_{mol}^2 + \left((C_s\Delta_x)^2 \frac{\Delta_t}{C_s} 4\sqrt{2}\tau\overline{\Pi} \right)} - \tau_{mol} \right) \tag{23}$$

Equation (22) links between viscosity and collision time (relaxation time) within the LBM framework and is derived from Chapman-Enskog analysis[11,12]. C_s and $\overline{\Pi}$ are the Smagorinsky constant and magnitude of second-order non equilibrium moment, respectively. Total viscosity, v, is given as[10]:

$$v = v_{mol} + v_{turb} = \frac{1}{3}\left(\tau - \frac{1}{2}\right)c^2\delta_t = \frac{1}{3}\left(\tau_{mol} + \tau_{turb} - \frac{1}{2}\right)c^2\delta_t \tag{24}$$

❖ **Appendix A₃: Lumped parameter model**

➤ **Input parameters and patient-specific parameter estimation**

The lumped parameter algorithm uses the following input parameters: forward left ventricular outflow tract stroke volume (*Forward LVOT-SV*), cardiac cycle duration (T), ejection time (T_{EJ}), ascending aorta area (A_{AO}), left ventricle outflow tract area (A_{LVOT}), aortic valve effective orifice area ($EOA|_{AV}$), mitral valve effective orifice area ($EOA|_{MV}$), , the effective orifice area of the COA ($EOA|_{coa}$), aortic cross-sectional area downstream of the COA (A), grading of the severity of aortic and mitral valves regurgitation and systolic and diastolic blood pressures.

1) Flow inputs: The algorithm uses only one measured flow parameter as an input: forward left ventricle stroke volume (*Forward LVOT-SV*). *Forward LVOT-SV* is defined as the volume of blood that passes through the LVOT cross sectional area every time the heart beats as the following:

$$Forward\ LV\text{-}SV = A_{LVOT}\ VTI_{LVOT} = \frac{\pi(D_{LVOT})^2}{4} VTI_{LVOT} \tag{25}$$

where D_{LVOT}, A_{LVOT}, and VTI_{LVOT} are LVOT diameter, LVOT area, and LVOT velocity-time integral, respectively.

2) Time inputs: Cardiac cycle time (T) and ejection time (T_{EJ}) were measured using Doppler echocardiography.

3) Aortic valve and mitral valve inputs: To model blood flow in forward direction, the algorithm requires aortic valve effective orifice area ($EOA|_{AV}$), mitral valve effective

orifice area ($EOA|_{MV}$), ascending aorta area (A_{AO}) and left ventricle outflow tract area (A_{LVOT}). $EOA|_{AV}$, A_{AO}, A_{LVOT} were calculated using the following equations:

$$EOA|_{AV} = \frac{\text{Forward LVOT-SV}}{VTI_{AO}} \tag{26}$$

$$A_{AO} = \frac{\pi(D_{AO})^2}{4} \tag{27}$$

$$A_{LVOT} = \frac{\pi(D_{LVOT})^2}{4} \tag{28}$$

where VTI_{AO}, D_{AO} and D_{LVOT} are the velocity time integral in the ascending aorta (amount of the blood flow going through the aorta), ascending aorta diameter and LVOT diameter, respectively.

Moreover, mitral valve is approximately an ellipse and its area was quantified using the following equation where d_1 and d_2 are mitral-valve diameters measured in the apical two-chamber and apical four-chamber views, respectively.

$$EOA|_{MV} = \frac{\pi d_1 d_2}{4} \tag{29}$$

4) Grading of aortic and mitral valve regurgitation severity inputs: To model blood flow in the reverse direction, the algorithm requires grading of aortic and mitral valve regurgitation severity (e.g., regurgitant effective orifice area of aortic valve and regurgitant effective orifice area of mitral valve) that were measured by Doppler echocardiography.

5) Systolic and diastolic blood pressures measured using a sphygmomanometer are additional input parameters for the algorithm.

6) Parameter estimation for systemic circulation: Parameters R_{SA}, C_{SAC}, and C_{ao} were optimized so that the aorta pressure calculated using the model matched the patient's systolic and diastolic brachial pressures measured using a sphygmomanometer (see Computational algorithm and Patient-specific response optimization sections for details).

7) Simulation execution: Please see the computational algorithm section.

References
(Used in appendix)

1   Garcia, D. Robust smoothing of gridded data in one and higher dimensions with missing values. *Computational statistics & data analysis* **54**, 1167-1178 (2010).

2   Garcia, D. A fast all-in-one method for automated post-processing of PIV data. *Experiments in fluids* **50**, 1247-1259 (2011).

3   Muth, S., Dort, S., Sebag, I. A., Blais, M.-J. & Garcia, D. Unsupervised dealiasing and denoising of color-Doppler data. *Medical image analysis* **15**, 577-588 (2011).

4   Craven, P. & Wahba, G. Smoothing noisy data with spline functions. *Numerische mathematik* **31**, 377-403 (1978).

5   Bhatnagar, P. L., Gross, E. P. & Krook, M. A model for collision processes in gases. I. Small amplitude processes in charged and neutral one-component systems. *Physical review* **94**, 511 (1954).

6   Mohamad, A. A. *Lattice Boltzmann method: fundamentals and engineering applications with computer codes*. (Springer Science & Business Media, 2011).

7   Sadeghi, R., Khodaei, S., Ganame, J. & Keshavarz-Motamed, Z. Towards non-invasive computational-mechanics and imaging-based diagnostic framework for personalized cardiology for coarctation. *Scientific Reports* **10**, 1-19, doi:10.1038/s41598-020-65576-y (2020).

8   d'Humieres, D. Generalized lattice-Boltzmann equations. *Progress in Astronautics and Aeronautics* **159**, 450-450 (1994).

9   Sukop, M. & DT Thorne, J. *Lattice Boltzmann Modeling* (Springer, Berlin, Heidelberg, 2006).

10   Nathen, P., Gaudlitz, D., Krause, M. & Kratzke, J. in *21st AIAA Computational Fluid Dynamics Conference. American Institute of Aeronautics and Astronautics.*

11   Guo, Z. & Shu, C. *Lattice Boltzmann method and its application in engineering*. Vol. 3 (World Scientific, 2013).

12   Krüger, T. *et al.* The lattice Boltzmann method. *Springer International Publishing* **10**, 4-15 (2017).